Three-dimensional Deformation and Stress Models:

Exploring One-Thousand Years of Earthquake History Along the San Andreas Fault System

by

Bridget Renee Smith

1857 M7.9 Fort Tejon Earthquake modeled velocity and displacements

UNIVERSITY OF CALIFORNIA, SAN DIEGO

SCRIPPS INSTITUTION OF OCEANOGRAPHY

2005

UNIVERSITY OF CALIFORNIA, SAN DIEGO

Three-dimensional Deformation and Stress Models:
Exploring One-Thousand Years of Earthquake History Along the San Andreas Fault System

A dissertation submitted in partial satisfaction of the requirements for the degree
Doctor of Philosophy in Earth Sciences

by

Bridget Renee Smith

Committee in charge:

David T. Sandwell, Chair
Bruce Bills
Steve Cande
Yuri Fialko
Catherine Johnson
Xanthippi Markenscoff

2005

The dissertation of Bridget Renee Smith is approved, and it is
acceptable in quality and form for publication on microfilm:
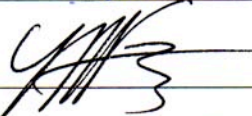
Chair

University of California, San Diego

2005

For my parents –
although I have never been a student in your classrooms,
you will always be my most treasured teachers of life.

TABLE OF CONTENTS

Chapter 1.   An Introduction to the San Andreas Fault System: Geologic, Geodetic, and Seismic Observations, Fault Modeling Techniques, and Stress Triggering………....1

Chapter 2. Coulomb Stress Along the San Andreas Fault System………..…………………23

Computer movie animations on file at Mandeville Special Collections.

LIST OF FIGURES AND TABLES

Chapter 5.

ACKNOWLEDGEMENTS

I have come to learn that graduate school is a lengthy and tedious journey of both scientific failures and successes. Yet it is also a real-life training exercise in communication and expression, learning and teaching, patience and consistency, and perhaps most importantly, hard work, focus, and commitment. While I proudly accept responsibility for the work and the time that went into this thesis, many others deserve recognition for helping me along the way, for teaching me the rules of good science, and for motivating me to do my best.

First, I would like to thank my advisor, David Sandwell, who graciously welcomed me into his lab, provided me with a project that was strangely, yet perfectly suited for me, and who never gave up on me and my disability to effectively program in Fortran (thanks Dave!). Over the years I have come to appreciate Dave's special knack for making even the most difficult of tasks seem less intimidating; the words "it's easy!" will forever ring in my head. I shall consider myself lucky if a tiny bit of Dave's intuitive approach, creative style, and effortless enthusiasm towards science has rubbed off on me over the years. If only the surfing-bug, inspired by the blur of orange surfboard running by the lab window, would have rubbed off on me as well! Dave, it has been both a pleasure and an honor to work with you – thank you for your time, your encouragement, and your countless words of support over the past five years.

I would also like to acknowledge the members of my dissertation committee, who have continually supported my work and made many important recommendations. I thank Yuri Fialko for his interest in my research and his insightful suggestions on how to make my modeling efforts more understandable and acceptable to the fault-modeling community. I thank Catherine Johnson for the many opportunities that she has extended me over the years and for showing me how great the combination of a friendly face and a role model can be. I would also like to thank Bruce Bills for his consistent interest in my research and for always having an open door and a listening ear. Donna Blackman has been monitoring my progress since the beginning, having been one of my first-year Departmental committee members; I thank her for overlooking my first-year defects and for supporting my work in the years following. I would also like to thank Steve Cande and Xanthippi Markenscoff for their additional encouragement and interest in my research.

I would never have made it past my first year of grad school if it weren't for the help of my fellow first-years, Christine Reif, Scott Nooner, and Jim Behrens. I thank Jim for providing a bit of laughter amidst the many times that I wanted to scream. I thank Scott for his consistent patience during all of the times when he could have left the rest of us in the dust. And Christine, thank you for your cheerful laugh, sense of humor, and enduring friendship. I owe you many things (including my first light-bulb moment when it came to P-waves!).

While my Sandwell lab-mates have come and gone over the years, I have many to acknowledge: Allison Jacobs, Suzanne Lyons, Lydie Sichoix, Davis Thomsen, JJ Becker, Karen Lutrell, and Robert Kern. Thank you all for making the lab a lighthearted, colorful, and fun place to work. In particular, thank you for your patience, particularly during those days when I appeared oblivious to all forms of human life due to the latest round of computing distractions. And thank you for the help, motivation, and various areas of expertise that have saved me many headaches over the years. I would like to especially thank Allison Jacobs, who I first met in the classroom, became friends with in the lab, and have remained so even though computers, offices, and advisors (amongst many other things!) have changed. Thank you for the beach runs, long chats, traveling adventures, and the many inside jokes. You have made the past four years both fun and memorable for me.

I would also like to extend a much deserved thank you to Liz Gil and Karen Scott, who help make all of our lives run smoothly every day and who can be the best source for laughter and good stories. Special

x

thanks to Debi Kilb as well, to whom I am forever indebt when it comes to proofreading papers. Thank you for your cheerfulness, approachability, and enthusiasm. Thanks also to Jen Bowen for providing the best-sounding voice at IGPP that helped cast my science into something truly fun. And a sincere thank you also goes out to Jake Perez, who has been there for me more times that I can count. From poster printing issues to annoying car troubles, Jake has always provided a lending hand without lifting an eyebrow. And while there are too many to list here, thanks to all of my fellow grad students, both to those that have come before me and to those that will soon follow – you guys are an entertaining, stimulating, and memorable group of friends. Each of you has brought something different to SIO, of which I have learned from and modeled myself after.

I would never have made the big move to grad school in the first place without the support of my family, who has seen me through the days of wanting to own my own dance studio to plans for studying the stars. My family has been my lifeline through all of these years, providing both a foundation of support to keep me driven and the occasional thump on the head to keep me grounded. I would like to thank my grandparents for their never-ending interest in both my professional *and* my personal life, their reliable support for all of my endeavors, and for always making family get-togethers that much more lively! I have my little sister, Brooke, to thank for teaching me how to take life a little less seriously at times (*I'm still practicing*) and for reminding me how important both adventures in life and the love of family really are. Together, my parents have prepared me for graduate school over the years (whether they knew it or not!) by teaching me how to set goals, make plans, and then simply go out and do the work. I would like to thank my dad for initially inspiring me to take an interest in science, as he has always impressed me with his common sense and clever knack for science. His fatherly coaching has taught me to keep my head up when times get tough and that a little ACDC, particularly when the nerves are raddled, never hurts either. I have my mother to thank for teaching me to truly care about my work and to take pride in all that I have accomplished. I also thank my mom for her meticulous attention to detail and tenacious character, of which I have undoubtedly inherited and have found particularly valuable for getting things accomplished in grad school! Mom and Dad, thank you both for making all the little events of my life seem like grand triumphs and for being my biggest supporters. I feel very fortunate to have parents like you.

And lastly, I would like to thank Jasper, my best friend and true companion. Perhaps it is just simple coincidence, but after you became a part of my life, everything else (including this thesis work!) just seemed to get easier. For nearly four years, not a day has passed in which you weren't there for me – whether it be to hash out the Gauss-Newton method over Saturday morning coffee (or tea), strawberries to assist with night-before-qualifying printing catastrophes, Roberto's (okay, El Cotixan too) runs, and for getting me through those days of stress and self-doubt, you have been my rock (*no pun intended*). You have taught me so much and for that I will always be thankful.

VITA

May 19, 1977	Born, Phoenix, Arizona
1997 - 1999	Research Intern, Lowell Observatory NASA Space Grant
1997	Research Intern, Stanford Linear Accelerator Center
1999	B.S., *magna cum laude*, Astronomy and Physics Northern Arizona University
1998	Research Intern, NASA Ames
1999 - 2005	Research Assistant, Scripps Institution of Oceanography University of California, San Diego
2000-2003	Teaching Assistant, Scripps Institution of Oceanography University of California, San Diego
2005	Ph.D., University of California, San Diego

PUBLICATIONS

Smith, B., and D.T. Sandwell, A Model of the Earthquake Cycle Along the San Andreas Fault System for the Past 1000 Years, *submitted to J. Geophys. Res*, 2005.

Smith, B., and D.T. Sandwell, A 3-D Semi-Analytic Viscoelastic Model for Time-Dependent Analyses of the Earthquake Cycle, *J. Geophys. Res.*, 109, doi:10.1029/2004JB003185, 2004.

Sandwell, D., and B. Smith, California Earthquakes, to be included in: *Our Changing Planet: A view from Space*, editors, King, Partington and Williams, submitted 2004.

Smith, B., and D.T. Sandwell, Coulomb Stress Along the San Andreas Fault System, *J. Geophys. Res*, 108 (B6), doi:10.1029/2002JB002136, 2003.

Smith, B., and D.T. Sandwell, Accuracy and Resolution of Shuttle Radar Topography Mission Data, *Geophys. Res. Lett.*, 30 (9), doi:10.1029/2002GL016643, 2003.

Sandwell, D.T., L. Sichiox, and B. Smith, The 1999 Hector Mine Earthquake, Southern California: Vector near-field displacements from ERS InSAR, *Bull. Seismol. Soc. Am.*, 92, 1341-1354, 2002.

ABSTRACTS

Smith, B.R., and D.T. Sandwell, A 3-D Semi-Analytic Viscoelastic Model of the San Andreas Fault System: A 1000-year Perspective of the Earthquake Cycle, *EOS Trans. AGU,* Fall Meet. Suppl., *85(47), G14A-02*, 2004.

Lutrell, K., B.R. Smith, D.T. Sandwell, and Y. Fialko, Models of Afterslip and Viscoelastic Response following the Landers and Hector Mine Ruptures, *EOS Trans. AGU,* Fall Meet. Suppl., *85(47), G13A-0794*, 2004.

Smith, B.R., and D.T. Sandwell, A 3-D Semi-Analytic Viscoelastic Model for Time-Dependent Analyses of the Earthquake Cycle: A 1000-year Perspective of the San Andreas Fault System, SCEC Annual Meeting, 2004.

Smith, B.R., and D.T. Sandwell, Time-Dependent Coulomb Stress Along the San Andreas Fault System, *EOS Trans. AGU*, *84*(46), Fall Meet. Suppl., G31B-0708, 2003.

Smith, B.R., and D.T. Sandwell, A 4-D Semi-Analytic Model of Stress Evolution Along the San Andreas Fault System, SCEC Annual Meeting, 2003.

Smith, B.R., and D.T. Sandwell, Magnitude of Deviatoric Stress Along the San Andreas Fault, *EOS Trans. AGU, Spring Meet. Suppl.*, EAE03-A-14336, 2003.

Smith, B.R., D.T. Sandwell, and B. Bills, Estimating SRTM Resolution for Applications of Fault Offset Recovery, *EOS Trans. AGU*, *83*(47), Fall Meet. Suppl., T71E-1221, 2002.

Sandwell, D.T., and B.R. Smith, Variations in Normal Stress Along the San Andreas Fault due to Isostatically Compensated Topography, *EOS Trans. AGU*, *82*(47), Fall Meet. Suppl., G52A-10, 2001.

Smith, B. R., and D. T. Sandwell, Variations in Coulomb Stress Accumulation Along the San Andreas Fault System, *EOS Trans. AGU*, *82*(47), Fall Meet. Suppl., G52A-12 *invited*, 2001.

Sandwell, D.T., L. Sichiox, and B.R. Smith, Hector Mine Earthquake: Vector Coseismic Displacement from ERS InSAR, *EOS Trans. AGU*, *81*(48), Fall Meet. Suppl., S61A-02, 2000.

FIELDS OF STUDY

Major Field: Earth Science (Geophysics)

Studies in Geodynamics
Professor David Sandwell

Studies in Geophysical Data Analysis
Professors Duncan Agnew and Frank Vernon

Studies in Gravity and Geomagnetism
Professor Cathy Constable

Studies in Marine Geophysics
Professors Leroy Dorman and John Hildebrand

Studies in Physics of Earth Materials
Professor Duncan Agnew

Studies in Satellite Remote Sensing
Professor David Sandwell

Studies in Seismology
Professor Peter Shearer

Studies in Tectonics of the Planets
Professor Catherine Johnson

ABSTRACT OF THE DISSERTATION

Three-dimensional Deformation and Stress Models:
Exploring One-Thousand Years of Earthquake History Along the San Andreas Fault System

by

Bridget Renee Smith
Doctor of Philosophy in Earth Sciences
University of California, San Diego, 2005

Professor David T. Sandwell, Chair

Modern crustal deformation measurements of the San Andreas Fault System have had a significant impact on present day tectonic studies. Yet while these measurements reveal a wealth of information about *how* the Earth is presently deforming, they unfortunately neglect to provide the answers for *why*. In addition, current measurements alone cannot determine future tectonic behavior of the Earth, nor can they account for deformation of the past. For these reasons, many disciplines of Earth science rely on the use of mathematical, physics-based models. Applied to crustal deformation studies, fault models constrained by geologic, geodetic, and seismic data can provide valuable insights into the characteristics of faults and their behaviors over time. Based on observations of the past, models can also provide estimates of future deformation and seismic hazards, a vital resource for communities living near active fault zones.

This dissertation presents a new and efficient approach to fault modeling that allows for deformation and stress calculations spanning not only large study areas (thousands of kilometers), but also long time periods (thousands of years). Chapter 1 provides background, motivation, and conclusions met by this modeling work when applied to the San Andreas Fault System. Chapter 2 documents the initial derivation of the model and reveals the steady-state behavior of the San Andreas Fault System through use of GPS measurements. Chapter 3 explores the technical details of incorporating time-dependence into the model. Using this model, Chapter 4 revisits the San Andreas Fault System, this time investigating the deformation and stress resulting from earthquakes over the past 1000 years, again constrained by present-day GPS measurements. Lastly, Chapter 5 presents the results of a brief, intermediate study of this thesis work, pertaining to the resolution capabilities of the Shuttle Radar Topography Mission data.

Chapter 1

The San Andreas Fault System: Geologic, Geodetic, and Seismic Observations, Fault Modeling Techniques, and Stress Triggering

1.1 Introduction

The sudden surge of energy unleashed by a major earthquake is one of nature's most destructive forces. While their occurrence is often unexpected and seemingly elusive, we must be reminded that earthquakes are simply an accomplice to a much grander process that has been plaguing Earth for millions of years – the process of plate tectonics. Tectonic plate motions and consequent earthquakes can be actively observed along the western United States, where a popular transform boundary defines the rendezvous junction of the Pacific Plate and the North American Plate. This plate boundary, commonly known as the San Andreas Fault System, has been vigorously deforming much of California for over the past several million years.

Today, the San Andreas Fault System is the most widely researched fault system in the world. It has long been recognized as a natural laboratory for investigating the many facets of plate boundary deformation revealed by geologic, geodetic, and seismic observations. It is through these observations that Earth scientists have uncovered unique fault system behaviors spanning many lengths of time. For example, California seismicity data reveal hundreds of micro-earthquakes generated by the San Andreas Fault System each week; these data record the immediate ~ 1000s of earthquake behavior. Likewise, continuous monitoring of surface motion using space geodetic techniques (i.e., GPS, InSAR) over the past few decades has produced observations ranging from mm-scale yearly displacements to meter-sized offsets from major earthquake events; these data provide information about fault zone behavior taking place on the order of ~ 1-10 years. And finally, from exposed geology, we can map nearly 1700 km of San Andreas Fault System and can estimate how it evolved and how fast it moved over time; these data recount the history of the San Andreas for over the past ~10,000 – 10^6 years. However, while there is indeed a wealth and variety of seismo-tectonic data spanning the San Andreas Fault System over the past million years, there remains a significant observational gap from the point at which geologic inferences end and geodetic observations begin – the temporal period spanning 10-10,000 years.

Sophisticated computer models can significantly help bridge this observational gap. Exploration of earthquake scenarios that span several thousand years, and deform over an equal number of kilometers, requires models that are three-dimensional, time-dependent, and computationally efficient. Models must also be capable of simulating realistic complexities in fault geometry. Results from such models have contributed significantly to our understanding of plate tectonic behavior. For example, they allow estimates to be made of fault conditions, such as stress changes, that we cannot measure in the 'real world'. Combined with measurements from laboratory experiments, seismic studies, and geologic mapping, modeling efforts have also helped identify inherent stress behaviors of the earthquake cycle that can indicate emerging seismic hazards, a major priority of earthquake studies. Combined with today's advanced computer technologies,

the ongoing integration of cutting-edge computer models and complicated deformation problems has become a significant component of present-day earthquake research.

1.2   The Earthquake Cycle

1.2.1   Early Observations

While today's interpretations of crustal motions are based on modernized and evolved theories, scientists have been studying deformation mechanisms in California for nearly a century [e.g., *Lawson*, 1908; *Nobel*, 1927; *Wallace*, 1949].   The first precise measurements of tectonic strain release came from the work of *Harry Fielding Reid* [1910] following the Great San Francisco Earthquake on April 18, 1906 (Figure 1.1). Reid analyzed offsets that accompanied the large event from triangulation stations located along the northern San Andreas Fault. From his observations, the first theory of elastic rebound associated with earthquake behavior was formulated: slow elastic deformation occurs in response to interseismic strain, which is completely and suddenly released during the event of an earthquake (Figure 1.2).
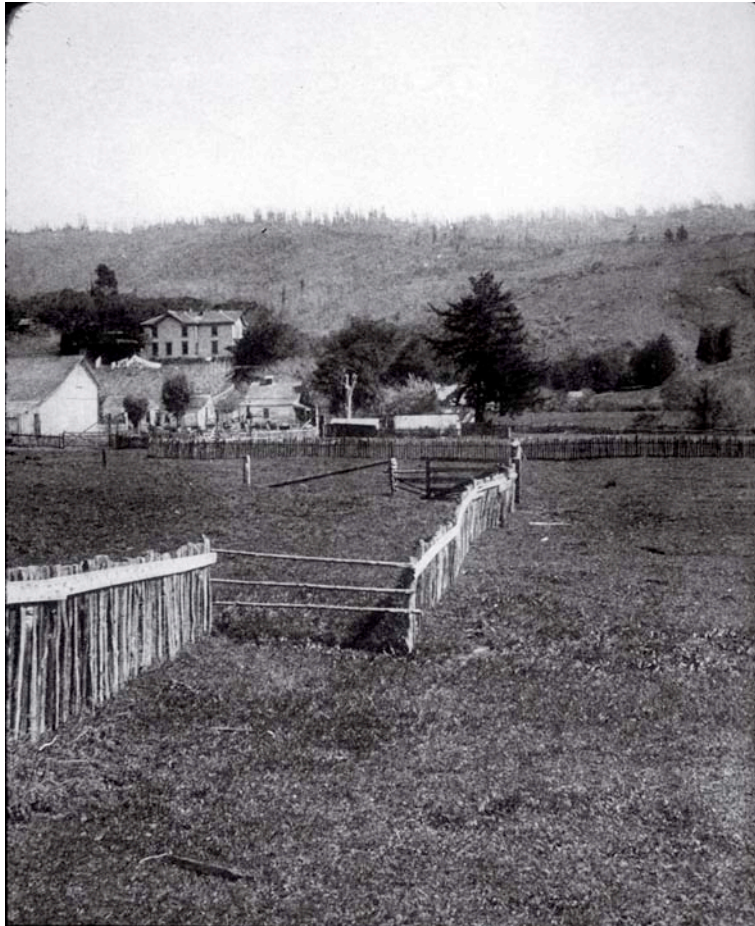
Figure 1.1. Fault rupture from the 1906 San Francisco Earthquake offset this fence by 2.5 meters in Marin County (Woodville, CA).   In this photograph, the fault crack accompanying the earthquake is not easily seen, although the horizontal displacement is obvious.   Photo by C.K. Gilbert, courtesy of the EERC Library/University of California, Berkeley. Used with permission.
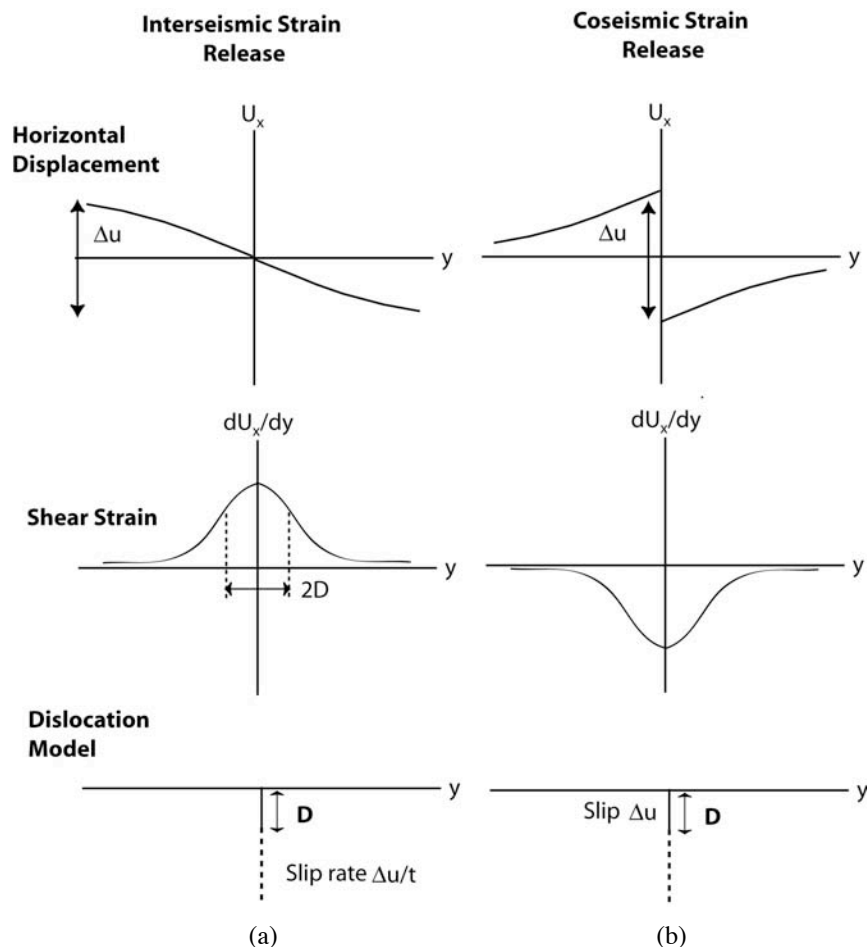
Figure 1.2. Elastic rebound theory. (a) Representation of a 2-D locked fault with deep interseismic slip below depth D, resulting in a steady slip (or displacement) rate and constant strain accumulation. (b) Representation of a 2-D model with slip on a locked fault above depth D, resulting in coseismic horizontal displacement and strain release. Figure modified from *Thatcher* [1986].

Complimentary to these observations, Reid also hypothesized that future earthquakes could be predicted from knowledge of the amount of shear strain accumulation over time and the amount of moment release recorded by prior events:

> To measure the growth of strains, we should build a line of piers, say a kilometer apart, at right angles to the fault….. A careful determination from time to time of the directions of the lines joining successive piers, the differences of level, and the exact distance between them, would reveal any strains which might be developing along the region the line of pier crosses….. Measures of the class described would be extremely useful, not only for the purpose of prediction, but also to reveal the nature of the earth-movements taking place, and thus lead to a better understanding of the causes of earthquakes. [*Reid*, 1910]

While Reid's strategy for earthquake prediction did not entirely hold, to first order, his hypotheses of strain accumulation and stress release were correct. His primitive, yet insightful plans for observing earthquake-related deformation were also well heeded. Following Reid's lead, most present-day geodetic surveys

straddle the San Andreas Fault with objectives of obtaining measurements that may help answer many questions related to the earthquake cycle.

1.2.2 Present-day Theory

The expression "earthquake cycle", in its most simplest form, is used to refer to the cyclic behavior of accumulation and release of stress and strain on a fault. After nearly one-hundred years of fault zone observations following Reid's elastic rebound theory, we now know that earthquakes are not completely periodic in nature and that subsequent events are not carbon copies of one another.   However, in general, many fault zones exhibit similar behaviors confirmed by earthquake cycle predictions [*Thatcher*, 1983]. These behaviors are often divided into three distinct phases: interseismic, coseismic, and postseismic. There has also been speculation that a possible fourth phase, the preseismic phase, might be observable, although this period of deformation has thus far been poorly documented.

Variations of crustal motions throughout the earthquake cycle can be attributed to many factors. Primarily though, these changes are due to temperature and pressure changes at depth as different layers of the Earth's crust respond at different time scales to tectonic forces. Because rocks at depths greater than 30 km are typically more ductile, tectonic plates are theorized to slide freely past one another at these depths, thus avoiding the accumulation of large amounts of stress over time. Conversely, shallow portions of the crust are colder, more brittle, and often remain locked because of friction and surface imperfections. The period in which shallow faulted sections remain locked while deeper layers slowly and freely slip is defined as the interseismic period (Figure 1.2a). Observed as smooth, largely unnoticeable displacement at the surface of the Earth, this period can last for hundreds of years. Over time, stress and strain slowly build and eventually surpass the frictional strength of the rocks, causing the fault to rupture. This sudden release of energy, defined as the coseismic period (Figure 1.2b), results in observable shaking, large ground offsets, and a sudden release of shear strain associated with an earthquake. While this loading/release process seems fairly straightforward, the cycle is complicated by a subsequent postseismic period. This behavior is identified by transient phenomena that occur as the lower crust and mantle slowly relax their grip on the upper crust. During this stage, the fault zone continues to deform, although much less dramatically. Stress concentrations dissipate at the margins of the rupture and aftershocks are generated at a decaying rate. Postseismic deformation and stress redistribution may occur over several time scales, although such behavior has thus far been observed for only a few decades. This overall periodic sequence, spanning interseismic, coseismic, and postseismic deformation phases, completes our present understanding of the earthquake cycle process, although it is likely that present day observations have only begun to scratch the surface of these properties.

1.3   The San Andreas Fault Zone

1.3.1   Geologic Observations: 10,000 – 10^6 yrs

For more than 200 million years, California has been the setting of a major plate boundary, and consequently, has been subjected to a turbulent history of deformation. Early on, the boundary was a subduction zone and the site of an oceanic trench along the west coast of present-day continental North America (Figure 1.3). This early history of subduction continued for millions of years, slowly pulling and subducting portions of the Farallon Plate beneath North America. Remnants of this tectonic regime can still be found to both the north and the south of California along the west coasts of the Pacific Northwest
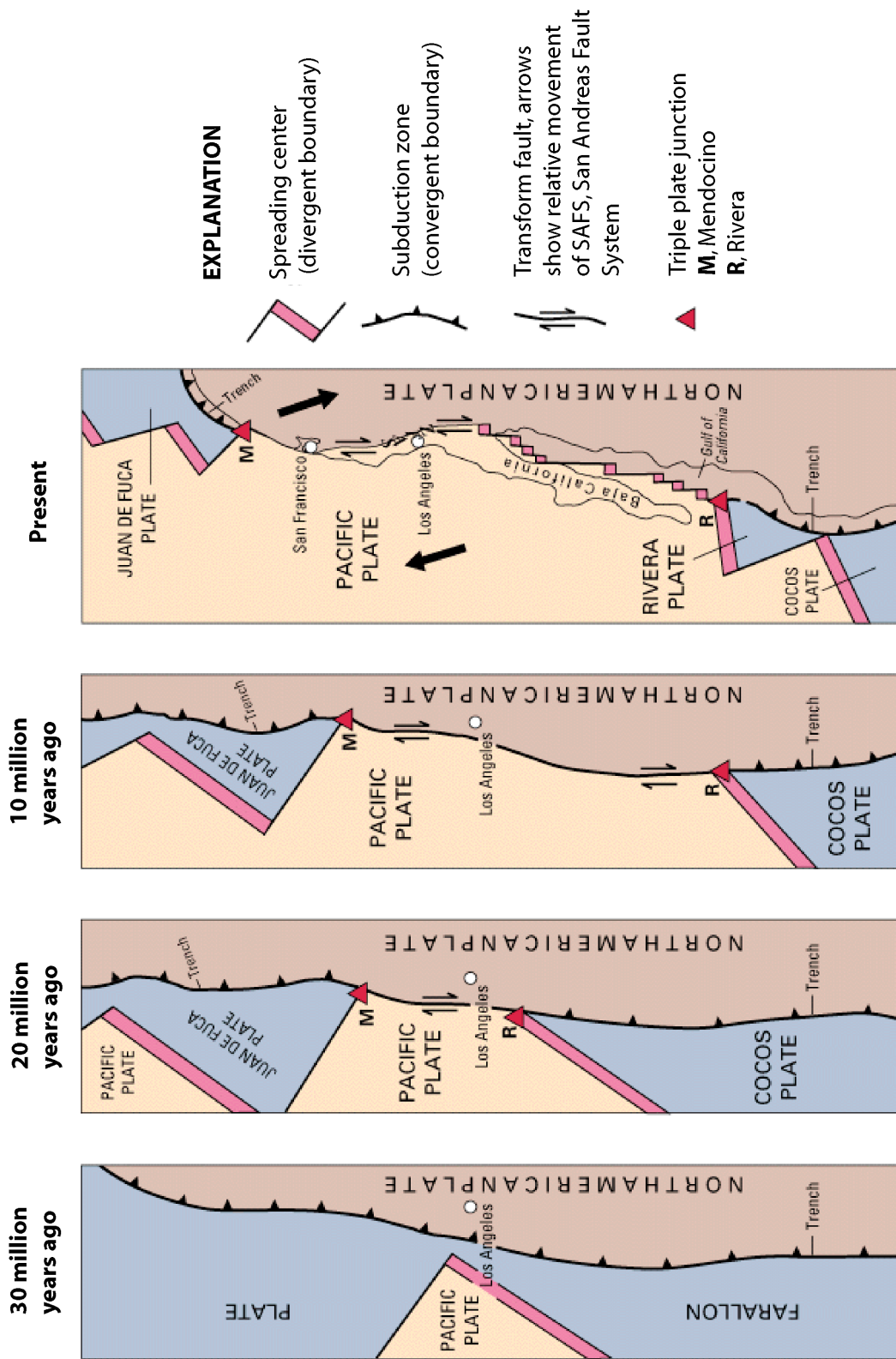
Figure 1.3. North American-Pacific Plate boundary history. Illustration depicts the subduction of the Farallon Plate beneath the North American Plate (30 Ma), the emergence of a primitive transform boundary (20 Ma), further consumption of the Juan de Fuca and Cocos Plates (10 Ma), and the present day transform and rifting boundary of the San Andreas Fault System. Arrows represent the direction of present-day relative motion between the North American and Pacific Plates. Figure modified from USGS Professional Paper 1515, used with permission.

Central/South America. Approximately 30 million years ago, a portion of the East Pacific spreading ridge, separating the Pacific and Farallon plates, began approaching the North American continental margin and eventually encountered the subducting plate boundary. Interaction between the two boundaries eventually destroyed both spreading and subducting mechanisms along most of the boundary and ultimately forced the adaptation of a transform fault boundary - the San Andreas fault [*Wilson*, 1965; *McKenzie and Morgan*, 1969; *Atwater*, 1970].   Although initially developing west of the continental margin, approximately 5 million years ago the San Andreas fault began a series of eastward steps near the Rivera triple junction, where it then jumped ashore and began actively transforming the landscape of the continent [*Dickinson*, 1981]. Coastal California began sliding in a northwestward direction as Baja California began separating from mainland Mexico [*Larson et al.*, 1968]. This behavior is actively observed in present-day California (Figure 1.4). Dominant tectonic features of the region are the northwest-trending San Andreas branch of faults (San Andreas, San Jacinto, Calaveras, Hayward, etc.), the intersection of the east-west trending Garlock fault, and the region of localized deformation spanning the Eastern California Shear Zone to the east.

While geologists have uncovered evidence for variations in slip along many portions of the San Andreas over the last five million years [*Dickson and Snyder*, 1979; *Atwater and Molnar*, 1973; *Minster and Jordan*, 1978], far-field plate motion measurements indicate a steady rate over the past $1\text{-}10^6$ yrs [*Stein*, 1987]. Global plate motion models estimate that approximately 48 mm of relative motion takes place each year [*DeMets et al.*, 1987]. This number can be further broken down, partitioning ~40 mm/yr of plate motion over the primary fault segments of the San Andreas Fault System and another 8 mm/yr to the remaining network of subfaults to the east and west [*WGCEP*, 1995]. Geological excavations of faults have also yielded approximate earthquake dates and locations preserved deep within the layers of the Earth for over the past 1000 years [e.g., *Grant and Lettis*, 2002]. While these observations allow estimates to be made about isolated instances of seismic activity on the San Andreas Fault System, they unfortunately cannot provide information about the conditions leading up to past earthquakes and how the Earth responded to these events.

1.3.2 Geodetic Observations: ~ 1-10 yrs

For nearly 100 years, Earth scientists have been observing crustal deformation through both slow plate motions exhibited by interseismic creep and sudden displacements caused by earthquakes. While triangulation techniques were used during the majority of this period, it was not until the arrival of space-based technologies, beginning approximately 25 years ago, that more modern and accurate contributions were made. Beginning in 1975, large astronomical satellite dishes were deployed around the world for Very Long Baseline Interferometry (VLBI) applications. These instruments provided excellent constraints on global plate motions through interferometric analysis of microwaves emitted by quasars [*Herring et al.*, 1986; *Minster and Jordan*, 1987], but unfortunately proved expensive and awkward to install [*Trialli and Tajima*, 1993]. Nearly ten years later, the Global Positioning System (GPS) was used in California to measure tectonic strains [*Dong and Bock*, 1989]. While originally designed for military navigational purposes, the satellite technique offered an excellent method for Earth science applications due to its cost-effective and extremely accurate crustal measurements. Likewise, in 1992, Interferometric Synthetic Aperture Radar (InSAR) was first used in California to measure deformation associated with the M7.3 Landers Earthquake [*Massonnet et al.*, 1993]. These measurements, while sometimes contaminated by topography or atmospheric conditions, surpass spatially isolated GPS measurements, to some degree, in that data are acquired over an extensive radar swath. Both GPS and InSAR measurements are commonly used today, combined with mathematical models, to infer information about fault geometry, earthquake slip, and
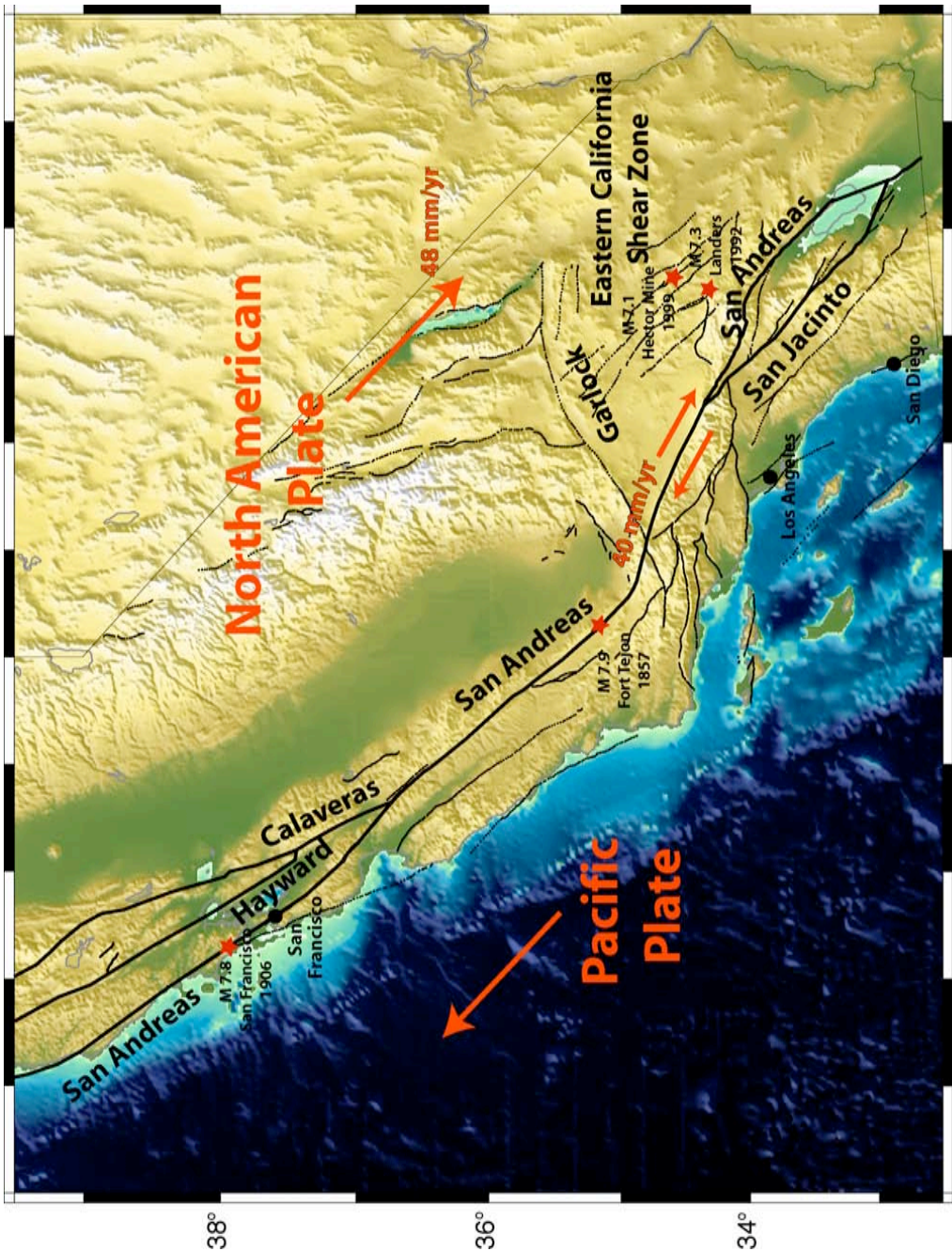
Figure 1.4. San Andreas Fault System tectonics. Regions referenced in the text are the San Andreas fault, San Jacinto fault, Hayward fault, and Calaveras fault segments, the Garlock fault, and the Eastern California Shear Zone. Large red arrows show relative plate motion between the North American and Pacific plates (48 mm/yr), while smaller red arrows show total San Andreas Fault System plate motion (40 mm/yr). Epicenters of the 1857 Fort Tejon, 1906 San Francisco, 1992 Landers, and 1999 Hector Mine earthquakes are identified by red stars.

the mechanical properties of the crust and mantle [e.g., *Feigl et al.*, 1993; *Savage and Svarc*, 1997; *Simons et al.*, 2002].

To obtain GPS data, precise timing measurements are made of radio waves that triangulate between a satellite network of at least four space-based antennas and a network of ground stations. Signals are sent from the satellite to the Earth's surface in order to identify accurate (mm-scale) position information, which can then be transformed into displacements through a sequence of observations. To determine GPS velocities and accurately define strain-rate measurements, a sequence spanning several years is often required. After nearly 20 years of observations, these requirements have been met; today over 1000 GPS monuments are periodically occupied to monitor mm-scale motions of North American-Pacific Plate boundary deformation (Figure 2.2, Chapter 2). Interseismic deformation has been observed over many years [e.g., *Lisowski et al.*, 1991; *Shen et al.*, 2003], while coseismic offsets from recent events such as the 1992 Landers Earthquake and the 1999 Hector Mine Earthquake have also been exposed through GPS measurements [e.g., *Bock et al.*, 1993; *Agnew et al.,* 2002.]. GPS-derived postseismic deformation was first observed following the 1992 Landers event [*Shen et al.*, 1994; *Bock et al.*, 1997; *Savage and Svarc*, 1997] and has become a crucial measurement ever since. The quest for future observations spanning a larger portion of the earthquake cycle (> 20 years) will be generously aided by the continuously operating GPS stations of today (e.g., Southern California Integrated GPS Network, SCIGN) [*Hudnut et al.*, 2001] and through future measurements obtained by the Plate Boundary Observatory (PBO) [*PBO Steering Committee*, 1999].

Interferometric Synthetic Aperture Radar, or InSAR, data are derived by combining the phase differences of two separate radar images acquired from either two different positions or at two different times [*Massonnet and Feigl*, 1998]. Topographic mapping applications from InSAR, for example, have recently provided global high-resolution measurements acquired from NASA's Shuttle Radar Topography Mission [*Farr and Kobrick*, 2001] (Figure 5.1, Chapter 5). InSAR techniques have also been heavily applied toward the detection of small deformations due to volcanoes and earthquakes [e.g., *Massonnet et al.*, 1993; *Massonent et al.*, 1995; *Rosen et al.*, 1996], as well as water and oil-depletion related subsidence [e.g., *Watson et al.*, 2002]. This type of InSAR has also been successful in identifying displacements due to temporal changes associated with the earthquake cycle. Coseismic displacements from recent major earthquakes have been observed by many workers over the past decade [e.g., *Massonnet and Feigl*, 1998; *Zebker et al.*, 1994; *Sandwell et al.*, 2002; *Fialko*, 2004b]. Likewise, postseismic displacements observed from InSAR data have lead to a refined understanding of plate boundary mechanics and have provided much-needed constraints on the role of vertical deformation [e.g., *Pollitz et al.* 2001; *Jacobs et al., 2002; Fialko*, 2004a].

1.3.3 Seismological Observations: < 1000 s

Because earthquake rupture is the direct response of accumulating strain between two tectonic plates, it comes as no surprise that the San Andreas Fault System has provided the backdrop for many significant earthquakes (Figure 4.1, Chapter 4). On average, the system generates thousands of small earthquakes each year. While such continuous activity has contributed to an extensive seismological database over the years, only those events occurring after 1932, when contemporary seismometers were first deployed in California, have been accurately recorded [*WGCEP*, 1995]. For events that have been detected by modern instruments, earthquake epicenters, focal mechanisms, and seismic moments have been identified. These data provide vital information about location and faulting mechanisms of earthquakes, as well as the amount of

instantaneous energy released. Seismic observations also reveal earthquake aftershock activity and track locations of earthquake sequences with time.

While many significant earthquakes have been historically documented on the San Andreas Fault System, two events have emerged over the past 150 years as archetype examples of the "big one", the term typically used by the popular press to infer the worst-case event scenario on the San Andreas fault [*WGCEP*, 1995]. Such events as the M7.9 1857 Fort Tejon Earthquake and the M7.8 1906 San Francisco Earthquake (Figure 1.4), the two largest earthquakes observed on the San Andreas, ruptured 350 and 430 km of the fault, respectively (Figure 4.1, Chapter 4). Major events such as these, consisting of significant moment release (large magnitude) and complimentary rupture length, changed the landscape of both local and far-field regions surrounding the fault. Events of this type can also reveal an immense amount of information due the simple fact that they are easier to record, both locally and globally. Of course, both historical events of 1857 and 1906 occurred prior to the era of modern instrumentation, and therefore data documenting these events are relatively few.

Alternatively, two more recent events, occurring in the Eastern California Shear Zone, have led to revolutionary theories regarding postseismic deformation and stress transfer over the past decade. Although not as significant in terms of rupture length and moment release, both the M7.3 1992 Landers Earthquake and the M7.1 1999 Hector Mine Earthquake have arguably been the best-recorded and densely instrumented events of the modern era (Figure 1.4). Seismological [e.g., *Hauksson*, 1994], geological [e.g., *Sieh et al.*, 1993], and geodetic studies [e.g., *Hudnut et al.*, 1994] have all revealed intriguing, yet often times controversial, evidence for postseismic processes. Aftershock patterns, both in time and space [e.g., *King et al.*, 1994], have also provided the first concrete evidence for stress triggering. These events also offer additional evidence that large earthquakes occur off of the San Andreas and that comprehensive seismic hazard assessments should include not only the primary San Andreas Fault System, but also the surrounding tectonic regions.

1.4 Fault Deformation Models: 10 - 10,000 yrs

1.4.1 Objectives and Necessary Ingredients

Observations of crustal motions, like those discussed in the previous sections, provide direct evidence for an active fault zone yet lack an obvious and testable explanation for such behavior. Consequently, we rely on physics-based models for assistance. Early models were based on Reid's fundamental ideas regarding elastic rebound, but also combined concepts of continuum mechanics, dislocation theory, and mathematical tools such as Green's functions [*Cohen*, 1999]. The basic objectives of these models was to provide an elegant, yet concise, mathematical explanation of how the Earth's crust spatially deforms, and ultimately predict how it will change with time. Thus early models of fault zone behavior focused on static displacements that coincided with earthquakes. Following the establishment of these models, efforts to understand earthquake deformation have since been focused on the behavior that occurs between major seismic events, or during the postseismic-interseismic transition. These models investigate both crustal structure and rheological properties of the Earth's mantle and crust through a variety of postseismic processes. While the physical models described in subsequent sections are primarily based on linear elastic and viscoelastic coupling theories, it should also be noted that alternative models have been proposed by other workers. These include models of deep afterslip [e.g., *Shen et al.*, 1994], poroelastic fluid flow in the upper crust [e.g., *Peltzer et. al*, 1996], fault zone collapse [e.g., *Massonnet et al.*, 1996], and power law flow [e.g., *Freed and Burgmann*, 2004].

A successful model of earthquake-related deformation, in addition to matching observed data, might be described as one that is straightforward, versatile, and computationally efficient. Model solutions should optimally describe deformation in three dimensions to allow for geometric complexities associated with planar (horizontal) and vertical (depth) displacements. Vertical layering is also an attractive model characteristic, as models with vertical structure allow for rheological variations with depth. Time-dependence is a practical attribute, as time-dependent models can be computed for extreme time periods, such as the 10-10000 year period of the earthquake cycle, where no geophysical observations exist. Temporal models can also offer valuable information regarding the relationship between earthquake recurrence interval and postseismic relaxation time. Of course, models reflecting thousands of years of earthquake history can become computationally challenging and thus require more efficient computational methods. Both analytic and numeric approaches to the fault-modeling problem strive to achieve these desirable properties, yet typically sacrifice spatial or temporal resolution, accuracy, or computational efficiency.

1.4.2   Common Approaches: Analytic and Numeric Models

Over the years, analytic methods have provided an intuitive, hands-on approach to solving complicated geophysical problems. Hence initial fault models were based on analytic solutions [*Chinnery*, 1961; *Weertman*, 1964; *Rybicki*, 1971; *Okada*, 1985, 1992] that describe stress, strain, and displacement of a vertical fracture (or fault) in an elastic medium (or half-space). Descriptively, this idealized elastic model simulates fault locking between earthquakes and free slip below that accommodates long-term plate motion at a constant slip rate (Figure 1.5a). More advanced viscoelastic contributions can be credited to the work of *Nur and Mavko* [1974], *Rundle and Jackson* [1977], and *Savage and Prescott* [1978]. These models enhanced the basic elastic solutions to account for the effects of an elastic layer and a time-dependent half-space (Figure 1.5b), thus establishing the first mathematical descriptions of postseismic relaxation following an earthquake. While both types of models can be applied to only the most elementary of situations, many researchers continue to use analytic models due to their intuitive nature, accuracy, and documented success in producing many of the observable features associated with interseismic and coseismic deformation [e.g. *Savage and Burford*, 1973] (Figure 1.2). Yet perhaps the biggest advantage of analytic methods is their computational efficiency, particularly when applied to individual faults or small fault systems. However, purely analytic models, like most approaches, may become computationally prohibitive when representing fault geometry over an extensive region.

Numerical methods extend the basic mathematics of analytic dislocation theory to allow for substantial flexibility in Earth structure and fault geometry. Many offspring of numerical methods have been spawn, such as finite element models, boundary element models, finite-difference models, and matrix propagator methods. Numerical techniques such as these are typically straightforward to program yet are often difficult to verify and lack the intuitive powers of analytic solutions [*Ward*, 1985]. Numerical methods can also be computationally inefficient, particularly when applied to complex problems spanning long temporal periods. Nevertheless, these models have made significant progress in tackling large-scale, complex plate boundary problems [e.g., *Ward*, 1985; *Freed and Lin*, 2001].

1.4.3   The Hybrid Approach: The Fourier Model

From the above discussion, it is obvious that analytic solutions offer simplicity and speed, while numerical methods offer geometrical flexibility. In this thesis, I combine these approaches, a hybrid approach, to achieve both speed and limited flexibility. As a primary component of this thesis work, Fourier analysis is used as a tool to simplify the mathematical problem into one that can be more easily solved and

11
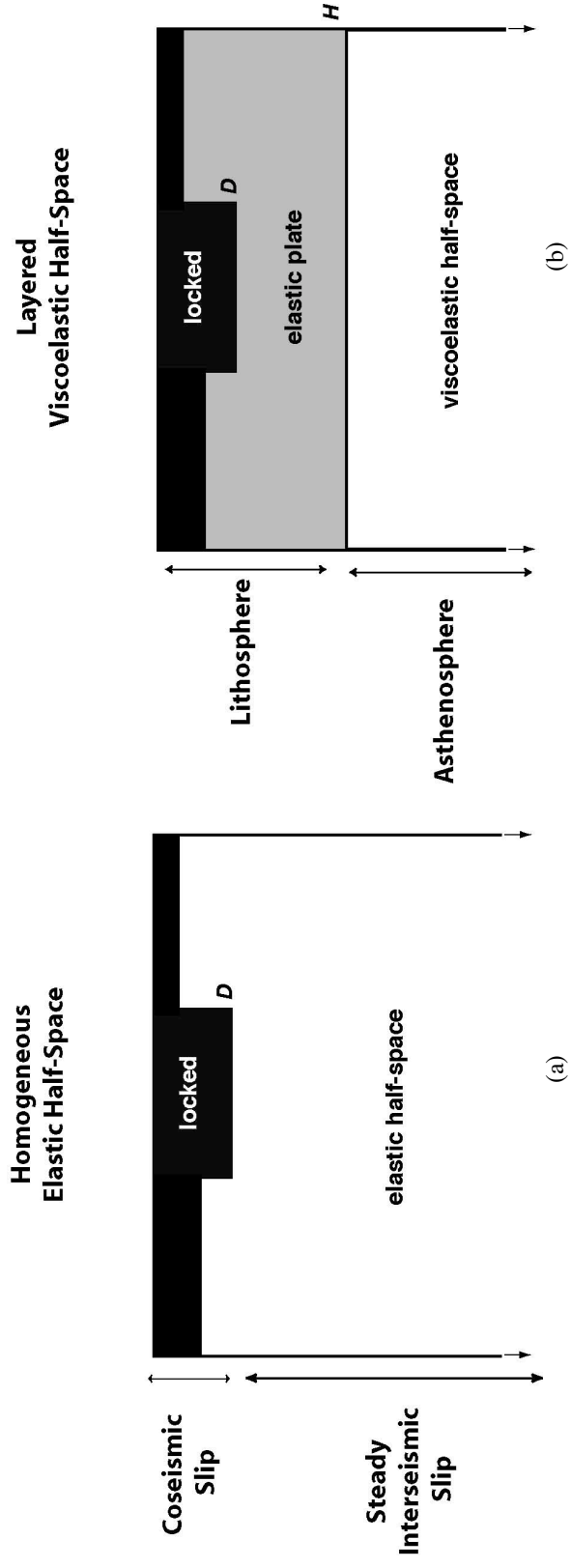
Figure 1.5. Cross-section geometry of homogeneous elastic half-space (a) and layered viscoelastic (b) models.

12

more rapidly computed. The Fourier transform tool decomposes the spatial variations of deformation into sinusoids of different frequency components, where calculations are then made in the spectral domain [*Bracewell*, 1965]. In addition, the Fast Fourier Transform (FFT) algorithm [*Cooley and Tukey*, 1965] speeds the computational process by rearranging and factoring summed terms of the discrete Fourier transform. This step drastically reduces the number of numerical computations, particularly those of powers of 2, from n^2 to $(n/2)\log_2 n$. For example, a problem requiring the calculation of $n = 1024$ data points requires n^2, or 1048576, calculations. Using the FFT, only 5120 calculations are necessary, thus reducing the number of computations by over a factor of 200 and dramatically speeding the computational process.

Using this hybrid approach, dislocation solutions are derived analytically in the Fourier transform domain in both the depth and time dimensions. Two-dimensional Fourier analysis is then used to simulate a realistic fault trace in the two horizontal dimensions. Because the model is analytic in time, the burden of numeric time stepping is eliminated. Moreover, a complex faulting scenario, spanning thousands of years of earthquake deformation, can be computed and analyzed in a matter of hours. With the hybrid approach, vertical slip variations can be implemented by superposition of component models, although the most complicated versions of this model, consisting of an elastic layer overlying a viscoelastic half-space, is a simplification of vertical crustal/mantle structure and requires input parameters that are laterally constant. In addition, the model does not directly account for dipping fault geometry, as numerical integration is required for this task. However, this model has demonstrated success on many levels, from reproducing first-order features of observed deformation, to simulating temporal spans of earthquake history that were previously unobtainable.

1.5 Tectonic Stress Triggering

1.5.1 "Earthquake Conversations"

After many years of recording earthquakes and aftershock activity from around the world, an interesting and bold statistic has emerged regarding earthquake probability: within 24 hours following a significant earthquake (M7.3 or greater), there is a 67% chance that another large event will strike within 100 km of the first shock – an occurrence that is 200000 times less likely to occur on any other day of the year [*Stein*, 1999]. Odds such as these eliminate the suggestion of coincidence, leading many scientists to suspect that major earthquakes disrupt the conditions of the surrounding crust significantly, enough to antagonize failure onto distant faults.

Interactions such as these, or "earthquake conversations" [*Stein*, 2003], have intrigued Earth scientists for decades, motivating numerous searches for a conclusive way to predict the location and timing of the next major earthquake. Some studies targeted the use of highly sensitive instruments to measure unusual stretches in the crust [e.g., *El-Fiky*, 2000], while others searched for slow, precursory motions [e.g., *Beroza and Ellsworth*, 1996]. Investigations have also been focused on the opening and closing behavior of cracks in rocks and the tracking of underground fluids and gases [e.g., *Raleigh et al.*, 1972; *King*, 1986]. Observations of the Earth's electromagnetic field have been analyzed as possible earthquake predictors [e.g., *Fraser-Smith et al.*, 1990], while pre-earthquake thermal anomalies have also been studied using the satellite images [e.g., *Ouzounov and Freund*, 2004]. Even prediction algorithms based on statistical analyses of seismicity have been devised [e.g., *Keilis-Borok et al.*, 1988]. Yet because no single study could conclusively link earthquakes and earthquake prediction, by the early 1990's most experts had concluded that large events were primarily random and admittedly unpredictable [*Stein*, 2003].

Following many years of observing the processes of plate tectonics, it is commonly understood that the role of major earthquakes is to release part of the stress that slowly accumulates as two plates grind past one another. Displacement across the earthquake rupture reduces the local stress. This ensures that a subsequent earthquake on the same fault will not repeat until after the stress rebuilds, which typically requires many, often hundreds of, years. Yet model calculations have recently shown that while their overall tendency is to eliminate stress on a fault, earthquakes can also increase stress levels elsewhere outside of the actual rupture zone, thus increasing the chances of subsequent earthquakes [e.g., *Harris*, 1998; *King and Cocco,* 2001].

This unusual behavior was first observed in 1992 by abnormal seismic activity occurring both before and after the June 18th M7.3 Landers Earthquake. The Landers sequence (Figure 6) began at least two months prior to the arrival of the main shock, with a M4.6 earthquake first striking the Palm Springs region on April 23rd. Two hours later, the M6.1 Joshua Tree Earthquake struck nearly the same location. Nearly two months later, the main Landers event occurred. A rich aftershock distribution was recorded, including the large M6.2 Big Bear earthquake that struck just three hours later and 30 km west of the Landers rupture. Following this event, many years passed with a relative quiescence in the region. However, seven years later this quiet period was dramatically interrupted by the M7.1 Hector Mine earthquake, who's epicenter occurred just 20 km east of the Landers rupture, on October 16th, 1999.
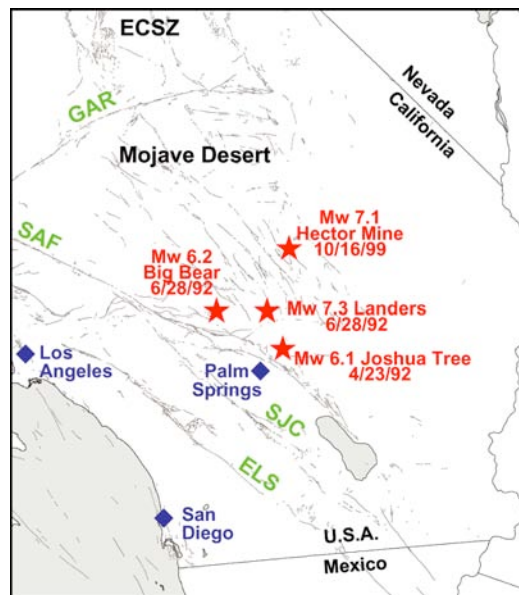
Figure 1.6 1992 Landers-1999 Hector Mine triggered earthquake sequence. Figure from *Nikolaidis* [2002], used with permission.

1.5.2 Coulomb Failure

The Landers sequence of events was one of the first to demonstrate such an extraordinary pattern of aftershocks and triggered earthquakes. These observations ultimately lead to the discovery of stress triggering, the mechanism by which faults interact in response to subtle acquired stresses (~ 0.1 - 0.01 MPa) as a result of neighboring fault ruptures [*Reasenburg and Simpson*, 1992; *King et al.,* 1994]. Note that these triggering stresses are only a small fraction of the accumulated tectonic stress, which is typically on the order of 1-10 MPa. Mathematically, the theory of stress interaction can be described, in abbreviated form, by the Coulomb Failure criterion,

$$\sigma_f = \tau - \mu_f \sigma_n$$

where σ_n and τ are the normal and shear stresses on a failure plane and μ_f is the effective coefficient of friction. In theory, plate motions force two sides of a fault plane in opposite directions (Figure 1.7). As the plates move, paralleling forces apply shear stress, τ, onto the fault plane. Conversely, frictional forces acting in a perpendicular direction to the fault, σ_n, are exerted from rocks on opposing sides as they grind past each other. An intricate balancing act between these two forces, or stresses, keeps the fault remaining locked. Yet once the normal forces holding the fault together are relaxed, or the shear stress surpasses the frictional resistance on the fault, the fault plane slips in the direction of plate motion and releases a significant amount of stored energy – an earthquake.
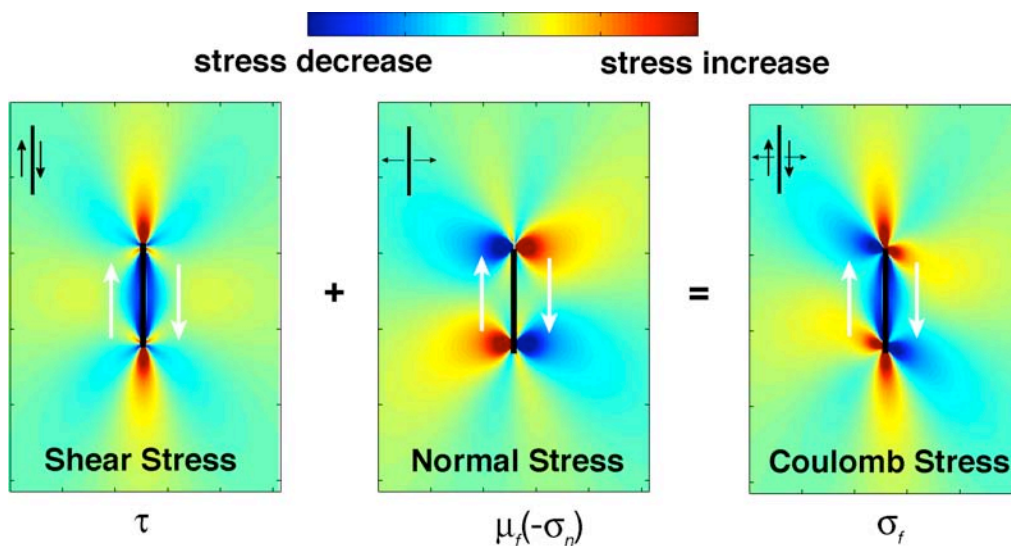
Figure 1.7. Coseismic Coulomb failure model for right-lateral faulting. The fault plane is represented by thick black line. Direction of plate motion is indicated by white arrows. The combination of shear (τ) and normal stress (σ_n and μ_f, an estimate of friction) form the Coulomb stress model.

From Figure 1.7, the coseismic Coulomb stress response of an earthquake is illustrated as shear and normal stresses combine to produce lobes of off-fault stress increase (red) and stress decrease (blue). Compared with observed data, elevated regions of stress typically accompany a rise in seismic activity, manifested as both aftershocks and subsequent main shocks. Alternatively, regions where stress levels have decreased, or stress shadows, typically accompany regions of seismic quiescence. From the sequence of Landers-related earthquakes, we observe a similar pattern (Figure 1.8). Coulomb stress calculated from the effects of the Landers quake increased the stress to the southwest of the fault rupture (Figure 1.8a). Three hours following this event, the Big Bear event struck, rupturing a fault located precisely in this zone of increased stress. Likewise, a vast number of smaller aftershocks occurred in regions of elevated Coulomb stress over the next several years (Figure 1.8b). Seven years later, the Hector Mine Earthquake occurred with an epicenter also located within a zone of increased stress, although this time to the northeast side of the Landers rupture.
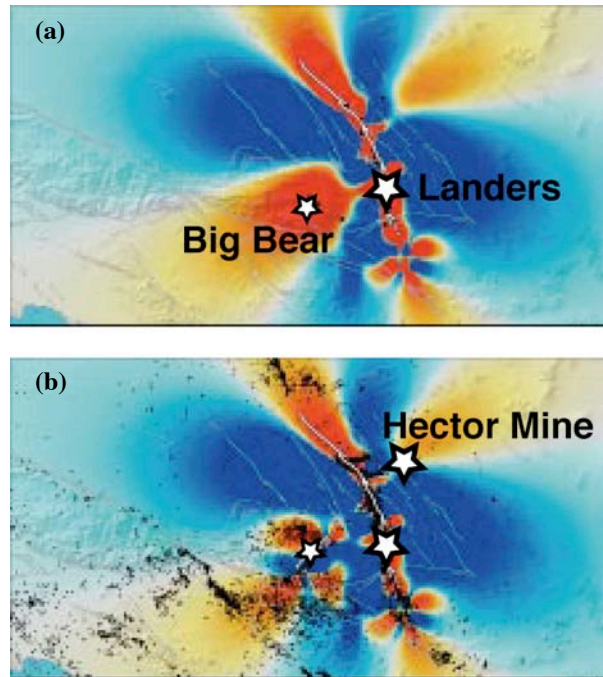
Figure 1.8. Coulomb stress model of Landers-Big Bear-Hector Mine earthquakes. (a) Coulomb stress model following Landers earthquake. (b) Coulomb stress model following Big Bear earthquake. Black dots show subsequent aftershocks following the Landers-Big Bear events. Stars identify epicenter locations of events. Regions of calculated stress increases are shown in red (~ + 0.1 MPa) while calculated stress shadows are shown in blue (~ -0.1 MPa) [modified from *Stein*, 2003].

From the above comparison between data (earthquake location and abundance) and model (Coulomb stress calculation), it is clear that stress models are useful for assessing seismic hazards. Models representing steady interseismic tectonic strain can show the accumulation rates of Coulomb stress on varying fault segments (Figure 2.4, Chapter 2). Time-dependent models, representing different phases of the earthquake cycle, can show impeded rates of stress accumulation due to the existence of a stress shadow (Figure 3.12, Chapter 3). Time-dependent studies have also shown that elevated regions of stress are not static, and that they migrate within the fault zone [*Freed and Lin*, 2001]. These results indicate how such roaming stress, although small, can drive surrounding faults to the point of failure, even after a significant amount of time has passed. Results such as these demonstrate the crucial need for Coulomb stress models characterizing future seismic hazards of the San Andreas Fault System and surrounding regions.

1.6 Thesis Organization

The purpose of this thesis is to derive, verify, and explore a hybrid approach to 3-D fault deformation modeling though a new Fourier transform method. This approach was first used to derive a model describing the static faulting response of an elastic medium. The model was then applied to the geometrically complex setting of the San Andreas Fault System, where GPS velocities spanning the Pacific-North American Plate boundary were used to constrain fault locking depths and calculate Coulomb stress accumulation rate. These results can be found in Chapter 2, where an abbreviated version of the model derivation is presented in Appendix 2.A. To incorporate time-dependence throughout the earthquake cycle, this simple homogeneous

elastic model was then expanded to accommodate viscoelastic effects through a similar Fourier approach. This work, along with multiple comparisons with analytic solutions and an example of simple fault system behavior throughout the earthquake cycle, can be found in Chapter 3. Appendices 3.A-3.E present additional material pertaining to the model details. This viscoelastic model was applied to the San Andreas Fault System, this time incorporating earthquakes occurring over the past 1000 years in order to account for long-term viscoelastic response. GPS velocities were again used to constrain the model, this time allowing inferences to be made about the elastic layer thickness and the mantle viscosity. Stress evolution models, simulating interseismic, coseismic, and postseismic changes over the past 200 years, were also constructed based on these findings. These results are summarized in Chapter 4. Finally, Chapter 5 presents the results of a brief study conducted during an intermediate stage of this thesis work, pertaining to the resolution capabilities of the Shuttle Radar Topography Mission.

1.7 Conclusions

1.7.1 Summary of Results

This thesis focuses on the development, verification, and application of a semi-analytical Fourier model describing the 3-D response of both elastic and viscoelastic mediums to an arbitrary distribution of body forces. Both models have demonstrated the basic 2-D and 3-D deformation behavior of previously published analytic solutions. Because Fourier analysis is used, the horizontal complexity of the fault system has no effect on the speed of the computation; likewise, because the solution is analytic in time, no numerical time stepping is required. The model has the accuracy and speed necessary for computing both geometrically and temporally complex models of the earthquake cycle. This efficiency enables the computation of kinematically realistic 3-D viscoelastic deformation and stress models spanning thousands of years with 1-km resolution in just a matter of hours.

Both elastic and viscoelastic models have been used to estimate the velocity and stress accumulation along the entire extent of the San Andreas Fault System. Average slip rates along individual fault strands are based on long-term geological rates; historical earthquake dates and locations (for the viscoelastic model) are derived from seismic estimates; recent geodetic measurements are used to identify locking depth variations along the fault system, as well as optimal values for elastic plate thickness and mantle viscosity. Vertical deformation, derived from purely horizontal forces, independently verifies the model, providing rates consistent with both geologic and geodetic measurements. Comparisons between the three-dimensional model and GPS measurements yield an average misfit of approximately 2.4 mm/yr. While earthquakes of the past are an important component to the modeling of a viscoelastic plate boundary, present-day GPS measurements are not very sensitive these deformations, as interseismic velocities provide a much larger signal. However, the postseismic process plays a very important role when modeling recent events such as the Landers and Hector Mine earthquakes.

Analysis of Coulomb stress behavior yields many interesting earthquake cycle properties as well. The rate at which interseismic Coulomb stress accumulates is dependent upon slip partitioning and is inversely proportional to fault locking depth. At mid-seismogenic depths, high Coulomb stress accumulation rate is correlated with shallow fault creep; low Coulomb stress accumulation occurs along sections where stress is partitioned on multiple strands or on faults that are deeply locked. Recurrence intervals of major earthquakes along the San Andreas Fault System are also inversely related to Coulomb stress accumulation rates, consistent with coseismic stress drops on the order of 1-10 MPa. In addition, the temporal behavior of Coulomb stress surrounding the occurrence of major earthquakes yields intriguing results, including the

continuation of major fault ruptures onto previously faulted regions with lower stress amplitudes. Elevated Coulomb stress is presently found along the entire southern San Andreas, the northern San Jacinto, and along the eastern Bay Area, reflecting the 150$^+$ years that have transpired since an earthquake ruptured these specific fault segments.

1.7.2 Avenues of Future Research

This thesis documents one of the first attempts to merge data from paleoseismic, geologic, and geodetic observations into a model simulating both large-scale and long-term deformation. While this work provides the initial framework for future analyses of its kind, it also reveals several areas for improvement. First, additional geodetic data, particularly those describing vertical deformation, are needed from locations within 50-200 km from the fault zone in order to place better constraints on the elastic layer thickness and the mantle viscosity. The signature of these model parameters is observable primarily at far-field distances from faults; present-day GPS stations are not optimally positioned to place firm constraints on these parameters. Future versions of the SCEC Crustal Motion Map will play an important role in shaping these constraints, as will future velocity observations from EarthScope's Plate Boundary Observatory.

Secondly, GPS displacement time-series data should be included in future analyses for model refinement. In the past, most large-scale models of plate boundary deformation have been time invariant [*Feigl et al.*, 1993; *Becker et al.*, 2003], based on velocity measurements obtained at the time of the study (Chapter 2). Yet several continuous GPS stations have been operating in California for more than a decade and have recorded seismic events, transients, and changes in velocity. These data may chronicle important earthquake cycle processes that are typically filtered from epoch year velocities [*Nikolaidis*, 2002], which are estimated from a site motion model that simultaneously estimates linear trends in the data over time, annual and semi-annual oscillations, nuisance offsets, coseismic offsets, and crustal deformation; these estimated data were used for the modeling applications of Chapter 4. Yet preliminary comparisons (not yet published) between vector model displacements and continuous ~10-year GPS time-series show unexplained discrepancies that may be associated with un-modeled phenomena; these data exhibit larger coseismic offsets and smaller-sloping postseismic behavior than that predicted by the model. Future time-dependent models should attempt to match the entire displacement time-series revealed by each GPS station. This direction of research will become increasingly important as the 1000 continuous GPS receivers associated with the Plate Boundary Observatory are deployed. In addition, GPS data with observations spanning longer time periods, such as those operating for more than 20 years, will allow for improved and more sensitive investigations of vertical transients.

Third, improved estimates of historical and prehistorical seismic moment release should be incorporated into future models. While the results presented in Chapter 4 of this thesis are based on the best available record of earthquakes at this time, several kinematic assumptions were made relating to accumulating slip deficit between earthquakes and coseismic moment release by such events. It is likely that the Earth behaves in a much more complicated manner and thus our present approach has over-simplified the physics of the earthquake cycle. Future models should be designed to allow for variations in coseismic slip according to recorded seismic moment, although this information is only available for the most recent of earthquakes.

Fourth, future constraints on vertical deformation models should be placed through comparison of costal tide gauge motions. Sea level change has been continuously recorded along the California coastline at several stations for at least 50 years, and at a few stations for over the past 150 years. Although sea level changes are generally attributed to post-glacial rebound and ocean climate phenomena [*Douglas et al.*, 2000], earthquake displacements have also been shown to produce sea level variations [*Melini et al.*, 2004]. The long-term extent and implication of tectonic deformations on sea level change is relatively unknown and

virtually unaccounted for. Depending on the viscosity of the mantle and the thickness of the assumed elastic plate, contributions of sea level change from earthquake-related events may vary significantly [*Melini et al.*, 2004]. By comparing time-series data of relative sea level changes to a variety of earthquake models spanning many years, further constraints can be placed on acceptable model parameters.

In conclusion, it is recommended that future seismic hazard analyses of both northern and southern California, particularly those used to better inform the general public about earthquake probabilities, pay special attention to the evolutionary behavior of Coulomb stress demonstrated by this work. Most probabilistic seismic hazard assessments, commonly relied upon by engineering, emergency-response, insurance, and financial groups, do not incorporate Coulomb stress triggering concepts into hazard calculations; these models assume earthquakes are uncorrelated in time and space [*Stein*, 1999]. While the deformation and stress models described in this thesis are not yet capable of predicting the timing and extent of future ruptures, they are an important tool for understanding how different sections of the San Andreas Fault System store energy and release stress over time. These efforts, like many others [e.g., *Toda et al.*, 1998], may have important implications for the occurrence and likelihood of future earthquakes, which should be seriously considered by future seismic hazard assessment groups.

1.8 References

Agnew, D.C., S. Owen, Z.K. Shen, G. Anderson, J. Svarc, H. Johnson, K. Austin, and R. Reilinger, Coseismic Displacement from the Hector Mine, California Earthquake: Results from Survey-Mode Global Positioning System Measurements, *Bull. Seismol. Soc. Am.*, 92, 1355-1344, 2002.

Atwater, T., Implications of plate tectonics for the Cenozoic tectonic evolution of western North America: *Geo. Soc. Am. Bull.*, 81, 3513-3536, 1970.

Atwater, T., and P. Molnar, Relative motion of the Pacific and North American plates deduced from sea-floor spreading in the Atlantic, Indian, and South Pacific Oceans, in R.L. Kovach and A. Nur, eds., *Proceedings of the conference on tectonic problems of the San Andreas fault system: Stanford, Calif.*, Stanford University Publications in the Geological Sciences, 13, 136-148, 1973.

Becker, T. W., J. Hardebeck, and G. Anderson, Constraints on fault slip rates of the southern California plate boundary from GPS velocity and stress inversions, *Geophys. J. Int.*, doi:10.1111/j.1365-246X.2004.02528.x, 2004.

Beroza, G.C., and W.L. Ellsworth, Properties of the seismic nucleation phase, *Tectonophysics*, 261, 209-227, 1996.

Bock, Y., D.C. Agnew, P. Fang, J.F. Genrich, B. H. Hager, T.A. Herring, K.W. Hudnut, R.W. King, S. Larson, J.B. Minster, K. Stary, S. Widowinski, and F. Wyatt, Detection of crustal deformation related to the Landers earthquake sequence using continuous GPS measurements, *Nature*, 361, 337-340, 1993.

Bock, Y., S. Wdowinski, P. Fang, J. Zhang, S. Williams, H. Johnson, J. Behr, J. Genrich, J. Dean, M. van Domselaar, D. Agnew, F. Wyatt, K. Stark, B. Oral, K. Hudnut, R. King, T. Herring, S. Dinardo, W. Young, D. Jackson, and W. Gurtner, Southern California Permanent GPS Geodetic Array: Continuous measurements of the regional crustal deformation between the 1992 Landers and 1994 Northridge earthquakes, *J. Geophys. Res.*, 102, 18013-18033, 1997.

Bracewell, R., *The Fourier transform and its applications*, Second edition, revised, McGraw-Hill, New York, 1965.

Chinnery, M.A., The deformation of the ground around surface faults, *Bull. Seismol. Soc. Am.*, 50, 355-372, 1961.

Cohen, S.C., Numerical Models of Crustal Deformation in Seismic Zones, *Adv. Geophys.*, 41, 133-231, 1999.

Cooley, J. W., and O.W. Tukey, An Algorithm for the Machine Calculation of Complex Fourier Series, *Math. Comput.*, 19, 297-301, 1965.

DeMets, C., R. G. Gordo, S. Stein, and D.F. Argns, A revised estimate of Pacific-North American motion and implications for western North American plate boundary zone tectonics: *Geophys. Res. Lett.*, 14, 911-914, 1987.

Dickinson, W.R., and W.S. Snyder, Geometry of triple junctions related to San Andreas transform, *J. Geophys. Res.*, 84, 561-572, 1979.

Dickinson, W.R., Plate tectonics and the continental margin of California, in Ernst, W.G., ed., *The geotectonic development of California (Rubey volume 1)*: Englewood Cliffs, N.J., Prentice-Hall, 1-28, 1981.

Dong, D., and Y. Bock, Global Positioning System network analysis with phase ambiguity resolution applied to crustal deformation studies in California, *J. Geophys. Res.*, 94, 3949-3966, 1989.

Douglas, B.C., M.S. Kearney, and S.P. Leatherman, *Sea level rise: history and consequences.* Academic Press, 272 pp, 2000.

El-Fiky, G., Elastic and inelastic strains in the Japanese Islands deduced from dense GPS array, *Earth Planets Space*, 52, 1107-1112, 2000.

Farr, T., and M. Kobrick, The Shuttle Radar Topography Mission, *Eos Trans. AGU, 82(47)*, Fall Meet. Suppl., Abstract G22B-0214, 2001.

Feigl, K. L., D. C. Agnew, Y. Bock, D. Dong, A. Donnellan, B. H. Hager, T.A. Herring, D. D. Jackson, T. H. Jordan, R. W. King, S. Larsen, K. M. Larson, M. H. Murray, Z. Shen, and F. H. Webb, Space geodetic measurements of crustal deformation in Central and Southern California, 1984-1992, *J. Geophys. Res.*, 98, 21,677-21,712, 1993.

Fialko, Y., Evidence of fluid-filled upper crust from observations of post-seismic deformation due to the 1992 M_w 7.3 Landers earthquake, *J. Geophys. Res.*, 109, doi:10.1029/2003JB002985, 2004a.

Fialko, Y., Probing the mechanical properties of seismically active crust with space geodesy: Study of the co-seismic deformation due to the 1992 M_w 7.3 Landers (southern California) earthquake, *J. Geophys. Res.*, 109, doi:10.1029/2003JB002756, 2004b.

Fraser-Smith, A.C., A. Bernardi, P.R. McGill, M. E. Ladd, R.A. Helliwell, and O.G. Villard, Jr., Low-frequency magnetic field measurements near the epicenter of the M_s 7.1 Loma Prieta earthquake, *Geophys. Res. Lett.*, 17, 1465-1468, 1990.

Freed, A.M., and J. Lin, Delayed triggering of the 1999 Hector Mine earthquake by viscoelastic stress transfer, *Nature*, 411, 180-183, 2001.

Freed, A.M., and R. Burgmann, Evidence of power-law flow in the Mojave desert mantle, *Nature*, 430, 548-551, 2004.

Grant, L.B., and W.R. Lettis, Introduction to the Special Issue on Paleoseismology of the San Andreas Fault System, *Bull. Seismol. Soc. Am.*, 92, 2552-2554, 2002.

Harris, R.A., Introduction to special section: Stress triggers, stress shadows, and implications for seismic hazard, *J. Geophys. Res.*, 103, 24,347-24,358, 1998.

Hauksson, E., State of stress from focal mechanisms before and after the 1992 Landers Earthquake Sequence, *Bull. Seismol. Soc. Am.*, 84, 917-934, 1994.

Herring, T.A., C.R. Gwinn, and I.I. Shapiro, Geodesy by radio interferometry: Studies of the forced nutations of the Earth; 1, Data analysis, *J. Geophys. Res.*, 91, 4745-4754, 1986.

Hudnut, K. W., Y. Bock, M. Cline, P. Fang, Y. Feng, J. Freymueller, X. Ge, W.K. Gross, D. Jackson, M. Kim, N.E. Kim, J. Langbein, S.C. Larsen, M. Lisowski, Z.K. Shen, J. Svarc, and J. Zhang, Co-seismic displacements of the 1992 Landers Earthquake sequence, *Bull. Seismol. Soc. Am.*, 84, 625-645, 1994.

Hudnut, K., Y. Bock, J. Galetzka, F.H. Webb, and W.H. Young, The Southern California Integrated GPS Network (SCIGN), The 10th Fig International Symposium on Deformation Measurements, 19-22 March 2001, Orange, CA, 20 pp., 2001.

Jacobs, A., D. Sandwell, Y. Fialko, and L. Sichoix, The 1999 (M_w7.1) Hector Mine, California, earthquake: Near-field postseismic deformation from ERS interferometry, *Bull. Seismol. Soc. Am.*, 92, 1433-1442, 2002.

Kellis-Borok, V.I., L. Knopoff, I.M. Rotwain, and C.R. Allen, Intermediate-term prediction of occurrence times of strong earthquakes, *Nature*, 335, 690-694, 1988.

King. G. C. P., R. S. Stein, and J. Lin, Static stress changes and the triggering of earthquakes, *Bull. Seismol. Soc. Am.*, 84, 935-953, 1994.

King, C.Y., Gas Geochemistry Applied to Earthquake Prediction: An Overview, *J. Geophys. Res.*, 91, 12,269-12,281, 1986.

King, G.C.P., and M. Cocco, Fault interaction by elastic stress changes: New clues from earthquake sequences, *Adv. Geophys.*, 44, 1-38, 2001.

Larson, R.L., H. W. Menard, and S.M. Smith, Gulf of California: A result of ocean-floor spreading and transform faulting, *Science*, 161, 781-784, 1968.

Lawson, A.C., The California earthquake of April 18, 1906: Report of the State Earthquake Investigation Commission: Carnegie Institution of Washington Publication 87, 2, 1908.

Lisowski, M., J.C. Savage, and W.H. Prescott, The velocity field along the San Andreas fault in central and southern California, *J. Geophys. Res.*, 93, 8369-8389, 1991.

Massonnet, D., M. Rossi, C. Carmona, F. Adragna, G. Peltzer, K. Feigl, and T. Rabute, The displacement field of the Landers earthquake mapped by radar interferometry, *Nature*, 364, 138-142, 1993.

Massonnet, D., P. Briole, and A. Arnaud, Deflation of Mount Etna monitored by spaceborne radar interferometry, *Nature,* 375, 567-570, 1995.

Massonnet, D., W. Thatcher, and H. Vadon, Radar interferometry detects two mechanism of postseismic relaxation following the Landers, California earthquake, *Nature*, 382, 612-612, 1996.

Massonnet, D., and K.L. Feigl, Radar interferometry and its application of changes in the Earth's surface, *Rev. Geophys.*, 36, 441-500, 1998.

McKenzie, D.P., and W.J. Morgan, Evolution of triple junctions, *Nature*, 224, 125-133, 1969.

Minster, J.B., and T.H. Jordan, Present-day plate motions, *J. Geophys. Res.*, 83, 5331-5354, 1978.

Minster, J.B., and T.H. Jordan, Vector constraints on Western U.S. deformation from space geodesy, neotectonics, and plate motions, *J. Geophys. Res.*, 92, 4798-4804, 1987.

Melini, D., A. Piersanti, G. Spada, G. Soldati, E. Casarotti, and E. Boschi, Earthquakes and relative sealevel changes, *Geophys. Res. Lett.*, 31, doi:10.1029/2003GL019347, 2004.

Nikolaidis, R., Observation of Geodetic and Seismic Deformation with the Global Positioning System, *Ph.D. Thesis*, University of California, San Diego, 2002.

Noble, L.F., The San Andreas rift and some other active faults in the desert region of southeastern California, *Bull. Seismol. Soc. Am.*, 17, 25-39, 1927.

Nur, A., and G. Mavko, Postseismic viscoelastic rebound, *Science*, 183, 204-206, 1974.

Okada, Y., Surface deformation due to shear and tensile faults in a half-space, *Bull. Seismol. Soc. Am.,* 75, 1135-1154, 1985.

Okada, Y., Internal deformation due to shear and tensile faults in a half-space, *Bull. Seismol. Soc. Am.*, *82*, 1018-1040, 1992.

Olsen, K.B., and G.T. Schuster, Site amplification in the Salt Lake Valley by three-dimensional elastic wave propagation, *Eos Trans. AGU*, 73, 338, 1992.

Ouzounov, D., and F. Freund, Mid-infrared emission prior to strong earthquakes analyzed by remote sensing data, *Adv. Space Res.*, 33, doi: 10.1016/S0273-1177(03)00486-1, 2004.

PBO Steering Committee, The Plate Boundary Observatory: Creating a four-dimensional image of the deformation of western North America, White Paper presented to the National Science Foundation, 52 pp., 1999.

Peltzer, G.P., P. Rosen, F. Rogez, and K. Hudnut, Postseismic rebound in fault step-overs cause by pore fluid flow, *Science*, 273, 1202-1204, 1996.

Pollitz, F.F., C. Wicks, and W. Thatcher, Mantle flow beneath a continental strike-slip fault: Postseismic deformation after the 1999 Hector Mine earthquake, *Science*, 293, 1814-1818, 2001.

Raleigh, C. B., J. H. Healy, and J. D. Bredehoeft, Faulting and crustal stress at Rangely, Colorado, in Flow and Fracture of Rocks, Geophys. Monogr. Ser., 16, edited by H. C. Heard et al., 275-284, AGU, Washington, D. C., 1972.

Reasenberg, P.A., and R.W. Simpson, Response of regional seismicity to the static stress change produced by the Loma Prieta earthquake, *Science*, 255, 1687-1690, 1992.

Reid, H.F., The mechanism of the earthquake, The California Earthquake of April 18, 1906, Report of the State Earthquake Investigation Commission, 2 Washington D.C.: Carnegie Institution, 1910.

Rosen, P.A., S. Hensley, H.A. Zebker, F.H. Webb, and E. J. Fielding, Surface deformation and coherence measurements of Kilauea Volcano, Hawaii, from SIR-C radar interferometry, *J. Geophys. Res.,* 101, 23109-23125, 1996.

Rundle, J.B., and D.D. Jackson, A three-dimensional viscoelastic model of a strike slip fault, *Geophys. J. Roy. Astron. Soc.*, 49, 575-591, 1977.

Rybicki, K., The elastic residual field of a very long strike-slip fault in the presence of a discontinuity, *Bull. Seismol. Soc. Am.*, 61, 72-92, 1971.

Sandwell, D.T., L. Sichoix, and B. Smith, The 1999 Hector Mine Earthquake, Southern California: Vector Near-Field Displacements from ERS InSAR, *Bull. Seismol. Soc. Am.*, 92, 1341-1354, 2002.

Savage, J.C., and R.O. Burford, Geodetic determination of relative plate motion in central California, *J. Geophys. Res.*, 78, 832-845, 1973.

Savage, J.C., and W.H. Prescott, Asthenosphere readjustment and the earthquake cycle, *J. Geophys. Res.*, 83, 3369-3376, 1978.

Savage, J. C., and J. L. Svarc, Postseismic deformation associated with the 1992 $M_w = 7.3$ Landers earthquake, southern California, *J. Geophys. Res.*, 102, 7565-7577, 1997.

Shen, Z., D. Jackson, Y. Feng, M. Cline, M. Kim, P. Fang, and Y. Bock, Postseismic deformation following the Landers earthquake, California, 28 June 1992, *Bull. Seismol. Soc. Am.*, 84, 780-791, 1994.

Shen, Z.K., D.C. Agnew, and R.W. King, The SCEC Crustal Motion Map, Version 3.0, http://epicenter.usc.edu/cmm3, 2003.

Sieh, K., L. Jones, E. Hauksson, K. Hudnut, D. Eberhart-Phillips, T. Heaton, S. Hough, K. Hutton, H. Kanamori, A. Lilje, S. Lindvall, S.F. McGill, J. Mori, C. Rubin, J.A. Spotila, J. Stock, H.K. Thio, J. Treiman, B. Wernicke, and J. Zachariasen, Near-field investigations of the Landers earthquake sequence, April to July 1992, *Science*, 260, 171-176, 1993.

Simons, M., Y. Fialko, and L. Rivera, Co-seismic static deformation from the 1999 M_w7.1 Hector Mine, California, earthquake, as inferred from InSAR and GPS observations, *Bull. Seismol. Soc. Am.*, 92, 1390-1402, 2002.

Stein, R.S., Contemporary plate motion and crustal deformation, *Rev. Geophys.*, 25, 855-863, 1987.

Stein, R.S., G.C.P. King, and J. Lin, Stress triggering of the 1994 M = 6.7 Northridge, California, earthquake by its predecessors, *Science*, 265, 1432-1435, 1994.

Stein, R.S., The role of stress transfer in earthquake occurrence, *Nature*, 402, 605-609, 1999.

Stein, R.S., Earthquake Conversations, *Sci. Amer.*, 288, 72-79, 203.

Thatcher, W., Nonlinear strain buildup and the earthquake cycle on the San Andreas Fault, *J. Geophys. Res.*, 88, 5893-5902, 1983.

Thatcher, W., The crustal deformation cycle at convergent plate margins, *R. Soc. New Zealand Bull.*, 24, 317-332, 1986.

Toda, S., R.S. Stein, P.A. Reasenberg, J.H. Dieterich, and A. Yoshida, Stress transferred by the 1995 M_w = 6.9 Kobe, Japan, shock: Effect on aftershocks and future earthquake probabilities, *J. Geophys. Res.*, 103, 1998.

Tralli, D.M., and F. Tajima, Seismology and Space-Based Geodesy, *Adv. Geophys.*, 34, 35-91, 1993.

Wallace, R.E., Structure of a portion of the San Andreas rift in southern California, *Geo. Soc. Am. Bull.*, 60, 781-806, 1949.

Ward, S.N., Quasi-static propagator matrices: creep on strike-slip faults, *Tectonophysics*, 120, 83-106, 1985.

Watson, K., Y. Bock, and D.T. Sandwell, Satellite interferometric observations of displacements associated with seasonal groundwater in the Los Angeles Basin, *J. Geophys. Res.*, 107, doi:10.1029/2001JB000470, 2002.

Weertman, J., Continuum distribution of dislocations on faults with finite friction, *Bull. Seismol. Soc. Am.*, 54, 1035-1058, 1964.

Wilson, J.T., A new class of faults and their bearing on continental drift, *Nature*, 207, 343-347, 1965.

Working Group on California Earthquake Probabilities (WGCEP), Seismic Hazards in Southern California: Probable Earthquakes, 1994 to 2024, *Bull. Seismol. Soc. Am.*, 85, 379-439, 1995.

Yang, M., and M.N. Toksoz, Time dependent deformation and stress relaxation after strike slip earthquakes, *J. Geophys. Res.*, 86, 2889-2901, 1981.

Zebker, H.A., P.A. Rosen, R.M Goldstein, A. Gabriel, and C.L. Werner, On the derivation of coseismic displacement fields using differential radar interferometry: The Landers earthquake, *J. Geophys. Res.*, 99, 19,617-19,634, 1994.

Chapter 2

Coulomb Stress Accumulation along the San Andreas Fault System

Bridget R. Smith and David T. Sandwell

Abstract. Stress accumulation rates along the primary segments of the San Andreas Fault System are computed using a three-dimensional (3-D) elastic half-space model with realistic fault geometry. The model is developed in the Fourier domain by solving for the response of an elastic half-space due to a point vector body force and analytically integrating the force from a locking depth to infinite depth. This approach is then applied to the San Andreas Fault System using published slip rates along 18 major fault strands of the fault zone. GPS-derived horizontal velocity measurements spanning the entire 1700 x 200 km region are then used to solve for apparent locking depth along each primary fault segment. This simple model fits remarkably well (2.43 mm/yr RMS misfit), although some discrepancies occur in the Eastern California Shear Zone. The model also predicts vertical uplift and subsidence rates that are in agreement with independent geologic and geodetic estimates. In addition, shear and normal stress along the major fault strands are used to compute Coulomb stress accumulation rate. As a result, we find earthquake recurrence intervals along the San Andreas Fault System to be inversely proportional to Coulomb stress accumulation rate, in agreement with typical co-seismic stress drops of 1-10 MPa. This 3-D deformation model can ultimately be extended to include both time-dependent forcing and viscoelastic response.

2.1 Introduction

The San Andreas Fault (SAF) System, spanning over 1700 km from the Mendocino Triple Junction in the north, to the Gulf of California in the south, defines the complex tectonic boundary between the Pacific and North American Plates. As the two plates slide past each other, the SAF System accommodates approximately 35-50 mm/yr of relative plate motion that is distributed across a 200 km wide zone [*Working Group on California Earthquake Probabilities (WGCEP),* 1995, 1999]. The SAF System is comprised of an intricate network of subfaults, each of varying geometry, locking depth, and associated failure properties. Earthquake recurrence intervals also vary dramatically along the SAF System subfaults, ranging from 20 years to over 300 years. In order to better understand the earthquake cycle and also help constrain faulting models of the San Andreas Fault System, geodetic measurements of interseismic, postseismic, and coseismic deformation are continually collected of the entire North American-Pacific Plate boundary.

While many previous studies of the SAF region have developed local fault-slip models to match regional geodetic observations of surface displacement [*Savage and Burford,* 1973; *Savage et al.,* 1979; *King et al.,* 1987; *Li and Lim,* 1988; *Eberhart-Phillips et al.,* 1990; *Savage, 1990; Lisowski et al.,* 1991; *Feigl et al.,* 1993; *Savage and Lisowski,* 1993; *Freymueller et al.,* 1999; *Burgmann et al.,* 2000; *Murray and Segall,* 2001], our objectives are somewhat different in that we investigate the steady-state behavior of the *entire* San Andreas Fault System. By constraining relative plate motion, maintaining appropriate fault geometry, and implementing geodetic measurements spanning the entire system, we are able to model 3-D deformation and

calculate stress accumulation. First, we investigate whether a single far-field plate velocity can be partitioned among parallel strands in order to accurately model near-field geodetic measurements. Second, we establish spatial variations in apparent locking depth along the main segments of the SAF System. Finally, we use our model to estimate secular buildup in Coulomb stress within the seismogenic layer and accumulation of scalar seismic moment.

The primary purpose for developing our model is to estimate Coulomb stress accumulation rate and to explore its relevancy to earthquake occurrence and failure potential. Following the assumption that major earthquakes typically produce stress drops on the order of 1-10 MPa, estimates of Coulomb stress accumulation rate can provide an upper bound on the recurrence interval of a particular fault segment. Furthermore, recent studies of induced Coulomb stress changes propose that earthquakes may be triggered by stress changes as small as 0.1 MPa [*King et al.*, 1994; *Stein et al.*, 1994; *Fialko and Simons*, 2000; *King and Cocco*, 2001; *Zeng*, 2001]. High Coulomb stress accumulation rate has also been linked to areas of surface creep [*Savage and Lisowski*, 1993]. A better understanding of such stress-release processes at major plate boundaries, along with estimates of seismic moment magnitude, have also been the focus of recent earthquake hazard potential studies [*WGCEP*, 1995, 1999; *WGNCEP*, 1996]. In this analysis, we inspect the role of locking depth, fault geometry, and paralleling fault strands on accumulating interseismic stress along San Andreas Fault System, and investigate how such accumulation is related to shallow fault creep, earthquake recurrence interval, and seismic moment accumulation.

2.2   Fourier Solution to 3-D Body Force Model

For the last several decades, the most commonly used analytic models of fault-induced deformation have been based on the dislocation solutions of *Chinnery* [1961, 1963], *Rybicki* [1971], and *Okada* [1985, 1992]. The latter provide analytic expressions for stress, strain, and displacement in an elastic half-space due to a displacement discontinuity. While these dislocation models are accurate and computationally efficient when applied to individual faults or small fault systems, they may become computationally prohibitive when representing fault geometry over the entire North American-Pacific Plate boundary. For example, 4×10^5 model calculations are required for 1000 GPS measurements and 400 fault patches. Modeling of InSAR observations could easily require 4×10^9 model calculations. However, if model calculations are performed in the spectral domain, the computational effort is substantially reduced. Rather than calculate the Fourier transform of the analytic solutions mentioned above, we instead solve the 3-D elasticity equations in the wave-number domain and then inverse Fourier transform to obtain space domain solutions. The key elements of our model derivation are summarized in Appendix 2.A. In the two-dimensional case, our model matches the classical arctangent solution of *Weertman* [1964], both analytically and numerically. While this elastic half-space model currently ignores crustal heterogeneities and does not explicitly incorporate non-elastic rheology below the brittle-ductile transition, it produces reasonable estimates of first-order tectonic features comparable to other simple models [e.g., *Savage and Burford*, 1973].

To summarize our analytic approach (Appendix 2.A), the elasticity equations are used to derive a set of transfer functions (in the wave-number domain) for the 3-D displacement of an elastic half-space due to an arbitrary distribution of vector body forces. The numerical components of this approach involve generating a grid of force couples that simulate complex fault geometry, taking the 2-D Fourier transform of the grid, multiplying by the appropriate transfer function, and finally inverse Fourier transforming. The force model must be designed to match the velocity difference across the plate boundary and have zero net force and zero net moment. There is a similar requirement in gravity modeling, where mass balance is achieved by imposing isostatic compensation and making the grid dimensions several times larger than the longest length

scale in the system (e.g., flexural wavelength or lithospheric thickness). For this fault model, the characteristic length scale is the locking depth of the fault. The key is to construct a model representing a complicated fault system where the forces and moments are balanced. Our numerical approach is as follows: i) Develop a force couple segment from the analytic derivative of a Gaussian approximation to a line segment as described in Appendix 2.A; this ensures exact force balance. For an accurate simulation, the half-width of the Gaussian must be greater than the grid size but less than the locking depth. ii) Construct a complicated force couple model using digitized fault segments. For each segment, the strength of the couple is proportional to the long-term slip rate on the fault segment and the direction of the couple is parallel to the overall plate boundary direction (not the local fault direction). This simulates the far-field plate tectonic force couple. Because the model has force couples, the vector sum of all of the forces in the model is zero but there is a large unbalanced moment because all of the force couples act in the same direction. iii) Double the grid size and place a mirror image of the force couple distribution in the mirror grid so the moment due to the image fault exactly balances the moment due to the real fault. Following these steps, we combine both analytic and numeric approaches to elastic fault modeling for analysis of the San Andreas Fault System.

2.3 Modeling the San Andreas Fault Zone

We apply our semi-analytic model (Appendix 2.A.) to the geometrically complex fault setting of the SAF System. After digitizing the major fault strands along the SAF System from geologic maps [*Jennings,* 1994] into over 400 elements, we group the elements into 18 fault segments spatially consistent with previous geologic and geodetic studies (Figure 2.1). Fault segments include the following regions: Imperial (1), Brawley (defined primarily by seismicity [*Hill et al.*, 1975] rather than by mapped surface trace) (2), Coachella Valley-San Bernardino Mountains (3), Borrego (includes Superstition Hills and Coyote Creek regions) (4), Anza-San Jacinto (includes San Bernardino Valley) (5), Mojave (6), Carrizo (7), Cholame (8), Parkfield Transition (9), San Andreas Creeping (10), Santa Cruz Mountains-San Andreas Peninsula (11), San Andreas North Coast (12), South-Central Calaveras (13), North Calaveras-Concord (14), Green Valley-Bartlett Springs (15), Hayward (16), Rodgers Creek (17), and Maacama (18). The fault system is rotated about its pole of deformation (52°N, 287°W) into a new co-ordinate system [*Wdowinski et al.*, 2001] and fault segments are embedded in a 1-km grid of 2048 elements along the SAF System and 1024 elements across the system (2048 across including the image). We assume that the system is loaded by stresses extending far from the locked portion of the fault and that locking depth and slip rate remain constant along each fault segment.

Each of the 18 SAF segments is assigned a deep slip rate based on geodetic measurements, geologic offsets, and plate reconstructions [*WGCEP*, 1995, 1999]. In some cases, slip rates (Table 2.1) were adjusted (+/- 5 mm/yr on average) in order to satisfy an assumed far-field plate velocity of 40 mm/yr. This constant rate simplifies the model and, as we show below, it has little impact on the near-field velocity, strain-rate, and Coulomb stress accumulation rate. Moreover, it provides a remarkably good fit to the geodetic data, except in the Eastern California Shear Zone, where misfit is expected due to omission of faults in this area. Because slip estimates remain uncertain for the Maacama and Bartlett Springs segments, we assume that these segments slip at the same rates as their southern extensions, the Rodgers Creek and Green Valley faults, respectively.

After assigning these *a priori* deep slip rates, we estimate lower locking depths for each of the 18 fault segments using a least squares fit to 1099 GPS-derived horizontal velocities. Geodetic data for the southern SAF region, acquired between 1970-1997, were provided by the Crustal Deformation Working Group of the Southern California Earthquake Center (SCEC) (D. Agnew, SCEC, Horizontal deformation velocity map

26
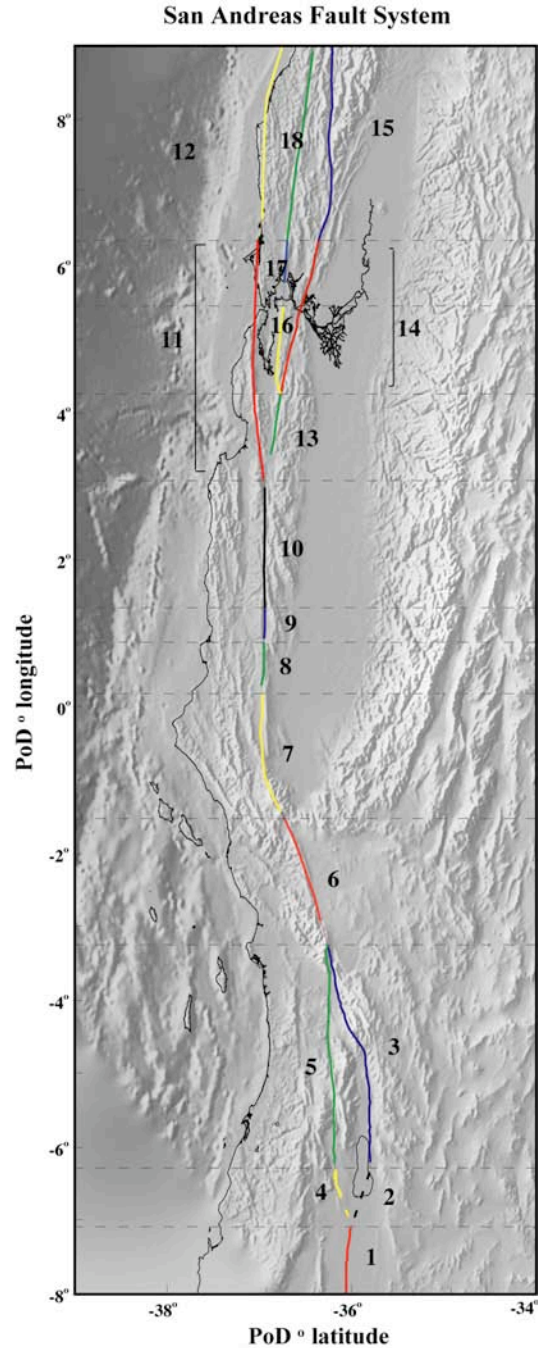
Figure 2.1. San Andreas Fault System segment locations in the Pole of Deformation (PoD) coordinate system over shaded regional topography. Fault segments coinciding with Table 1 are: Imperial (1), Brawley (2), Coachella Valley-San Bernardino Mountains (3), Borrego (4), Anza-San Jacinto (5), Mojave (6), Carrizo (7), Cholame (8), Parkfield Transition (9), San Andreas Creeping (10), Santa Cruz Mountains-San Andreas Peninsula (11), SAF North Coast (12), South-Central Calaveras (13), North Calaveras-Concord (14), Green Valley-Bartlett Springs (15), Hayward (16), Rodgers Creek (17), Maacama (18). We use the Pole of Deformation (PoD) of *Wdowinski et al.* [2001] (52°N, 287°W) and note that the longitude axis has been shifted in order to place 0° in the center of the grid. Dashed lines represent horizontal corridor sections, bounded by fault segments, constrained to total 40 mm/yr.

Table 2.1. San Andreas Fault System parameters and results.

Segment	Name	Slip*	Locking depth	σ	Coulomb Stress	Moment Rate	τ_r*
#		(mm/yr)	(km)	(km)	(MPa/100yr)	(Nm/100yr per km)10^{14}	(yr)
1	Imperial	40	5.9	1.20	10.0	7.1	40
2	Brawley Seismic Zone	36	6.3	1.30	8.5	6.8	24
3	Coachella-San Bernardino Mts.	28	22.6	1.70	1.7	19.0	146
4	Borrego	4	2.0	7.70	0.5	0.2	175
5	Anza-San Jacinto	12	13.1	2.30	1.7	4.7	83
6	Mojave	40	26.0	1.70	0.6	31.2	150
7	Carrizo	40	25.2	2.60	1.6	30.2	206
8	Cholame	40	12.7	2.40	4.0	15.2	140
9	Parkfield Transition	40	14.5	2.90	4.0	17.4	25
10	San Andreas Creeping	40	1.3	0.20	n/a	1.6	n/a
11	Santa Cruz-San Andreas Peninsula	21	9.3	0.60	3.2	5.9	401
12	San Andreas North Coast	25	19.4	2.10	2.3	14.6	759
13	South-Central Calaveras	19	1.6	0.20	12.5	0.9	75
14	North Calaveras-Concord	7	13.7	4.60	1.1	2.9	701
15	Green Valley-Bartlett Springs	5	9.1	8.40	1.2	1.4	230
16	Hayward	12	15.7	3.70	1.5	5.7	525
17	Rodgers Creek	12	18.9	6.70	1.1	6.8	286
18	Maacama	10	12.3	4.30	1.7	3.7	220

. * *WGCEP* [1995, 1999] and *WGNCEP* [1996]

version 3.0, personal communication, 2002). GPS velocities for the Calaveras-Hayward region were provided by the U.S. Geological Survey, Stanford University, and the University of California, Berkeley and reflect two data sets, one of campaign measurements (1993-1999) and one of BARD network continuous measurements. Data used to model the northern region of the SAF System were obtained from *Freymeuller et al.* [1999], and represent campaign measurements from 1991-1995. These four geodetic data sets combine to a total of 1099 horizontal velocity vectors spanning the entire San Andreas Fault zone (Figure 2.2a).

2.4 Geodetic Inversion

The relationship between surface velocity and locking depth is nonlinear, thus we estimate the unknown depths of the 18 locked fault segments using an iterative, least-squares approach based on the Gauss-Newton method. We solve the system of equations $V_{gps}(x,y) = V_m(x,y,\mathbf{d})$, where V_{gps} is the geodetic velocity measurement, V_m is the modeled velocity, and $\mathbf{d}$ is the set of locking depth parameters that minimize the weighted residual misfit χ^2. The data misfit is

$$V_{res}^i = \frac{V_{gps}^i - V_m^i}{\sigma^i} \tag{2.1}$$

$$\chi^2 = \frac{1}{N}\sum_{i=1}^{N}\left(V_{res}^i\right)^2 \tag{2.2}$$

where σ^i is the uncertainty estimate of the ith geodetic velocity measurement and N is the number of geodetic observations. Uncertainties in each measurement are used to form the diagonal covariance matrix of the data.

The modeled velocity, V_m, is expanded in a Taylor series about an initial locking depth, $\mathbf{d}$

$$V_m[\mathbf{d} + \Delta] = V_m[\mathbf{d}] + \sum_{j=1}^{M}\Delta_j\frac{\partial V_m}{\partial d_j} + \dots \tag{2.3}$$

where Δ_j is a small perturbation to the jth depth parameter. Partial derivatives are computed analytically using the pre-integrated body force solution (Appendix 2.A). Because $V_m[\mathbf{d} + \Delta]$ is an approximation to the observed velocity, V_{gps}, the residual velocity may be expressed as the depth perturbation Δ times the matrix of partial derivatives $\delta\mathbf{V}_m$

$$V_{res} = \delta\mathbf{V}_m\,\Delta \;. \tag{2.4}$$

The model perturbation is then calculated using the standard weighted least squares approach

$$\Delta = \left(\delta\mathbf{V}_m{}^T\mathbf{C}^{-1}\delta\mathbf{V}_m\right)^{-1}\delta\mathbf{V}_m{}^T\mathbf{C}^{-1}V_{res} \tag{2.5}$$

where $\mathbf{C}$ is the diagonal covariance matrix of measurement uncertainties. Due to the nonlinear aspects of the inversion, a step-length damping scheme is used for each iteration, k,

29
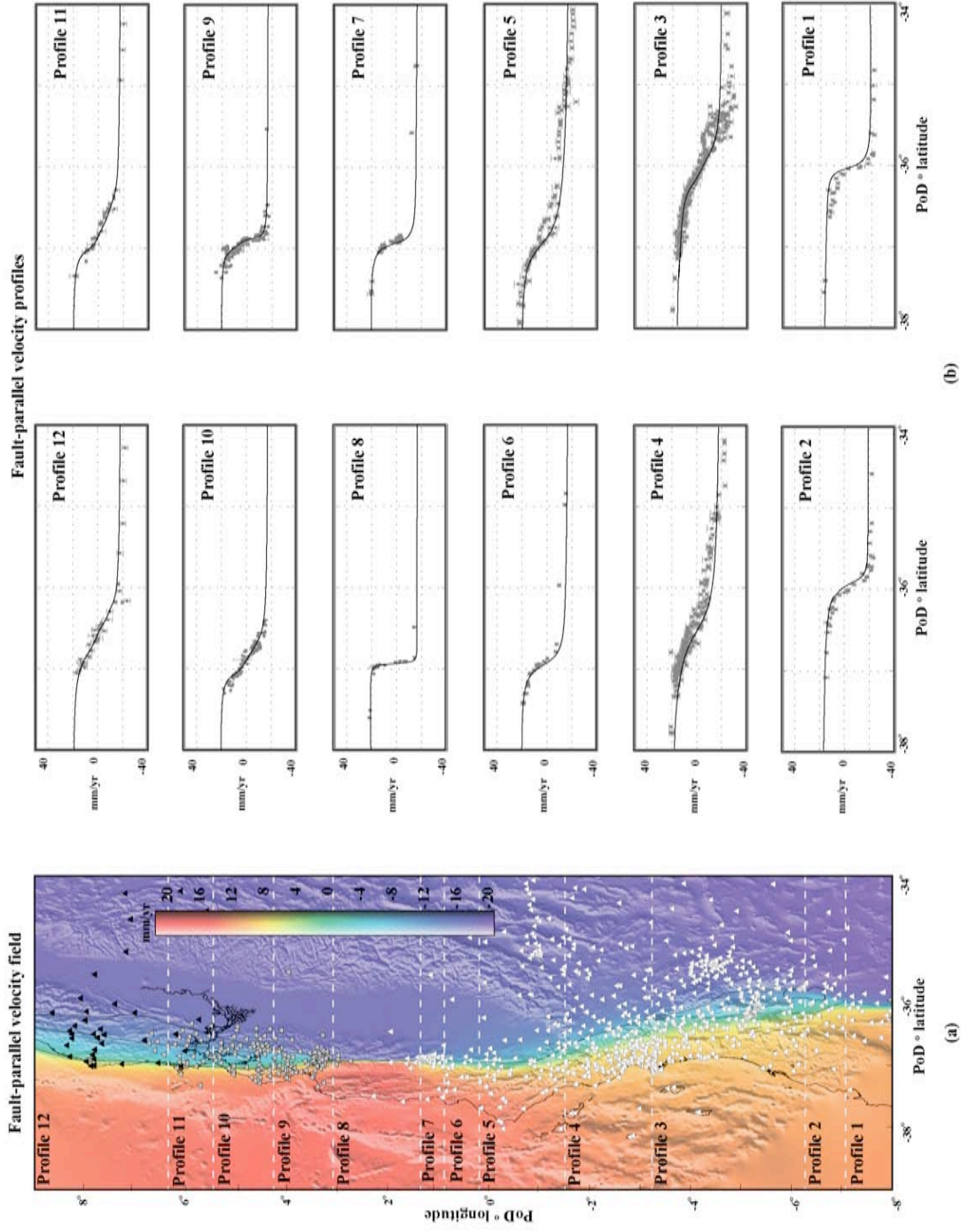
Figure 2.2. (a) Fault-parallel velocity map of best-fitting model with shaded topography. Triangles represent GPS station locations used in locking depth analysis. White triangles represent SCEC locations, gray triangles represent the U.C. Berkeley-Stanford-USGS stations (two sets), and black triangles represent stations of *Freymueller et al.* [1999]. Dashed lines represent horizontal fault corridor sections of model profiles of Figure 2.2b. (b) Modeled velocity profiles acquired across the center of each fault corridor with GPS velocities projected onto profile for visual comparison. (Note, the RMS differences between model and data were evaluated at actual GPS locations).

$$d_\gamma^k = d^{k-1} + \gamma \Delta \qquad 0 < \gamma < 1 \tag{2.6}$$

where γ is the damping parameter [*Parker*, 1994]. Damping parameter γ is chosen such that

$$\chi^2\left[m_\gamma\right] = \chi^2\left[m_k\right] - 2\gamma\, \chi^2\left[m_k\right] + o\|\gamma\Delta\| \tag{2.7}$$

will guarantee a smaller misfit than $\chi^2\left[m_k\right]$. The best fit is obtained by cautiously repeating this algorithm until all 18 locking depth solution parameters converge. Uncertainties in estimated locking depths are determined from the covariance matrix of the final iteration.

2.5   Results

2.5.1   Horizontal Motion and Locking Depth

Our locking depth inversion involves 26 free parameters: two unknown velocity components for each of the four GPS networks and 18 locking depths (Figures 2.1 and 2.2). The unknown velocity components for each of the GPS data sets is estimated by removing the mean misfit from a starting model (uniform locking depth of 10 km). The initial RMS misfit with respect to the starting model is 5.31 mm/yr (unweighted). After 10 iterations, the RMS misfit improves to 2.43 mm/yr (Figure 2.2). Comparisons between GPS data and fault-parallel modeled velocities for twelve fault corridors are shown in Figure 2.2b. Each model profile is acquired along a single fault-perpendicular trace, while the geodetic measurements are binned within the fault corridors and projected onto the perpendicular trace, thus some of the scatter is due to projection of the data onto a common profile.

Locking depth inversion results (Table 2.1) are primarily dependent on data acquired near the fault trace. Uncertainties in these estimates (1σ standard deviation) are relatively low in the southern portion of the SAF System where there is a high density of GPS stations. In contrast, uncertainties are much higher along the northern segments where there is a relatively low density of GPS stations. Our depth solutions are generally consistent with previously published locking depths and distributions of seismicity [e.g., *Savage*, 1990; *Johnson et al.*, 1994; *Feigl et al.*, 1993; *Freymueller et al.*, 1999]. Again, we emphasize that these are apparent locking depths since we have not included the viscoelastic response of the earth to intermittent earthquakes [*Thatcher*, 1983]. A more detailed discussion of model characteristics and GPS agreement for each of the 18 fault segments is provided in Appendix 2.B.

2.5.2   Far-field Constraint: 40 mm/yr

Because we are primarily interested in stress behavior close to the fault, the magnitude of the far-field velocity is not the most critical parameter in our analysis. Nevertheless, we attempt to justify the usage of a single far-field rate of 40 mm/yr for the entire SAF System. The full North American-Pacific Plate motion is approximately 46 mm/yr [*DeMets et al.*, 1990, 1994]. While the San Andreas Fault System accommodates the majority of deformation occurring between the two plates, substantial regions of deformation also exist far from the SAF System [*Minster and Jordan*, 1987; *Ward*, 1990]. These regions include the Eastern California Shear Zone, the Sierra Nevada-Great Basin shear zone, the Garlock fault zone, the Owens Valley

fault zone, and the San Jacinto, Whittier-Elsinore, Newport-Inglewood, Palos Verdes, and San Clemente faults. Partitioning details of the total slip rate remain uncertain. The *WGCEP* [1995, 1999] propose a total slip rate of 36-50 mm/yr along the northern portion of the San Andreas Fault System and a rate of 35 mm/yr along the southern portion of the San Andreas Fault System. In this analysis, we adopt a constant far-field velocity of 40 mm/yr for both northern and southern portions of the SAF System. Our results, using realistic fault geometry and variable locking depth, provide an adequate fit to all of the data (Figure 2.2b), especially close to the fault zones where we wish to calculate stress accumulation. The far-field regions of the extreme southern and northern SAF System are underestimated by our model (Figure 2.2b, profiles 1-4, 11, 12), while the middle portions of the system are well matched in the far-field (Figure 2.2b, profiles 6, 7, 9). There is significant misfit on the eastern sides of profiles 3, 4, and 5, which reflect both coseismic and interseismic shear in the Mojave desert. The apparent locking depth along these profiles may be artificially high in order to minimize the misfit in the Eastern California Shear Zone. Nevertheless, we have found that increasing the far-field velocity to 45 mm/yr, for example, does not significantly improve the fit to the GPS data and yields long-term slip rates that are inconsistent with published estimates [*WGCEP*, 1995, 1999]. Overall, the match to the GPS data is quite good considering the simplicity of the model.

2.5.3 Vertical Motion

An intuitive, yet important aspect of our 3-D model is the vertical component of deformation (Figure 2.3), driven entirely by horizontal force. Moreover, because the model parameters are constrained using only horizontal GPS velocity measurements, resulting vertical deformation can be checked against both geologically inferred and geodetically measured vertical rates. For simplicity, our model does not include the effects of topography. To develop the model, we assume that the far-field driving stress is always parallel to the relative plate motion vector. Because the fault segments are not always parallel to this driving stress, horizontal motion on free-slipping fault planes has both a fault-parallel and fault-perpendicular component. It is the fault-perpendicular component that drives most of the vertical deformation. For example, in the Big Bend area (Figure 2.3a) where the fault trace is rotated counter-clockwise with respect to the far-field stress vector, the fault-normal stress is compressional; this results in uplift rates of 2-4 mm/yr in this region. Fault-normal extensional stress occurs where the strike of the fault is rotated clockwise with respect to the far-field stress vector. This occurs in regions such as the Salton Trough, where our model predicts subsidence rates of 1-4 mm/year.

Our predicted vertical motion is in good agreement with recent geological activity. Approximately 8 million years ago, the North American-Pacific Plate boundary began to acquire a transpressional, or shortening, component as its relative velocity vector rotated clockwise with respect to the strike of the present SAF. Approximately 5 million years ago, the Pacific Plate captured Southern California and Baja California [*Atwater*, 1998], initiating the strike-slip plate boundary of the San Andreas Fault System. As a result, the current geometry of the SAF System has a prominent bend between Fort Tejon and the San Gorgonio Pass where the fault orientation has rotated from its conventional N40$°$W strike to a N70$°$W orientation [*Jones*, 1988]. This transpressional bend has produced the San Bernardino Mountains along with numerous thrust faults and the east-west trending Transverse Ranges. The Garlock fault and its left-lateral motion is a response to such transpressional behavior [*Atwater*, 1998].

Regions of prominent uplift produced by our model coincide with present topographic features such as the Transverse Ranges, the San Gabriel, and the San Bernardino Mountains (Figure 2.3a). We find a maximum uplift rate of 4.5 mm/yr occurring where the Garlock fault intersects the main San Andreas fault strand. We do not include the effects of the east-west striking Garlock fault into this analysis, but suspect that slip along the Garlock fault would reduce the fault-normal compressional stress and thus reduce the uplift
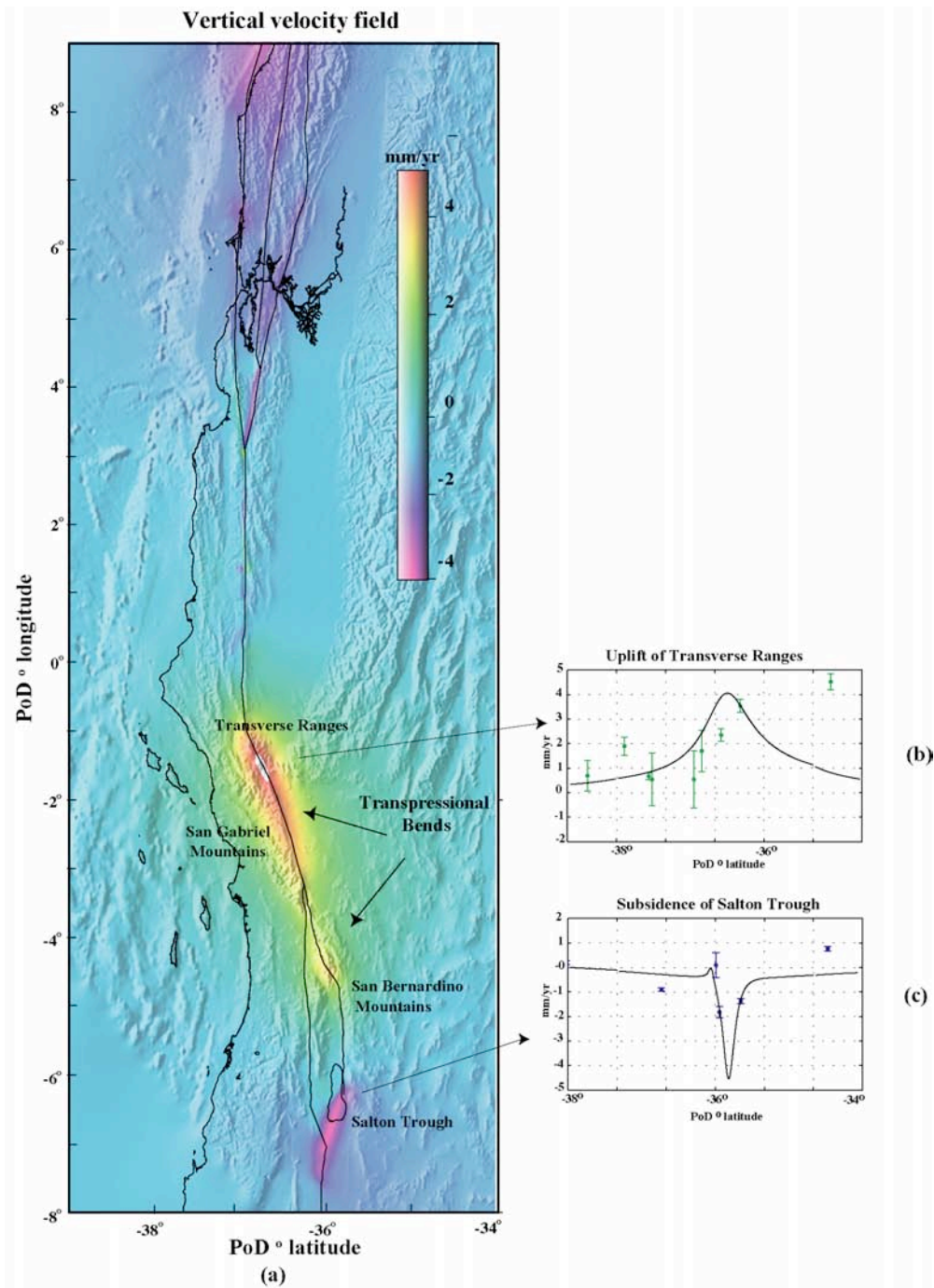
Figure 2.3. (a) Vertical velocity model with shaded topography (positive uplift and negative subsidence). Transpressional bends [*Atwater*, 1998] are shown, along with corresponding topographical features of the Transverse Ranges, San Gabriel, and San Bernardino Mountains. (b) Profile of vertical velocity model across uplifting region the Big Bend and sampled SCIGN vertical velocities. (c) Profile of vertical velocity model across subsiding region of Salton Trough and sampled SCIGN vertical velocities.

rate. *Williams and Richardson* [1991] report similar uplift rates of up to 3.5 mm/yr for this area from their 3-D kinematic finite element model. Further south, the uplifting region of the Carrizo-Mojave segment gradually decreases (3 mm/yr), following the San Andreas fault trace and the San Gabriel Mountains. Geologic estimates of late Quaternary uplift rate for the southern and central San Gabriel Mountains range from 3-10 mm/yr [*Brown*, 1991]. The intersection of the San Jacinto and San Bernardino-Coachella segments corresponds to a local minimum in the uplift rate. Even further south, our model predicts a local maximum uplift rate of 2 mm/yr at the San Bernardino Mountains. *Yule and Sieh* [1997] estimate a minimum uplift rate of 2 mm/yr just south of the San Bernardino Mountains based on excavation measurements near the San Gorgonio Pass.

Another primary feature of our vertical model is the subsiding region of the Salton Trough (Figure 2.3a). Although the geologic extension of the Salton Trough is well mapped, there is no consensus on how the strike-slip motion on the Imperial fault is transferred to the southern San Andreas along the Brawley Seismic Zone. This extensional step-over is likely to form a rifting site that will eventually evolve into a spreading center similar to that of the Gulf of California [*Lomnitz et al.,* 1970; *Elders et al.,* 1972; *Johnson and Hadley,* 1976; *Larsen and Reilinger,* 1991]. Leveling surveys of this region reveal a subsidence estimate of 3 mm/yr [*Larsen and Reilinger*, 1991]. Our model predicts approximately 4-8 mm/yr of localized subsidence in the Brawley-Imperial zone, located just south of the Salton Sea. *Johnson et al.* [1994] find a similar dilatational pattern in the Salton Trough from a kinematic model of slip transfer between the southern San Andreas and Imperial faults.

Vertical deformation predicted by our model is also in general agreement with geodetic measurements. Historically, vertical uplift has been estimated from repeated leveling surveys, and the interpretation of these results has often been speculative due to the low signal to noise ratio [*Stein*, 1987; *Craymer and Vanicek*, 1989]. More recent surveys, using methods such as VLBI, SLR, and GPS, have significantly improved the acquisition and accuracy of vertical measurements [*Williams and Richardson*, 1991]. While such observations along the San Andreas fault are spatially restricted and generally accompany large uncertainties, it is conceivable that these measurements may play a role in refining our understanding of the rheological structure of the Earth's crust [*Pollitz et al.*, 2001]. A preliminary comparison of continuous geodetic vertical measurements from the Southern California Integrated GPS Network (SCIGN) [*R. Nikolaidis*, personal communication, 2002] from the Big Bend and Salton Trough shows reasonable agreement with the model predictions (Figures 2.3b and c). Note that the vertical rates inferred from the GPS data have relatively large uncertainties (up to +/- 2mm/yr).

2.5.4 Static Coulomb Stress and Seismic Moment Accumulation

Deep slip along the San Andreas Fault System gives rise to stress accumulation on the upper locked portions of the fault network. After a period of time, often described as the recurrence interval, these stresses are released by seismic events. The rate of stress accumulation and earthquake recurrence interval can be used to estimate the average stress drops during major seismic events. Similarly, the seismic moment accumulation rate per unit length of a fault [*Ward*, 1994; *Savage and Simpson,* 1997], combined with recurrence intervals, can provide an estimate of the seismic "potential" of a fault segment. Our model can be used to estimate these quantities in the form of Coulomb stress and seismic moment accumulation rate.

To calculate Coulomb stress, we follow the approach of *King et al.* [1994] and *Simpson and Reasenberg* [1994] [also see *Stein and Lisowski*, 1983; *Oppenheimer et al.*, 1988; *Hudnut et al.*, 1989; *Harris and Simpson*, 1992]. The Coulomb failure criterion is

$$\sigma_f = \tau - \mu_f \sigma_n \qquad (2.8)$$

where σ_n and τ are the normal and shear stresses on a failure plane and μ_f is the effective coefficient of friction. Our semi-analytic model (Appendix 2.A) provides the three-dimensional vector displacement field from which we compute the stress tensor. For a vertical fault plane with strike-slip motion, only the horizontal stress components are needed: σ_{xx}, σ_{yy}, and τ_{xy}. The normal and shear stresses resolved on the fault plane are

$$\sigma_n = \sigma_{xx} \sin^2 \theta - 2\sigma_{xy} \sin \theta \cos \theta + \sigma_{yy} \cos^2 \theta$$

$$\qquad (2.9)$$

$$\tau = \frac{1}{2}\left(\sigma_{yy} - \sigma_{xx}\right)\sin 2\theta + \tau_{xy}\cos 2\theta$$

where θ is the orientation of the fault plane with respect to the x-axis. Right-lateral shear stress and extension are assumed to be positive.

Our objective is to calculate Coulomb stress accumulation rate on each of the 18 fault segments. Coulomb stress is zero at the surface and becomes singular at the locking depth as $d_j/d^2_j - z^2$. Each segment has a different locking depth d_j, so to avoid the singularity, we calculate the representative Coulomb stress accumulation rate at 1/2 of the local locking depth [*King et al.*, 1994]. This calculation is performed on a fault-segment by fault-segment basis, thus only the local fault contributes to the final Coulomb stress result. For the SAF System, the largest angular deviation of a local segment from the average slip direction is ~18˚, thus the normal stress contribution to the total Coulomb stress calculation is generally less than 10% (equation 2.8). Therefore, the exact value of the effective coefficient of friction is not important. Choosing μ_f to be 0.6, our model predicts Coulomb stress accumulation rates ranging from 0.5-12.5 MPa/100yrs (Figure 2.4a) for the segments of the SAF System. Average values of Coulomb stress accumulation along each segment are listed in Table 2.1. Because stress drops during major earthquakes rarely exceed 10 MPa, this calculation may provide an upper bound on the expected recurrence interval on each of the 18 fault segments as discussed below.

In addition to calculating the stress accumulation rate, our model provides a straightforward estimate of seismic moment accumulation rate per unit length of fault, l. Moment accumulation rate $\dot{M}$ depends on locking depth d_j, slip rate v_j, and the rock shear modulus μ

$$\frac{\dot{M}_j}{l} = \mu d_j v_j. \qquad (2.10)$$

Moment accumulation rate is often calculated from observed rates of surface strain accumulation [*WGCEP*, 1995, 1999; *Ward,* 1994; *Savage and Simpson*, 1997] and typically evaluated for a locking depth of 11-12 km [*WGCEP*, 1995; *WGNCEP*, 1996]. For this analysis, we use our locking depth estimates (Table 2.1) and equation 2.10 to calculate seismic moment accumulation rate per unit length for each fault segment of the SAF System, shown in Figure 2.4b (Table 2.1). As expected, high rates of moment accumulation (31.2 x 10^{14} Nm/100yr per km) occur where the locking depth is greatest, such as along the Big Bend area (segment 6 of the SAF), and low rates (1.6 x 10^{14} Nm/100yr per km) occur where the fault creeps from nearly top-to-bottom (SAF creeping segment) of the SAF System.
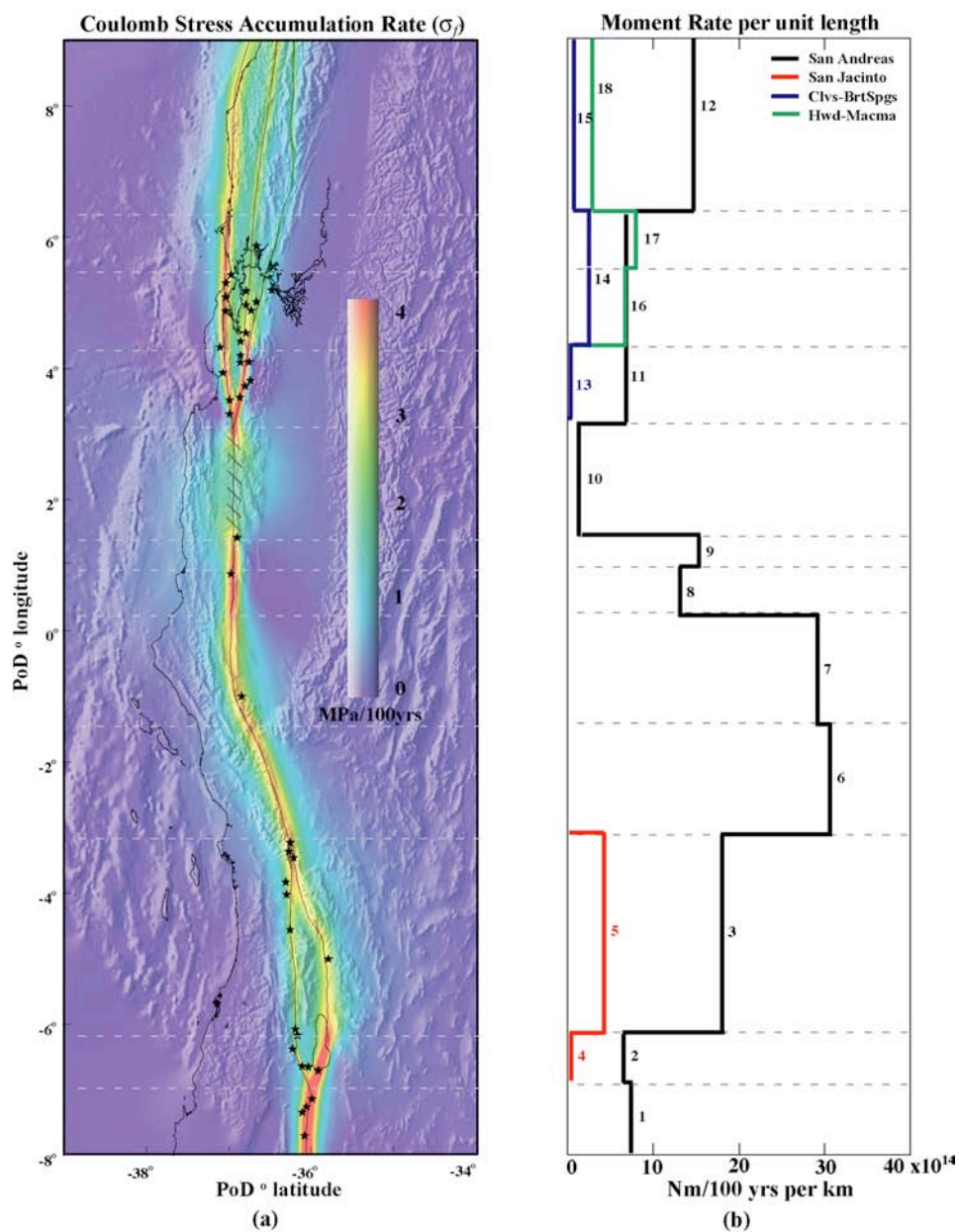
Figure 2.4. (a) Coulomb stress accumulation of the SAF System in MPa/100yrs with shaded topography. Color scale is saturated at 4 MPa/100yrs. Locations of significant earthquakes occurring on the San Andreas Fault System from 1769-2000 (primarily contributed by *Ellsworth* [1990]) are shown as black stars. Segment 10 (creeping SAF) was not included in the stress calculation and is marked with hash marks. Dashed lines represent horizontal fault corridor sections used in Figures 2.1 and 2.2. (b) Seismic moment accumulation per unit length of modeled segments in Nm/100yrs per length, labeled by segment numbers. The black solid line represents moment rate along the primary San Andreas strand (segments 1-3, 6-12). The red solid line represents moment rate along the San Jacinto strand (segments 4 and 5). The blue solid line represents moment rate of the Calaveras-Bartlett Springs strand (segments 13-15). The green solid line represents moment rate along the Hayward-Maacama strand (segments 16-18). Dashed lines represent horizontal fault corridor sections used in Figures 2.1 and 2.2.

2.6 Discussion

The main parameters affecting Coulomb stress accumulation are locking depth, slip rate, and fault strike. Coulomb stress accumulates fastest in regions of shallow locking depth and high slip rate (Figure 2.4a). It is also slightly enhanced or reduced if the fault orientation is releasing or restraining, respectively. Moreover, there is a correlation between locking depth and fault orientation suggesting that tectonically induced normal stress has an important influence on depth-averaged fault strength. *Wdowinski et al.* [2001] observe similar regions of high strain rate within the creeping Parkfield segment, the Cholame segment, the lower Coachella Valley segment, and along the Imperial segment where the relative plate motion vector is well-aligned with fault strike. In addition, they also find diffuse regions of lower magnitude strain-rate corresponding to the lower Carrizo segment and along the entire Mojave segment.

We also note an intriguing correlation between regions of high Coulomb stress accumulation and nucleation sites of large historical earthquakes along the San Andreas Fault System. Epicenters of such earthquakes occurring between 1796 and 2000 with magnitudes greater than 5.0 (contributed primarily by *Ellsworth* [1990]) are shown in Figure 2.4a. Moderate earthquakes (M = 5.0-7.0) are frequently found to occur in regions such as the Imperial Valley, San Jacinto-San Bernardino junction, Central San Andreas, Santa Cruz-Peninsula, and Southern Calaveras-Hayward faults. However, large events such as the Fort Tejon earthquake of 1857 (M = 7.9), the Great San Francisco earthquake of 1906 (M = 7.8), the Imperial Valley event of 1940 (M = 7.0), and the more recent Loma Prieta event of 1989 (M = 6.9) have all nucleated in zones of high Coulomb stress accumulation. The San Jacinto-San Bernardino region, where the two major fault strands converge, is particularly interesting because it has moderate Coulomb stress accumulation and has also experienced numerous magnitude 6.0-7.0 events between 1858-1923 (San Bernardino, Wrightwood, San Jacinto, and Lytle Creek).

2.6.1 Coulomb Stress and Fault Creep

Coulomb stress accumulation rate is also positively correlated with shallow fault creep. Faults are relatively weak at shallow depth because the normal stress due to overburden pressure is low. Thus creep may occur on segments where most of the stress is supported at shallow depths [*Savage and Lisowski*, 1993]. Our model demonstrates such behavior in the Imperial region, the Brawley Seismic Zone, and the Calaveras segment, where shallow creep has been known to occur [*Genrich and Bock*, 1997; *Bakun*, 1999; *Lyons et al.*, 2002]. We also note that while the Parkfield segment is found to have moderate locking depth (14 km) in our analysis, it also demonstrates high shallow stress accumulation. As discussed above, this is due to "straight" fault geometry and the fact that there is no partitioning of stress between sub-parallel fault strands. We do not find a significant correlation of high Coulomb stress with the Maacama, Hayward, and Concord-Green Valley segments (also known to have contributions of shallow creep [*WGNCEP*, 1996; *Burgmann et al.*, 2000, *Savage and Lisowski,* 1993]), which we attribute to our larger locking depth estimates.

2.6.2 Moment Accumulation Rate

As described above, our model is also used to estimate seismic moment accumulation rate per unit length along each fault segment (Figure 2.4b). These rates can be compared with stress accumulation rate and recurrence interval to establish seismic hazard [*WGCEP*, 1995, 1999; *WGNCEP*, 1996]. In our analysis, fault segments with high seismic moment accumulation rate are associated with deep locking depth, while faults with shallow locking depth have lower seismic moment accumulation rate and corresponding hazard potential [*Burgmann et al.*, 2000]. In general, we find that the main San Andreas Fault strand (segments 1-3, 6-12) accumulates most of the seismic moment (Figure 2.4b, black line), while subfaults (segments 4-5, 13-18) tend to accumulate less seismic moment (Figure 2.4b, red, green, and blue lines). One exception is the

Hayward and Rodgers Creek segments (green) where moment accumulation rate is comparable to the adjacent San Andreas segment. The *WGCEP* [1999] similarly recognizes the Hayward-Rodgers Creek faults as regions of elevated seismic potential.

Comparing the accumulation rates of both seismic moment and Coulomb stress, we find an inverse correlation, primarily due to the locking depth proportionality of each calculation. Seismic moment is directly proportional to locking depth, whereas Coulomb stress is approximately inversely proportional to locking depth. For example, more shallowly locked regions such as the Imperial fault, the Brawley Seismic Zone, and the Calaveras fault segments have high Coulomb stress accumulation rate and low seismic moment accumulation rate. Conversely, regions of the Mojave and San Bernardino-Coachella Valley segments have high seismic moment accumulation rate and low Coulomb stress accumulation rate. These areas have deep locking depths, greater than 20 km, which tend to absorb seismic moment while diluting accumulated stress. Other areas of interest include the Cholame and Parkfield segments with moderate seismic moment accumulation but high Coulomb stress accumulation rate. The Cholame and Parkfield segments have moderate locking depths (12-14 km) and produce expected amounts of seismic moment rate. However, these segments have nearly zero azimuthal angle with respect to driving stress vector and also support the entire motion of the SAF in this region, giving rise to high Coulomb stress accumulation.

2.6.3 Coulomb Stress and Earthquake Frequency

Average recurrence interval provides a more quantitative association between earthquake hazard potential (i.e., stress drop) and Coulomb stress accumulation rate. Estimates of recurrence interval, τ_r, compiled by the *WGCEP* [1995, 1999] and the *WGNCEP* [1999], are listed in Table 1 for each of the 18 fault segments. Assuming that all accumulated stress is released during major earthquakes, and given that earthquake stress drops are typically less than 10 MPa, an inverse correlation should exist between recurrence interval and Coulomb stress accumulation rate (Figure 2.5). The data for segments of the SAF System clearly demonstrate this inverse correlation, lying primarily within the margins of 1-10 MPa stress drop events with one primary exception; Segment 11 (Santa Cruz - Peninsula) has an exceptionally long recurrence interval, which may be due to the San Gregorio fault to the west [*WGCEP*, 1999]. The correlation is particularly good for remaining segments, implying that over a characteristic time period, these regions accumulate sufficient amounts of tectonic stress that result in large periodic earthquakes of 1-10 MPa stress drops.

Heat flow measurements suggest that the San Andreas fault may not support shear stresses greater than 10 MPa [*Lachenbruch and Sass*, 1988], implying that the SAF is much weaker than predictions based on simple rock friction [*Byerlee,* 1978]. Our estimates of Coulomb stress accumulation over realistic seismic intervals fall well within this limit. However, it is still possible that typical earthquake stress drop is only a fraction of the total tectonic stress if some of the heat is transported by hydrothermal processes.

2.7 Conclusions

In summary, we have developed and tested a semi-analytical model for the 3-D response of an elastic half-space to an arbitrary distribution of single-couple body forces. For a vertical fault, 2-D convolutions are performed in the Fourier transform domain, and thus displacement, strain, and stress due to a complicated fault trace can be computed very quickly. Using the Correspondence Principle, the method can be easily extended to a viscoelastic half-space without unreasonable computational burden.

We have used this method to estimate the velocity and stress accumulation rate along the entire San Andreas Fault System. Average slip rates along individual fault strands are based on long-term geological
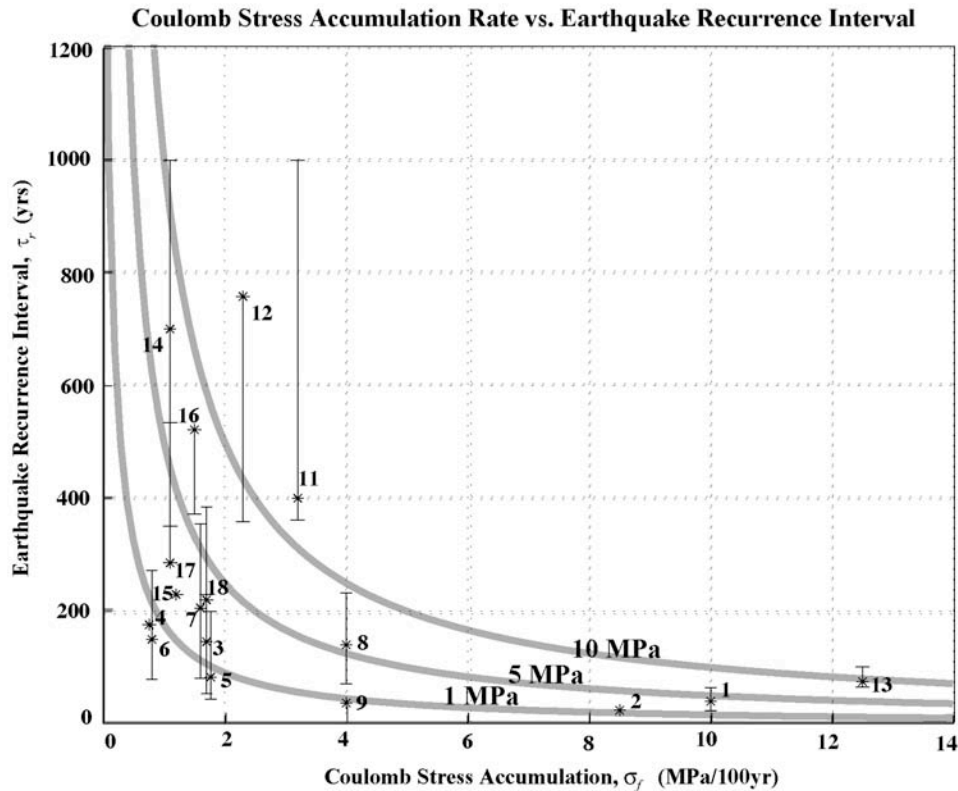
Figure 2.5. Published recurrence intervals of the SAF System, τ_r [*WGCEP*, 1995, 1999; *WGNCEP*, 1996] verses Coulomb stress accumulation rate, σ_f (Table 2.1). Segment 4 was acquired from *Peterson et al.* [1996]. Error bars were estimated by combining published results and uncertainty estimates. Segment numbers are labeled according to Table 2.1. Three characteristic stress drops are shown as thick gray lines, derived from the equation, $\tau_r = \Delta\sigma/\sigma_f$ reflecting constant stress drops of $\Delta\sigma = 1$, 5, and 10 MPa.

rates as well as recent geodetic measurements. The far-field slip rate is set to the best long-term average for the entire SAF System of 40 mm/yr. Horizontal components of GPS-derived velocities (1099 rates and uncertainties) are used to solve for variations in apparent locking depth for 18 primary segments. Locking depths vary between 1.3 km and 26.0 km. The horizontally-driven model also predicts vertical deformation rates consistent with geological estimates and geodetic measurements. From the analysis of shear and normal stress near the major fault strands, we find: i) Coulomb stress accumulation rate is dependent on slip partitioning and inversely proportional to locking depth. At mid-seismogenic depths, high Coulomb stress accumulation rate is correlated with shallow fault creep. Low Coulomb stress accumulation occurs along sections where stress is partitioned on multiple strands. ii) Seismic moment accumulation rate is greatest along deeply locked segments of the SAF System that accommodate the full relative plate motion. iii) Recurrence intervals of major earthquakes along the San Andreas Fault System are inversely related to Coulomb stress accumulation rate consistent with coseismic stress drops from 1-10 MPa.

This steady-state model is obviously too simple to explain the complex time-dependent stress evolution of the SAF System and we have ignored several important processes such as postseismic deformation, changes in local pore-pressure, and stress perturbations due to nearby earthquakes. Nevertheless, the agreement and predictions of this simple model are encouraging and provide a baseline for the development of more realistic 3-D time-dependent models.

2.8 Acknowledgements

2.9 References

Archuleta, R.J., A faulting model for the 1979 Imperial Valley earthquake, *J. Geophys. Res.*, 89, 4559-4585, 1984.

Atwater, T., Plate tectonic history of Southern California with emphasis on the Western Transverse Ranges and Santa Rosa Island, in *Contributions to the Geology of the Northern Channel Islands, Southern California*, edited by P. W. Weigand, pp. 1-8, Am. Assoc. of Pet. Geol., Pac. Sect., Bakersfield, Calif., 1998.

Bakun, W., Seismic Activity of the San Francisco Bay Region, *Bull. Seismol. Soc. Am.*, 89, 764-784, 1999.

Bird, P., and R.W. Rosenstock, Kinematics of present crust and mantle flow in southern California, *Geo. Soc. Am. Bull.*, 95, 946-957,1984.

Brown, R.D. Jr., Quaternary deformation, in Wallace, R.E., ed., The San Andreas Fault System, California, *U.S. Geol. Surv. Prof. Paper*, *1515*, 104-109, 1991.

Budding, K.E., D.P Schwartz, and D.H. Oppenheimer, Slip rate, earthquake recurrence, and seismogenic potential of the Rodgers Creek Fault Zone, Northern California: Initial results, *Geophys. Res. Lett.*, 18, 447-450, 1991.

Burgmann, R., D. Schmidt, R.M. Nadeau, M. d'Alessio, E. Fielding, D. Manaker, T.V. McEvilly, and M.H. Murray, Earthquake potential along the northern Hayward fault, California, *Science*, 289, 1178-1182, 2000.

Byerlee, J.D., Friction of rock, *Pure Appl. Geophys.*, 116, 615-626, 1978.

Castillio, D.A., and W.L. Ellsworth, Seismotectonics of the San Andreas fault system between Point Arena and Cape Mendocino in Northern California: Implications for the development and evolution of a young transform, *J. Geophys.. Res*, 98, 6543-6560, 1993.

Chinnery, M.A., The deformation of the ground around surface faults, *Bull. Seismol. Soc. Am.*, 51, 355-372, 1961.

Chinnery, M.A., The stress changes that accompany strike-slip faulting, *Bull. Seismol. Soc. Am.*, 53, 921-932, 1963.

Craymer, M.R. and P. Vanicek, Comment on "Saugus-Palmdale, California, field test for refraction error in historical leveling surveys" by R. S. Stein, C. T. Whalen, S. R. Holdahl, W. E. Strange, and W. Thatcher, and reply to "Comment on 'Futher analysis of the 1981 Southern California field test for levelling refraction by M. R. Craymer and P. Vanicek' by R. S. Stein, C. T. Whalen, S. R. Holdahl, W. E. Strange, and W. Thatcher", *J. Geophys. Res.*, 94, 7667-7672, 1989.

DeMets, C., R.G. Gordon, D.F. Argus, and S. Stein, Current plate motions, *Geophys. J. Int.*, 101, 425-478, 1990.

DeMets, C., R.G. Gordon, D.F. Argus, and S. Stein, Effect of recent revisions to the geomagnetic reversal time scale on estimates of current plate motions, *Geophys. Res. Lett.*, 21, 2191-2194, 1994.

Dokka, R.K., and C.J. Travis, Role of the Eastern California Shear Zone in accommodating Pacific-North American plate motion, *Geophys. Res. Lett.,* 17, 1323-1326, 1990.

Eaton, J.P., M.E. O'Neill, and J.N. Murdock, Aftershocks of the 1966 Parkfield-Cholame, California earthquake: A detailed study, *Bull. Seismol. Soc. Am.*, 60, 1151-1197, 1970.

Eberhart-Phillips, D., M. Lisowski, and M.D. Zoback, Crustal strain near the Big Bend of the San Andreas fault: Analysis of the Los Padres-Tehachapi trilateration networks, California, *J. Geophys. Res.*, 95, 1139-1153, 1990.

Elders, W.A., R.W. Rex, T. Meidav, P.T. Robinson, and S. Biehler, Crustal spreading in Southern California, *Science*, 178, 15-24, 1972.

Ellsworth, W.L., Earthquake history, 1769-1989, chap. 6 of Wallace, R.E., ed., The San Andreas Fault System, California, *U.S. Geol. Surv. Prof. Paper*, 1515, 152-187, 1990.

Feigl, K.L., D.C. Agnew, Y. Bock, D. Dong, A. Donnellan, B.H. Hager, T.A. Herring, D.D. Jackson, T.H. Jordan, R.W. King, S. Larsen, K.M. Larson, M.H. Murray, Z. Shen, and F.H. Webb, Space geodetic measurements of crustal deformation in Central and Southern California, 1984-1992, *J. Geophys. Res.*, 98, 21, 677-21,712, 1993.

Fialko, Y., and M. Simons, Deformation and seismicity in the Coso geothermal area, Inyo County, California: Observations and modeling using satellite radar interferometry, *J. Geophys. Res.*, 105, 21,781-21,794, 2000.

Freymueller, J.T., M.H. Murray, P. Segall, and D. Castillo, Kinematics of the Pacific-North America plate boundary zone, northern California, *J. Geophys. Res.,* 104, 7419-7441, 1999.

Furlong, K.P., W.D. Hugo, and G. Zandt, Geometry and evolution of the San Andreas Fault Zone in Northern California, *J. Geophys. Res.*, 94, 3100-3110, 1989.

Genrich, J.F., and Y. Bock, Crustal deformation across the Imperial Fault: Results from kinematic GPS surveys and trilateration of a densely spaced, small-aperture network, *J. Geophys. Res.*, 102, 4985-5004, 1997.

Harris, R.A., and P. Segall, Detection of a locked zone at depth on the Parkfield, California, segment on the San Andreas Fault, *J. Geophys. Res.*, 92, 7945-7962, 1987.

Harris, R., and R. Simpson, Changes in static stress on southern California faults after the 1992 Landers earthquake, *Nature*, 360, 251-254, 1992.

Hill, D.P., P. Mowinckel, and L.G. Peake, Earthquakes, active faults, and geothermal areas in the Imperial Valley, California, *Science*, 188, 1306-1308, 1975.

Hill, D.P., J.P. Eaton, and L.M. Jones, Seismicity, 1980-1986, in Wallace, R. E., ed., The San Andreas Fault System, California, *U.S. Geol. Surv. Prof. Paper*, *1515*, 1306-1308, 1991.

Hudnut, K.W., L. Seeber, and J. Pacheco, Cross-fault triggering in the November 1987 Superstition Hills earthquake sequence, Southern California, *Geophys. Res. Lett.*, 16, 199-202, 1989.

Jennings, C.W., Fault activity map of California and adjacent areas with locations and ages of recent volcanic eruptions: California Division of Mines and Geology Data Map Series No. 6, 92, 2 plates, map scale 1:750,000, 1994.

Johnson, C.E. and D.M. Hadley, Tectonic implications of the Brawley earthquake swarm, Imperial Valley, California, January 1975, *Bull. Seismol. Soc. Am.*, 66, 1133-1144, 1976.

Johnson, H.O., D.C. Agnew, and F.K. Wyatt, Present-day crustal deformation in southern California, *J. Geophys. Res.*, 99, 23,951-23,974, 1994.

Jones, L.M., Focal mechanisms and the state of stress on the San Andreas Fault in southern California, *J. Geophys. Res.*, 93, 8869-8891, 1988.

King, G.C.P. and M. Cocco, Fault interaction by elastic stress changes: New clues from earthquake sequences, *Adv. Geophys.*, 44, 1-38, 2001.

King. G.C.P., R.S. Stein, and J. Lin, Static stress changes and the triggering of earthquakes, *Bull. Seismol. Soc. Am.*, 84, 935-953, 1994.

King, N.E., P. Segall, and W. Prescott, Geodetic measurements near Parkfield, California, 1959-1984, *J. Geophys. Res.*, 92, 2747-2766, 1987.

Lachenbruch, A.H. and J.H. Sass, The stress heat-flow paradox and thermal results from Cajon Pass, *Geophys. Res. Lett.*, 15, 981-984, 1988.

Larsen, S.C., and R.S. Reilinger, Age constraints for the present fault configuration in the Imperial Valley, California: Evidence for northwestward propagation of the Gulf of California rift system, *J. Geophys. Res.*, 96, 10,339-10,346, 1991.

Larson, S., R. Reilnger, H. Neubegauer, and W. Strange, Global positioning system measurements of deformations associated with the 1987 Superstition Hills earthquake: Evidence of conjugate faulting, *J. Geophys. Res.*, 97, 4885-4902, 1992.

Li., V.C., and H.S. Lim, Modeling surface deformations at complex strike-slip plate boundaries, *J. Geophys. Res.*, 93, 7943-7954, 1988.

Lisowski, M., J. C. Savage, and W. H. Prescott, The velocity field along the San Andreas Fault in central and southern California, *J. Geophys. Res., 96*, 8369-8389, 1991.

Lomnitz, C., F. Mooser, C. R. Allen, J. N. Brune, and W. Thatcher, Seismicity and tectonics of the northern gulf of California region, Mexico - Preliminary results, *Geophys. Int.,* 10, 37-48, 1970.

Lyons, S.N., Y. Bock and D.T. Sandwell, Creep along the Imperial Fault, southern California, from GPS measurements, *J. Geophys. Res.*, 107(B10), 2249, doi:10.1029/2001JB000763, 2002.

Matthews, M. V., and P. Segall, Estimation of depth-dependent fault slip from measured surface deformation with application to the 1906 earthquake, *J. Geophys. Res.*, 98, 12,153-12,163, 1993.

Minster, J.B., and T.H. Jordan, Vector constraints on western U.S. deformations from space geodesy, neotectonics and plate motions, *J. Geophys. Res.*, 92, 4798-4804, 1987.

Murray, M.H., and P. Segall, Modeling broadscale deformation in northern California and Nevada from plate motions and elastic strain accumulation, *Geophys. Res. Lett.*, 28, 3215-4318, 2001.

Okada, Y., Surface deformation due to shear and tensile faults in a half-space, *Bull. Seismol. Soc. Am., 75*, 1135-1154, 1985.

Okada, Y., Internal deformation due to shear and tensile faults in a half-space, *Bull. Seismol. Soc. Am., 82*, 1018-1040, 1992.

Oppenheimer, D.H., P.A. Reasenberg, and R.W. Simpson, Fault plane solutions of the 1984 Morgan Hill, California, earthquake sequence: Evidence for the state of stress on the Calaveras Fault, *J. Geophys. Res.*, 93, 9007-9026, 1988.

Parker, R.L., *Geophysical Inverse Theory*, Chapter 5: Nonlinear Problems, 293-368, 1994.

Peterson, M., W. Bryant, C. Cramer, T. Cao, M. Reichle, A. Frankel, J. Lienkaemper, P. McCrory, and D. Schwartz, Probabilistic seismic hazard assessment for the state of California, *U.S. Geol. Surv. Open File Rep.*, 96-706, 1-64, 1996.

Pollitz, F.F., C. Wicks, and W. Thatcher, Mantle flow beneath a continental strike-slip fault: Postseismic deformation after the 1999 Hector Mine earthquake, *Science*, 293, 1814-1818, 2001.

Richards-Dinger, K.B., and P.M. Shearer, Earthquake locations in southern California obtained using source-specific station terms, *J. Geophys. Res.*, 10,939-10,960, 2000.

Rockwell, T., C. Loughman, and P. Merifield, Late Quaternary rate of slip along the San Jacinto fault zone near Anza, southern California, *J. Geophys. Res.*, 95, 8593-8605, 1990.

Rybicki, K., The elastic residual field of a very long strike-slip fault in the presence of a discontinuity, *Bull. Seismol. Soc. Am.*, 61, 72-92, 1971.

Sanders, C.O., Earthquake depths and the relation to strain accumulation and stress near strike-slip faults in southern California, *J. Geophys. Res.*, 95, 4751-4762, 1990.

Sauber, J., W. Thatcher, and S.C. Solomon, Geodetic measurements of deformation in the central Mojave Desert, California, *J. Geophys. Res.*, 91, 12,683-12,693, 1986.

Savage, J.C., Equivalent strike-slip earthquake cycles in half-space and lithosphere-asthenosphere earth models, *J. Geophys. Res., 95*, 4873-4879, 1990.

Savage, J.C. and R.O. Burford, Geodetic determination of relative plate motion in central California, *J. Geophys. Res., 78*, 832-845, 1973.

Savage, J.C., and M. Lisowski, Inferred depth of creep on the Hayward fault, central California, *J. Geophys. Res.*, 98, 787-793, 1993.

Savage, J.C. and R.W. Simpson, Surface strain accumulation and the seismic moment tensor, *Bull. Seismol. Soc. Am.*, 87, 1345-1353, 1997.

Savage, J.C., W.H. Prescott, M. Lisowski, and N. King, Deformation across the Salton Trough, California, 1973-1977, *J. Geophys. Res.*, 84, 3069-3079, 1979.

Sieh, K.E., and P.L. Williams, Behavior of the southernmost San Andreas Fault during the past 300 years, *J. Geophys. Res.*, 95, 6629-6645, 1990.

Simpson, R.W., and P.A. Reasenberg, Earthquake-induced static stress changes on central California faults, *U.S. Geol. Surv. Prof.* Paper, 1550-*F*, F55-F89, 1994.

Simpson, R.W., J.J. Lienkaemaper, and J.S. Galehouse, Variations in creep rate along the Hayward Fault, California, interpreted as changes in depth of creep, *Geophys. Res. Lett.*, 28, 2269-2271, 2001.

Stein, R.S., Contemporary plate motion and crustal deformation, *Rev. Geophys., 25*, 855-863, 1987.

Stein, R.S. and M. Lisowski, The 1979 Homestead Valley earthquake sequence, California: Control of aftershocks and postseismic deformation, *J. Geophys. Res.*, 88, 6477-6490, 1983.

Stein, R.S., G.C.P. King, and J. Lin, Stress triggering of the 1994 M = 6.7 Northridge, California, earthquake by its predecessors, *Science*, 265, 1432-1435, 1994.

Steinbrugge, K. V., W. K. Cloud, and N. H. Scott, The Santa Rosa, California, earthquakes of October 1, 1969, vol. 1970, pp. 1-63, U.S. Environ. Sci. Serv. Admin., Silver Spring, Md., 1970.

Steketee, J.A., On Volterra's dislocations in a semi-infinite elastic medium, *Can. J. Phys., 36*, 192-205, 1958.

Thatcher, W., Systematic inversion of geodetic data in central California, *J. Geophys. Res.*, 84, 2283-2295, 1979.

Thatcher, W., Nonlinear strain buildup and the earthquake cycle on the San Andreas Fault, *J. Geophys. Res.*, 88, 5893-5902, 1983.

Ward, S.N., Pacific-North America plate motions: New results from very long baseline interferometry, *J. Geophys. Res.*, 95, 21,965-21,981, 1990.

Ward, S.N., A multidisciplinary approach to seismic hazard in southern California, *Bull. Seismol. Soc. Am.*, 84, 1293-1309, 1994.

Wdowinski, S., Y. Sudman, and Y. Bock, Geodetic detection of active faults in S. California, *Geophys. Res. Lett*, 28, 2321-2324, 2001.

Weldon, R.J. II, and K.E. Sieh, Holocene rate of slip and tentative recurrence interval for large earthquakes on the San Andreas Fault, Cajon Pass, southern California, *Bull. Seismol. Soc. Am.*, 96, 793-812, 1985.

Weertman, J., Continuum distribution of dislocations on faults with finite friction, *Bull. Seismol. Soc. Am.*, 54, 1035-1058, 1964.

Williams, C.A., and R.M. Richardson, A rheologically layered three-dimensional model of the San Andreas Fault in central and southern California, *J. Geophys. Res.*, 96, 16,597-16,623, 1991.

Working Group on California Earthquake Probabilities (WGCEP), Seismic hazards in southern California: Probable earthquakes, 1994 to 2024, *Bull. Seismol. Soc. Am., 85*, 379-439, 1995.

Working Group on California Earthquake Probabilities (WGCEP), Earthquake probabilities in the San Francisco Bay Region: 2000 to 2030 – A summary of findings, *U.S. Geol. Surv. Open File Rep., [Online] 99-517,* version 1.0, 1999.

Working Group on Northern California Earthquake Potential (WGNCEP), Database of potential sources for earthquakes larger than magnitude 6 in northern California, *U.S. Geol. Surv. Open File Rep., 96-705,* 1996.

Yule, D., and K. Sieh, Neotectonic and paleoseismic investigation of the San Andreas fault system, San Gorgonio Pass, *1996 SCEC annual report* 14-08-001-A0899, C.70-74, 1997.

Zeng, Y., Viscoelastic stress-triggering of the 1999 Hector Mine earthquake by the 1992 Landers earthquake, *Geophys. Res. Lett.*, 28, 3007-3010, 2001.

APPENDIX 2.A   Analytic 3-D Body Force Model

We wish to calculate the displacement vector **u***(x,y,z)* on the surface of the Earth due to a vector body force at depth. This approach is used to describe motion on both curved and discontinuous faults, and is also used to evaluate stress regimes above the upper locking depth. For simplicity, we ignore the effects of Earth's sphericity. We assume a Poisson material and maintain constant moduli with depth. A major difference between this solution and the *Okada* [1985, 1992] solutions is that we consider deformation due to a vector body force, while the Okada solution considers deformation due to a dislocation.

While the following text provides a brief outline of our model formulation, the full derivation and source code of our semi-analytic Fourier model can be found at http://topex.ucsd.edu/body_force. Our solution is obtained as follows:

(1) Develop three differential equations relating a three-dimensional (3-D) vector body force to a 3-D vector displacement. We apply a simple force balance in a homogeneous, isotropic medium and after a series of substitutions for stress, strain, and displacement, we arrive at equation 2.A1, where *u,v,* and *w* are vector displacement components in *x, y,* and *z,* λ and μ are Lame parameters, ρ_j are vector body force components:

$$\mu\nabla^2 u + (\lambda + \mu)\left[\frac{\partial^2 u}{\partial x^2} + \frac{\partial^2 v}{\partial y \partial x} + \frac{\partial^2 w}{\partial z \partial x}\right] = -\rho_x$$

$$\mu\nabla^2 v + (\lambda + \mu)\left[\frac{\partial^2 u}{\partial x \partial y} + \frac{\partial^2 v}{\partial y^2} + \frac{\partial^2 w}{\partial z \partial y}\right] = -\rho_y \qquad (2.\text{A}1)$$

$$\mu\nabla^2 w + (\lambda + \mu)\left[\frac{\partial^2 u}{\partial x \partial z} + \frac{\partial^2 v}{\partial y \partial z} + \frac{\partial^2 w}{\partial z^2}\right] = -\rho_z$$

A vector body force is applied at $x = y = 0$, $z = a$. To partially satisfy the boundary condition of zero shear traction at the surface, an image source is also applied at $x = y = 0$, $z = -a$ [*Weertman, 1964*]. Equation 2.A2 describes a point body force at both source and image locations, where **F** is a vector force with units of force.

$$\rho(x,y,z) \; = \; \mathbf{F}\delta(x)\delta(y)\delta(z\text{-}a) \; + \; \mathbf{F}\delta(x)\delta(y)\delta(z+a) \tag{2.A2}$$

(2) Take the 3-D Fourier transform of equations 2.A1 and 2.A2 to reduce the partial differential equations to a set of linear algebraic equations.

(3) Invert the linear system of equations to isolate the 3-D displacement vector solution for $U(\mathbf{k})$, $V(\mathbf{k})$, and $W(\mathbf{k})$.

$$\begin{bmatrix} U(\mathbf{k}) \\ V(\mathbf{k}) \\ W(\mathbf{k}) \end{bmatrix} = \frac{(\lambda+\mu)}{|\mathbf{k}|^4 \mu(\lambda+2\mu)} \begin{bmatrix} \left(k_y^2+k_z^2\right)+\dfrac{\mu|\mathbf{k}|^2}{(\lambda+\mu)} & -k_y k_x & -k_z k_x \\[2mm] -k_x k_y & \left(k_x^2+k_z^2\right)+\dfrac{\mu|\mathbf{k}|^2}{(\lambda+\mu)} & -k_z k_y \\[2mm] -k_x k_z & -k_y k_z & \left(k_x^2+k_y^2\right)+\dfrac{\mu|\mathbf{k}|^2}{(\lambda+\mu)} \end{bmatrix} \dfrac{(e^{-i2\pi k_z a}+e^{i2\pi k_z a})}{4\pi^2} \begin{bmatrix} F_x \\ F_y \\ F_z \end{bmatrix}$$

where $\mathbf{k} = \left(k_x,k_y,k_z\right)$ and $|\mathbf{k}^2| = \mathbf{k}\bullet\mathbf{k}$.

$$\tag{2.A3}$$

(4) Perform the inverse Fourier transform in the z-direction (depth) by repeated application of the Cauchy Residue Theorem. We assume z to be positive upward.

(5) Solve the Boussinesq problem to correct for non-zero normal traction on the half-space. This derivation follows the approach of *Steketee* [1958] where we impose a negative surface traction in an elastic half-space in order to cancel the non-zero traction from the source and image in the elastic full-space.

(6) Integrate the point source Green's function to simulate a fault. For a complex dipping fault, this integration could be done numerically. However, if the faults are assumed to be vertical, the integration can be performed analytically. The body force is applied between the lower depth d_1 (e.g., minus infinity) and the upper depth d_2 (Figure 2.A1). The displacement or stress (derivatives are computed analytically) can be evaluated at any depth z above d_2. Note that the full displacement solution is the sum of three terms: a source, an image, and a Boussinesq correction.

$$\begin{bmatrix} U(\mathbf{k}) \\ V(\mathbf{k}) \\ W(\mathbf{k}) \end{bmatrix} = \begin{bmatrix} U_{xs} & U_{ys} & U_{zs} \\ U_{ys} & V_{ys} & V_{zs} \\ U_{zs} & V_{zs} & W_{zs} \end{bmatrix} \begin{bmatrix} F_x \\ F_y \\ F_z \end{bmatrix} + \begin{bmatrix} U_{xi} & U_{yi} & -U_{zi} \\ U_{yi} & V_{yi} & -V_{zi} \\ U_{zi} & V_{zi} & -W_{zi} \end{bmatrix} \begin{bmatrix} F_x \\ F_y \\ F_z \end{bmatrix} + \begin{bmatrix} U_B \\ V_B \\ W_B \end{bmatrix} \tag{2.A4}$$

The individual elements of the source and image tensors are

$$U_{xs}(\mathbf{k}) = \frac{C}{\beta^2}\left\{e^{-\beta(z-d_2)}\left[D + \frac{k_y^2}{|\mathbf{k}|^2} - \frac{k_x^2}{|\mathbf{k}|^2}\left(1 + \beta(z - d_2)\right)\right] - e^{-\beta(z-d_1)}\left[D + \frac{k_y^2}{|\mathbf{k}|^2} - \frac{k_x^2}{|\mathbf{k}|^2}\left(1 + \beta(z - d_1)\right)\right]\right\}$$

$$U_{ys}(\mathbf{k}) = -\frac{C}{\beta^2}\frac{k_x k_y}{|\mathbf{k}|^2}\left\{e^{-\beta(z-d_2)}\left(2 + \beta(z - d_2)\right) - e^{-\beta(z-d_1)}\left(2 + \beta(z - d_1)\right)\right\}$$

$$U_{zs}(\mathbf{k}) = -i\frac{C}{\beta^2}\frac{k_x}{|\mathbf{k}|}\left\{e^{-\beta(z-d_2)}\left(1 + \beta(z - d_2)\right) - e^{-\beta(z-d_1)}\left(1 + \beta(z - d_1)\right)\right\}$$

$$V_{ys}(\mathbf{k}) = \frac{C}{\beta^2}\left\{e^{-\beta(z-d_2)}\left[D + \frac{k_x^2}{|\mathbf{k}|^2} - \frac{k_y^2}{|\mathbf{k}|^2}\left(1 + \beta(z - d_2)\right)\right] - e^{-\beta(z-d_1)}\left[D + \frac{k_x^2}{|\mathbf{k}|^2} - \frac{k_y^2}{|\mathbf{k}|^2}\left(1 + \beta(z - d_1)\right)\right]\right\}$$

$$V_{zs}(\mathbf{k}) = -i\frac{C}{\beta^2}\frac{k_y}{|\mathbf{k}|}\left\{e^{-\beta(z-d_2)}\left(1 + \beta(z - d_2)\right) - e^{-\beta(z-d_1)}\left(1 + \beta(z - d_1)\right)\right\}$$

$$W_{zs}(\mathbf{k}) = \frac{C}{\beta^2}\left\{e^{-\beta(z-d_2)}\left[D + 1 + \beta(z - d_2)\right] - e^{-\beta(z-d_1)}\left[D + 1 + \beta(z - d_1)\right]\right\}$$

$$U_{xi}(\mathbf{k}) = \frac{C}{\beta^2}\left\{e^{\beta(z+d_2)}\left[D + \frac{k_y^2}{|\mathbf{k}|^2} - \frac{k_x^2}{|\mathbf{k}|^2}\left(1 - \beta(z + d_2)\right)\right] - e^{\beta(z+d_1)}\left[D + \frac{k_y^2}{|\mathbf{k}|^2} - \frac{k_x^2}{|\mathbf{k}|^2}\left(1 - \beta(z + d_1)\right)\right]\right\}$$

$$U_{yi}(\mathbf{k}) = -\frac{C}{\beta^2}\frac{k_x k_y}{|\mathbf{k}|^2}\left\{e^{\beta(z+d_2)}\left(2 - \beta(z + d_2)\right) - e^{\beta(z+d_1)}\left(2 - \beta(z + d_1)\right)\right\}$$

$$U_{zi}(\mathbf{k}) = i\frac{C}{\beta^2}\frac{k_x}{|\mathbf{k}|}\left\{e^{\beta(z+d_2)}\left(1 - \beta(z + d_2)\right) - e^{\beta(z+d_1)}\left(1 - \beta(z + d_1)\right)\right\}$$

$$V_{yi}(\mathbf{k}) = \frac{C}{\beta^2}\left\{e^{\beta(z+d_2)}\left[D + \frac{k_x^2}{|\mathbf{k}|^2} - \frac{k_y^2}{|\mathbf{k}|^2}\left(1 - \beta(z + d_2)\right)\right] - e^{\beta(z+d_1)}\left[D + \frac{k_x^2}{|\mathbf{k}|^2} - \frac{k_y^2}{|\mathbf{k}|^2}\left(1 - \beta(z + d_1)\right)\right]\right\}$$

$$V_{zi}(\mathbf{k}) = i\frac{C}{\beta^2}\frac{k_y}{|\mathbf{k}|}\left\{e^{\beta(z+d_2)}\left(1 - \beta(z + d_2)\right) - e^{\beta(z+d_1)}\left(1 - \beta(z + d_1)\right)\right\}$$

$$W_{zi}(\mathbf{k}) = \frac{C}{\beta^2}\left\{e^{\beta(z+d_2)}\left[D + 1 - \beta(z + d_2)\right] - e^{\beta(z+d_1)}\left[D + 1 - \beta(z + d_1)\right]\right\}$$

(2.A5)

$$C = \frac{(\lambda + \mu)}{4\mu(\lambda + 2\mu)} \qquad D = \frac{\lambda + 3\mu}{\lambda + \mu} \qquad \alpha = \frac{\lambda + \mu}{\lambda + 2\mu} \qquad |\mathbf{k}| = \left(k_x^2 + k_y^2\right)^{1/2} \qquad \beta = 2\pi|\mathbf{k}|.$$

The individual elements of the Boussinesq correction are

$$U_B = -i2\pi k_x \frac{1}{2\mu}\frac{\tau_3(\mathbf{k})}{\beta^3}\left[1 - \frac{1}{\alpha} - \beta z\right]e^{\beta z}$$

$$V_B = -i2\pi k_y \frac{1}{2\mu}\frac{\tau_3(\mathbf{k})}{\beta^3}\left[1 - \frac{1}{\alpha} - \beta z\right]e^{\beta z}$$

(2.A6)

$$W_B = -\frac{1}{2\mu}\frac{\tau_3(\mathbf{k})}{\beta^2}\left[\frac{1}{\alpha} - \beta z\right]e^{\beta z}$$

where

$$\tau_3 = -i\frac{k_x}{|\mathbf{k}|}\left\{e^{\beta d_2}\left(\alpha\beta d_2 - \frac{\lambda}{(\lambda + 2\mu)}\right) - e^{\beta l_1}\left(\alpha\beta d_1 - \frac{\lambda}{(\lambda + 2\mu)}\right)\right\}F_x$$

$$-i\frac{k_y}{|\mathbf{k}|}\left\{e^{\beta d_2}\left(\alpha\beta d_2 - \frac{\lambda}{(\lambda + 2\mu)}\right) - e^{\beta d_1}\left(\alpha\beta d_1 - \frac{\lambda}{(\lambda + 2\mu)}\right)\right\}F_y \qquad (2.A7)$$

$$+\left\{e^{\beta d_2}\left(\alpha\beta d_2 - \frac{\mu}{(\lambda + 2\mu)} - 2\alpha\right) - e^{\beta d_1}\left(\alpha\beta d_1 - \frac{\mu}{(\lambda + 2\mu)} - 2\alpha\right)\right\}F_z.$$

(7) Construct a force couple by taking the derivative of the point source in the direction normal to the fault trace. In practice, the body forces due to the stress discontinuity across a fault plane are approximated by the derivative of a Gaussian function, effectively producing a model fault with a finite thickness (Figure 2.A1). Curved faults are constructed with overlapping line segments having cosine tapered ends and are typically 6-10 km long.

The fault trace is imbedded in a two-dimensional grid which is Fourier transformed, multiplied by the transfer functions above (2.A5-7), and inverse Fourier transformed. A constant shear modulus (4.12 x 10^{10} Pa) and Poisson ratio (0.25) were adopted for all calculations. When the lower edge of the fault is extended to infinite depth, as in the case of the SAF System model, a Fourier cosine transform (mirrored pair) is used in the across-fault direction to maintain the far-field velocity V step across the plate boundary, effectively conserving moment within the grid. Note that this requires the velocity-difference (i.e., stress drop) across a system of connecting faults to have a constant value $F = \mu V$. To avoid Fourier artifacts where the fault enters the bottom of the grid and leaves the top of the grid, the fault is extended beyond the top of the model and angled to match the intersection point at the bottom (Figure 2.A1). In addition to computing the velocity field, strain and stress rates are computed from the derivatives of the model. Horizontal derivatives are computed by multiplication of $i2\pi k$ in the Fourier transform domain and vertical derivatives are computed analytically from the transfer functions in 2.A5 and 2.A6.
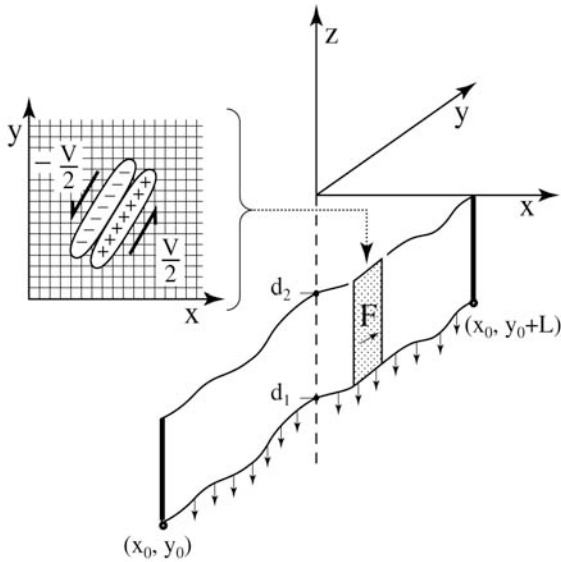
Figure 2.A1. Sketch of 3-D fault model in an elastic half-space. The fault extends from a lower depth of d_1 to an upper depth of d_2; in our model, $d_1 \rightarrow \infty$. A displacement discontinuity across the fault is simulated using a finite-width force couple, F, imbedded in the fine grid. The analytic form of the force couple is the derivative of a Gaussian function where the half-width of the Gaussian is equal to the cell spacing. The solution (2.A4) satisfies the zero-traction surface boundary condition. The x-boundary condition of constant velocity difference across the plate boundary is simulated using an image fault or a cosine transform in the x-direction. The y-boundary condition of uniform velocity in the far-field is simulated by arranging the fault trace to be cyclic in the y-dimension. That is, the slip at the end of the fault $(x_0, y_0 + L)$ is equal to the slip at the start of the fault (x_0, y_0).

Equations (2.A4-7) were checked using the computer algebra capabilities in Matlab and then compared to the simple arctangent function for a two-dimensional fault [*Weertman*, 1964]

$$V(x) = \frac{V}{\pi} \tan^{-1}\left(\frac{x}{d_2}\right) \cdot$$

Of course, in the two-dimensional case, the Boussinesq correction is not needed and equation 2.A5 reduces to the above arctangent formula. Figure 2.A2 provides a numerical comparison between the above arctangent function (analytic profile) and our semi-analytic Fourier solution (Fourier profile). The numerical solutions have relative errors less than 1% as long as the observation depth z is more than one grid cell size above the locking depth d_2.

The numerical approach is very efficient; for example, writing and displaying of the deformation/stress grids requires more computer time than the actual computation of the model. The horizontal complexity of the fault system has no effect on the speed of the computation. However, variations in locking depth along the fault system require computing the model for each different locking depth and summing the outputs to form the full solution. The extension to a viscoelastic half-space would not introduce a computational burden on an ordinary workstation.
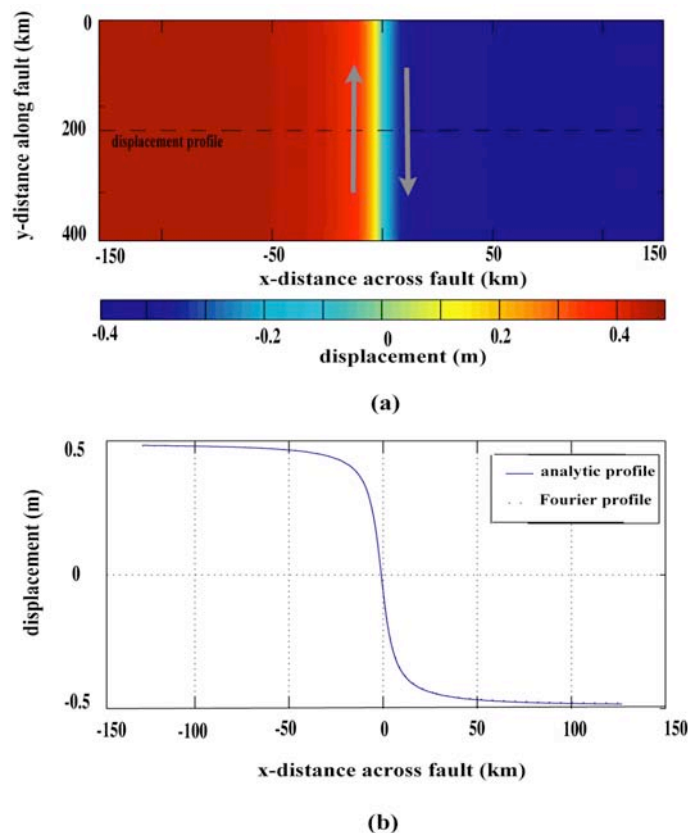
Figure 2.A2. Example model output with arctangent function comparison. (a) Map view of an infinitely long fault in the *y*-dimension imbedded in a 1-km spaced grid. We have assigned an upper locking depth of 5 km (d_2) to the fault plane and have extended the lower depth to infinity (d_1). (b) Comparison between the analytic solution of *Weertman* [1964] and a fault-perpendicular profile of our semi-analytic Fourier model. The two solutions are virtually indistinguishable and have relative errors less than 1%.

APPENDIX 2.B Locking Depth Analysis of Individual Fault Segments

We estimate lower locking depth for each of the 18 fault segments of the SAF System using a least squares fit to 1099 GPS-derived horizontal velocities (Figure 2.2) and an assigned cumulative deep slip rate of 40 mm/yr (Table 2.1). In some cases, as addressed below, locking depth results proved larger than previously published studies. We attribute this behavior to both lack of geodetic data and a slight over-estimate in assigned slip rate, due to the omission of external active faults within the region that tend to absorb some of the plate boundary motion. Hence, a larger applied plate velocity is effectively compensated by deeper locking of SAF segments. However, applying a deep slip rate other than 40 mm/yr does not significantly improve the fit to the GPS data, and yields inconsistent long-term slip rates for individual fault segments [*WGCEP*, 1995, 1999]. The locking depth results of our best fitting model are summarized below.

2.B.1 Profile 1: Segment 1

The Imperial fault, shown in Profile 1 of Figure 2.2b, is best modeled by a locking depth of 5.9 +/- 1.2 km. Published values of locking depth for the Imperial fault range from 8-13 km [*Archuleta*, 1984; *Genrich and Bock*, 1997; *Lyons et al.*, 2002], typically accompanying 45 mm/yr of slip with variations of surface creep. *Genrich and Bock* [1997] argue for a 9 km locking depth, but also cite 5 km as a reasonable minimum. Seismicity locations are identified at depths of 7.5 km +/- 4.5 km [*Richards-Dinger and Shearer*, 2000], lending equal validity to our more shallow locking depth estimate.

The Imperial fault is known to exhibit fairly complex slip behavior with associated creep and perhaps cannot be accurately modeled as a single fault segment that is simply locked at depth. Because we do not included the effects of shallow creep into our analysis, it is possible that our model is forced to shallower locking depths in order to satisfy data that do reflect fault creep. Conversely, the improved SCEC velocities may actually reveal the nature of a more shallowly locked fault than that of previous published models of the Imperial fault based on earlier data. It is also possible that the Imperial segment has a significant dipping component, producing an asymmetric displacement [*Lyons et al.*, 2002]. Our model neglects the case of dipping faults as we assume that all segments of the SAF System are vertical fault planes.

2.B.2 Profile 2: Segments 2 and 4

Profile 2 compares velocities of both the Brawley segment and Borrego segment. Our inversion results in a locking depth estimate of 6.3 +/- 1.3 km for the Brawley region. *Johnson and Hadley* [1976] identified hypocentral depths of earthquake swarms in the 4-8 km range for this region, placing our solution within acceptable range. Similarly, *Johnson et al.* [1994] present a 5 km locking depth model for the Brawley region based on work by *Bird and Rosenstodk* [1984], *Weldon and Sieh* [1985], *Rockwell et al.* [1990], and *Sieh and Williams* [1990]. Data are fairly sparse in the Borrego region, as evident in Profile 2, and do not show significant evidence for fault deformation, resulting in a locking depth of 2.0 +/- 7.7 km. Our model produced rather unstable results for this segment, often leaning towards 0 km locking depth. We attribute this behavior to not only lack of data, but also the fact that the fault trace of this region was estimated by connecting the lower Anza segment with the upper Imperial fault trace. In this region, many small sub-parallel branches exist [*Larsen et al.*, 1992] and we have most likely oversimplified the fault geometry. Seismicity is not particularly evident within 10 km of our estimated fault trace, and is found primarily to the southwest and constricted to the upper 10 km of the crust [*Hill et al., 1991*]. *Johnson et al.* [1994] show seismicity clustered heavily in the upper 5 km of the crust for the southernmost portion of our modeled region. They also identify a 5 km shallow locking depth solution for this region from geodetic observations.

2.B.3   Profile 3: Segments 3 and 5

Profile 3 displays the major region of the San Jacinto and Coachella-San Bernardino fault segments (Figure 2.1, segments 5 and 3, respectively). We find a locking depth of 22.6 +/- 1.7 km for the greater portion of the Coachella-San Bernardino segment, providing a good match to the 25 km depth chosen by *Feigl et al*. [1993]. The San Jacinto region is best modeled at 13.1 km +/- 2.3 km, corresponding within limits of uncertainty to the 10-11 km locking depth estimated by previous models [*Sanders*, 1990; *Savage*, 1990; *Li and Lim*, 1988]. Seismicity is heavily confined to 10-20 km depths for the San Jacinto region [*Johnson et al*., 1994], placing our modeled estimate of 13 km within acceptable limits. A visual inspection of Profile 3 also reveals the anomalous velocities associated with regional deformation due to the Eastern California Shear Zone (ECSZ), located east of the San Bernardino-Coachella trace. Our modeling efforts do not account for the complex deformation evident in this region [*Dokka and Travis,* 1990; *Sauber et al*., 1986; *Savage,* 1990], nor do we include the left-lateral Pinto Mountain fault into our analysis, also known to contribute additional complications in this area.

2.B.4   Profile 4: Segment 6

Profile 4 displays our modeled Mojave segment at 26 +/- 1.7 km depth. Similarly, *Eberhart-Phillips et al*. [1990] propose a 25 km locking depth for this region. *Savage* [1990] argues for a 30 km locking depth estimate for this portion of the Transverse Ranges using an elastic plate model overlying a viscoelastic half-space, providing a realistic match to our simple elastic half-space model. *Thatcher* [1983] illustrated a similar comparison for this region, making the valid point that two physically different mechanisms (elastic vs. viscoelastic half-space) produce indistinguishable surface deformation. Again, we note the evident un-modeled velocities to the east of the fault trace that are related to complex deformation patterns of the ECSZ.

2.B.5   Profile 5: Segment 7

The Carrizo segment, located just north of the Big Bend, is shown in Profile 5, modeled at 25.2 +/- 2.6 km. This value agrees well with previously published models of 25 km locking depth [*Harris*, 1987; *Eberhart-Phillips et al*., 1990]. We again note anomalous velocities to the east of this region, consistent with Eastern California Shear Zone deformation.

2.B.6   Profile 6: Segment 8

The Cholame segment, located in Profile 6, is modeled best by a locking depth of 12.7 +/- 2.4 km. Similarly, *Richards-Dinger and Shearer* [2000] note seismicity located down to 12.5 km for this segment. *King et al*. [1987] prefer a model with a deep slip rate of 33 mm/yr and a locking depth of 16 km for this region, but also discuss the potential for locking between 14-18 km for constrained deep slip of 36 mm/yr. Our estimate of 12.7 km +/- 2.4 km places our results within reasonable agreement, although we constrain our deep slip at 40 mm/yr for this segment. Alternatively, *Li and Lim* [1988] explore shallow locking depths (4-9 km) as a plausible fit to the Cholame region.

2.B.7   Profile 7: Segment 9

The Parkfield segment is shown in Profile 7, modeled at a 14.5 +/- 2.9 km locking depth. It should be noted that the Parkfield segment incorporates a transitioning region of slip from a locked fault to that of aseismic creep [*Harris and Segall*, 1987]. Because this slip transition occurs along the 25 km length of the fault segment, our model finds a minimized misfit relating to the deeper locked portion to the south. *Harris and Segall* [1987] also report a 14 km transition depth for the locked portion of the Parkfield segment. Our model estimate and uncertainty lie slightly deeper than the 8-10 km locking depth published by *King et al*.

[1987] but within uncertainty limits of the locking depth estimate of *Eaton et. al.* [1970] of 10-12 km from aftershocks of the 1966 earthquake that occurred along the fault. *Richards-Dinger and Shearer* [2000] provide seismicity depths ranging from 11.4 km +/- 6.7 km.

2.B.8 Profile 8: Segment 10

Profile 8 shows our result for the creeping section of the SAF, just north of the Parkfield segment. Our inversion provides a locking depth of 1.3 km +/- 0.2 km, which does not imply continuous or quasi-continuous slip (fault creep) at the surface, as would be expected from geologic and geodetic estimates [*Savage and Burford*, 1973; *Thatcher*, 1979]. Data coverage is rather weak for this region, and it is possible that the geodetic measurements used in our analysis do not completely capture the true behavior of aseismic surface creep.

2.B.9 Profile 9: Segments 11 and 13

Profile 9 displays modeled segments of the San Andreas (Santa-Cruz and Peninsula) fault along with the Southern and Central Calaveras fault. We find that a 9.3 km +/- 0.6 km locking depth for the San Andreas region satisfies the data well, corresponding nicely to the 10 km estimate used by *Feigl et al.* [1993], and within acceptable limits to the estimate of 12 km by *Murray and Segall* [2001]. The Calaveras fault, located to the east of the San Andreas fault trace, exhibits regions of aseismic slip as it branches off in the northeastward direction from the creeping portion of the main San Andreas strand. This segment is known to have a high creep rate of 12-17 mm/yr [*WGECP*, 1996; *Bakun*, 1999], matching its long-term slip rate. We find that a locking depth of 1.6 km is required to accurately model the geodetic data for this region. This estimate agrees with *Oppenheimer et al.'s* [1988] estimate of 1-2 km based on aftershock solutions of the Morgan Hill event of 1984.

2.B.10 Profile 10: Segments 14 and 16

Further north, the Calaveras fault branches into the Southern Hayward fault to the west and the Northern Calaveras-Concord faults to the east. Profile 10 illustrates this behavior and also captures the Santa Cruz-Peninsula segment of the San Andreas as discussed above. We find a locking depth of 13.7 +/- 4.6 km for the Northern Calaveras-Concord and 15.7 km +/- 3.7 km for the Hayward region. While our model finds satisfactory locking depth estimates for this region, our results are rather unstable in that they tend to dramatically over and under estimate regions of the northern SAF System if left unbounded. The results we present here are most likely an unfortunate product of sparse data for this region, as illustrated by their associated uncertainties. Attempts to constrain either of these segments to a more shallow depth (e.g., 10.4 km [*Murray and Segall*, 2001] for Northern Calaveras-Concord or 12-14 km [*Burgmann et al.*, 2000; *Simpson et al.*, 2001] for Southern Hayward) simply result in unacceptably deep locking depth results for the remaining segments. Additions to the data set for the northern SAF System will be required in order to place better locking depth estimates for these regions.

2.B.11 Profile 11: Segments 11, 17, and 14

We obtain similar results for the segments incorporated into Profile 11. Again, we model the Santa Cruz-Peninsula segment and Northern Calaveras-Concord segment, now along with the Rodgers Creek segment. We again find a deeper locking depth than expected for the Rodgers Creek segment at 18.9 km +/- 6.7 km. This fault segment is thought to be completely locked to the base of the seismogenic zone, exhibiting zero properties of shallow creep [*WGCEP*, 1999]. Microseismicity suggests that this fault segment extends to a depth of approximately 12 km [*Budding et al.*, 1991], while hypocentral depths of two

1969 events of the Rodgers Creek fault were estimated at 9.5 and 10.5 km depths [*Steinbrugge et al*., 1970]. While our model estimate of this fault is admittedly higher than such published depths, our regions of uncertainty are also high, placing the modeled Rodgers Creek locking depth within acceptable limits. Again, additional data are necessary to make a better locking depth estimate of this segment.

2.B.12   Profile 12: Segments 12, 15, and 18

Finally, we present our results for the northernmost region of the San Andreas Fault System in Profile 12, modeling segments of North Coast San Andreas, Maacama, and Green Valley-Bartlett Springs faults. We find a 19.4 +/- 2.1 km locking depth best fits the North Coast section of the San Andreas Fault region, which agrees with *Matthews and Segall* [1993] who propose a 15-20 km locking depth. *Furlong et al*. [1989] provide a valid explanation for such deep locking behavior, suggesting that the northern San Andreas is connected to a deep shear zone by a sub-horizontal detachment at approximately 20 km depth. We also find locking depth values of 12.3 +/- 4.3 km for the Maacama fault and 9.1 km +/- 8.4 km for the Bartlett Springs fault. Unfortunately, seismicity depths are dispersed from 0-15 km [*Castillo and Ellsworth*, 1993] for the eastern region and do not help constrain our results. These three regions are well modeled by *Freymueller et al*. [1999] with locking depth estimates of 14.9 km (+12.5/-7.1 km), 13.4 km (+7.4/-4.8 km), and 0 km (+5km) for the North Coast San Andreas, Maacama, and Green Valley-Barlett Springs faults, respectively. While our estimates match those of *Freymueller et al*. [1999] within their limits of uncertainty, we again note that the data coverage for this region is particularly sparse and not extremely well posed for our locking depth inversion.

This chapter, in full, is a reprint of the material is it appears in the *Journal of Geophysical Research*, Bridget, Smith; Sandwell, David, 2003. The dissertation author was the primary investigator and author of this paper. The co-author directed and supervised the research.

Chapter 3

A 3-D Semi-Analytic Viscoelastic Model for Time-Dependent Analyses of the Earthquake Cycle

Bridget R. Smith and David T. Sandwell

Abstract. Exploring the earthquake cycle for large, complex tectonic boundaries that deform over thousands of years requires the development of sophisticated and efficient models. In this paper, we introduce a semi-analytic 3-D linear viscoelastic Maxwell model that is developed in the Fourier domain to exploit the computational advantages of the convolution theorem. A new aspect of this model is an analytic solution for the surface loading of an elastic plate overlying a viscoelastic half-space. When fully implemented, the model simulates (1) interseismic stress accumulation on the upper locked portion of faults, (2) repeated earthquakes on prescribed fault segments, and (3) the viscoelastic response of the asthenosphere beneath the plate following episodic ruptures. We verify both the analytic solution and computer code through a variety of 2-D and 3-D tests and examples. Based on the methodology presented here, it is now possible to explore thousands of years of the earthquake cycle along geometrically complex 3-D fault systems.

3.1 Introduction

Long-term tectonic loading, instantaneous fault rupture, and transient postseismic rebound are key components of the earthquake cycle that expose important spatial and temporal characteristics of crustal deformation. Understanding these dynamics for complicated continental transform boundaries requires 3-dimensional (3-D), time-dependent models that are able to simulate deformation over a wide range of spatial and temporal scales. Such ideal models must capture both the 3-D geometry of real fault systems and the viscoelastic response of repeated earthquakes. Even by limiting the problem to the quasi-static case (i.e., no seismic waves), such models must include timescales ranging from the rupture duration (~100 s) to the vertical rebound timescale (> 1000 yr) and length scales ranging from the fault thickness (~500 m) to the length of the transform boundary (~1000 km). Purely numerical algorithms, implemented on even the most powerful computers, cannot adequately resolve this wide range of length and timescales. Therefore, improved analytic methods are needed to reduce the scope of the numerical problem.

Here we develop a semi-analytic solution for the response of an elastic plate overlying a viscoelastic half-space due time-dependent point body forces (Figure 3.1). Our solution extends the analytic approach of *Rundle and Jackson* [1977] while enhancing computational efficiency and maintaining qualitative agreement with many purely numerical studies. The 3-D problem is solved analytically in both the vertical dimension (z) and the time dimension (t), while the solution in the two horizontal dimensions (x,y) is developed in the Fourier transform domain to exploit the efficiency offered by the convolution theorem. Using this numerical approach, the horizontal fault pattern and slip distribution can be arbitrarily complex without increasing the computational burden. The full 3-D time-dependent model presented here can be comfortably implemented

on a desktop computer using a grid that spans spatial scales ranging from 1 km to 2048 km, although larger grids are possible.

Figure 3.1. 3-D sketch of Fourier fault model simulating an elastic layer overlying a linear Maxwell viscoelastic half-space. Fault elements are embedded in a plate of thickness H (or h) and extend from a lower depth of d_1 to an upper depth of d_2. A displacement discontinuity across each fault element is simulated using a finite width force couple, F, imbedded in a fine grid (see Appendix 3.E). Model parameters include plate velocity (V_o), shear modulus (μ_1, μ_2), Young's modulus (E_1, E_2), density (ρ), and viscosity (η). Note that the elastic moduli for the viscoelastic half-space (μ_2, E_2) are time- and viscosity-dependent and depend upon values given to their elastic plate counterparts, μ_1 and E_1 (Appendix 3.D).

In this first paper, we develop the semi-analytic solutions to the 3-D viscoelastic problem for a vertical fault model and compare numerical results against known analytic solutions in order to assess the accuracy and efficiency of the technique. In a supplemental paper, we will apply this method to simulate the earthquake cycle along the San Andreas Fault System for the past several thousand years. These models are necessary, as seismic and geodetic measurements have recorded only a small portion of the earthquake cycle on major fault segments and therefore the viscoelastic response of the asthenosphere, which will introduce long-term fault-to-fault coupling, remains poorly constrained. Furthermore, postseismic deformation mechanics pose many unanswered questions relating to the rheological parameters and time-dependent relaxation processes of the Earth.

Several postseismic models have been developed to match geodetically-measured surface velocities. These models include poroelastic flow of fluids in the upper crust [e.g., *Peltzer et. al*, 1996, 1998; *Fialko*, 2004a], deep afterslip [e.g., *Shen et al.*, 1994; *Heki et al.*, 1997; *Savage and Svarc*, 1997; *Wdowinski et al.*, 1997], and fault zone collapse [e.g., *Massonnet et al.*, 1996]. While many efforts are being made to examine these models as possible explanations of postseismic behavior, in this paper we explore a model based on viscoelastic coupling between an upper elastic plate and a lower linear viscoelastic half-space [e.g., *Savage*

and Prescott, 1978; *Thatcher*, 1983, 1984; *Ivins*, 1996; *Deng et al.*, 1998; *Pollitz et al.,* 2001; *Hearn et al.*, 2002]. We also include the restoring force of gravity in our viscoelastic model to ensure sensible vertical results. We are particularly concerned with the time-dependent vertical response of the Earth to horizontal displacements given that recent studies have shown that vertical geodetic measurements are sensitive to the thickness of the elastic layer and the viscosity of the mantle [*Deng et al.*, 1998; *Pollitz et al.*, 2000; *Pollitz et al.*, 2001].

In addition to understanding postseismic deformation, many studies have focused on the 3-D evolution of the stress field. Coulomb stress change from large earthquakes has been used to explain the triggering of subsequent earthquakes and aftershocks [e.g., *King et al.*, 1994; *Stein et al.*, 1994; *Kilb et al.*, 2000; *King and Cocco*, 2001; *Zeng*, 2001; *Kilb et al.*, 2002; *Toda et. al*, 2002; *Anderson et al.*, 2003]. Many stress-transfer calculations are based on purely elastic models because analytic solutions [*Okada*, 1985, 1992] can be computed efficiently in three dimensions for realistic fault geometries and rupture histories. However, layered viscoelastic models are needed to investigate time-dependent deformation and the triggering of earthquakes over timescales comparable to the recurrence interval. Consequently, several realistic viscoelastic models have been developed and applied to stress relaxation problems following large earthquakes [e.g., *Freed and Lin*, 1998; *Deng et al.*, 1999; *Kenner and Segall*, 1999; *Freed and Lin*, 2001; *Zeng,* 2001; *Hearn et al.*, 2004]. However, because of computer speed and memory limitations, most of these numerical models are limited to a single recurrence interval and relatively simple fault geometries. Hence, current models do not adequately address 3-D deformation of *multiple* interacting fault strands spanning *multiple* earthquake cycles. A complete model, incorporating both of these aspects, could improve seismic hazard analyses and also provide greater insight into the physics of the earthquake cycle.

While the approach we develop here is capable of addressing elaborate faulting and earthquake scenarios, it also incorporates two important improvements to the analytic model developed by *Rundle and Jackson* [1977]. First, we satisfy the zero-traction surface boundary condition by developing a new analytic solution to the vertical loading problem for an elastic plate overlying a viscoelastic half-space where the gravitational restoring force is included (Appendix 3.A). The development of this analytic solution follows the approach of *Burmister* [1943] and *Steketee* [1958], but uses computer algebra to analytically invert the 6 by 6 matrix of boundary conditions. Second, rather than develop the Green's function for the spatial response of a point body force, we solve the differential equations and boundary conditions in the 2-D Fourier transform domain. This substantially reduces the computational burden associated with an arbitrarily complex distribution of force couples necessary for fault modeling.

The remaining sections of this paper focus on the derivation of the 3-D Fourier solution, comparisons with analytic tests, and a 3-D demonstration of the earthquake cycle for a simplified fault system. In Section 3.2, we provide a complete mathematical development of the model. This includes Appendices 3.A through 3.E, where many important details are provided. The computer code required to implement these equations is available at http://topex.ucsd.edu/body_force. Section 3.3 provides a number of tests of the Fourier solution and related code against a series of analytic solutions to end-member problems (e.g., 2-D dislocations and cylindrically-symmetric vertical loads). Section 3.4 provides several numerical examples of the time-evolution of the deformation and stress fields over an earthquake cycle using simple fault geometry. These examples focus on the vertical velocity that is driven by purely horizontal dislocations, as well as the temporal evolution of stress shadows following major earthquakes. Simple examples such as these provide important aspects of the earthquake cycle that will ultimately lead to a greater understanding of complex faulting scenarios spanning thousands of years.

3.2   Fourier 3-D Viscoelastic Model for Fault Deformation

3.2.1   New Developments to the Analytic Approach

At present, there are a variety of analytic and numeric 2-D and 3-D models used to investigate the behavior of elastic and viscoelastic deformation. Commonly used 2-D models include analytic solutions of *Weertman* [1964], *Rybicki* [1971], *Nur and Mavko* [1974], and *Savage and Prescott* [1978], and analytic 3-D solutions include those of *Rundle and Jackson* [1977] and *Okada* [1985, 1992].   More advanced 3-D numerical methods such as finite element models [e.g., *Lysmer and Drake*, 1972; *Yang and Toksoz*, 1981; *Melosh*, 1983; *Cohen*, 1984, *Williams and Richardson*, 1991], boundary element models [e.g., *Crouch and Starfield*, 1983; *Zang and Chopra*, 1991; *Thomas*, 1993], finite-difference models [e.g., *Olsen and Schuster*, 1992; *Frankel*, 1993], matrix propagator methods [e.g., *Haskell*, 1963; *Singh*, 1970; *Sato*, 1971; *Ward*, 1985; *Wang et al.*, 2003], etc. have been explored more recently in order to efficiently treat large-scale deformation problems with complex boundary conditions.   Numerical methods such as these provide improved computational efficiency but unfortunately lack the simplicity and speed of analytic solutions.

Rundle and Jackson [1977] developed a 3-D analytic viscoelastic solution (i.e., Green's function) based on the dislocation solutions of *Steketee* [1958], *Rybicki* [1971], and *Nur and Mavko* [1974]. While the Green's function is computationally efficient for calculating displacement or stress at a few points due to slip on a small number of faults, it is less efficient for computing deformation on large grids, especially when the fault system has hundreds or thousands of segments. Because the force-balance equations are linear, the convolution theorem can be used to speed the computation as follows: take the Fourier transform of the body-force couples representing fault elements, multiply by the Fourier transform of the Green's function of the model, and finally, take the inverse Fourier transform of the product to obtain the displacement or stress field. Using this approach, the horizontal complexity of the model fault system has no effect on the speed of the computation. For example, computing vector displacement and stress on a 2048 x 2048 grid for a fault system consisting of 400 segments and a single locking depth requires less than 40 seconds of CPU time on a desktop computer.   Because multiple time steps are required to fully capture viscoelastic behavior, a very efficient algorithm is needed for computing 3-D viscoelastic models with realistic 1000-year recurrence interval earthquake scenarios in a reasonable amount of computer time (i.e., days).

In addition to enhancing computational speed of the 3-D viscoelastic problem, we have also constructed a new solution for balancing normal stress in a layered half-space (Appendix 3.A). The method of images is commonly used to solve continuum mechanics problems having a free surface boundary condition. An image source is used to cancel the surface shear traction, although in three dimensions, the vertical traction remains nonzero. *Steketee* [1958] showed how to balance this vertical traction by adding a complementary solution corresponding to a vertical load on an elastic half-space - the Boussinesq problem [*Boussinesq*, 1885]. *Rundle and Jackson* [1977] used this elastic half-space solution to approximately balance the normal traction in the layered model and noted small depth-dependent errors associated with this approximation - they were chiefly concerned with horizontal deformation in their model. *Burmister* [1943] solved the surface loading problem for a plate overlying an elastic half-space but assumed an incompressible solid (Poisson's ratio $v = 0.5$). While our approach is similar to that of *Burmister* [1943], we solve the more general layered Boussinesq Problem without any restrictions on Poisson's ratio and have also included the restoring force of gravity.

The full solution for the layered Boussinesq-like problem is provided in Appendix 3.A. The important aspects of the derivation are related to the boundary conditions: 1) A vertical point load is applied at the free surface, 2) The two components of stress (normal and shear) as well as the two components of displacement (vertical and horizontal) must be continuous across the boundary between the layer and the half-space, 3) At

infinite depth, stresses and displacements within the half-space must go to zero. In the Fourier transform domain, the differential equations and boundary conditions simplify to a 6 x 6 system of algebraic equations (3.A12). This system was initially inverted using computer algebra, resulting in many pages of computer-generated equations. These pages were simplified by hand to the solutions provided in equations 3.A13 – 3.A21. The simplified solutions were checked again using computer algebra. Finally, the computer code was tested against existing analytic solutions (Section 3.3). The new Boussinesq solutions, combined with the mathematical solutions describing displacements and stresses in a layered viscoelastic medium (Section 3.2.2) form the full 3-D Fourier solution set.

3.2.2   3-D Fourier Model Formulation

The Fourier model consists of a Fourier transformed grid of body-force couples (representing multiple fault elements) embedded in an elastic plate overlying a viscoelastic half-space (Figure 3.1). We begin by solving for the displacement vector $\mathbf{u}(x,y,z)$ due to a point vector body force at depth. The following text provides a brief outline of our mathematical formulation while the full derivation and source code are available at http://topex.ucsd.edu/body_force.

(1) Develop differential equations relating a three-dimensional (3-D) vector body force to a 3-D vector displacement

$$\mu\nabla^2 u + (\lambda + \mu)\left[\frac{\partial^2 u}{\partial x^2} + \frac{\partial^2 v}{\partial y\partial x} + \frac{\partial^2 w}{\partial z\partial x}\right] = -\rho_x$$

$$\mu\nabla^2 v + (\lambda + \mu)\left[\frac{\partial^2 u}{\partial x\partial y} + \frac{\partial^2 v}{\partial y^2} + \frac{\partial^2 w}{\partial z\partial y}\right] = -\rho_y \tag{3.1}$$

$$\mu\nabla^2 w + (\lambda + \mu)\left[\frac{\partial^2 u}{\partial x\partial z} + \frac{\partial^2 v}{\partial y\partial z} + \frac{\partial^2 w}{\partial z^2}\right] = -\rho_z$$

where u, v, and w are vector displacements, λ and μ are Lame parameters, and ρ_x, ρ_y, and ρ_z are vector body force components. A vector body force is applied at $x = y = 0$, $z = a$. Note that z is positive upward and a has a value less than zero. To partially satisfy the boundary condition of zero shear traction at the surface, an image source [*Weertman, 1964*] is applied at a mirror location at $x = y = 0$, $z = -a$:

$$\boldsymbol{\rho}(x,y,z) = \mathbf{F}\delta(x)\delta(y)\delta(z-a) + \mathbf{F}\delta(x)\delta(y)\delta(z+a). \tag{3.2}$$

(2) Take the 3-D Fourier transform of equations 3.1 and 3.2 to reduce the partial differential equations to a set of linear algebraic equations.

(3) Invert the linear system of equations to obtain the 3-D displacement vector solution for $U(\mathbf{k})$, $V(\mathbf{k})$, and $W(\mathbf{k})$:

$$\begin{bmatrix} U(\mathbf{k}) \\ V(\mathbf{k}) \\ W(\mathbf{k}) \end{bmatrix} = \frac{(\lambda + \mu)}{|\mathbf{k}|^4 \mu(\lambda + 2\mu)} \begin{bmatrix} \left(k_y^2 + k_z^2\right) + \frac{\mu|\mathbf{k}|^2}{(\lambda+\mu)} & -k_y k_x & -k_z k_x \\ -k_x k_y & \left(k_x^2 + k_z^2\right) + \frac{\mu|\mathbf{k}|^2}{(\lambda+\mu)} & -k_z k_y \\ -k_x k_z & -k_y k_z & \left(k_x^2 + k_y^2\right) + \frac{\mu|\mathbf{k}|^2}{(\lambda+\mu)} \end{bmatrix} \frac{(e^{-i2\pi k_z a} + e^{i2\pi k_z a})}{4\pi^2} \begin{bmatrix} F_x \\ F_y \\ F_z \end{bmatrix} \tag{3.3}$$

where λ and μ are elastic constants, $\mathbf{k} = (k_x, k_y, k_z)$, $|\mathbf{k}|^2 = \mathbf{k} \cdot \mathbf{k}$, and where exponents raised to the power of $\pm i 2\pi k_z a$ correspond to the image and source components, respectively.

(4) Perform the inverse Fourier transform in the z-direction (depth) by repeated application of the Cauchy Residue Theorem. In the following equation, $\mathbf{U}(\mathbf{k}, z)$ represents the deformation matrix, where $|\mathbf{k}| = (k_x^2 + k_y^2)^{1/2}$ and subscripts s and i refer to source and image components.

$$\begin{bmatrix} U(\mathbf{k}) \\ V(\mathbf{k}) \\ W(\mathbf{k}) \end{bmatrix} = \mathbf{U}(\mathbf{k}, z) = \mathbf{U}_s(\mathbf{k}, z-a) \begin{bmatrix} F_x \\ F_y \\ F_z \end{bmatrix} + \mathbf{U}_i(\mathbf{k}, -z-a) \begin{bmatrix} F_x \\ F_y \\ F_z \end{bmatrix} \tag{3.4}$$

(5) Introduce a layer of thickness H into the system through an infinite summation of image sources [*Weertman*, 1964; *Rybicki*, 1971], reflected both above and below the surface $z = 0$ (Appendix 3.B).

$$\begin{bmatrix} U(\mathbf{k}) \\ V(\mathbf{k}) \\ W(\mathbf{k}) \end{bmatrix} = \mathbf{U}_s(\mathbf{k}, z-a) \begin{bmatrix} F_x \\ F_y \\ F_z \end{bmatrix} + \mathbf{U}_i(\mathbf{k}, -z-a) \begin{bmatrix} F_x \\ F_y \\ F_z \end{bmatrix} + \sum_{m=1}^{\infty} \left(\frac{\mu_1 - \mu_2}{\mu_1 + \mu_2} \right)^m \begin{bmatrix} \mathbf{U}_i(\mathbf{k}, z-a-2mH) \\ + \mathbf{U}_i(\mathbf{k}, -z-a+2mH) \\ + \mathbf{U}_i(\mathbf{k}, z-a+2mH) \\ + \mathbf{U}_i(\mathbf{k}, -z-a-2mH) \end{bmatrix} \begin{bmatrix} F_x \\ F_y \\ F_z \end{bmatrix} \tag{3.5}$$

In equation 3.5, shear moduli μ_1 and μ_2 refer to the elastic constants of the layer and underlying half-space, respectively. The development of this solution requires an infinite number of image sources, m, to satisfy the stress-free surface and layer boundary conditions, and therefore convergence of the series in the case $\mu_2 = 0$ is problematic. This special case, which corresponds to the end-member case of an elastic plate overlying a fluid half-space, is solved in Appendix 3.C.

(6) Integrate the point source Green's function over depths $[d_1, d_2]$ to simulate a fault plane (equation 3.6). For the general case of a dipping fault, this integration can be done numerically. However, if the fault is vertical, the integration can be performed analytically. The displacement or stress can be evaluated at any depth $z > d_1$. In the following equation, $\mathbf{U}'(\mathbf{k}, z)$ represents the depth-integrated solution:

$$\int_{d_1}^{d_2} \mathbf{U}(\mathbf{k}, z) dz = \mathbf{U}'(\mathbf{k}, z) = \left[\mathbf{U}_s'(\mathbf{k}, z-d_2) - \mathbf{U}_s'(\mathbf{k}, z-d_1) \right] \begin{bmatrix} F_x \\ F_y \\ F_z \end{bmatrix} + \left[\mathbf{U}_i'(\mathbf{k}, -z-d_2) - \mathbf{U}_i'(\mathbf{k}, -z-d_1) \right] \begin{bmatrix} F_x \\ F_y \\ F_z \end{bmatrix}$$

$$+ \sum_{m=1}^{\infty} \left(\frac{\mu_1 - \mu_2}{\mu_1 + \mu_2} \right)^m \begin{bmatrix} \left(\mathbf{U}_i'(\mathbf{k}, z-d_2-2mH) - \mathbf{U}_i'(\mathbf{k}, z-d_1-2mH) \right) \\ - \left(\mathbf{U}_i'(\mathbf{k}, -z-d_2+2mH) - \mathbf{U}_i'(\mathbf{k}, -z-d_1+2mH) \right) \\ + \left(\mathbf{U}_i'(\mathbf{k}, z-d_2+2mH) - \mathbf{U}_i'(\mathbf{k}, z-d_1+2mH) \right) \\ - \left(\mathbf{U}_i'(\mathbf{k}, -z-d_2-2mH) - \mathbf{U}_i'(\mathbf{k}, -z-d_1-2mH) \right) \end{bmatrix} \begin{bmatrix} F_x \\ F_y \\ F_z \end{bmatrix}. \tag{3.6}$$

The individual elements of the source and image matrices are

$$\mathbf{U}_s'(\mathbf{k},Z) = \begin{bmatrix} U_x & U_y & U_z \\ U_y & V_y & V_z \\ U_z & V_z & W_z \end{bmatrix} \quad \text{and} \quad \mathbf{U}_i'(\mathbf{k},Z) = \begin{bmatrix} U_x & U_y & U_z \\ U_y & V_y & V_z \\ -U_z & -V_z & -W_z \end{bmatrix} \tag{3.7}$$

where $\mathbf{Z}$ represents all z-dependent terms, including all combinations of z, d_n, and $2mH$. The six independent functions of the deformation matrix are

$$\begin{bmatrix} U_x \\ U_y \\ U_z \\ V_y \\ V_z \\ W_z \end{bmatrix} = \frac{C}{\beta^2} \begin{bmatrix} D + \dfrac{k_y^2}{|\mathbf{k}|^2} - \dfrac{k_x^2}{|\mathbf{k}|^2} & -\dfrac{k_x^2}{|\mathbf{k}|^2} \\[2mm] -2\dfrac{k_x k_y}{|\mathbf{k}|^2} & -\dfrac{k_x k_y}{|\mathbf{k}|^2} \\[2mm] -i\dfrac{k_x}{|\mathbf{k}|} & -i\dfrac{k_x}{|\mathbf{k}|} \\[2mm] D + \dfrac{k_x^2}{|\mathbf{k}|^2} - \dfrac{k_y^2}{|\mathbf{k}|^2} & -\dfrac{k_y^2}{|\mathbf{k}|^2} \\[2mm] -i\dfrac{k_y}{|\mathbf{k}|} & -i\dfrac{k_y}{|\mathbf{k}|} \\[2mm] D+1 & 1 \end{bmatrix} \begin{bmatrix} e^{-\beta z} \\ \beta Z e^{-\beta z} \end{bmatrix}, \tag{3.8}$$

where $\quad C = \dfrac{(\lambda_1 + \mu_1)}{4\mu_1(\lambda_1 + 2\mu_1)} \qquad D = \dfrac{\lambda_1 + 3\mu_1}{\lambda_1 + \mu_1} \qquad |\mathbf{k}| = \left(k_x^2 + k_y^2\right)^{1/2} \quad \text{and} \quad \beta = 2\pi|\mathbf{k}|.$

The solutions of equation 3.8 are identical to those of *Smith and Sandwell* [2003] but have been simplified for further manipulation of the exponential terms.

(7) Analytically solve for Maxwell viscoelastic time-dependence using the Correspondence Principle and assuming a Maxwell time defined by $\tau_m = 2\eta/\mu$ (Appendix 3.D). Following an approach similar to that of *Savage and Prescott* [1978], we map time and viscosity into an implied half-space shear modulus, μ_2. We require the bulk modulus to remain constant, and thus also solve for an implied E_2.

(8) Calculate the non-zero normal traction at the surface and cancel this traction by applying an equal but opposite vertical load on an elastic layer overlying a viscoelastic half-space (Appendix 3.A).

The numerical aspects of this approach involve generating grids of vector force couples (i.e., F_x, F_y, and F_z) that simulate complex fault geometry (Appendix 3.E), taking the 2-D horizontal Fourier transform of the grids, multiplying by the appropriate transfer functions and time-dependent relaxation coefficient, and finally inverse Fourier transforming to obtain the desired results. Arbitrarily complex curved and discontinuous faults can easily be converted to a grid of force vectors (Figure 3.1). The model parameters are: plate thickness (H), locking depths (d_1, d_2), shear modulus (μ), Young's modulus (E), density (ρ), gravitational acceleration (g), and half-space viscosity (η). As previously mentioned, the solution satisfies the zero-traction surface boundary condition and maintains stress and displacement continuity across the base of the plate (Appendix 3.A). The x-boundary condition of constant far-field velocity difference across the plate boundary is simulated using a cosine transform in the x-direction. The y-boundary condition of uniform velocity in the far field is simulated by arranging the fault trace to be cyclic in the y-dimension. This fault

model will be used to efficiently explore the 3-D viscoelastic response of the Earth throughout the earthquake cycle.

3.3 Analytic and Numeric Tests of Layered Viscoelastic Solution

3.3.1 2-D Analytic Comparisons

Although the solutions described above have been checked using computer algebra, it is necessary to verify the accuracy of our computer code through comparison with known analytic solutions. These include 2-D analytic examples of dislocations in (1) a homogeneous elastic half-space, (2) a layered elastic half-space, and (3) a layered viscoelastic half-space. For these tests, fault slip is simulated by embedding a straight, vertical fault in the y-dimension of a 1-km spaced grid of nominal dimension 2048 by 2048, performing a 2-D horizontal Fourier transform of the grid, multiplying by appropriate transfer functions (equations 3.6-3.8), and inverse transforming to arrive at the final solution. In the subsequent models, the following parameters are used, unless otherwise specified: $V_o = 40$ mm/yr, $H = 50$ km, $d_2 = -25$ km, $\mu_1 = 28$ GPa, $E_1 = 70$ GPa, and $\eta = 10^{19}$ Pa s.

3.3.1.1 Homogeneous elastic half-space

First we test the surface displacement due to an infinitely long 2-D fault in a homogeneous elastic medium that is locked between depths of d_1 and d_2 (Figure 3.2, solid line). The analytic solution [*Weertman*, 1964] is given by

$$V(x) = \frac{V_o}{\pi}\left[\tan^{-1}\left(\frac{d_2}{x}\right) - \tan^{-1}\left(\frac{d_1}{x}\right)\right],$$

(3.9)

where V_o is fault slip rate, d_1 is lower locking depth, d_2 is upper locking depth, and x is the perpendicular distance across the fault-plane. When d_1 is set to minus infinity, this solution is used to describe interseismic deformation (deep slip). Comparing this solution with our Fourier model (uniform elastic properties $E_2 = E_1$, $\mu_2 = \mu_1$) results in an error of 0.2% (gray inset, solid line). Because the fault length is assumed to be infinite, the x-length of the grid must be extended (e.g., 4096 elements) to achieve even higher accuracy.

In addition to this 2-D example, we have also compared the 3-D results of this model to the 3-D solutions of *Okada* [1985, 1992] for a finite-length dislocation in a homogeneous elastic half-space. Although not presented here, the two models are in excellent agreement for both horizontal and vertical displacements (http://topex.ucsd.edu/body_force).

3.3.1.2 Layered elastic half-space

As a second test, we compare the Fourier model to the 2-D analytic solution for a dislocation in an elastic layer of shear modulus μ_1 overlying a half-space of shear modulus μ_2 (Figure 3.2, dashed line). The analytic solution for the surface displacement due to a fault that is locked between depths of d_1 and d_2 [*Rybicki*, 1971] is given by

$$V = \frac{V_o}{\pi}\left[\tan^{-1}\left(\frac{d_2}{x}\right) - \tan^{-1}\left(\frac{d_1}{x}\right) + \sum_{m=1}^{\infty}\left(\frac{\mu_1 - \mu_2}{\mu_1 + \mu_2}\right)^m\left\{\begin{array}{l}\tan^{-1}\left(\frac{d_2 - 2mH}{x}\right) - \tan^{-1}\left(\frac{d_1 - 2mH}{x}\right) \\ + \tan^{-1}\left(\frac{d_2 + 2mH}{x}\right) - \tan^{-1}\left(\frac{d_1 + 2mH}{x}\right)\end{array}\right\}\right],$$

(3.10)

where H is the layer thickness and m refers to the number of image sources. Figure 3.2 (dashed line) shows the end-member case of deep slip ($d_1 = -H$) of a fluid half-space ($\mu_2 = 0$). The models agree to 0.1% (gray inset, dashed line), although larger far-field deviations are possible due to the slow convergence of the *Rybicki* [1971] solution. We must sum more than 10^5 terms of equation 3.10 to achieve full far-field convergence; the Fourier solution does not suffer from this convergence problem because the infinite sum is performed analytically (Appendix 3.C).
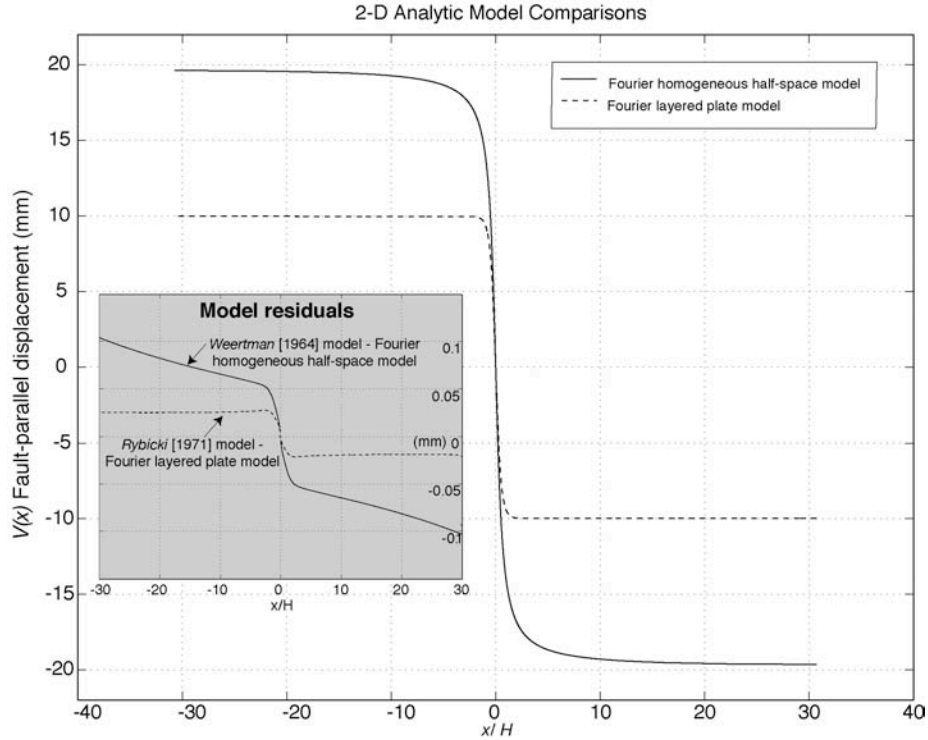
Figure 3.2. Comparison of fault-parallel displacement as a function of distance from the fault, x, with respect to plate thickness, H, for Fourier model profiles and existing 2-D analytic solutions. Deep-fault displacement for a homogeneous half-space Fourier model is represented by the solid black line; displacement for a layered half-space model simulating an elastic plate overlying a fluid half-space is represented by the dashed black line. Note how the layered half-space model has only half the amplitude of the homogeneous half-space model due to the inherent relationship that exists between the far-field displacement and the fraction of the plate that is cracked. Both homogenous and layered half-space Fourier models have relative errors (gray inset) less than 0.2% when compared to their respective analytic solutions, the *Weertman* [1964] and *Rybicki* [1971] models, respectively. Although the *Rybicki* [1971] solution is limited by the number of terms (m) included in the infinite series, the homogeneous half-space model comparison yields larger relative errors in the longer wavelengths, requiring a larger grid size to lower the relative error.

3.3.1.3 Layered viscoelastic half-space

The final 2-D comparison presented here tests our implementation of the Correspondence Principle for mapping the viscoelastic properties of the model into an equivalent elastic model. In 3-D, one must be careful to maintain a time-invariant bulk modulus. The analytic solution for this model is described by *Nur and Mavko* [1974], although their paper does not provide the equations for mapping the Maxwell-normalized time into the rigidity of each of the image layers. This mapping is provided in *Savage and Prescott* [1978], although our approach differs in that we do not explicitly include a constant earthquake recurrence interval (Appendix 3.D). We prefer to allow a variable recurrence interval to better simulate known earthquake

sequences. Therefore, we have no method of testing the numerical accuracy of this time-dependent model, although the above comparisons test the end-member cases.

Here we model an infinitely long vertical strike-slip fault that is embedded in a 50 km thick elastic plate overlying a viscoelastic half-space with Maxwell time constant τ_m. We consider the two cases of deep slip and shallow slip, representing interseismic and coseismic deformation, respectively. In the deep-slip case, a constant slip-rate is applied along the fault in the lower half of the plate (Figure 3.3a) to simulate interseismic deformation. The initial deformation rate ($t = 0$) matches the elastic half-space solution but eventually evolves to the solution for an elastic plate overlying a fluid half-space ($t = \infty$). A full step-function of plate velocity is achieved at times greater than $t = 100\tau_m$, which we will henceforth refer to as the "secular model". In the shallow-slip case (Figure 3.3b), 4 m of slip are applied to the upper half of the plate to simulate coseismic and postseismic deformation. The combined displacement (secular model + coseismic/postseismic) (Figure 3.3c) achieves a full 4-m step after $20\tau_m$ of postseismic relaxation. This model shows good qualitative agreement with previous studies [e.g., *Nur and Mavko*, 1974; *Rundle and Jackson*, 1977; *Savage and Prescott*, 1978; *Ward*, 1985; *Cohen*, 1999].
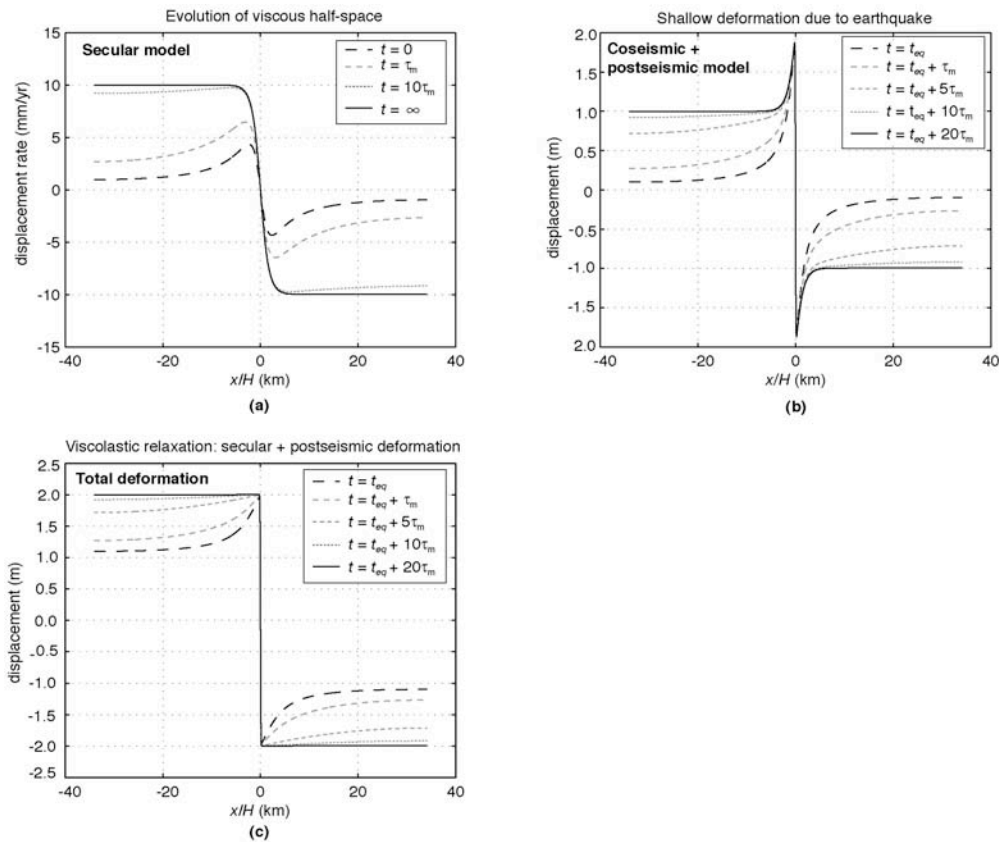
Figure 3.3. Fault-parallel displacement profiles of the Fourier model as a function of distance from the fault, x, with respect to plate thickness, H. Model results are obtained at multiples of Maxwell time ($\tau_m = 24$ yrs). Black dashed ($t = 0$) and black solid ($t = \infty$) profile lines represent time-dependent end-member cases reviewed by *Cohen* [1999] of the *Nur and Mavko* [1974] model. (a) Evolution of the secular model showing deep slip over geologic time. Note that the black solid line represents the fully-relaxed "secular" model that is used in further models to describe deep slip occurring from the lower depth of the locked fault to the base of the elastic plate. (b) Coseismic (black dashed line) and postseismic models (gray dashed lines) showing shallow deformation from an earthquake occurring at t_{eq} that resulted from 4 m of accumulated slip. (c) Total deformation resulting from the combination of the secular model (a, $t = \infty$) and the time-dependent postseismic models of (b) that capture the full 4 m of displacement. Note the full block offset of the elastic plate that is illustrated by the step-function of (c) for times greater than $20\ \tau_m$. This behavior is due to deformation contributions from all plate depths (locked and secular).

3.3.2 Boussinesq Analytic Comparisons

With the exception of the 3-D elastic half-space solution [*Okada*, 1985, 1992], thus far we have only discussed 2-D models where the surface normal stress is zero. However, to test our solutions in 3-D requires testing the response of the model to vertical loads (Appendix 3.A). To do this, we first compare our solution to the analytic solution for the response of an elastic half-space to an applied vertical load [*Love*, 1944]. We then qualitatively examine layered half-space models with and without a gravitational restoring force. Finally, we provide a numerical comparison between our 3-D layered model and the flexure model of a thin elastic plate overlying a fluid half-space [*Brotchie and Sylvester*, 1969; *Turcotte and Schubert*, 1982].

3.3.2.1   Vertical point load on an elastic half-space

As an initial test, we compare our Boussinesq solution (Appendix 3.A) to the analytic solution for a point load applied to a uniform elastic half-space. The *Love* [1944] solution for 3-D displacement of an elastic half-space subjected to a point load ($z \neq 0$) is

$$U(x,y) = \frac{P}{4\pi}\left[\frac{1}{\mu}\frac{xz}{r^3} - \frac{1}{(\lambda+\mu)}\frac{x}{r(z+r)}\right]$$

$$V(x,y) = \frac{P}{4\pi}\left[\frac{1}{\mu}\frac{yz}{r^3} - \frac{1}{(\lambda+\mu)}\frac{y}{r(z+r)}\right] \tag{3.11}$$

$$W(x,y) = -\frac{P}{4\pi}\left[\frac{1}{\mu}\frac{z^2}{r^3} - \frac{(\lambda+2\mu)}{\mu(\lambda+\mu)}\frac{1}{r}\right],$$

where U, V, and W are displacement components as a function of x, y, and z spatial coordinates, P is the point load magnitude, r is the radial distance ($r^2 = x^2 + y^2 + z^2$), and λ and μ are the elastic constants.

For the Fourier model, we apply a vertical point load ($F_z = P = 1$ MPa) to the center of the grid and compare the results at depths of 2 (Figure 3.4) and 10 grid-cell spacings to avoid the singular point in the *Love* [1944] solutions. The comparison with the analytic solution shows agreement to one part in 10^2, as most of the disagreement occurs directly under the load, which is only two grid-cells deep. For these tests, initially we do not include the restoring force of gravity. The code is tested in two ways: first, by equating the elastic constants of the layer and the half-space and second, by increasing the layer thickness H to 10 times the largest dimension of the grid. These two approaches show agreement to one part in 10^5, which is the accuracy of our single-precision FFT code. (Note that in our computer code, the transfer functions are all computed in double precision but the 2-D arrays are stored in single precision to save computer memory.)

3.3.2.2   Gravitational restoring force

We qualitatively investigate the effects of the gravitational restoring force for both half-space and layered models to illustrate that gravity is essential for modeling the long-term behavior of a layered Earth in response to vertical loads. In Appendix 3.A, we solve for the Boussinesq coefficients for the following four cases:

- (1) Homogeneous half-space (no gravity)
- (2) Homogeneous half-space *with* gravity
- (3) Layered half-space solution (no gravity)
- (4) Layered half-space solution *with* gravity
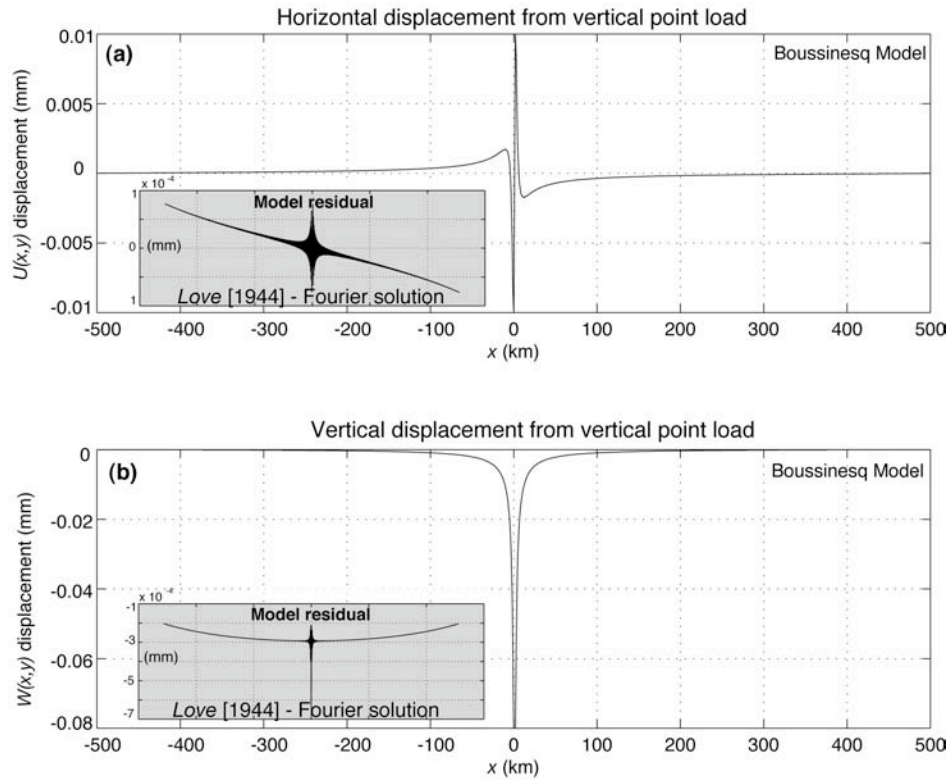
Figure 3.4. Horizontal and vertical response to a vertical point load applied to a homogeneous elastic medium ($\mu_1 = \mu_2$, or $H = \infty$) at a depth of 2 grid cell spacings (2 km). Boussinesq models are shown for both (a) horizontal U_B and (b) vertical W_B solutions (Appendix 3.A). Comparisons with the *Love* [1944] solutions (equation 3.11) yield relative errors (gray insets) for both horizontal and vertical components that are primarily less than 1%.

Here we demonstrate the different vertical responses of these special cases to a vertical point load. In the subsequent examples we use the following parameters: $F_z = 1$ MPa, $H = 10$ km, $\mu_1 = 28$ GPa, and $E_1 = 70$ GPa. For the two examples that examine the effects of a layered half-space (cases 3 and 4), we use a half-space shear modulus of $\mu_2 = 0$ to simulate an elastic plate overlying a fluid half-space, but require the bulk modulus, κ, to remain constant. In addition, for those examples that include the gravitational contribution (cases 2 and 4), $\rho = 3300$ kg/m^3 and $g = 9.81$ m/s^2.

(1) Homogeneous half-space Boussinesq solution (no gravity): $\mu_2 = \mu_1$, $g = 0$

This case was discussed in the previous section and is provided here as a reference model. Figure 3.5a shows the vertical solution in planform, demonstrating the negative bulls-eye region in the center of the grid. Figure 3.6 (gray dashed curve) shows the solution in profile.

(2) Homogeneous half-space Boussinesq solution *with* gravity: $\mu_2 = \mu_1$, g included

Next we include the restoring force of gravity in the homogenous elastic half-space model (Figure 3.5b and Figure 3.6, black dashed curve). Note that this solution compares to that of Figure 3.5a, although magnitudes are slightly larger. It is clear that gravity has little effect on the solution for this model, confirming that gravity can be ignored in elastic half-space dislocation models.

(3) Layered half-space Boussinesq solution (no gravity): $\mu_2 = 0$, $g = 0$

Next we consider the response of a point load applied to an elastic plate overlying a fluid half-space, ignoring the gravitational restoring force (Figure 3.5c). This approach leads to an absurd result with a spatially-magnified deflection that is highly dependent upon the dimensions of the grid. This is clearly an unphysical case because the vertical forces are not balanced. The restoring force of gravity is essential in layered dislocation models when the substrate is a fluid.

(4)   Layered half-space Boussinesq solution *with* gravity: $\mu_2 = 0$, g included

Lastly, we consider an elastic plate overlying a fluid half-space, this time including the restoring force of gravity (Figure 3.5d and Figure 3.6, gray solid curve). Including gravity balances the vertical forces and eliminates unreasonable amplitudes as seen in Figure 3.5c. Note that the layered model has significantly more vertical deformation than the half-space model.
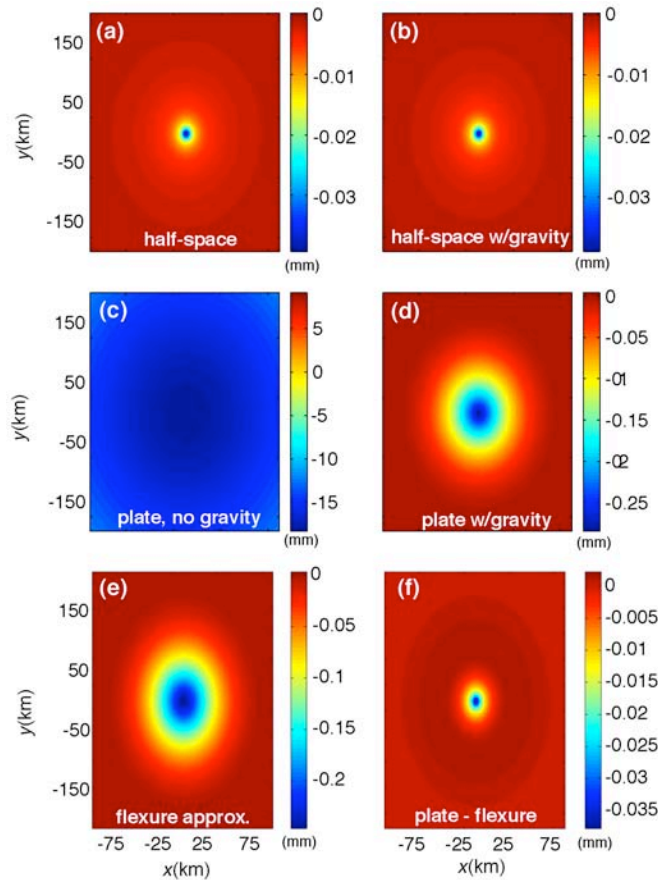
Figure 3.5. Map view of the vertical Boussinesq response (in mm) to a vertical point load. (a) homogeneous elastic half-space model *without* a gravitational restoring force (b) homogeneous elastic half-space model *with* a gravitational restoring force (c) elastic plate overlying a fluid half-space model *without* a gravitational restoring force (d) elastic plate overlying a fluid half-space model *with* a gravitational restoring force (e) flexural response from the thin plate approximation [*Le Pichon et al.*, 1973; *McKenzie and Bowin*, 1976] (f) residual difference between (d) and (e). Note that color scale differs for each plot.

3.3.2.3 Thin plate flexure approximation

As a partial numerical test of the layered model, we compare our Boussinesq solution to the analytic solution for the flexural response of a thin elastic plate due to a point surface load. The vertical force balance for flexure, w, of a thin elastic plate floating on a fluid half-space [*Turcotte and Schubert*, 1982] is given by

$$D\frac{d^4w}{dx^4} \quad + \quad \rho g w \quad = \quad P(x),$$

(3.12)

where the vertical load, *P(x)*, is balanced by the flexural resistance of the plate and the gravitational restoring force, ρg; *D* is the flexural rigidity. The flexure solution in the wave-number domain is given by

$$W(k) = P(k)\left[Dk^4 + \rho g\right]^{-1},$$

(3.13)

where the flexural rigidity is related to the plate thickness and elastic constants *E* and v (Poisson's ratio) by

$$D = \frac{EH^3}{12(1-v^2)}.$$

(3.14)

We compare the flexure solution of equation 3.13 (Figure 3.5e, Figure 3.6, solid black curve) to the point load response of the layered Boussinesq solution (Figure 3.5d). Far from the center of the load, the two models show excellent agreement, although they disagree near the load where the thin-plate approximation is no longer valid (Figure 3.5f). It is interesting to note that the sum of the flexure model (Figure 3.6, solid black line) and the half-space model (Figure 3.6, dashed gray line) provides a numerical agreement with the Boussinesq plate solution (Figure 3.6, solid gray line) to an accuracy of 0.1%. These results are also confirmed by the static flexure solution of *Brotchie and Silvester* [1969] with similar parameters.
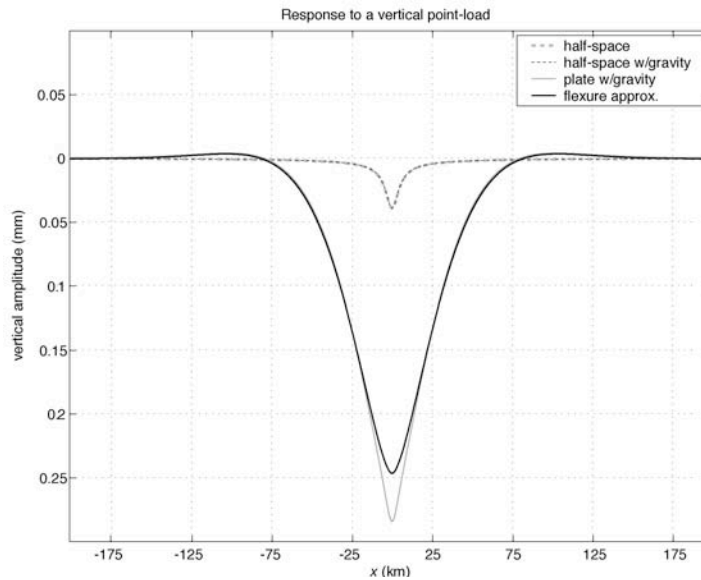
Figure 3.6. Vertical profiles as a function of distance, *x*, acquired for the Boussinesq results of Figure 3.5 for a half-space model *with*out a gravitational restoring force (dashed gray line, a), a half-space model *with* a gravitational restoring force (dashed black line, b), an elastic plate overlying a fluid half-space model (solid gray line, d), and the thin plate flexure approximation (solid black line, e). Combining the vertical results of the half-space model (dashed gray line) and the flexure solution (solid black line) yields a model with numerical accuracy of 10^{-3} when compared to the Boussinesq plate model (solid gray line).

3.4 3-D Time-Dependent Deformation and Stress

Having demonstrated the 2-D behavior and accuracy of our Fourier model, along with the vertical response of the layered Boussinesq solution, we now present a 3-D simulation of the earthquake cycle that includes multiple fault elements and explores postseismic deformation for intermediate time scales following an earthquake. The basic model (Figure 3.7) consists of a fault with three independent segments, A, B, and C, that are imbedded in a 50 km thick elastic plate that is loaded by 40 mm/yr of strike-slip plate motion. Between earthquakes, the middle fault segment, B, is locked from the surface to a depth of 25 km, below which deep, secular slip occurs. The two adjacent fault segments, A and C, are allowed to slip completely to the surface, simulating uniform fault creep. In this model, the fault system is a mature one (geologically evolved), where although $t = 0$ years represents the time of model initiation, we assume a full secular velocity plate step is already in place. The model spans 300$^+$ years, where the first 100 years include secular tectonic loading. At $t = 100$ years, we simulate an earthquake by initiating 4 m of coseismic shallow slip (depths < 25 km) on segment B. Postseismic deformation, due to viscoelastic relaxation of the half-space, begins immediately after the event. We present single-year-averaged snapshots at multiples of Maxwell time for both 3-D velocity and Coulomb stress. Animated movies of these models can be found online at http://topex.ucsd.edu/body_force.
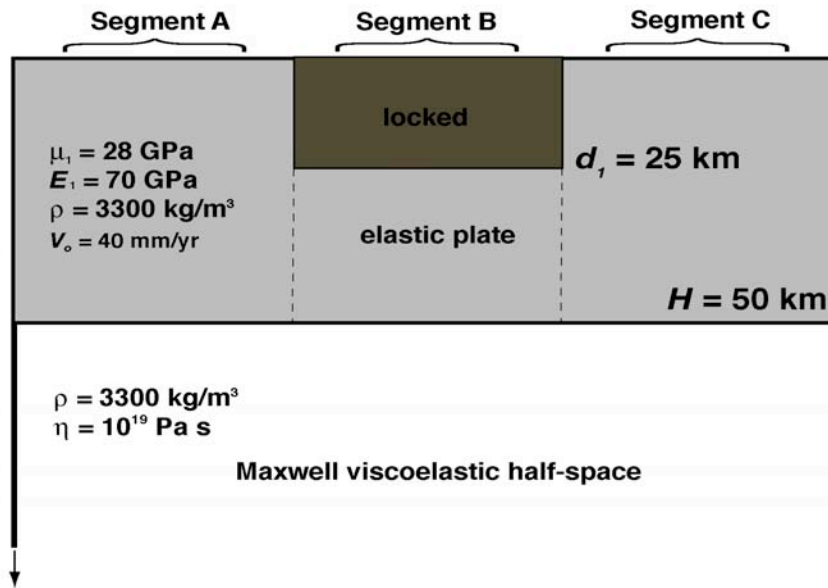
Figure 3.7. Along-fault vertical transect of the three-segment model embedded in an elastic plate of 50 km overlying a Maxwell viscoelastic half-space. Segments A and C are identified by zero locking depths (creeping), while segment B is locked from the surface ($d_2 = 0$) to a depth of 25 km.   Model parameters included shear modulus (μ_1), Young's modulus (E_1), density (ρ), and half-space viscosity (η).   Secular plate velocity, V_o, is set to 40 mm/yr.

3.4.1. 3-D Velocity

The 3-D velocity field is computed by calculating the change in displacement over 1-year time increments. For secular velocity, the time increment is largely irrelevant, as the secular model behavior is assumed steady state. However, when an earthquake occurs during the time interval, the velocity is equal to the coseismic/postseismic deformation divided by one year. Secular velocity is shown in map view (Figure 3.8a) where U represents fault-perpendicular velocity, V represents fault-parallel velocity, and W represents

vertical velocity. The fault-parallel velocity V shows a step-change across the creeping segments (A and C) and a more gradual transition across the locked section. Alternatively, the U and W components show little velocity contribution from the segments that are creeping, while moderate amplitudes, 10 mm/yr and 4 mm/yr, respectively, are exhibited at the fault tips. Also noted are the reversing quadrants of the vertical velocity field, W, and also the reversal of amplitude in the near and far fields. For example, in the far field, positive velocity (uplift) is noted in the direction of fault movement, while in the near field, negative velocity (subsidence) is found at the fault tip. The 3-D secular behavior of the earthquake cycle demonstrated here is assumed to be steady-state.

Coseismic velocity is shown in Figure 3.8b. Both U and W velocities reverse sign and reach amplitudes of +/- 0.8 m/yr and +/- 0.2 m/yr, respectively, in response to the earthquake. Alternatively, the fault-parallel velocity component, V, coseismically responds by lurching forward in the direction of tectonic motion at +/- 2 m/yr at the time of the earthquake. This type of behavior has been established by previous fault models [e.g., *Chinnery*, 1961; *Okada*, 1985, 1992; *Yang and Toksoz*, 1981] for elastic strike-slip deformation of a vertical fault.
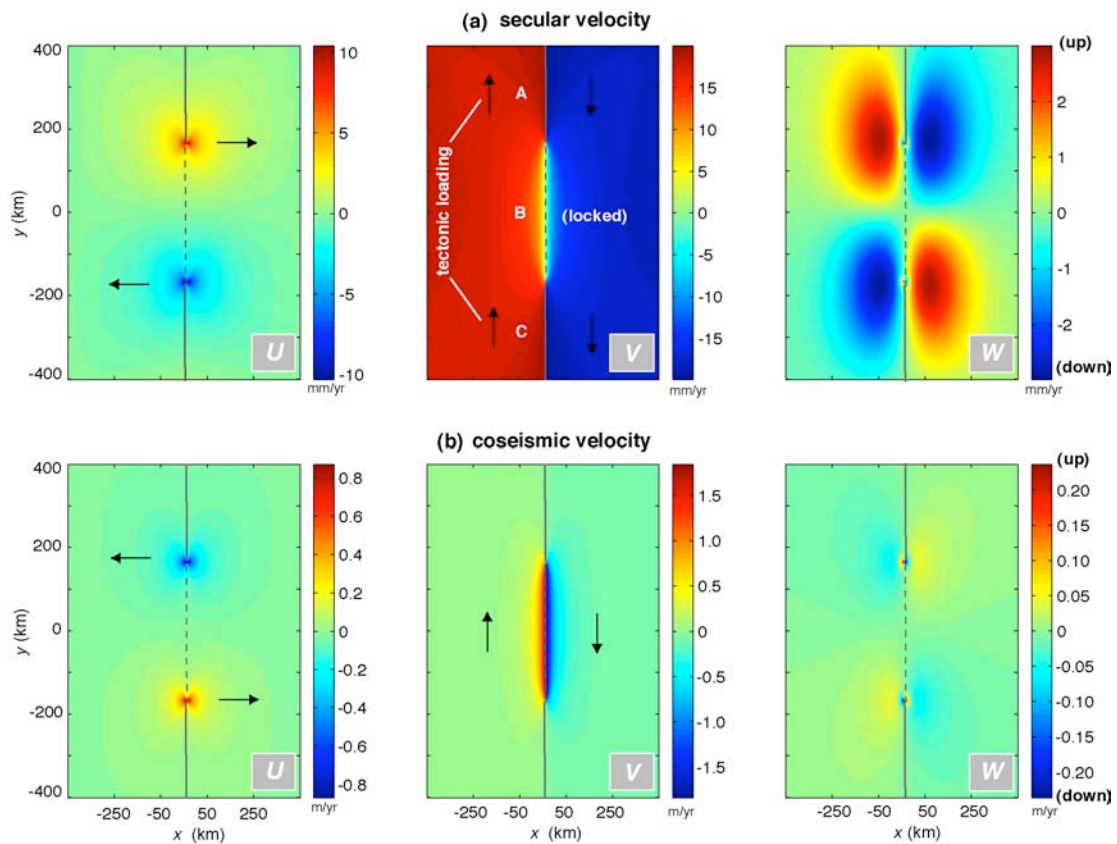
Figure 3.8. Map view of velocity results of the three-segment model (segments A, B, and C) shown for U (fault-perpendicular), V (fault-parallel), and W (vertical) components for (a) secular velocity (mm/yr) and (b) coseismic velocity (or displacement difference over one year, m/yr) from an earthquake event at $t = t_{eq} = 100$ years. Because the secular behavior of our model is assumed to be steady state, (a) represents the 3-D velocity field for times $t = 0$ - 99 years. Creeping segments A and C are identified by a solid gray line, while locked fault segment B is indicated by a gray dashed line.

Deformation continues for several Maxwell times (Figures 3.9-3.11) following the earthquake. Note that we have removed the secular (tectonic loading) component for times following the earthquake in order to isolate the postseismic velocity response. The U component (Figure 3.9) is reversed in sign with respect to the secular model and slowly diminishes in both wavelength and magnitude, completely dissipating by $\sim 10\tau_m$, or approximately 240 years, after the earthquake. Likewise, the V component (Figure 3.10) slowly decreases in magnitude and spatial dimension before completely disappearing by $\sim 10\tau_m$. Finally, the vertical velocity component, W (Figure 3.11), demonstrates an accelerative behavior for a short time after the earthquake. The vertical velocity field increases for times less than $2\tau_m$, followed by a slow decrease that remains for times greater than $5\tau_m$. The time scale for such an acceleration/deceleration of deformation direction depends strongly on plate thickness and half-space viscosity. Like the other components, the vertical velocity diminishes completely by $10\tau_m$ following the earthquake.
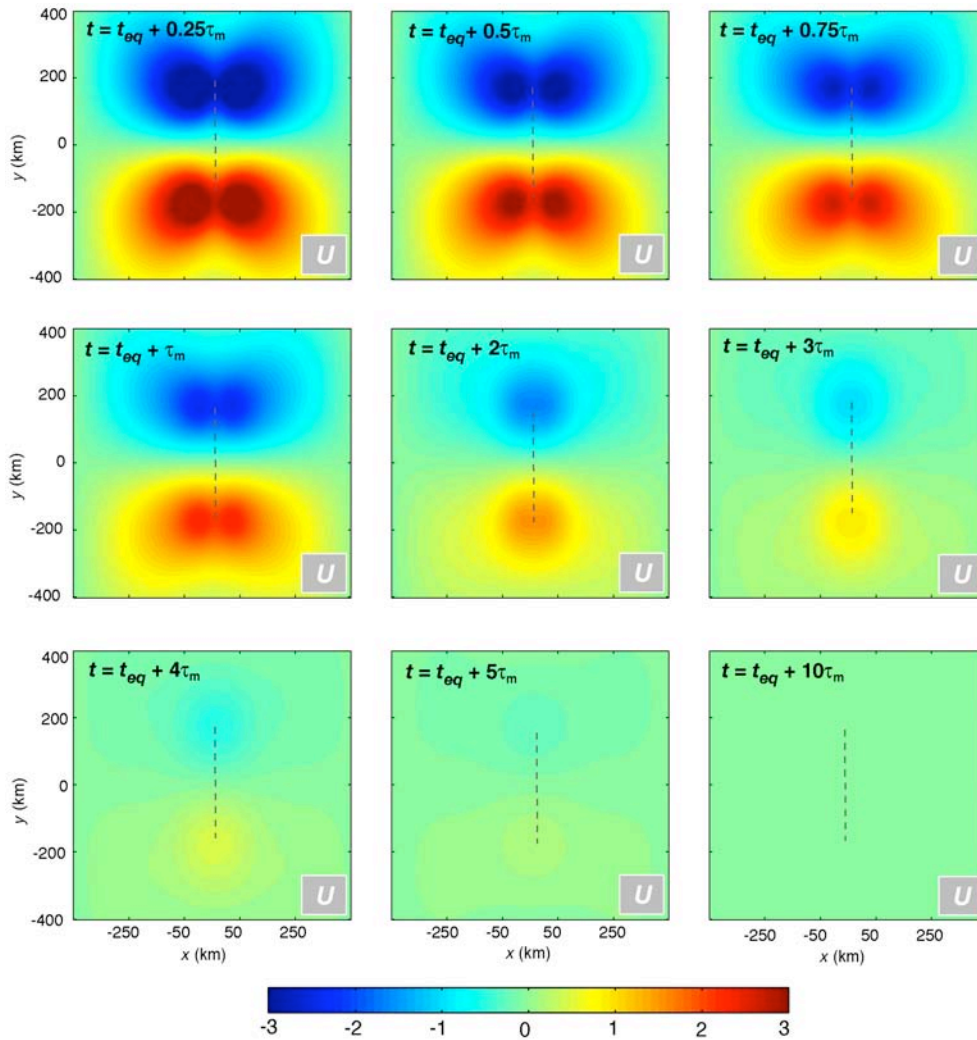
Figure 3.9. Map view of postseismic response for U (fault-perpendicular) horizontal velocity component at t = 100 yrs (t_{eq}) + multiples of Maxwell time (0.25, 0.5, 0.75, 1, 2, 3,4, 5, and 10 τ_m) in mm/yr. Displacement is calculated at half-year increments and velocity is computed by differencing two of these increments spanning one year. The gray dashed line indicates location of fault segment B. Positive velocities indicate change in displacement in the positive x-direction; negative velocities indicate change in displacement in the negative x-direction. The velocity for the U component slowly decreases after the earthquake and diminishes completely by approximately $10\tau_m$.
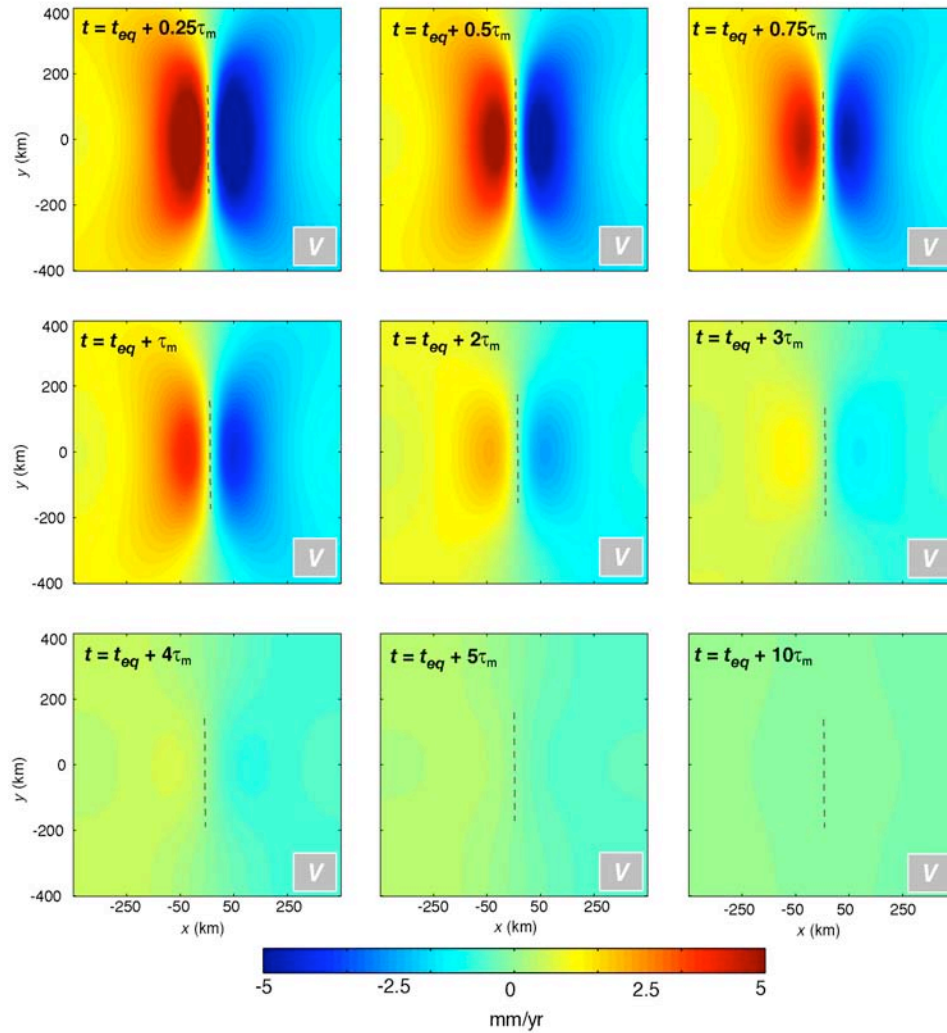
Figure 3.10. Map view of postseismic response for V (fault-parallel) horizontal velocity component at $t = 100$ yrs (t_{eq}) + multiples of Maxwell time (0.25, 0.5, 0.75, 1, 2, 3,4, 5, and 10 τ_m) in mm/yr. Positive velocities indicate change in displacement in the positive y-direction; negative velocities indicate change in displacement in the negative y-direction. The velocity for the V component slowly decreases after the earthquake and diminishes completely by approximately $10\tau_m$.
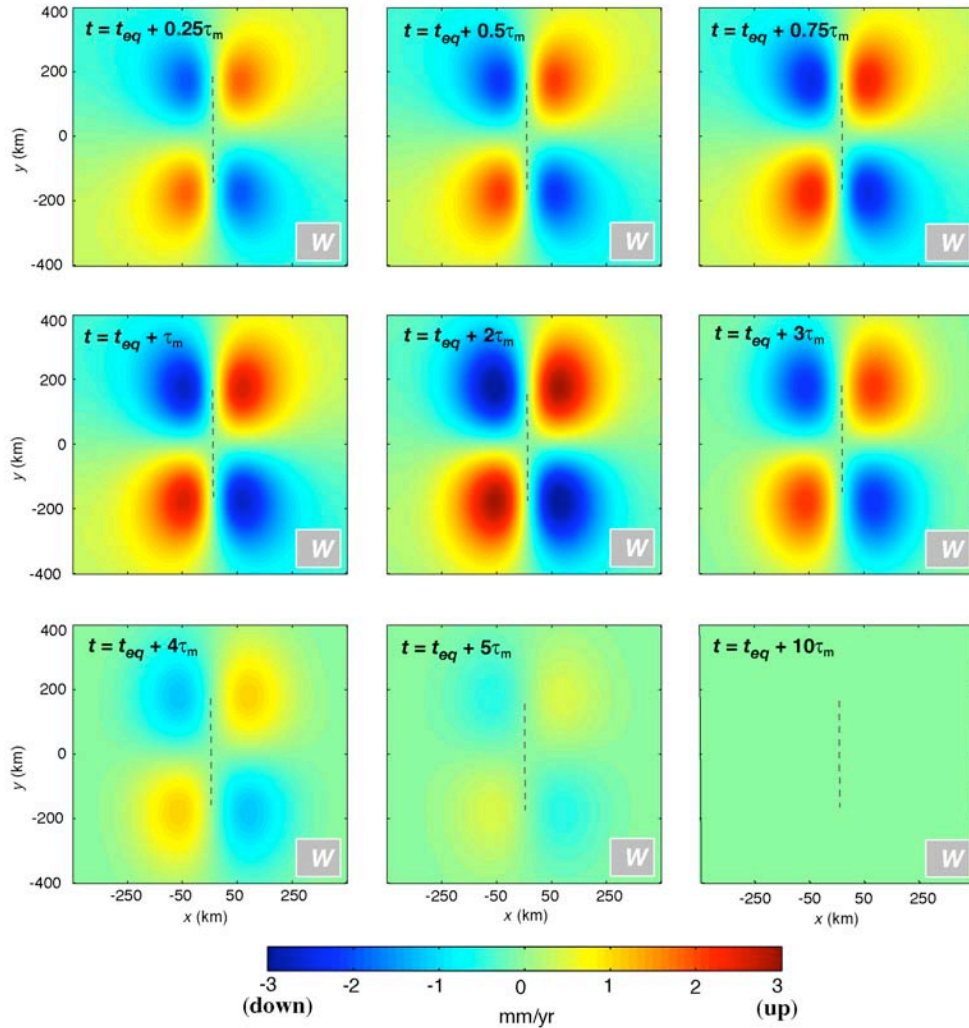
Figure 3.11. Map view of postseismic response for W (vertical) velocity component at $t = 100$ yrs (t_{eq}) + multiples of Maxwell time (0.25, 0.5, 0.75, 1, 2, 3,4, 5, and 10 τ_m) in mm/yr. Positive velocities indicate change in displacement in the positive z-direction (uplift); negative velocities indicate change in displacement in the negative z-direction (subsidence). The velocity for the W component temporarily increases after the earthquake until approximately $2\tau_m$, followed by a decrease in velocity in the same directional sense.
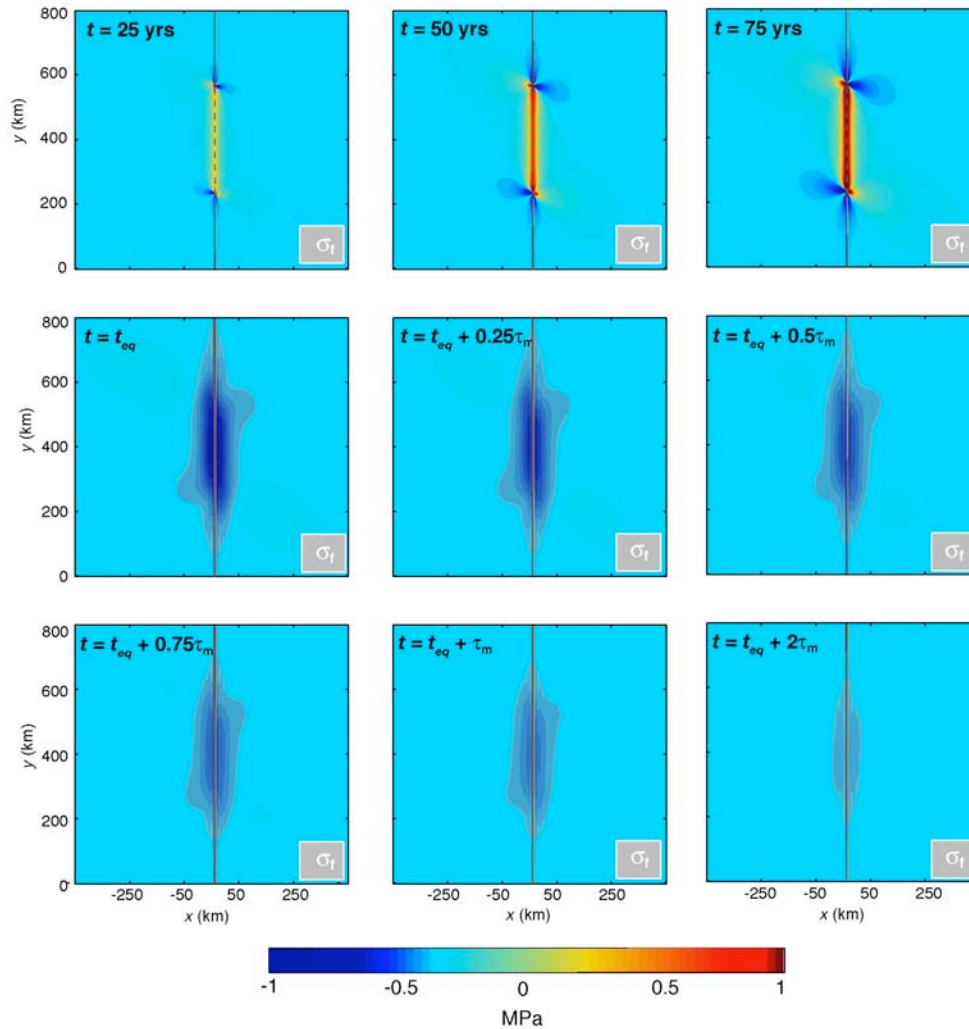
Figure 3.12. Map view results of Coulomb stress in MPa for a typical earthquake cycle. For the first 100 years (t = 25, 50, 75, … yrs), secular Coulomb stress accumulates on the locked fault at a rate off ~ 0.04 MPa/year. At $t = t_{eq}$ =100 yrs, an earthquake occurs that removes all of the positive stress, followed by snapshots of the Coulomb stress shadow ($t = 100^{+}$ yrs) marked by regions of negative stress. In order to isolate the postseismic effects due to stress transfer, we have removed the secular (tectonic loading) component for times greater than t = 100 yrs.

3.4.2 Coulomb Stress

Coulomb stress provides a measure of the shear loading on faults of a particular azimuth [e.g., *Stein et al.*, 1994; *Harris*, 1998; *Harris and Simpson*, 1998] where positive Coulomb stress indicates that a fault plane is brought closer to failure, while negative stress indicates that the fault plane has moved away from failure. To calculate Coulomb stress, we follow the approach of *King et al.* [1994] where the Coulomb failure criterion, σ_f, is defined by

$$\sigma_f = \tau - \mu_f \sigma_n.$$

In this equation, σ_n and τ are the normal and shear stress, respectively, on a failure plane and μ_f is the effective coefficient of friction. Our model provides the three-dimensional vector displacement field from which we compute the stress tensor. Right-lateral shear stress and extension are assumed to be positive. Because Coulomb stress is zero at the surface and becomes singular at the locking depth, we calculate Coulomb stress at 1/2 of the local locking depth [*King et al.*, 1994] and choose μ_f to be 0.6.

Our objective is to track the accumulation of Coulomb stress both before and after an earthquake (Figure 3.12). During the 100 years prior to the earthquake, Coulomb stress accumulates near the locked fault at a rate of approximately 0.04 MPa/year, ultimately increasing to a peak value of 4 MPa (Figure 12, $t = 25$, 50, 75 yrs). An earthquake releases all accumulated stress and even reverses the sign. In order to isolate the postseismic effects due to viscoelastic relaxation, we have removed the secular (tectonic loading) component for times greater than $t = 100$ yrs. A zone of negative Coulomb stress (stress shadow) develops and then decreases in amplitude and wavelength for at least $2\tau_m$, or approximately 50 years. Had we included the secular tectonic component, the Coulomb stress shadow would have existed for only $\sim 0.5\tau_m$, or approximately 13 years, followed by a repeated stress accumulation process.

3.5 Discussion

These examples demonstrate essential features of 3-D deformation and stress during the earthquake cycle and agree with other full 3-D numerical models of the earthquake cycle [*Deng et al., 1998; Kenner and Segall*, 1999; *Pollitz et al.*, 2000; *Pollitz et al.*, 2001; *Zeng*, 2001]. The primary difference between a layered viscoelastic model and an elastic half-space model is in the vertical velocity. Following a right-lateral earthquake, we observe increasing vertical velocity (Figure 3.11) that produces uplift in the northeast and southwest quadrants and subsidence in the northwest and southeast quadrants. This behavior persists for at least two Maxwell times (~ 50 years) and then gradually subsides.

The wavelength and timescale of this vertical velocity feature is largely dependent upon the elastic plate thickness and half-space viscosity. The wavelength of vertical deformation is related to the flexural wavelength and thus for a 50 km thick plate, the characteristic wavelength of the vertical deformation pattern is approximately 440 km. However, the observed lobate vertical velocity patterns following the Landers and Hector Mine earthquakes had a much smaller horizontal wavelength, requiring a much thinner plate ($\sim$10 km) [*Deng et al., 1998; Pollitz et al.*, 2001].

The timescale of the vertical velocity acceleration and decay also depends on both the plate thickness and the half-space viscosity. A plate of 25 km thickness, as opposed to a 50 km thick plate, responds on a longer time scale suggesting the postglacial rebound time scale is providing a minor contribution to the vertical response. The postglacial rebound time scale [*Turcotte and Schubert*, 1982] is given by

$$\tau_g = 4\pi\eta / \rho g \lambda,$$

where λ is the wavelength of deformation and η, ρ, and g are viscosity, density, and gravity, respectively. Because rebound time scale is inversely proportional to the wavelength of the deformation (which is controlled by the flexural wavelength of the elastic plate), a thinner plate (i.e. smaller λ) has a longer postglacial rebound timescale. The 50 km thick plate has a postglacial time scale of 280 years for a viscosity of 10^{19} Pa s, while the shorter wavelength associated with the thinner plate has a longer postglacial timescale (500 yr).

Our model also demonstrates stress behavior due to time-dependent postseismic readjustment (Figure 3.12) in agreement with previous studies [*Harris and Simpson*, 1993, 1996; *Zeng*, 2001]. Following an earthquake, a stress shadow develops. This stress shadow should, in theory, inhibit the occurrence of subsequent seismic events such as aftershocks and large triggered earthquakes. As time advances, the spatial extent and magnitude of the stress shadow decays non-uniformly [*Ward*, 1985]. Eventually the locked fault becomes re-loaded with tectonic stress and relaxation ceases, resulting in positive stress accumulation surrounding the fault and a resumption of the earthquake cycle.

Realistic models exhibiting similar stress shadowing behaviors and fault interactions have been explored by other workers [e.g., *Kenner and Segall*, 1999; *Parsons*, 2002]. A 2-D postseismic shear stress model of *Kenner and Segall* [1999] demonstrated that an initial stress decrease, followed by viscoelastic relaxation, encouraged increases of stress duration and magnitude for particular fault geometries. In addition, changes in Coulomb stress are shown to be highly sensitive to kinks in fault geometry and jumps in slip distribution [*Freed and Lin*, 2001; *Kilb et al.*, 2002]. While we have obviously eliminated such geometrical effects by embedding a straight fault system of constant slip with depth for this analysis, more complicated simulations have shown high rates of stress at junctions of fault bends. A fault system with bends and kinks produces anomalous Coulomb stress at fault segment tips that is never fully released by strike-slip motion. Alternative mechanisms, such as normal faulting, may be required to cancel accumulating stress due to geometrical effects. These ideas will be more completely explored in a following paper (Chapter 4).

3.6 Conclusions

We have developed and tested a semi-analytic model for the 3-D response of a Maxwell viscoelastic layered half-space due to an arbitrary distribution of body forces. For a vertical fault, 2-D convolutions are performed in the Fourier transform domain, and thus displacement, strain, and stress due to a complicated fault trace can be computed very quickly. Using the Correspondence Principle, the solutions for a layered elastic half-space are easily extended to that of a viscoelastic half-space without increasing the computational burden. The horizontal complexity of the fault system has no effect on the speed of the computation; a model with a prescribed time, consisting of hundreds of fault elements, requires less than 40 seconds of CPU time on a desktop computer. Because multiple earthquakes are required to fully capture viscoelastic behavior, our model is capable of efficiently computing 3-D viscoelastic models spanning 1000s of years.

Our model has the accuracy and speed necessary for computing both geometrically and temporally complex models of the earthquake cycle. Here we have demonstrated the basic 2-D and 3-D deformation behavior of a generalized simple fault system. We find that the evolving velocity field, particularly the vertical component, demonstrates an overall decelerative behavior dependent upon plate thickness, although a temporary velocity increase is also observed. We also investigate the temporal behavior of the Coulomb stress field and find that a stress shadow exists for at least two Maxwell times and slowly decays as stress is redistributed in the plate and tectonic loading dominates.

Now that this modeling approach is understood and fully tested, it will be used to simulate the complex time-dependent stress evolution of realistic tectonic boundaries on Earth, such as the San Andreas Fault

System. We are currently establishing a suite of models, consistent with both geodetic and geological observations, that will increase our understanding of how temporal plate-boundary deformation and stress variations within the seismogenic crust can result from different tectonic settings throughout the earthquake cycle.

3.7 Acknowledgements

3.8 References

Anderson, G., B. Aagaard, and K. Hudnut, Fault interactions and large complex earthquakes in the Los Angeles area, *Science*, 302, 1946-1949, 2003.

Boussinesq, J., Application des Potentiels a l'Etude de l'Equilibre et du Mouvement des Solides Elastiques, Gauthier-Viallars, Paris, 508, 1885.

Brotchie, J.F., and R. Silvester, On Crustal Flexure, *J. Geophys. Res.*, 74, 5240-5252, 1969.

Burmister, D.M., The theory of stresses and displacements in layered systems and applications of the design of airport runways, paper presented at the Annual Meeting, Highway Res. Board, Natl. Res. Counc., Washington, D.C., 1943.

Burridge, R. and L. Knopoff, Body force equivalents for seismic dislocations, *Bull. Seismol. Soc. Am., 54*, 1875-1888, 1964.

Chinnery, M.A., The deformation of the ground around surface faults, *Bull. Seismol. Soc. Am.*, 50, 355-372, 1961.

Cohen S.C., Postseismic deformation due to subcrustal viscoelastic relaxation following dip-slip earthquakes, *J. Geophys. Res.*, 89, 4,358-4,544, 1984.

Cohen, S.C., Numerical Models of Crustal Deformation in Seismic Zones, *Adv. Geophys.*, 41, 133-231, 1999.

Crouch, S.L., and A.M. Starfield, *Boundary Element Methods in Solid Mechanics*, Allen and Unwin, Inc., Winchester, Massachusetts, 322 pp., 1983.

Deng, J., M. Gurnis, H. Kanamori, and E. Hauksson, Viscoelastic flow in the lower crust after the 1992 Landers, California, earthquake, *Science*, 282, 1689-1692, 1998.

Dent, J., K. Hudnut, M. Gurnis, and E. Hauksson, Stress Loading From Viscous Flow in the Lower Crust and Triggering of Aftershocks Following the 1994 Northridge, California, Earthquake, *Geophys. Res. Lett.*, 26, 3209-3212, 1999.

Fialko, Y., Evidence of fluid-filled upper crust from observations of post-seismic deformation due to the 1992 M_w7.3 Landers earthquake, *J. Geophys. Res.*, 109, doi:10.1029/2003JB002985, 2004a.

Fialko, Y., Probing the mechanical properties of seismically active crust with space geodesy: Study of the co-seismic deformation due to the 1992 M_w 7.3 Landers (southern California) earthquake, *J. Geophys. Res.*, 109, doi:10.1029/2003JB002756, 2004b.

Frankel, A., Three-dimensional simulations of the ground motions in the San Bernardino valley, California, for hypothetical earthquakes on the San Andreas fault, *Bull. Seismol. Soc. Am.*, 83, 1020-1041, 1993.

Freed, A.M., and J. Lin, Time-dependent changes in failure stress following thrust earthquakes, *J. Geophys. Res.*, 103, 24,393-24,409, 1998.

Freed, A.M., and J. Lin, Delayed triggering of the 1999 Hector Mine earthquake by viscoelastic stress transfer, *Nature*, 411, 180-183, 2001.

Harris, R.A., Introduction to special section: Stress triggers, stress shadows, and implications for seismic hazard, *J. Geophys. Res.*, 103, 24,347-24,358, 1998.

Harris, R.A., and R.W. Simpson, In the shadow of 1857: An evaluation of the static stress changes generated by the M8 Ft. Tejon, California, earthquake, *Eos Trans. AGU*, 74(43), Fall Meet. Suppl., 427, 1993.

Harris, R.A., and R.W. Simpson, In the shadow of 1857 – The effect of the great F. Tejon earthquake on subsequent earthquakes in southern California, *Geophys. Res. Lett.*, 23, 229-232, 1996.

Harris, R.A., and R.W. Simpson, Suppression of large earthquakes by stress shadows: A comparison of Coulomb and rate-and-state failure, *J. Geophys. Res.*, 103, 24,439-24,452, 1998.

Haskell, N.A., The dispersion of surface waves on multilayered media, *Bull. Seismol. Soc. Am.*, 54, 17-34, 1953.

Hearn, E.H., B.H. Hager, and R.E. Reilinger, Viscoelastic deformation from North Anatolian Fault Zone earthquakes and the eastern Mediterranean GPS velocity field, *Geophys. Res. Lett.*, 29, 10,1029-10,1031, 2002.

Heki, K., S. Miyazaki, and H. Tsuji, Silent fault slip following an interplate thrust earthquake at the Japan Trench, *Nature*, 386, 595-598, 1997.

Ivins, E.R., Transient creep of a composite lower crust, 2, A polymineralic basis for rapidly evolving postseismic deformation modes, *J. Geophys. Res.*, 101, 28,005-28,028, 1996.

Jaeger, J.C., *Elasticity, Fracture, and Flow*, Metheun, New York, 102 pp., 1956.

Kenner, S., and P. Segall, Time-dependence of the stress shadowing effect and its relation to the structure of the lower crust, *Geology*, 27, 119-122, 1999.

Kilb, D., J. Gomberg, and P. Bodin, Triggering of earthquake aftershocks by dynamic stresses, *Nature*, 408, 570-574, 2000.

Kilb, D., J. Gomberg, and P. Bodin, Aftershock triggering by complete Coulomb stress changes, *J. Geophys. Res.*, 107(B4), 10.1029/2001JB000202, 2002.

King, G.C.P., and M. Cocco, Fault interaction by elastic stress changes: New clues from earthquake sequences, *Adv. Geophys.*, 44, 1-38, 2001.

King. G.C.P., R.S. Stein, and J. Lin, Static stress changes and the triggering of earthquakes, *Bull. Seismol. Soc. Am.*, 84, 935-953, 1994.

Le Pinchon, X., J. Francheteau, and J. Bonnin, *Developments in Geotectonics*, vol. 6, *Plate Tectonics*, Elsevier Sci., New York, 1973.

Love, A.E.H., The stress produced in a semi-infinite solid by pressure on part of the boundary, *Philos. Trans. R. Soc. London.*, *Ser A*, 667, 377-420, 1929.

Love, A.E.H., *The Mathematical Theory of Elasticity*, 2nd ed., Cambridge University Press, New York, 1944.

Lysmer, J., and L.A. Drake, A finite element method for seismology, *Methods in Computational Physics*, Academic Press, edited by B. Alder, S. Fernbach, and B.A. Bolt, pp. 181-126, Academic, San Diego, Calif., 1972.

Massonnet, D., W. Thatcher, and H. Vadon, Radar interferometry detects two mechanism of postseismic relaxation following the Landers, California earthquake, *Nature*, 382, 612-612, 1996.

McKenzie D., and C. Bowin, The relationship between bathymetry and gravity in the Atlantic Ocean, *J. Geophys. Res.*, 81, 1903-1915, 1976.

Melosh, H.J., Vertical movements following a dip-slip earthquake, *Geophys. Res. Lett.*, 10, 47-50, 1983.

Nur, A., and G. Mavko, Postseismic viscoelastic rebound, *Science*, 183, 204-206, 1974.

Okada, Y., Surface deformation due to shear and tensile faults in a half-space, *Bull. Seismol. Soc. Am., 75*, 1135-1154, 1985.

Okada, Y., Internal deformation due to shear and tensile faults in a half-space, *Bull. Seismol. Soc. Am.*, *82*, 1018-1040, 1992.

Olsen, K.B., and G.T. Schuster, Site amplification in the Salt Lake Valley by three-dimensional elastic wave propagation, *Eos Trans. AGU*, 73, 338, 1992.

Parsons, T., Post-1906 stress recovery of the San Andreas fault system calculated from three-dimensional finite element analysis, *J. Geophys. Res.*, 107, 2002.

Peltzer, G.P., P. Rosen, F. Rogez, and K. Hudnut, Postseismic rebound in fault step-overs cause by pore fluid flow, *Science*, 273, 1202-1204, 1996.

Peltzer, G., P. Rosen, F. Rogez, and K. Hudnut, Poro-elastic rebound along the Landers 1992 earthquake surface rupture, *J. Geophys. Res.*, 103, 30,131-30,145, 1998.

Pollitz, F.F., G. Peltzer, and R. Burgmann, Mobility of continental mantle: Evidence from postseismic geodetic observations following the 1992 Landers earthquake, *J. Geophys. Res.*, 105, 8035-8054, 2000.

Pollitz, F.F., C. Wicks, and W. Thatcher, Mantle flow beneath a continental strike-slip fault: Postseismic deformation after the 1999 Hector Mine earthquake*, Science*, 293, 1814-1818, 2001.

Rundle, J.B. and D.D. Jackson, A three-dimensional viscoelastic model of a strike slip fault, *Geophys. J. Roy. Astron. Soc.*, 49, 575-591, 1977.

Rybicki, K., The elastic residual field of a very long strike-slip fault in the presence of a discontinuity, *Bull. Seismol. Soc. Am.* 61, 72-92, 1971.

Sato, R., Crustal deformation due to a dislocation in a multi-layered medium, *J. Phys. Earth*, 19, 31-46, 1971.

Savage, J.C., and W.H. Prescott, Asthenosphere readjustment and the earthquake cycle, *J. Geophys. Res.*, 83, 3369-3376, 1978.

Savage, J.C., and J.L. Svarc, Postseismic deformation associated with the 1992 M_w = 7.3 Landers earthquake, southern California, *J. Geophys. Res*, 102, 7565-7577, 1997.

Shen, Z., D. Jackson, Y. Feng, M. Cline, M. Kim, P. Fang, and Y. Bock, Postseismic deformation following the Landers earthquake, California, 28 June 1992*, Bull. Seismol. Soc. Am.*, 84, 780-791, 1994.

Singh, S.J., Static deformation of a multilayered half-space by internal sources, *J. Geophys. Res.*, 75, 3257-3263, 1970.

Smith, B.R., and D.T. Sandwell, Coulomb Stress along the San Andreas Fault System, *J. Geophys. Res.*, 108, doi:10.1029/2002JB002136, 2003.

Stein, R.S., G.C.P. King, and J. Lin, Stress triggering of the 1994 M = 6.7 Northridge, California, earthquake by its predecessors, *Science*, 265, 1432-1435, 1994.

Steketee, J.A., On Volterra's dislocations in a semi-infinite elastic medium*, Can. J. Phys., 36*, 1958.

Thatcher, W., Nonlinear strain buildup and the earthquake cycle on the San Andreas Fault*, J. Geophys. Res.*, 88, 5893-5902, 1983.

Thatcher, W., The earthquake cycle at the Nankai Trough, southwest Japan, *J. Geophys. Res.*, 89, 3087-3101, 1984.

Thomas, A.L., Poly3D: A three-dimensional, polygon element, displacement discontinuity boundary element computer program with applications to fractures, faults, and cavities in the Earth's crust, *Master's Thesis*, Stanford Univ., Stanford, California, 1993.

Timoshenko, S., *Theory of elasticity*, McGraw-Hill, New York, 1934.

Toda, S., R. Stein, and T. Sagiya, Evidence from the AD 2000 Izu Islands earthquake swarm that stressing rate governs seismicity, *Nature*, 419, 58-61, 2002.

Turcotte, D.L., and G. Schubert, *Geodynamics*, 1st ed., Cambridge Univ. Press, New York, 1982.

Wang, R., F. Martin, and F. Roth, Computation of deformation induced by earthquakes in a multi-layered elastic crust – FORTRAN programs EDGRN/EDCMP, *Comp. Geosci.*, 29, 195-207, 2003.

Ward, S.N., A note on lithospheric bending calculations, *Geophys. J. R. Astron. Soc.*, 78, 241-253, 1984.

Ward, S.N., Quasi-static propagator matrices: creep on strike-slip faults, *Tectonophysics*, 120, 83-106, 1985.

Wdowinski, S., Y. Bock, J. Zhang, P. Fang, and J. Genrich, Southern California Permanent GPS Geodetic Array: Spatial filtering of daily position from estimating coseismic and postseismic displacement induced by the 1992 Landers earthquake, *J. Geophys. Res.*, 102, 18,057-18,070, 1997.

Weertman, J., Continuum distribution of dislocations on faults with finite friction, *Bull. Seismol. Soc. Am.*, 54, 1035-1058, 1964.

Williams, C.A., and R.M. Richardson, A rheologically layered three-dimensional model of the San Andreas Fault in central and southern California, *J. Geophys. Res.*, 96, 16,597-16,623, 1991.

Yang, M., and M.N. Toksoz, Time dependent deformation and stress relaxation after strike slip earthquakes, *J. Geophys. Res.*, 86, 2889-2901, 1981.

Zang, L., and A.K. Chopra, Three-dimensional analysis of spatially varying ground motions around a uniform canyon in a homogeneous half space, *Earthquake Eng. Struct. Dyn.*, 20, 911-926, 1991.

Zeng, Y., Viscoelastic stress-triggering of the 1999 Hector Mine earthquake by the 1992 Landers earthquake, *Geophys. Res. Lett.*, 28, 3007-3010, 2001.

Appendix 3.A   Boussinesq Problem for a Layered Half-space

The Boussinesq Problem [*Boussinesq*, 1885; *Steketee*, 1958] offers a supplemental solution for removing anomalous vertical normal stress that arises from the method of images [*Weertman*, 1964], used to partially satisfy the zero-shear surface boundary condition for a homogeneous elastic half-space. Likewise, for a layered elastic half-space, multiple image sources must be included to partially satisfy the surface boundary condition (Appendix 3.B) and the Boussinesq approach must be used to remove the remaining normal tractions. Unfortunately, the Boussinesq solution for a homogeneous half-space does not fully satisfy the boundary conditions for a layered elastic half-space and an alternative solution must be derived. Our contribution to this problem is to develop a Boussinesq-like solution that reflects a new set of elastic solutions that accounts for normal tractions in a layer overlying a half-space.

When solving the Boussinesq problem for a layered elastic half-space, an approach similar to that of the homogeneous half-space applies [e.g., *Steketee*, 1958; *Smith and Sandwell*, 2003]. The major exceptions to this approach are the additional boundary conditions [*Burmister*, 1943] (note that the following notation uses subscripts 1 and 2 to refer to layer and half-space displacement and stress, respectively, and a lower-case '*h*' is used in place of *H* for the plate thickness, or layer interface):

1. The surface layer must be free of shear and normal stress, except those imposed to balance the remaining normal tractions (τ_{33}) and provide gravitational support (ρg), if necessary. Gravity plays an important role in modulating long-term vertical motion.

$$\tau_{zz1} = -\tau_{33} + \rho g W_1\big|_{z=0} \qquad\qquad \tau_{xz1} = \tau_{yz1} = 0\big|_{z=0} \qquad\qquad (3.A1)$$

2. Stress and displacement across the layer interface must be continuous.

$$\tau_{xz1} = \tau_{xz2}\big|_{z=-h} \qquad U_1 = U_2\big|_{z=-h}$$

$$\tau_{yz1} = \tau_{yz2}\big|_{z=-h} \qquad V_1 = V_2\big|_{z=-h} \qquad (3.A2)$$

$$\tau_{zz1} = \tau_{zz2}\big|_{z=-h} \qquad W_1 = W_2\big|_{z=-h}$$

3. At infinite depth, stress and displacements below the layer must go to zero.

$$\tau_{xz2} = \tau_{yz2} = \tau_{zz2} = 0\big|_{z=-\infty} \qquad U_2 = V_2 = W_2 = 0\big|_{z=-\infty} \qquad (3.A3)$$

Our approach is to find the Galerkin vector Γ_i [*Steketee*, 1958] for the complimentary solutions that satisfy the above boundary conditions for both displacements and stress in both the elastic layer (layer 1) and the half-space below (layer 2). We begin by writing both displacement and stress in terms of the Galerkin vector:

$$u_i = \Gamma_{i,kk} - \alpha\Gamma_{k,ki}$$
$$\tau_{ij} = \lambda(1-\alpha)\delta_{ij}\Gamma_{k,kll} + \mu\left(\Gamma_{j,ikk} + \Gamma_{i,jkk}\right) - 2\mu\alpha\Gamma_{k,kij} \qquad (3.A4)$$

or more explicitly,

$$U_B = -\alpha\frac{\partial^2\Gamma}{\partial x\partial z} \qquad \tau_{xz} = \mu\frac{\partial}{\partial x}\left\{\nabla^2\Gamma - 2\alpha\frac{\partial^2\Gamma}{\partial z^2}\right\}$$

$$V_B = -\alpha\frac{\partial^2\Gamma}{\partial y\partial z} \qquad \tau_{yz} = \mu\frac{\partial}{\partial y}\left\{\nabla^2\Gamma - 2\alpha\frac{\partial^2\Gamma}{\partial z^2}\right\} \qquad (3.A5)$$

$$W_B = -\alpha\frac{\partial^2\Gamma}{\partial z^2} + \nabla^2\Gamma \qquad \tau_{zz} = \mu\frac{\partial}{\partial z}\left\{\left(\frac{\alpha}{\xi}\right)\nabla^2\Gamma - 2\alpha\frac{\partial^2\Gamma}{\partial z^2}\right\}$$

where μ and λ are the elastic constants, $\alpha = \dfrac{(\lambda+\mu)}{(\lambda+2\mu)}$, and $\xi = \dfrac{(\lambda+\mu)}{(3\lambda+4\mu)}$.

As described by *Love* [1929] and *Timoshenko* [1934], the stress and displacement equations of elasticity must satisfy the equation of compatibility, most commonly known as the biharmonic equation:

$$\nabla^4\Gamma = \frac{\partial}{\partial x^2}\left(\nabla^2\Gamma\right) + \frac{\partial}{\partial y^2}\left(\nabla^2\Gamma\right) + \frac{\partial}{\partial z^2}\left(\nabla^2\Gamma\right) = 0 \cdot \qquad (3.A6)$$

The general solution to this problem is

$$\Gamma = (A + Cz)e^{\beta z} - (B + Dz)e^{-\beta z}. \qquad (3.A7)$$

where $\beta = 2\pi|\mathbf{k}|$ and $|\mathbf{k}| = k_x^2 + k_y^2$. For the layered model, layers 1 and 2 will have the following representation with corresponding elastic constants μ_1, λ_1, and μ_2, λ_2:

$$\Gamma_1 = (A_1 + C_1 z)e^{\beta z} - (B_1 + D_1 z)e^{-\beta z} \qquad \Gamma_2 = (A_2 + C_2 z)e^{\beta z} - (B_2 + D_2 z)e^{-\beta z}. \qquad (3A.8)$$

Likewise, the two layers will have displacements and stress as functions of their respective Galerkin vectors:

$$\text{layer 1}: \ U_{B1}(\Gamma_1), \ V_{B1}(\Gamma_1), \ W_{B1}(\Gamma_1), \ \tau_{xz1}(\Gamma_1), \ \tau_{yz1}(\Gamma_1), \ \tau_{zz1}(\Gamma_1)$$
$$\text{layer 2}: \ U_{B2}(\Gamma_2), \ V_{B2}(\Gamma_2), \ W_{B2}(\Gamma_2), \ \tau_{xz2}(\Gamma_2), \ \tau_{yz2}(\Gamma_2), \ \tau_{zz2}(\Gamma_2).$$

To satisfy the zero displacement boundary condition as $z \rightarrow -\infty$, $B_2 = D_2 = 0$. The Galerkin vectors (3A.8) then take on the form

$$\Gamma_1 = (A_1 + C_1 z)e^{\beta z} - (B_1 + D_1 z)e^{-\beta z} \quad \text{and} \quad \Gamma_2 = (A_2 + C_2 z)e^{\beta z}. \qquad (3.A9)$$

By substituting the above Galerkin vectors and their associated derivatives into the equations for stress and displacement in both layers (3.A5), the Boussinesq solutions become:

$$U_{B1} = -i2\pi k_x \alpha_1 \left[A_1 \beta e^{\beta z} + B_1 \beta e^{-\beta z} + C_1(1 + \beta z)e^{\beta z} - D_1(1 - \beta z)e^{-\beta z} \right]$$

$$V_{B1} = -i2\pi k_y \alpha_1 \left[A_1 \beta e^{\beta z} + B_1 \beta e^{-\beta z} + C_1(1 + \beta z)e^{\beta z} - D_1(1 - \beta z)e^{-\beta z} \right]$$

$$W_{B1} = -\beta \alpha_1 \left[A_1 \beta e^{\beta z} - B_1 \beta e^{-\beta z} + C_1(2 + \beta z - 2/\alpha_1)e^{\beta z} + D_1(2 - \beta z - 2/\alpha_1)e^{-\beta z} \right]$$

$$U_{B2} = -i2\pi k_x \alpha_2 \left[A_2 \beta e^{\beta z} + C_2(1 + \beta z)e^{\beta z} \right]$$

$$V_{B2} = -i2\pi k_y \alpha_2 \left[A_2 \beta e^{\beta z} + C_2(1 + \beta z)e^{\beta z} \right]$$

$$W_{B2} = -\beta \alpha_2 \left[A_2 \beta e^{\beta z} + C_2(2 + \beta z - 2/\alpha_2)e^{\beta z} \right] \qquad (3.A10)$$

$$\tau_{xz1} = -i4\pi k_x \mu_1 \alpha_1 \beta \left[A_1 \beta e^{\beta z} - B_1 \beta e^{-\beta z} + C_1(2 + \beta z - 1/\alpha_1)e^{\beta z} + D_1(2 - \beta z - 1/\alpha_1)e^{-\beta z} \right]$$

$$\tau_{yz1} = -i4\pi k_y \mu_1 \alpha_1 \beta \left[A_1 \beta e^{\beta z} - B_1 \beta e^{-\beta z} + C_1(2 + \beta z - 1/\alpha_1)e^{\beta z} + D_1(2 - \beta z - 1/\alpha_1)e^{-\beta z} \right]$$

$$\tau_{zz1} = -2\mu_1 \alpha_1 \beta^2 \left[A_1 \beta e^{\beta z} + B_1 \beta e^{-\beta z} + C_1(3 + \beta z - 1/\xi_1)e^{\beta z} - D_1(3 - \beta z - 1/\xi_1)e^{-\beta z} \right]$$

$$\tau_{xz2} = -i4\pi k_x \mu_2 \alpha_2 \beta \left[A_2 \beta e^{\beta z} + C_2(2 + \beta z - 1/\alpha_2)e^{\beta z} \right]$$

$$\tau_{yz2} = -i4\pi k_y \mu_2 \alpha_2 \beta \left[A_2 \beta e^{\beta z} + C_2(2 + \beta z - 1/\alpha_2)e^{\beta z} \right]$$

$$\tau_{zz2} = -2\mu_2 \alpha_2 \beta^2 \left[A_2 \beta e^{\beta z} + C_2(3 + \beta z - 1/\xi_2)e^{\beta z} \right]$$

where $\alpha_1 = \alpha(\mu_1, \lambda_1)$, $\xi_1 = \xi(\mu_1, \lambda_1)$, $\alpha_2 = \alpha(\mu_2, \lambda_2)$, and $\xi_2 = \xi(\mu_2, \lambda_2)$.

We can use these solutions and the appropriate boundary conditions (3.A1-3.A3) to solve for the six remaining Boussinesq coefficients A_1, B_1, C_1, D_1, A_2, and C_2. Noting the symmetry between U_B, V_B and τ_{xz}, τ_{yz} in equation 3.A10, we reduce the set of boundary conditions from nine to six:

$$U_1 = U_2\big|_{z=-h} \qquad \tau_{zz1} = -\tau_{33} + \rho g W\big|_{z=0}$$

$$W_1 = W_2\big|_{z=-h} \qquad \tau_{xz1} = 0\big|_{z=0}$$

$$\tau_{xz1} = \tau_{xz2}\big|_{z=-h}$$

$$\tau_{zz1} = \tau_{zz2}\big|_{z=-h}$$

(3.A11)

This step results in six equations and six unknown Boussinesq coefficients. By substituting equations 3.A10 into 3.A11, we have the following linear system of equations where $\psi = \dfrac{\alpha_1\beta}{\tau_{33}}$:

$$\begin{bmatrix} 1 \\ 0 \\ 0 \\ 0 \\ 0 \\ 0 \end{bmatrix} = \begin{bmatrix} \psi\beta(2\mu_1\beta - \rho g) & \psi\beta(2\mu_1\beta + \rho g) & 2\psi(\mu_1\beta(3-1/\xi_1) - \rho g(1-1/\alpha_1)) & -2\psi(\mu_1\beta(3-1/\xi_1) + \rho g(1-1/\alpha_1)) & 0 & 0 \\ \beta & -\beta & (2-1/\alpha_1) & (2-1/\alpha_1) & 0 & 0 \\ \mu_1\alpha_1\beta e^{-\beta h} & -\mu_1\alpha_1\beta e^{\beta h} & \mu_1\alpha_1(2-\beta h-1/\alpha_1)e^{-\beta h} & \mu_1\alpha_1(2+\beta h-1/\alpha_1)e^{\beta h} & -\mu_2\alpha_2\beta e^{-\beta h} & -\mu_2\alpha_2(2-\beta h-1/\alpha_2)e^{-\beta h} \\ \mu_1\alpha_1\beta e^{-\beta h} & \mu_1\alpha_1\beta e^{\beta h} & \mu_1\alpha_1(3-\beta h-1/\xi_1)e^{-\beta h} & -\mu_1\alpha_1(3+\beta h-1/\xi_1)e^{\beta h} & -\mu_2\alpha_2\beta e^{-\beta h} & -\mu_2\alpha_2(3-\beta h-1/\xi_2)e^{-\beta h} \\ \alpha_1\beta e^{-\beta h} & \alpha_1\beta e^{\beta h} & \alpha_1(1-\beta h)e^{-\beta h} & -\alpha_1(1+\beta h)e^{\beta h} & -\alpha_2\beta e^{-\beta h} & -\alpha_2(1-\beta h)e^{-\beta h} \\ \alpha_1\beta e^{-\beta h} & -\alpha_1\beta e^{\beta h} & \alpha_1(2-\beta h-2/\alpha_1)e^{-\beta h} & \alpha_1(2+\beta h-2/\alpha_1)e^{\beta h} & -\alpha_2\beta e^{-\beta h} & -\alpha_2(2-\beta h-2/\alpha_2)e^{-\beta h} \end{bmatrix} \begin{bmatrix} A_1 \\ B_1 \\ C_1 \\ D_1 \\ A_2 \\ C_2 \end{bmatrix},$$

(3.A12)

We next invert equation 3.A12 to solve for the A_1, B_1, C_1, D_1, A_2, and C_2. The solutions for the six Boussinesq coefficients, of arbitrary elastic constants and including the gravitational restoring force, ρg, are:

$$A_1 = \frac{1}{d}\beta^2 \frac{(\lambda_2 + \mu_2)}{(\lambda_1 + 2\mu_1)^2(\lambda_2 + 2\mu_2)^2}\left\{\begin{array}{l} \mu_1^2\lambda_2(\lambda_1 + \mu_1)\left[2\mu_1(\beta^2 h^2 e^{-2\beta h}) - \lambda_1(1 - e^{-2\beta h}(1 - 2\beta h + 2\beta^2 h^2))\right] \\ -\mu_2^2\lambda_1(\lambda_2 + \mu_2)\left[\lambda_1(1 + e^{-2\beta h}(1 - 2\beta h + 2\beta^2 h^2))\right] \\ \mu_1\left[\begin{array}{l} 4\lambda_1\lambda_2 - 8\mu_1\mu_2 e^{-2\beta h}(1 - \beta^2 h^2) \\ +3(\lambda_1 + \mu_1)\left\{\begin{array}{l}\lambda_1(1 - e^{-2\beta h}(1 - 2\beta h + 2\beta^2 h^2)) \\ -2\mu_1\beta^2 h^2 e^{-2\beta h}\end{array}\right\}\end{array}\right] \\ -\mu_1\mu_2\left[+\mu_2\left[\begin{array}{l} 4\lambda_1^2(1 - e^{-2\beta h}(\beta h + \beta^2 h^2)) \\ +\lambda_1(\lambda_2 + \mu_2)(3 - e^{-2\beta h}(3 - 2\beta h + 4\beta^2 h^2))\end{array}\right]\right] \\ +2\mu_1\mu_2\left[\begin{array}{l}\lambda_1(5 - 2e^{-2\beta h}(1 + \beta h + 2\beta^2 h^2)) \\ +2\mu_1 e^{-2\beta h}(1 - \beta^2 h^2) \\ +(\lambda_2 + \mu_2)e^{-2\beta h}(2 + \beta^2 h^2)\end{array}\right] \\ +2\lambda_1^2\lambda_2 \end{array}\right\}$$

(3.A13)

$$B_1 = \frac{1}{d}e^{-2\beta h}\beta^2 \frac{(\lambda_2+\mu_2)}{(\lambda_1+2\mu_1)^2(\lambda_2+2\mu_2)^2}\left\{
\begin{aligned}
&\mu_1^2\lambda_2(\lambda_1+\mu_1)\begin{bmatrix}\lambda_1\big(1+2\beta h(1+\beta h)-e^{-2\beta h}\big)\\+2\mu_1\big(\beta^2 h^2\big)\end{bmatrix}\\
&-\mu_2^2\lambda_1(\lambda_2+\mu_2)\big[\lambda_1\big(1+2\beta h(1+2\beta h)+e^{-2\beta h}\big)\big]\\
&+\mu_1\mu_2\left\{
\begin{aligned}
&\mu_1\begin{bmatrix}4\lambda_1\lambda_2 e^{-2\beta h}+3\mu_1\lambda_1\big(1+2\beta h(1+2\beta h)-e^{-2\beta h}\big)\\+3\lambda_1^2\big(1+2\beta h(1+\beta h)-e^{-2\beta h}\big)\end{bmatrix}\\
&-\mu_2\begin{bmatrix}4\lambda_1^2\big(\beta h(1+\beta h)-e^{-2\beta h}\big)\\+\lambda_1(\lambda_2+\mu_2)\big(3+2\beta h(1+2\beta h)+3e^{-2\beta h}\big)\end{bmatrix}\\
&+2\mu_1\mu_2\begin{bmatrix}\lambda_1\big(2-2\beta h(1+2\beta h)+3e^{-2\beta h}\big)\\+2\mu_1\big(1-\beta^2 h^2\big)\\-(\lambda_2+\mu_2)\big(2+\beta^2 h^2\big)\end{bmatrix}\\
&+2\lambda_1^2\lambda_2 e^{-2\beta h}+6\mu_1^3\beta^2 h^2
\end{aligned}
\right\}
\end{aligned}
\right\} \qquad (3.A14)$$

$$C_1 = \frac{1}{d}\beta^3 \frac{(\lambda_1+\mu_1)(\lambda_2+\mu_2)}{(\lambda_1+2\mu_1)^2(\lambda_2+2\mu_2)^2}\left\{
\begin{aligned}
&\mu_1^2\lambda_2(\lambda_1+\mu_1)\big[1-e^{-2\beta h}(1-2\beta h)\big]\\
&+\mu_2^2\lambda_1(\lambda_2+\mu_2)\big[1+e^{-2\beta h}(1-2\beta h)\big]\\
&+\mu_1\mu_2\left\{
\begin{aligned}
&\mu_1\big[3(\lambda_1+\mu_1)\{1-e^{-2\beta h}(1-2\beta h)\}\big]\\
&+\mu_2\begin{bmatrix}(\lambda_2+\mu_2)\big(3+e^{-2\beta h}(1-2\beta h)\big)\\+2\lambda_1\big(2+e^{-2\beta h}(1-2\beta h)\big)\end{bmatrix}\\
&+2\mu_1\mu_2\big[5+e^{-2\beta h}(1-2\beta h)\big]\\
&+2\lambda_2(\lambda_1+2\mu_1)
\end{aligned}
\right\}
\end{aligned}
\right\} \qquad (3.A15)$$

$$D_1 = \frac{1}{d}e^{-2\beta h}\beta^3 \frac{(\lambda_1+\mu_1)(\lambda_2+\mu_2)}{(\lambda_1+2\mu_1)^2(\lambda_2+2\mu_2)^2}\left\{
\begin{aligned}
&\mu_1^2\lambda_2(\lambda_1+\mu_1)\big[1+2\beta h-e^{-2\beta h}\big]\\
&-\mu_2^2\lambda_1(\lambda_2+\mu_2)\big[1+2\beta h+e^{-2\beta h}\big]\\
&+\mu_1\mu_2\left\{
\begin{aligned}
&\mu_1\big[3(\lambda_1+\mu_1)\{1+2\beta h-e^{-2\beta h}\}\big]\\
&-\mu_2\begin{bmatrix}(\lambda_2+\mu_2)\big(1+2\beta h-3e^{-2\beta h}\big)\\+2\lambda_1\big(1+2\beta h-2e^{-2\beta h}\big)\end{bmatrix}\\
&-2\mu_1\mu_2\big[1+2\beta h-3e^{-2\beta h}\big]\\
&+2\lambda_2(\lambda_1+2\mu_1)e^{-2\beta h}
\end{aligned}
\right\}
\end{aligned}
\right\} \qquad (3.A16)$$

$$A_2 = \frac{1}{d} 2\beta^2 \mu_1 \frac{(\lambda_1 + \mu_1)}{(\lambda_2 + 2\mu_2)(\lambda_1 + 2\mu_1)^2} \left\{ \begin{array}{l} \mu_1^2 \left\{ \begin{array}{l} \mu_2 \left[e^{-2\beta h}\left(2\beta^2 h^2 + 1\right) - 2\beta h - 1 \right] \\ + \lambda_2 \left[e^{-2\beta h}\left(2\beta h(\beta h - 1) + 1\right) - 1 \right] \end{array} \right\} \\ -\mu_2^2 \left\{ \begin{array}{l} \mu_1 \left[e^{-2\beta h}\left(2\beta^2 h^2 + 1\right) - 2\beta h - 1 \right] \\ + 2\lambda_1 \left[e^{-2\beta h}\left(\beta^2 h^2\right) \right] \end{array} \right\} \\ +\mu_1\mu_2 \left\{ \begin{array}{l} \lambda_1 \left[e^{-2\beta h}\left(2\beta^2 h^2 + 1\right) - 2\beta h - 1 \right] \\ -2\lambda_2 \left[e^{-2\beta h}\left(\beta h(\beta h - 1) + 1\right) - \beta h + 1 \right] \end{array} \right\} \\ +\mu_1\lambda_1\lambda_2 \left\{ e^{-2\beta h}\left[2\beta h(\beta h - 1) + 1\right] - 1 \right\} \\ -\mu_2\lambda_1\lambda_2 \left\{ e^{-2\beta h}\left[2\beta h(\beta h - 1) + 1\right] + 1 \right\} \end{array} \right\} \tag{3.A17}$$

$$C_2 = \frac{1}{d} 2\mu_1 \beta^3 \frac{(\lambda_1 + \mu_1)(\lambda_2 + \mu_2)}{(\lambda_2 + 2\mu_2)(\lambda_1 + 2\mu_1)^2} \left\{ \begin{array}{l} \mu_1^2 \left\{ 1 - e^{-2\beta h}\left(1 - 2\beta h\right) \right\} \\ +\mu_1\mu_2 \left\{ 3 + e^{-2\beta h}\left(1 - 2\beta h\right) \right\} \\ +\mu_1\lambda_1 \left\{ 1 - e^{-2\beta h}\left(1 - 2\beta h\right) \right\} \\ +\mu_2\lambda_1 \left\{ 1 + e^{-2\beta h}\left(1 - 2\beta h\right) \right\} \end{array} \right\} \tag{3.A18}$$

where

$$d = \beta^4 \frac{(\lambda_1 + \mu_1)(\lambda_2 + \mu_2)}{(\lambda_1 + 2\mu_1)^2(\lambda_2 + 2\mu_2)^2} \frac{1}{\tau_{33}} \left\{ \frac{-2\mu_1\beta}{(\lambda_1 + 2\mu_1)} d_1 + \rho g d_2 \right\} \tag{3.A19}$$

and

$$d_1 = \left\{ \begin{array}{l} \mu_1^2(\lambda_1 + \mu_1)^2(\lambda_2 + 3\mu_2)\left[e^{-4\beta h} - 2e^{-2\beta h}\left(1 + 2\beta^2 h^2\right) + 1 \right] \\ +\mu_2^2\lambda_1^2(\lambda_2 + \mu_2 + 4\mu_1)\left[e^{-4\beta h} + 2e^{-2\beta h}\left(1 + 2\beta^2 h^2\right) + 1 \right] \\ \\ +\mu_1\mu_2 \left\{ \begin{array}{l} \mu_1\mu_2 \left\{ \begin{array}{l} (\lambda_2 + \mu_2)\left[3e^{-4\beta h} + 2e^{-2\beta h}\left(5 + 2\beta^2 h^2\right) + 3 \right] \\ -2\mu_1 \left[3e^{-4\beta h} + 2e^{-2\beta h}\left(1 - 2\beta^2 h^2\right) - 5 \right] \\ -2\lambda_1 \left[5e^{-4\beta h} + 2e^{-2\beta h}\left(1 - 4\beta^2 h^2\right) - 7 \right] \end{array} \right\} \\ +4\mu_2 \left[\begin{array}{l} \lambda_1(\lambda_2 + \mu_2)\left[e^{-4\beta h} + 2e^{-2\beta h}\left(1 + \beta^2 h^2\right) + 1 \right] \\ -2\lambda_1^2\left[e^{-4\beta h} + e^{-2\beta h}\left(1 + \beta^2 h^2\right) \right] \end{array} \right] \\ -2\lambda_2(\lambda_1 + \mu_1)(\lambda_1 + 2\mu_1)\left(e^{-4\beta h} - 1 \right) \end{array} \right\} \end{array} \right\} \tag{3.A20}$$

$$
d_2 = \left\{
\begin{array}{l}
-\mu_1^2 \lambda_2 (\lambda_1 + \mu_1)\left[e^{-4\beta h} - 4\beta h e^{-2\beta h} - 1\right] \\
-\mu_2^2 \lambda_1 (\lambda_2 + \mu_2)\left[e^{-4\beta h} + 4\beta h e^{-2\beta h} - 1\right] \\
+\mu_1\mu_2 \left\{
\mu_1 \left[
\begin{array}{l}
4\lambda_2\left[e^{-4\beta h} + 1\right] \\
-3(\lambda_1 + \mu_1)\left[e^{-4\beta h} - 4\beta h e^{-2\beta h} - 1\right]
\end{array}
\right]
+\mu_2 \left[
\begin{array}{l}
4\lambda_1\left[e^{-4\beta h} - 2\beta h e^{-2\beta h} + 1\right] \\
-(\lambda_2 + \mu_2)\left[3e^{-4\beta h} + 4\beta h e^{-2\beta h} - 3\right]
\end{array}
\right] \\
+2\mu_1\mu_2\left[3e^{-4\beta h} - 4\beta h e^{-2\beta h} + 5\right] \\
+2\lambda_1\lambda_2\left(e^{-4\beta h} + 1\right)
\end{array}
\right\}
\end{array}
\right\} .
\tag{3.A21}
$$

These Boussinesq coefficients are greatly simplified for the case of an elastic plate overlying a fluid half-space where $\mu_2 = 0$:

$$
A_1 = \frac{1}{d}\beta^2 \frac{(\lambda_1 + \mu_1)}{(\lambda_1 + 2\mu_1)^2}\left\{2\mu_1\left(\beta^2 h^2 e^{-2\beta h}\right) - \lambda_1\left(1 - e^{-2\beta h}\left(1 - 2\beta h + 2\beta^2 h^2\right)\right)\right\}
\tag{3.A22}
$$

$$
B_1 = \frac{1}{d}e^{-2\beta h}\beta^2 \frac{(\lambda_1 + \mu_1)}{(\lambda_1 + 2\mu_1)^2}\left\{2\mu_1\left(\beta^2 h^2\right) + \lambda_1\left(1 + 2\beta h(1 + \beta h) - e^{-2\beta h}\right)\right\}
\tag{3.A23}
$$

$$
C_1 = \frac{1}{d}\alpha_1^2 \beta^3\left\{1 - e^{-2\beta h}\left(1 - 2\beta h\right)\right\}
\tag{3.A24}
$$

$$
D_1 = \frac{1}{d}e^{-2\beta h}\alpha_1^2 \beta^3\left\{1 + 2\beta h - e^{-2\beta h}\right\}
\tag{3.A25}
$$

$$
A_2 = \frac{1}{d}2\beta^2 \mu_1^2 \alpha_1^2\left\{e^{-2\beta h}\left(2\beta h(\beta h - 1) + 1\right) - 1\right\}
\tag{3.A26}
$$

$$
C_2 = \frac{1}{d}2\beta^3 \mu_1^2 \alpha_1^2\left\{1 - e^{-2\beta h}\left(1 - 2\beta h\right)\right\}
\tag{3.A27}
$$

where

$$
d = -\alpha_1^2 \beta^4 \frac{1}{\tau_{33}}\left\{2\mu_1\alpha_1\beta d_1 + \rho g d_2\right\}
\tag{3.A28}
$$

and

$$
d_1 = e^{-4\beta h} - 2e^{-2\beta h}\left(1 + 2\beta^2 h^2\right) + 1
\tag{3.A29}
$$

$$
d_2 = e^{-4\beta h} - 4\beta h e^{-2\beta h} - 1 .
\tag{3.A30}
$$

In addition to the general coefficients (equations 3.A13-3.A21) and those for the special case of an elastic plate overlying a fluid half-space (equations 3.A22-3.A30), both including the gravitational restoring force, we have also solved for the Boussinesq coefficients for two other cases: (1) a homogeneous elastic half-space without gravity ($\mu_1 = \mu_2$, $\rho g = 0$) and (2) a layered medium with arbitrary μ_1 and μ_2, also without gravity. These solutions can be found at http://topex.ucsd.edu/body_force. They have been individually validated using computer algebra and have been numerically compared to known analytic models (Figures 3.5-3.6).

Appendix 3.B   Method of images

As addressed in Section 3.2.2, for a simple homogeneous half-space model, we can use the method of images [*Weertman*, 1964] to place an image vector source opposite the original vector source to satisfy the requirements of a stress-free surface (equations 3.2 & 3.4)

$$\begin{bmatrix} U(\mathbf{k}) \\ V(\mathbf{k}) \\ W(\mathbf{k}) \end{bmatrix} = \mathbf{U}(\mathbf{k},z) = \mathbf{U}_s(\mathbf{k},z-a)\begin{bmatrix} F_x \\ F_y \\ F_z \end{bmatrix} + \mathbf{U}_i(\mathbf{k},-z-a)\begin{bmatrix} F_x \\ F_y \\ F_z \end{bmatrix}. \tag{3.B1}$$

In equation 3.B1, the *z-a* term refers the source body-force vector and the *-z-a* term refers to the image body-force vector. For a layered half-space though, we must also require that the displacements and consequent stresses remain continuous at the boundary layer between varying shear moduli. To do this, we must superpose multiple image sources, reflected both above and below the horizontal axis, to account for both the source and also the layer thickness (Figure 3.A1). In this approach, an infinite number of secondary images,
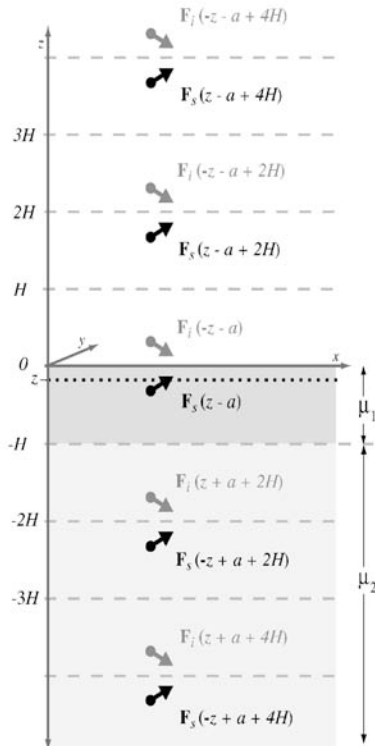
Figure 3.B1. Sketch of the source-image method for a layered elastic medium of rigidities μ_1 (layer of thickness H) and μ_2 (underlying half-space) used to cancel all shear stress at the surface and preserve continuity across the layer/half-space interface. Following the method of images [*Weertman*, 1964], an infinite number of image terms are reflected above and below the source vector. For a half-space model of zero rigidity (a fluid), this sum (equation 3.5 or 3.B2) is mathematically achieved by an infinite series. These additional image contributions are represented by body forces F_s and F_i, and are multiplied by the source and image matrices of equation 3.7. Note that the mathematical expressions for the image sources for $z < 0$ have an opposite sign in equation 3.5 or 3.B2.

m, are reflected above and below the source vector, located at distances of *2mH* (equation 3.5):

$$
\begin{bmatrix} U(\mathbf{k}) \\ V(\mathbf{k}) \\ W(\mathbf{k}) \end{bmatrix} = \mathbf{U}_s(\mathbf{k}, z-a) \begin{bmatrix} F_x \\ F_y \\ F_z \end{bmatrix} + \mathbf{U}_i(\mathbf{k}, -z-a) \begin{bmatrix} F_x \\ F_y \\ F_z \end{bmatrix} + \sum_{m=1}^{\infty} \left(\frac{\mu_1 - \mu_2}{\mu_1 + \mu_2} \right)^m \begin{bmatrix} U_i(z-a-2mH) \\ +U_i(-z-a+2mH) \\ +U_i(z-a+2mH) \\ +U_i(-z-a-2mH) \end{bmatrix} \begin{bmatrix} F_x \\ F_y \\ F_z \end{bmatrix}.
$$

(3.B2)

In equation 3.B2, the $z-a\pm 2mH$ and $-z-a\pm 2mH$ terms are mirror images of the primary source and image, respectively. The contrasting shear moduli ratio coefficient to the left of these terms indicates the level of convergence of the layered solution. For a layer and half-space of similar elastic constants, the shear moduli coefficient converges easily. Yet a special case exists when the underlying half-space has a shear modulus that approaches zero (Appendix 3.C).

Appendix 3.C   Analytic Treatment of an Infinite Sum

Inspection of equation 3.5 (or 3.B2) shows that when the shear modulus of the half-space, μ_2, goes to zero, the convergence of the layered solution becomes problematic. We can treat the infinite sum analytically by summing the terms from equation 3.8 that are dependent upon Z: $e^{-\beta Z}$ and $\beta Z e^{-\beta Z}$.

We first analytically treat the simple exponential, $e^{-\beta Z}$:

$$
\sum_{m=1}^{\infty} e^{-\beta(z'+2mH)} = e^{-\beta z'} e^{-\beta 2H} \sum_{m=0}^{\infty} e^{-\beta 2mH} = e^{-\beta z'} \frac{e^{-\beta 2H}}{1-e^{-\beta 2H}}
$$

(3.C1)

where z' now represents all terms of the form $(\pm z \pm d_n)$, as in those of equation 3.6. Next we treat the $\beta Z e^{-\beta Z}$ term by noting that

$$
-\beta \frac{\partial}{\partial \beta} e^{-\beta Z} = \beta Z e^{-\beta Z}.
$$

(3.C2)

Therefore, to evaluate the sum of $\beta Z e^{-\beta Z}$, we take the derivative of the sum of $e^{-\beta Z}$ with respect to β:

$$
\sum_{m=1}^{\infty} \beta(z'+2mH) e^{-\beta(z'+2mH)} = -\beta \frac{\partial}{\partial \beta} \sum_{m=1}^{\infty} e^{-\beta(z'+2mH)} = -\beta \frac{\partial}{\partial \beta} \frac{e^{-\beta(z'+2H)}}{1-e^{-\beta 2H}}
$$

$$
= \frac{e^{-\beta(z'+2H)}}{\left(1-e^{-\beta 2H}\right)} \left[\beta(z'+2H) + \frac{2\beta H e^{-\beta 2H}}{\left(1-e^{-\beta 2H}\right)} \right].
$$

(3.C3)

For the special case of an elastic plate over a fluid half-space ($\mu_2 = 0$), computing the infinite sum of equation 3.5 (or 3.B2) is not necessary, as equations 3.C2 and 3.C3 can be used instead to increase the computational convergence speed.

Appendix 3.D   Including Time Dependence: The Maxwell Model

Following the method of *Nur and Mavko* [1974] and *Savage and Prescott* [1978], we now describe our approach for the development of a time-dependent Maxwell model for 3-D displacement and stress caused by a dislocation in an elastic layer overlying a linear viscoelastic half-space. Here we develop viscoelastic coefficients that are used in conjunction with equations 3.6-3.8 to manipulate the time-dependence of the viscoelastic problem. This model will ultimately be used to demonstrate the viscoelastic response of the Earth throughout the earthquake cycle.

Our theory begins with the description of the viscoelastic behavior of a Maxwell body made up of an elastic element and a viscous element, connected in series [*Cohen*, 1999].   The elastic and viscous element can be represented mathematically [*Jaeger*, 1956] by stress, σ, and stress rate, σ', respectively:

$$\sigma = \mu\varepsilon \tag{3.D1}$$

$$\sigma' = \eta\varepsilon'. \tag{3.D2}$$

The elastic element (3.D1) describes a relationship between strain, ε, and the shear modulus, μ, while the viscous element (3.D2) describes a relationship between strain rate, ε', and viscosity, η.   Combining both of these linear elements for a Maxwell body in series, the constituative equation becomes

$$\varepsilon' = \frac{1}{\mu}\sigma' + \frac{1}{\eta}\sigma \cdot \tag{3.D3}$$

In addition, the Maxwell time, τ_m, is a parameter used in describing the behavior of viscoelastic relaxation. In our model, we define Maxwell time as, $\tau_m = 2\eta/\mu$, although it should be noted that Maxwell time is defined differently by various authors (e.g., η/μ, $\eta/2\mu$).

We now use the Correspondence Principle for relating the constitutive equation for a Maxwell body (3.D3) to our elastic solutions (equations 3.6-3.8).   According to the Correspondence Principle, when time-dependent equations are Laplace transformed, stress and strain relations retain the same "form" for all linear rheologies.   Thus when the elastic solution is known, a corresponding solution describing a different rheology can be derived. Hence our first step is to take the Laplace transform of equation 3.D3

$$L\{\varepsilon\} = s\varepsilon(s) = \frac{s}{\mu}\sigma(s) + \frac{1}{\eta}\sigma(s), \tag{3.D4}$$

where *s* is the Laplace transform variable. Solving for stress, σ, we obtain

$$\sigma(s) = \frac{\mu s}{s + \dfrac{\mu}{\eta}} \, \varepsilon(s).$$

(3.D5)

From equation 3.D5, we note that as Laplace variable s approaches zero (zero frequency), the stress, $\sigma(s)$, goes to zero. Alternatively, as s approaches infinite values, the stress takes on the form $\sigma = \mu\varepsilon$.

As it is our intent to define the half-space shear modulus, μ_2, in terms of time, we will assume $\mu = \mu_1$ and set

$$\mu_2(s) = \frac{\mu s}{s + \dfrac{\mu}{\eta}} \, .$$

(3.D6)

The Laplace transformed viscoelastic equation,

$$\sigma(s) = \mu_2(s)\varepsilon(s),$$

(3.D7)

now takes on the same form as that of the purely elastic constituative equation (3.D1).

Through the Correspondence Principle, the viscoelastic solution can be obtained as follows:
  (1)   Replace the shear modulus in the elastic solution by the Laplace transformed shear modulus variable.
  (2)   Compute the inverse transform of the layered solution.
  (3)   Integrate the solution (impulse response function) to obtain the response to a step function used to represent an earthquake.
  (4)   Identify a recursion formula for rapid and convenient calculation.
  (5)   Solve for the implied μ_2 associated with each image in the infinite layers.
  (6)   Ensure the bulk modulus remains constant by varying λ_2 for each μ_2.

Our goal is to map time (t) and viscosity (η) into an implied μ_2 and then solve for the corresponding elastic constant λ_2 by requiring a constant bulk modulus. We have already shown that the layered elastic solution may be described by adding the sources and images associated with the layer in an infinite series (equations 3.5-3.6). We now focus on the treatment of the shear modulus ratio inside the infinite series solution, which we will now refer to as χ:

$$\chi = \frac{\mu_1 - \mu_2}{\mu_1 + \mu_2} \, .$$

(3.D8)

We substitute equation 3.D6 into 3.D8 and again assume $\mu = \mu_1$. The Laplace transform of χ then becomes

$$\chi(s) \quad = \quad \frac{\mu - \dfrac{\mu s}{s + \mu/\eta}}{\mu + \dfrac{\mu s}{s + \mu/\eta}} \quad = \quad \frac{\dfrac{\mu}{2\eta}}{s + \dfrac{\mu}{2\eta}} \, .$$

(3.D9)

By setting $a = \mu/2\eta = 1/\tau_m$, the inverse of the Maxell time, we find

$$\chi(s) = \frac{a}{s+a}.$$

(3.D10)

Because the infinite sum of equations 3.5-3.6 is raised to the power of m, we next take the inverse Laplace Transform of $\chi^m(s)$,

$$\chi^m(t) = \frac{a^m t^{m-1}}{(m-1)!}e^{-at},$$

(3.D11)

which is the impulse response function. We next integrate this impulse response function to obtain the response to a step function, $H(t)$, which represents seismic faulting events over time. Let coefficients $A_m(t)$ and $B_m(t)$ describe this behavior:

$$\int_0^t \chi^m(t)dt \;=\; \frac{a^m}{(m-1)!}\int_0^t t^{m-1}e^{-at}dt \;=\; A_m(t)$$

and

$$B_m(t) = \frac{(m-1)!}{a^m}A_m(t)$$

(3.D12)

where

$$B_m(t) = \int_0^t t^{m-1}e^{-at}dt.$$

(3.D13)

Integrating by parts reveals the following recursion formula:

$$B_m = -\frac{t^{m-1}}{a}e^{-at} + \frac{m-1}{a}B_{m-1}$$

(3.D14)

where

$$B_1 = \int_0^t e^{-at}dt = \frac{1}{a}\left[1 - e^{-at}\right].$$

(3.D15)

Substituting $a = \mu/2\eta = 1/\tau_m$ into 3.D12 and 3.D14, the first three terms in this infinite series are:

m	B_m	A_m
1	$\tau_m\left[1-e^{-\frac{t}{\tau_m}}\right]$	$\left[1-e^{-\frac{t}{\tau_m}}\right]$
2	$-\tau_m t e^{-\frac{t}{\tau_m}}+\tau_m^2\left[1-e^{-\frac{t}{\tau_m}}\right]$	$-\frac{t}{\tau_m}e^{-\frac{t}{\tau_m}}+\left[1-e^{-\frac{t}{\tau_m}}\right]$
3	$-\tau_m t^2 e^{-\frac{t}{\tau_m}}+2\left\{-\tau_m t e^{-\frac{t}{\tau_m}}+\tau_m^2\left[1-e^{-\frac{t}{\tau_m}}\right]\right\}$	$-\left(\frac{t}{\tau_m}\right)^2\frac{e^{-\frac{t}{\tau_m}}}{2}-\frac{t}{\tau_m}e^{-\frac{t}{\tau_m}}+\left[1-e^{-\frac{t}{\tau_m}}\right].$

$$(3.\text{D}16)$$

We next replace the time-integrated shear modulus ratio (3.D8) with the new A_m coefficients, where each image source will have its own implied μ_2:

$$\left(\frac{\mu_1-\mu_2}{\mu_1+\mu_2}\right)^m = A_m. \qquad (3.\text{D}17)$$

Solving for the implied μ_2 corresponding to each A_m coefficient, we obtain

$$\mu_2 = \mu_1\left(\frac{1-A_m^{\frac{1}{m}}}{1+A_m^{\frac{1}{m}}}\right).$$

In addition to the time-dependent behavior of the effective shear modulus of the viscoelastic half-space, we also must ensure that the bulk modulus, κ, remains constant:

$$\kappa_2 = \lambda_2 + \frac{2}{3}\mu_2 = \text{constant}.$$

If we set

$$\mu_2 = \mu_1\left(\frac{1-A_m^{\frac{1}{m}}}{1+A_m^{\frac{1}{m}}}\right), \qquad (3.\text{D}18)$$

then

$$\lambda_2 = \kappa_2 - \frac{2}{3}\mu_1\left(\frac{1-A_m^{\frac{1}{m}}}{1+A_m^{\frac{1}{m}}}\right). \qquad (3.\text{D}19)$$

In addition, we must also note that the vertical Boussinesq load assumes the shear response of a single Maxwell time. Since we have only solved the vertical loading problem for an elastic plate overlying a viscoelastic half-space, we must select the most appropriate viscosity or Maxwell time. We choose the viscosity of the uppermost image ($m = 1$), noting that this is an approximation to the exact layered behavior. This approach follows the time-dependent loading problem discussed by *Brotchie and Silvester* [1969] where loading is scaled by a similar viscosity-dependent coefficient. If a vertical load is applied at $t = 0$ and the

initial elastic response is described as $W(\mathbf{k},0)$, then the long-term response of the elastic plate overlying a fluid half-space is $W(\mathbf{k},\infty)$. For a Maxwell time of $\tau_m = 2\eta/\mu$, the viscoelastic response becomes

$$W(\mathbf{k},t) = W(\mathbf{k},0) + \left[1 - e^{-\frac{t}{\tau_m}}\right]\left[W(\mathbf{k},\infty) - W(\mathbf{k},0)\right]$$

$$= W(\mathbf{k},0)e^{-\frac{t}{\tau_m}} + \left[1 - e^{-\frac{t}{\tau_m}}\right]W(\mathbf{k},\infty). \tag{3.D20}$$

By assuming $\mu_2(t)$ from $A_m(1)$, the Maxwell coefficients become

$$A_m(1) = \left(1 - e^{-\frac{t}{\tau_m}}\right)$$

and

$$\mu_2 = \mu_1 \left(\frac{e^{-\frac{t}{\tau_m}}}{2 - e^{-\frac{t}{\tau_m}}}\right). \tag{3.D21}$$

As a check, we can verify that shear time variations are consistent with those expected for end-member models. For example, for times approaching zero, shear moduli of the layer and half-space are equal ($\mu_1 = \mu_2$). Alternatively, for times approaching infinity, the shear modulus of the half-space goes to zero ($\mu_2 = 0$). The 2-D models of Figures 3.3a-b demonstrate this behavior.

Appendix 3.E   Force Couples on a Regular Grid

A dislocation in a fault plane is commonly represented by body force couples. In the case of a horizontal strike-slip fault, a double-couple should be used to ensure local balanced moment in the horizontal plane [*Burridge and Knopoff,* 1964]. Here we describe the algorithm for generating single- and double-couple body forces for a segmented fault trace mapped onto a regular grid (Figure 3.1).

Consider a grid with cell spacing Δx. The final displacement and stress model cannot resolve features smaller than the cell spacing, thus we approximate a fault segment with a finite length L, oriented along the x-axis, and a finite thickness $\sigma \geq \Delta x$ as follows

$$f(x,y) = g(x)h(y) \tag{3.E1}$$

where the across-fault function $h(y)$ is a Gaussian function

$$h(y) = \frac{1}{\sigma\sqrt{2\pi}} \exp\left(\frac{y^2}{2\sigma^2}\right). \tag{3.E2}$$

We represent a curved fault trace as a large number of straight overlapping segments of the form

$$g(x) = \begin{cases} \dfrac{1}{2}\left[1 - \cos\dfrac{\pi(x+2\Delta x)}{4\Delta x}\right] & -2\Delta x < x < 2\Delta x \\ 1 & 2\Delta x < x < L - 2\Delta x \\ \dfrac{1}{2}\left[1 - \cos\dfrac{\pi(L+2\Delta x - x)}{4\Delta x}\right] & L - 2\Delta x < x < L + 2\Delta x \end{cases} \tag{3.E3}$$

where x is the distance from the start of the segment and L is the segment length. The segments are arranged end-to-end so that the sum of the overlapping cosine functions equals one. The spatial variations in the force-couple are constructed by taking the derivatives of the fault function. The primary couple is parallel to the fault (x-direction) and corresponds to the fault-normal derivative

$$f_1(x,y) = g(x)\frac{\partial h}{\partial y}, \tag{3.E4}$$

where

$$\frac{\partial h}{\partial y} = \frac{-y}{\sigma^3\sqrt{2\pi}}\exp\left(\frac{y^2}{2\sigma^2}\right). \tag{3.E5}$$

The secondary force couple is perpendicular to the fault (y-direction) and corresponds to the fault-parallel derivative

$$f_2(x,y) = \frac{\partial g}{\partial x}h(y), \tag{3.E6}$$

where

$$\frac{\partial g}{\partial x} = \begin{cases} \dfrac{\pi}{8\Delta x}\sin\dfrac{\pi(x+2\Delta x)}{4\Delta x} & -2\Delta x < x < 2\Delta x \\ 1 & 2\Delta x < x < L - 2\Delta x \\ \dfrac{-\pi}{8\Delta x}\sin\dfrac{\pi(L+2\Delta x - x)}{4\Delta x} & L - 2\Delta x < x < L + 2\Delta x \end{cases} \cdot \tag{3.E7}$$

A rotation matrix is used to rotate the force couple functions to the proper orientation

$$\begin{pmatrix} x \\ y \end{pmatrix} = \begin{pmatrix} \cos\theta & -\sin\theta \\ \sin\theta & \cos\theta \end{pmatrix}\begin{pmatrix} x' \\ y' \end{pmatrix}, \tag{3.E8}$$

where θ is the angle between the x-axis and the fault trace ($\theta > 0$) represents counter-clockwise rotation.

Three modes of displacement can be applied on each fault segment. F_1 is strike-slip, F_2 is dip-slip, and F_3 is opening of the fault. Once the primary and secondary force couple functions are computed and rotated into

the fault direction, they are multiplied by the strength of the dislocation to form three grids corresponding to the F_1, F_2, and F_3 modes. These three force components must then be rotated into the Cartesian frame F_x, F_y, and F_z using the following formulas:

$$\begin{pmatrix} F_x(x,y) \\ F_y(x,y) \\ F_z(x,y) \end{pmatrix} = f_1(x,y) \begin{pmatrix} -\cos\theta & 0 & \sin\theta \\ \sin\theta & 0 & \cos\theta \\ 0 & 1 & 0 \end{pmatrix} \begin{pmatrix} F_1 \\ F_2 \\ F_3 \end{pmatrix}. \tag{3.E9}$$

Balancing of the moment due to the horizontal strike-slip force couple F_1 requires a second force component given by

$$\begin{pmatrix} F_x^2(x,y) \\ F_y^2(x,y) \end{pmatrix} = f_2(x,y) \begin{pmatrix} F_1 \sin\theta \\ F_1 \cos\theta \end{pmatrix}. \tag{3.E10}$$

Note that this force couple only applies to the end of each fault segment and the forces largely cancel where fault segments abut as described in *Burridge and Knopoff* [1964]. The moment generated by the vertical dip-slip F_2 and the opening F_3 of the fault will produce topography that will balance the moment under the restoring force of gravity.

This chapter, in full, is a reprint of the material is it appears in the *Journal of Geophysical Research*, Bridget, Smith; Sandwell, David, 2004. The dissertation author was the primary investigator and author of this paper. The co-author directed and supervised the research.

Chapter 4

A Model of the Earthquake Cycle Along the San Andreas Fault System for the Past 1000 Years

Bridget R. Smith and David T. Sandwell

Abstract. We simulate 1000 years of the earthquake cycle along the San Andreas Fault System by convolving best estimates of interseismic and coseismic slip with the Green's function for a point dislocation in an elastic plate overlying a viscoelastic half-space. Interseismic slip rate is based on long-term geological estimates while fault locking depths are derived from horizontal GPS measurements. Coseismic and postseismic deformation is modeled using 70 earthquake ruptures, compiled from both historical data and paleoseismic data. This time-dependent velocity model is compared with 290 present-day geodetic velocity vectors to place bounds on plate thickness and viscosity of the underlying substrate. Best-fit models (RMS residual of 2.46 mm/yr) require an elastic plate thickness greater than 60 km and a substrate viscosity between 2×10^{18} and 5×10^{19} Pa s. These results highlight the need for vertical velocity measurements developed over long time spans (> 20 years). Our numerical models are also used to investigate the 1000-year evolution of Coulomb stress. Stress is largely independent of assumed rheology, but is very sensitive to the slip history on each fault segment. As expected, present-day Coulomb stress is high along the entire southern San Andreas because there have been no major earthquakes over the past 150 years. Animations of the time evolution of vector displacement and Coulomb stress are available as an electronic supplement.

4.1. Introduction

The San Andreas Fault (SAF) System extends from the Gulf of California to the Mendocino Triple Junction and traverses many densely populated regions. This tectonically complex zone has generated at least six major earthquakes ($M_w > 7.0$) over past 200 years: the 1812 Wrightwood-Santa Barbara Earthquakes ($M_w \sim 7.5$), the 1838 San Francisco Earthquake ($M_w = 7.4$), the 1857 Great Fort Tejon Earthquake ($M_w = 7.9$), the 1868 South Hayward Earthquake ($M_w = 7.0$), the 1906 Great San Francisco Earthquake ($M_w = 7.8$), and the 1940 Imperial Valley Earthquake ($M_w = 7.0$). The SAF System has also produced at least 37 moderate earthquakes ($M_w > 6.0$) over the past 200 years. Recently, major earthquake activity has occurred primarily on faults paralleling the San Andreas Fault System, such as the 1992 Landers Earthquake ($M_w = 7.3$), the 1999 Hector Mine Earthquake ($M_w = 7.1$), and the 2003 San Simeon Earthquake ($M_w = 6.8$). Yet several sections of the SAF System have not ruptured during the past 150 years. These relatively long periods of quiescence, coupled with matching recurrence intervals, indicate that these segments of the San Andreas Fault System are primed for another rupture.

A major earthquake on the San Andreas Fault System has the potential for massive economic and human loss and so establishing seismic hazards is a priority [*WGCEP*, 1995; *WGNCEP*, 1999; *WGCEP*, 2003]. This involves characterizing the spatial and temporal distribution of both coseismic and interseismic deformation, as well as modeling stress concentration, transfer, and release [*Anderson et al.*, 2003]. Furthermore, it is

important to understand how postseismic stress varies in both time and space and how it relates to time-dependent relaxation process of the Earth [*Cohen*, 1999; *Kenner*, 2004]. Many questions remain regarding the characteristics of earthquake recurrence, the rupture patterns of large earthquakes [*Grant and Lettis*, 2002], and long-term fault-to-fault coupling throughout the earthquake cycle. Arrays of seismometers along the SAF System provide tight constraints on the coseismic processes but geodetic measurements are needed for understanding the slower processes. The large array of GPS receivers currently operating along the North American-Pacific Plate boundary has aided in the discovery of several types of aseismic slip and postseismic deformation [e.g., *Bock et al.*, 1997; *Murray and Segall*, 2001], however the 1-2 decade record is too short to sample a significant fraction of the earthquake cycle. Full 3-D, time-dependent models that span several earthquake cycles and capture the important length scales are needed to explore a range of earthquake scenarios, to provide estimates of present-day stress, and to provide insight on how best to deploy future geodetic arrays.

Models of the earthquake cycle usually sacrifice resolution of either the space or time dimensions or are rheologically simple in order to be implemented on even the fastest modern computers. For example, time-independent elastic half-space models have been used to match geodetic observations of surface displacement of the San Andreas Fault System [e.g., *Savage and Burford*, 1973; *Li and Lim*, 1988; *Savage, 1990; Lisowski et al.*, 1991; *Feigl et al.*, 1993; *Murray and Segall*, 2001; *Becker et al.*, 2003; *Meade and Hager*, 2004]. Likewise, several local viscoelastic slip models, consisting of an elastic plate overlying a linear viscoelastic half-space, have been developed to match geodetically-measured postseismic surface velocities [e.g., *Savage and Prescott*, 1978; *Thatcher*, 1983; *Deng et al.*, 1998; *Pollitz et al.*, 2001; *Johnson and Segall*, 2004]. Many studies have also focused on the 3-D evolution of the local stress field due to coseismic and postseismic stress transfer [e.g., *Pollitz and Sacks, 1992; Kenner and Segall*, 1999*; Freed and Lin, 2001*; *Zeng*, 2001; *Hearn et al.*, 2004; *Parsons*, 2002]. Displacement and stress models such as these have provided important constraints on fault locking depth, viscoelastic relaxation time scales, fault zone rheologies, and local fault interactions. However, because of computer speed and memory limitations, most of these numerical models are limited to a single earthquake cycle and relatively simple fault geometries.

Our objective is to model the full 3-D deformation of multiple interacting fault strands spanning multiple earthquake cycles using a relatively simple layered viscoelastic model. While this is possible using purely numerical models [e.g., *Bird and Kong*, 1994; *Furlong and Verdonck*, 1994; *Parsons*, 2002; *Segall*, 2002], studies such as these are rare due to the considerable computational requirements [*Kenner*, 2004]. Furthermore, purely numerical algorithms (e.g., finite element), implemented on even the most powerful computers, do not yet have the efficiency to explore the range of parameters that can match the geodetic observations.

In a previous paper [*Smith and Sandwell*, 2004], we developed a 3-D semi-analytic solution for the vector displacement and stress tensor in an elastic plate overlying a viscoelastic half-space in response to a vertical strike-slip dislocation. The problem is solved analytically in both the vertical and time dimension (z, t), while the solution in the two horizontal dimensions (x, y) is developed in the Fourier transform domain to exploit the efficiency offered by the convolution theorem. The restoring force of gravity is included to accurately model vertical deformation. Arbitrarily complex fault traces and slip distributions can be specified without increasing the computational burden. For example, a model computation for slip on a complex fault segment in a 2-D grid that spans spatial scales from 1 km to 2048 km requires less than a minute of CPU on a desktop computer. Models containing multiple fault segments are computed by summing the contribution for each locking depth and every earthquake for at least ten Maxwell times in the past. For example, a model for the present-day velocity, which involves 27 fault segments (each having a different locking depth) and ~100 earthquakes during a 1000-year time period, requires 230 component

model computations costing 153 minutes of CPU time. Efficiency such as this enables the computation of kinematically realistic 3-D viscoelastic models spanning thousands of years.

In this paper, we apply the Fourier method to develop a kinematically realistic, time-dependent model of the San Andreas Fault System (i.e., secular plus episodic). The secular model was largely developed in a previous publication [*Smith and Sandwell*, 2003] where we used 1099 GPS horizontal velocity measurements and long-term slip rates from geology to establish the locking depths along 18 curved fault segments. Since our initial model used a simple elastic half-space, the inferred locking depths are an upper bound; for a viscoelastic model, the apparent locking depth depends on whether velocities are measured early or late in the earthquake cycle [*Meade and Hager*, 2003]. The episodic model uses a completely prescribed earthquake slip history (i.e., timing, rupture length, depth, and slip) on each fault segment for at least ten Maxwell times in the past. The timing and surface rupture for each event is inferred from published historical and paleoseismic earthquake records, as well earthquake recurrence intervals. We prescribe the rupture depth to be equal to the present-day locking depth and prescribe the amount of slip on each rupture to be equal to the slip rate times the time since the previous earthquake on that segment. Note that these simplifying assumptions do not allow for partial slip or spatially overlapping ruptures. The complete model (secular plus episodic) is matched to the present-day vector GPS data to solve for elastic plate thickness, half-space viscosity, geologic Poisson's ratio (i.e., representing the compressibility of the plates at infinite timescales), and apparent locking depth factor. Finally, the best-fit model is used to estimate secular and postseismic Coulomb stress change within the seismogenic layer. While this kinematic model of the entire San Andreas Fault System is one of the first of its kind to consider deformation changes over the past millennium, this is a difficult problem and future studies using more realistic rheologies and earthquake slip histories will certainly help further bound the solution. Nevertheless, this work provides new insights into the physics of the earthquake cycle and will hopefully improve future seismic hazard analyses of the San Andreas Fault System.

4.2. Great Earthquakes of the SAF System: 1000 A.D. to Present Day

While present-day motion of the San Andreas Fault System is continuously monitored by contemporary geodetic techniques, deformation occurring prior to the modern era is highly uncertain [*Toppozada et al.*, 2002]. However, historians and paleoseismologists have worked to piece together evidence for past seismic activity on the San Andreas Fault System. These efforts make up two earthquake databases: 1) historical earthquakes, based on written records and personal accounts [e.g., *Bakun*, 1999; *Toppozada et al.*, 2002], and 2) prehistorical earthquakes, or events estimated from paleoseismic trench excavations [e.g., *Sieh et al.*, 1989; *Fumal et al.*, 1993]. The prehistorical earthquake record of the San Andreas Fault System is based on a collaborative effort from many workers of paleoseismic community [*Grant and Lettis*, 2002 and references therein] and provides estimates for past earthquake ages dating back to 500 A.D. in some locations. A variety of dating methods have been used for these estimates, including radiocarbon dating, tree ring dating, earthquake-induced subsidence, and sea level changes. Alternatively, the historical earthquake records spans the past ~200 years and is bounded by the establishment of Spanish missions along coastal California in the early 1770s. Missionary documents existed sporadically from about 1780 to 1834, at which point all missions were secularized. Soon following the 1849 California Gold Rush, newspapers were regularly published, providing the San Francisco Bay region with the most complete earthquake record of this time. Based on the increase in California population and published newspapers in the following years, it is likely that the historical earthquake record is complete for M > 6.5 events from about 1880 and for M > 6.0 events from about 1910 [*Toppozada et al.*, 1981; *Agnew*, 1991]. For the period of modern instrumentation, the

earthquake record for M = 5.5 events is complete in southern California starting in 1932 [*Hileman et al.*, 1973] and starting in 1942 in northern California [*Bolt and Miller*, 1975].

4.2.1   Historical Earthquakes

From evidence gathered to date [*Jennings*, 1994; *Bakun*, 1999; *Toppozada et al.*, 2002], the San Andreas Fault System has experienced a rich seismic history over the past ~ 200 years, producing many significant earthquakes (Figure 4.1, Table 4.1). From 1812 to 1906, four major earthquakes (M > 7.0) were recorded on two main sections of the fault system. In the southern-central region of the system, a pair of major earthquakes occurred when the 1812 rupture was overlapped by the major event of 1857. Likewise, another pair of major earthquakes were recorded on the northern region of the fault system, where faulting of the Great 1906 event overlapped the rupture of the 1838 earthquake.   In addition, significant events of M ~ 7 occurred in 1868 and 1989 in the San Francisco Bay area on the Hayward fault and in the Santa Cruz Mountains near Loma Prieta, respectively, and in 1940 near the Mexican border on the Imperial fault.

While over 35 significant earthquakes (M≥ 6.0) have ruptured the San Andreas Fault System and caused significant damage over the past 200 years (Table 4.1), quiescent periods following events greater than M = 7.0 indicate that only earthquakes of this size relieve significant tectonic stress [*Toppozada et al*, 2002]. We will further address this hypothesis later in the text, but for now it is worthwhile to briefly review these major events that ruptured the San Andreas Fault System:

December 1812 – Wrightwood-Santa Barbara

The first major historical earthquake known to rupture the San Andreas Fault System took place on December 8, 1812, near the town of Wrightwood [*Toppozada et al.*, 2002], causing damage in regions such as San Juan Capistrano, San Gabriel, and San Fernando. This event was previously thought to have occurred near San Juan Capistrano [*Toppozada et al.*, 1981], although *Jacoby et al.* [1988] more recently determined that it was likely associated with a San Andreas rupture that damaged major branches and root systems of trees near Wrightwood in 1812, as inferred from tree ring data. Thirteen days later, on December 21, 1812, a second major earthquake was reported and strongly felt in the Santa Barbara region (often referred to as the Santa Barbara Earthquake) [*Toppozada et al.*, 1981]. Although neither the epicenters nor rupture extents of these two events were clearly defined, it is likely that both were centered on two approximate halves of a total rupture that extended ~170 km from Cajon Pass to Tejon Pass [*Toppozada et al.*, 2002; *Jacoby et al.*, 1988]. *Deng and Sykes* [1996] calculated the change in Coulomb stress for a northwest trending rupture on the Mojave segment of the San Andreas fault terminating near Pallet Creek and showed that a rupture on December 8th of this segment would have promoted a second rupture further to the northwest, suggested to be the December 21st event. The combination of the two 1812 events caused damage in both Orange and Santa Barbara Counties; extreme shaking forced the toppling of a church tower at the San Juan Capistrano Mission, killing 40 people [*Toppozada et al.*, 2002].

June 1838 – San Francisco-San Juan Bautista

Following the establishment in 1776 of the Mission San Francisco Dolores in San Francisco, the first major event on the northern San Andreas Fault System was observed in 1838. Extensive damage from this earthquake, unsurpassed by any other historical earthquake other than the Great 1906 quake, was noted throughout the Bay Area from San Francisco in the north to Monterey in the south [*Toppozada et al.*, 2002]. Personal accounts describe large ground cracks and broken redwood trees [*Bakun, 1999*; *Louderback*, 1947]. Faulting extent has been suggested from San Francisco to San Juan Bautista due to aftershock activity and reports of extensive damage.

Figure 4.1. Historical earthquake ruptures (M ≥ 6.0) of the San Andreas Fault System from 1800-2004 [*Jennings*, 1994; *Toppozada et al.*, 2002]. Colors depict era of earthquake activity from 1800-1850 (red), 1850-1900 (yellow), 1900-1950 (green), and 1950-2004 (blue). Calendar years corresponding to each rupture are also given and can be cross-referenced with Table 4.1. Note that we represent the two adjacent events of 1812 along the southern San Andreas as one event and that widths of highlighted fault ruptures are not proportional to earthquake magnitude. Although not directly occurring on the San Andreas Fault System, both 1992 Landers and 1999 Hector Mine events are also shown in the Eastern California Shear Zone (ECSZ). Grey octagons represent locations of paleoseismic sites used in this study. Letters a-s identify each site with the information in Table 4.2: (a) Imperial Fault, (b) Thousand Palms, (c) Burrow Flats, (d) Plunge Creek, (e) Pitman Canyon, (f) Hog Lake, (g) Wrightwood, (h) Pallet Creek, (i) Frazier Mountain, (j) Bidart Fan, (k) Las Yeguas, (l) Grizzly Flat, (m) Bolinas Lagoon, (n) Dogtown, (o) Olema, (p) Bodego Harbor, (q) Ft. Ross, (r) Point Arena, and (s) Tyson's Lagoon. Labeled fault segments referred to in the text include the Imperial, San Andreas, San Jacinto, Parkfield, Creeping section, and Hayward. Other locations that are referenced in the text include EC = El Centro, Br = Brawley, SJC = San Juan Capistrano, CP = Cajon Pass, SG = San Gabriel, SF = San Fernando, TP = Tejon Pass, V = Ventura, M = Monterey, SJB = San Juan Bautista, and Ok = Oakland.

Table 4.1. Historical earthquakes of the San Andreas Fault System (M ≥ 6.0) from 1800-2004 [*Jennings*, 1994; *Toppozada et al.*, 2002]. The following moment abbreviations are used: M_w = moment magnitude, M_a = area-determined magnitude [*Toppozada and Branum*, 2002], M_s = surface-wave magnitude [*Toppozada et al.*, 2002], and M_i = intensity magnitude [*Bakun and Wentworth*, 1997]. M_w is typically used for modern earthquake magnitudes, while M_a, M_s, and M_i are used for preinstrumentally estimated earthquake magnitudes.

Year	Event name	Magnitude
1812	Wrightwood	M_w 7.5
1838	San Francisco	M_a 7.4
1857	Fort Tejon	M_w 7.9
1858	East Bay Area	M_a 6.2
1864	East Bay Area	M_a 6.1
1864	Calaveras	M_a 6.1
1868	South Hayward	M_w 7.0
1875	Imperial Valley	M_i 6.2
1881	Parkfield	M_a 6.0
1890	S. San Jacinto	M_w 6.8
1890	Pajaro Gap	M_a 6.3
1892	S. San Jacinto	M_a 6.5
1897	Gilroy	M_a 6.3
1898	Mare Island	M_a 6.4
1898	Fort Bragg-Mendicino	M_s 6.7
1899	San Jacinto/Hemet	M_w 6.7
1901	Parkfield	M_s 6.4
1906	San Francisco	M_w 7.8
1906	Imperial Valley	M_w 6.2
1911	SE of San Jose	M_w 6.4
1918	San Jacinto	M_w 6.8
1922	Parkfield	M_w 6.3
1923	N. San Jacinto	M_w 6.2
1934	Parkfield	M_w 6.0
1940	Imperial Valley	M_w 7.0
1948	Desert Hot Springs	M_w 6.0
1954	Arroyo Salado	M_w 6.3
1966	Parkfield	M_w 6.0
1968	Borrego Mountain	M_w 6.6
1979	Imperial Valley	M_w 6.5
1984	Morgan Hill	M_w 6.2
1986	N. Palm Springs	M_w 6.0
1987	Superstition Hills	M_w 6.6
1989	Loma Prieta	M_w 6.9
1992	Landers	M_w 7.3
1999	Hector Mine	M_w 7.1
2004	Parkfield	M_w 6.0

January 1857 – The Great Fort Tejon Earthquake

The Great Fort Tejon Earthquake (M = 7.9) was the largest event ever recorded in California and one of the greatest events on record in the United States. It ruptured the southern San Andreas fault from San Bernardino County in the south to Monterey County in the north [*Wood*, 1955; *Sieh*, 1978a] and left a ~350 km long surface scar in its wake. Two foreshocks, occurring approximately 1-2 hours before the main shock, were identified by *Sieh* [1978b] just north of Parkfied. It is likely that faulting began in this region, traversed southeastward, and terminated at Cajon Pass [*Toppozada et al.*, 2002]. The southern portion of this event faulted the same portion of the San Andreas as did the 1812 earthquake sequence thirty years prior. Strong shaking caused by the 1857 earthquake lasted for at least one minute, causing severe damage as far as Ventura [*Townley,* 1939*; Agnew and Sieh*, 1978]. Fortunately, the 1857 main shock was to blame for only one death due to the lack of major structures near the ruptured fault. A few structures in downtown Los Angeles, 60 km from the fault, were reportedly cracked, while much stronger damage was sited in San Fernando, approximately 40 km from the rupture [*Agnew and Sieh*, 1978].

October 1868 – The Hayward Earthquake

The 1868 event on the south Hayward fault, a branch of the northern San Andreas Fault System, was the largest earthquake to hit the Bay Area since the 1838 San Andreas event, although seismic activity was very high during the ~10 years leading up to this event. The Hayward rupture extended ~ 50 km southward from the Oakland region [*Yu and Segall*, 1996] and caused 30 deaths [*Toppozada et al.*, 2002]. Although rupture did not actually occur on the San Andreas, much of San Francisco was damaged by this major Bay Area earthquake. Following the 1868 Hayward Earthquake, seismicity levels dropped significantly and remained low for approximately 13 years [*Toppozada et al.*, 2002].

April 1906 – The Great San Francisco Earthquake

The Great 1906 San Francisco Earthquake (M = 7.8), the largest historical earthquake of northern California, ruptured the northern San Andreas fault for over 430 km from San Juan Bautista in the south to Shelter Cove in the north. The 1906 San Andreas event re-ruptured portions of the 1838 rupture from San Juan Bautista to San Francisco. Extensive damage resulted from northern Monterey County to southern Humboldt County. Even inland regions like Napa were significantly damaged. Shaking was estimated at over one minute; the quake was felt from southern Oregon to south of Los Angeles and inland as far as central Nevada [*Ellsworth*, 1990]. Over 3000 deaths and more than 225,000 injures were attributed to the quake and the fire storm that followed due to downed power lines.

May 1940 – The Imperial Valley Earthquake

Known as the strongest recorded earthquake to hit the Imperial Valley of southern California, the 1940 earthquake ruptured over 30 km of the Imperial fault and also extended ~60 km southeast of Brawley [*Stein and Hanks*, 1998]. Severe property damage devastated the El Centro region where nine people lost their lives. Irrigation systems were extensively damaged and railroad tracks were bent out of line where they crossed the Imperial fault in three separate locations [*Ulrich,* 1941]. At least 5.8 m of right-lateral displacement were observed on the Imperial fault [*Toppozada et al.*, 2002]. This significant M7.0 southern California earthquake was felt as far away as Los Angeles and Tucson, Arizona.

The remaining historical earthquakes of the San Andreas Fault System over the past 200 years include at least thirteen earthquakes in southern California (1875, 1890, 1892, 1899, 1906, 1918, 1923, 1948, 1954, 1968, 1979, 1986, and 1987), over nine earthquakes in northern California (1858, 1864, 1890, 1897, 1898,

1911, 1984, and 1989), and the repeated sequence along the Parkfield segment in central California (1881, 1901, 1922, 1934, 1966, and 2004) [*Toppozada et al.*, 2002; *Jennings*, 1994; *Langbein*, 2004; *Murray et al.*, 2004].   Alternatively, the creeping zone of the San Andreas, bounded by the Parkfield segment to the south and the San Andreas-Calaveras split to the north, is noticeably void of large historical earthquakes; this is because tectonic plate motion is accommodated by creep instead of a locked fault at depth.   While other portions of the SAF System have been known to accommodate plate motion through creeping mechanisms [e.g., *Burgmann et al.*, 2000; *Lyons and Sandwell*, 2003], we assume that the remaining sections of the fault zone are locked at depth throughout the interseismic period of the earthquake cycle to ensure a coseismic response at known event dates.   It is also important to note that while we have cautiously adopted realistic rupture scenarios based on information available in the literature, some poorly constrained events, particularly those without a mapped surface rupture, have been approximately located.   We have chosen pre-defined fault segments that simplify the model organization without entirely compromising the locations and hypothesized rupture extents of historical earthquakes.

4.2.2 Prehistorical Earthquakes

In addition to the recorded earthquake data available, rupture history of the San Andreas Fault System from paleoseismic dating can be used to estimate prehistorical events (Table 4.2).   Paleoseismic trenching at nineteen sites (Figure 4.1) has allowed for estimates of slip history along the primary trace of the San Andreas, along the Imperial fault, along the northern San Jacinto fault, and at one site on the Hayward fault. These data contribute greatly toward understanding the temporal and spatial rupture history of the San Andreas Fault System over multiple rupture cycles, particularly during the past few thousand years where seismic events can only be assumed based on recurrence interval estimates.   For example, while the recurrence interval of the Imperial fault segment is estimated to be ~ 40 years [*WGCEP*, 1995], *Thomas and Rockwell* [1996] found that no major earthquakes prior to the 1940 and 1979 events have produced significant surface slip over the past 300 years.   *Fumal et al.* [2002] document the occurrence of at least four surface-rupturing earthquakes along the southern San Andreas strand near the Thousand Palms site during the past 1200 years.   Likewise, excavations at Burro Flats, Plunge Creek, and Pitman Canyon along the southern San Andreas strand [*Yule*, 2000; *McGill et al.*, 2002] provide age constraints for at least five prehistoric events during the past 1000 years.   Along the San Jacinto strand, *Rockwell et al.* [2003] estimate at least five paleoevents at Hog Lake over the past 1000 years.   *Fumal et al.* [2002], *Biasi et al.* [2002], and *Lindevall et al.* [2002] report evidence for 5-6 surface-rupturing events in total at the Wrightwood, Pallet Creek, and Frazier Mountain trench sites along the Big Bend of the San Andreas.   Further to the north, trenching at Bidart Fan [*Grant and Sieh*, 1994] reveal three prehistoric events, while at Las Yeguas, *Young et al.* [2002] estimate at least one event between Cholame Valley and the Carrizo Plain.   In northern California, *Knudsen et al.* [2002] interpret several episodes of sea level change (earthquake-induced subsidence) along the northern section of the San Andreas at Bolinas Lagoon and Bodego Harbor and compare evidence for two 1906-like ruptures from work done by *Cotton et al.* [1982], *Schwartz et al.* [1998], *Heingartner* [1998], *Prentice* [1989], *Niemi and Hall* [1992], *Niemi* [1992], *Noller* [1993], *Baldwin* [1996], and *Simpson et al.* [1998].   And lastly, excavations of the southern Hayward fault at Tyson's Lagoon [*Lienkaemper et al.*, 2002] reveal evidence for at least three paleoseismic events over the past millennium.   While uncertainty ranges for paleoseismic dating can be fairly large, we do our best to adhere to the results of experts in the field and estimate prehistorical earthquake dates, locations, and rupture extents based on their findings.   These earthquakes, in addition to the known historical ruptures discussed above, will be used in the subsequent 3-D viscoelastic model of San Andreas Fault System deformation of the past 1000 years.

Table 4.2. Prehistorical San Andreas Fault System earthquakes from 1000 A.D. based on paleoseismic trench excavations. Letters in the first column correspond to paleoseismic locations plotted in Figure 4.1. Trench site name, referenced authors, and calendar year event dates are also listed.

	Trench Site	Reference	Dates (A.D)
a	Imperial Fault	*Thomas and Rockwell, 1996; Sharp, 1981*	< 1700; 1670
b	Thousand Palms	*Fumal et al., 2002*	> 1520-1680; 1450-1555; 1170-1290; 840-1150
c	Burrow Flats	*Yule, 2000*	1450-1600; 1120-1350; 780-1130
d	Plunge Creek	*McGill et al., 2002*	1690; 1630; 1450
e	Pitman Canyon	*McGill et al., 2002*	~1450
f	Hog Lake	*Rockwell et al., 2003*	1020; 1230; 1290; 1360; 1630; 1760
g	Wrightwood	*Fumal et al., 2002; Biasi et al., 2002*	1647-1717; 1508-1569; 1448-1578; 1191-1305; 1047-1181
h	Pallet Creek	*Biasi et al., 2002*	1496-1599; 1343-1370; 1046-1113; 1031-1096
i	Frazier Mountain	*Lindevall et al., 2002*	1460-1600
j	Bidart Fan	*Grant and Sieh, 1994*	1405-1510; 1277-1510; 1218-1276
k	Las Yeguas (LY4)	*Young et al., 2002*	1030-1460
l	Grizzly Flat	*Schwartz, et al., 1998; Heingartner, 1998*	1020-1610; 1430-1670
m	Bolinas Lagoon	*Knudsen et al., 2002*	1050-1450
n	Dogtown	*Cotton et al., 1982*	1100-1330; 1520-1690
o	Olema	*Niemi and Hall, 1992; Niemi, 1992*	1300-1660; 1560-1660
p	Bodego Harbor	*Knudsen et al., 2002*	900-1390; 1470-1850
q	Ft. Ross	*Noller, 1993; Simpson et al., 1996*	560-950; 920-1290; 1170-1650
r	Point Arena	*Prentice, 1989; Baldwin, 1996*	680-1640; 1040-1640
s	Tyson's Lagoon	*Lienkamper et al., 2002*	1650-1790; 1530-1740; 1360-1580

4.3. 3-D Viscoelastic Model

For purposes of investigating the viscoelastic response over multiple earthquake cycles, we apply a semi-analytic Fourier model (Appendix 4.A) to the geometrically complex fault setting of the SAF System. The model consists of an elastic plate (of thickness H) overlying a viscoelastic half-space. Faults within the elastic plate extend from the surface to a prescribed locking depth (d). Below the locked faults, fully-relaxed secular slip (assuming infinite time) takes place down to the base of the elastic plate. The model is kinematic, given that the time, extent, and amount of slip is prescribed. Coseismic slip occurs on prescribed fault segments and the amount of slip is based on slip deficit assumptions. Transient deformation follows each earthquake as slip in the elastic layer stimulates viscoelastic flow in the underlying half-space.   The duration of the viscoelastic response, characterized by the Maxwell time, depends on the viscosity of the underlying half-space and the elastic plate thickness.

The complete earthquake cycle is modeled with two components: secular and episodic. The secular model simulates interseismic slip that occurs between the fault locking depth and the base of the elastic plate (d to H, see Figure 3.1, Chapter 3).   We construct this model in two parts. First, we permit fully-relaxed slip over the entire length of the elastic plate (0 to H) – the geologic, or block, model. Second, secular backslip within the locked fault region (0 to d) compensates for shallow slip deficit – the backslip model. The episodic model (or earthquake-generating model) prescribes spatially uniform slip over the locked section of each fault segment, eventually canceling out the secular backslip component discussed above. Fault slip rate, historical/pre-historical earthquake sequence, and recurrence intervals are used to establish the magnitude of coseismic slip events. Slip amounts are determined by multiplying the slip rate of each ruptured fault segment by (1) the time spanning the previous event, if one exists or (2) the recurrence interval time if no previous event exists.

The numerical aspects of this approach involve generating a grid of vector force couples that simulate complex fault geometry, taking the 2-D horizontal Fourier transform of the grid, multiplying by the appropriate transfer functions and time-dependent relaxation coefficients, and finally inverse Fourier transforming to obtain the desired results [*Smith and Sandwell*, 2004]. The solution satisfies the zero-traction surface boundary condition and maintains stress and displacement continuity across the base of the plate (Appendix 4.A). A far-field velocity step across the plate boundary of 40 mm/yr is simulated using a cosine transform in the *x*-direction (i.e., across the plate boundary). The far-field boundary condition at the top and bottom of the grid is simulated by arranging the fault trace to be cyclic in the *y*-direction (i.e., parallel to the plate boundary). We solve for four variable model parameters: elastic plate thickness (H), half-space viscosity (η), geologic Poisson's ratio (v_g), and locking depth factor (f_d). We assume fixed values for the shear modulus $\mu = 28$ GPA, Young's modulus $E = 70$ GPA, Poisson's ratio (episodic model) $v = 0.25$, density $\rho = 3300$ kg/m^3, and gravitational acceleration $g = 9.81$ m/s^2. The entire computational process for a single time-step requires ~ 40s for a grid size of 2048 x 2048 elements, the size used for this analysis. This complete fault model will be used to efficiently explore the 3-D viscoelastic response of the upper mantle throughout the 1000-year earthquake cycle.

4.4.   Application to the San Andreas Fault System

We apply the 3-D viscoelastic model described above to study deformation and stress associated with fault segments of the San Andreas Fault System. We adopt a fault segmentation scheme of a previous elastic half-space analysis [*Smith and Sandwell*, 2003], obtained from digitizing the major fault strands along the SAF System from the *Jennings* [1994] fault map. Some modifications have been made to the fault segmentation design of *Smith and Sandwell* [2003] in order to better accommodate along-strike variations in

fault-segmented ruptures. We group the San Andreas Fault System into 27 main fault segments, comprised of over 400 elements, spatially consistent with previous geologic and geodetic studies. The fault system is rotated about its pole of deformation (52°N, 287°W) [*Wdowinski et al.*, 2001] into a new co-ordinate system, after which fault segments are embedded in a grid of 2048 elements along the SAF System (*y*-direction) and 1024 elements across the system (*x*-direction) with a grid spacing of 1 km. The large grid width of 1024 km is needed to accurately model the flexural wavelength of the elastic plate. The fault model includes the following primary segments (Figure 4.2, Table 4.3): Imperial, Brawley, Coachella-San Andreas, Palm Springs-San Andreas, San Bernardino Mountains-San Andreas, Superstition, Borrego-San Jacinto, Coyote Creek-San Jacinto, Anza-San Jacinto, San Jacinto Valley, San Jacinto Mountains, Mojave, Carrizo, Cholame, Parkfield Transition, San Andreas Creeping, Santa Cruz Mountains-San Andreas, San Francisco Peninsula-San Andreas, North Coast-San Andreas, South-Central Calaveras, North Calaveras, Concord, Green Valley-Bartlett Springs, South Hayward, North Hayward, Rodgers Creek, and Maacama. We assume that slip rate, locking depth, and recurrence interval remain constant along each fault segment (Table 4.3) and that the system is loaded by stresses extending far from the locked portion of the fault. Each fault segment is assigned a deep slip rate based on geodetic measurements, geologic offsets, and plate reconstructions [*WGCEP*, 1995, 1999]. In some cases, slip rates were adjusted (+/- 5 mm/yr on average) in order to satisfy an assumed far-field plate velocity of 40 mm/yr. We adopt locking depths from a previous inversion of the Southern California Earthquake Center (SCEC) Crustal Motion Map (version 3; *Shen et al.* [2003]) using a complimentary elastic half-space model [*Smith and Sandwell*, 2003]. Because these depths are based on purely elastic assumptions, we allow the entire set of locking depths to be adjusted in our parameter search through a locking depth factor. Due to the large uncertainty in locking depth for the Superstition segment reported by *Smith and Sandwell* [2003], we arbitrarily set this locking depth to 7 km. Likewise, we adjusted the locking depth of the South-Central Calaveras segment to 7 km to allow for episodic coseismic events. Recurrence intervals for each segment were adopted from various sources [*WGCEP*, 1995, 1999; *WGNCEP*, 1996] and estimate the time span between characteristic earthquakes on each fault segment where no prehistorical data are presently available.

In addition to the above faulting parameters, we also define the temporal sequence and rupture length of past earthquakes (M $\geq$ 6.0) based on the earthquake data history discussed in Section 4.2. We estimate calendar year rupture dates and surface ruptures on fault segments as identified by Table 4.3. For years 1812-2004, fault segments rupture coseismically according to their historical earthquake sequence. For years prior to 1812, we estimate prehistorical ruptures by calculating the average date from the paleoseismological evidence summarized in Table 4.2 and extrapolating rupture lengths to our defined fault segments based on discussions provided by the relevant references. It should also be noted that we include the recent coseismic/postseismic response of both the 1992 M_w = 7.3 Landers Earthquake and the 1999 M_w = 7.1 Hector Mine Earthquake (Figure 4.1, Table 4.1), both occurring west of the SAF System in the Eastern California Shear Zone (ECSZ). These two earthquakes have been studied in detail [e.g., *Savage and Svarc*, 1997; *USGS et al.,* 2000*; Sandwell et al.,* 2002*; Fialko et al.,* 2001; *Fialko*, 2004b] and well-constrained surface slip models and seismic moment estimates are available. To simplify the model, we specify slip on both Landers and Hector Mine fault planes by assuming that slip is constant with depth and solving for a slip depth that preserves seismic moment. For the Landers Earthquake, we use a seismic moment of 1.1×10^{20} Nm [*Fialk*o, 2004b] and adopt a fault locking depth of 16 km. For the Hector Mine Earthquake, we use a seismic moment of 5×10^{19} Nm [*Fialko et al.*, 2001] and adopt a fault locking depth of 12 km.
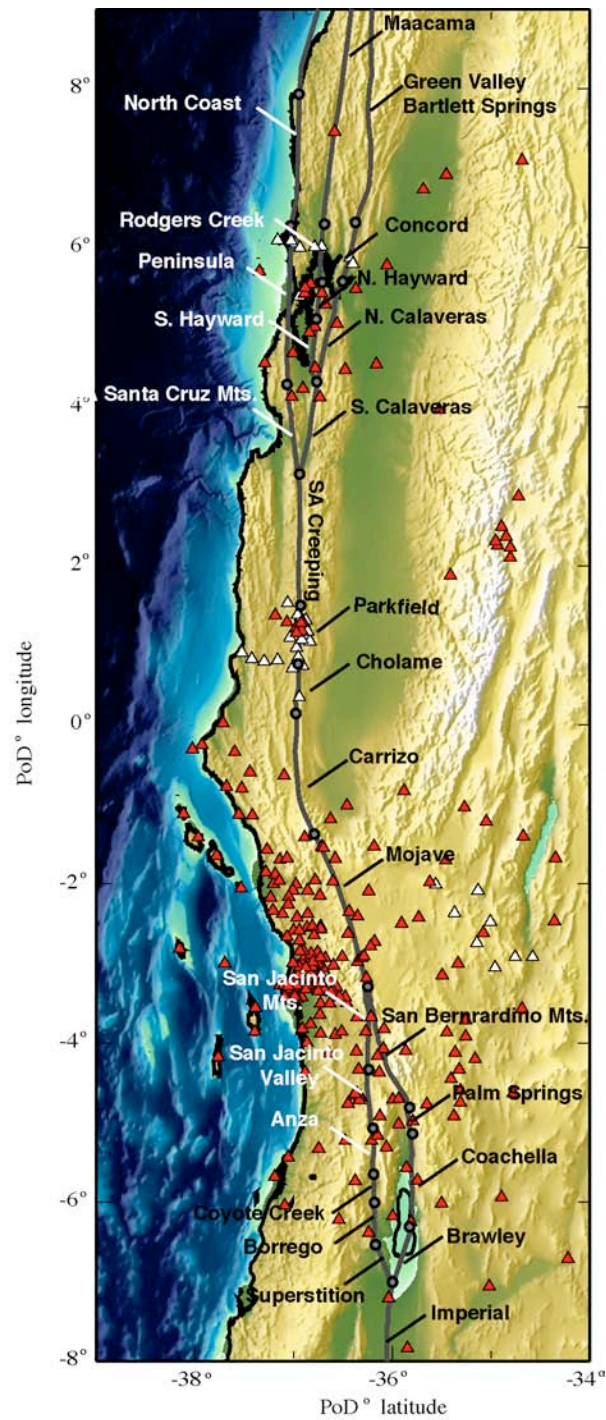
Figure 4.2. San Andreas Fault System segment locations in the pole of deformation (PoD) coordinate system [*Wdowinski et al.*, 2001 (52º N, 287º W)]. Fault segments coinciding with Table 4.3 are labeled and separated by grey circles. SOPAC station locations (red triangles) and USGS station locations (white triangles) used in this analysis are also shown.

Table 4.3. San Andreas Fault System parameters. Slip rates are based on geodetic measurements, geologic offsets, and plate reconstructions [*WGCEP*, 1995, 1999] and satisfy an assumed far-field plate velocity of 40 mm/yr. Locking depths are based on the previous results of *Smith and Sandwell* [2003], although slight modifications have been made to the Superstition and South-Central segments (see text). Recurrence intervals (τ_r) for each segment were adopted from various sources [*WGCEP*, 1995, 1999; *WGNCEP*, 1996]. Calendar year rupture dates on fault segments, determined by historical events (Table 4.1) and prehistorical events (Table 4.2) are also included. SA = San Andreas segments, SJ = San Jacinto segments.

Segment Name	Slip (mm/yr)	Locking depth (km)	τ_r (yrs)	Historical Earthquakes (calendar year)	Prehistorical Earthquakes (calendar year)
Imperial	40	6	40	1875, 1906, 1940, 1979	1680
Brawley	36	6	48		
Coachella (SA)	28	23	160		1350, 1690
Palm Springs (SA)	28	23	160	1948, 1986	1110, 1502, 1690
San Bernardino Mountains (SA)	28	23	146		1450, 1630, 1690
Superstition (SJ)	4	7	250	1987	
Borrego (SJ)	12	13	175	1892, 1968	
Coyote Creek (SJ)	12	13	175	1890, 1954	
Anza (SJ)	12	13	250		1020, 1230, 1290, 1360, 1630, 1760
San Jacinto Valley (SJ)	12	13	83	1899, 1918	
San Jacinto Mountains (SJ)	12	13	100	1923	
Mojave	40	26	150	1812, 1857	1016, 1116, 1263, 1360, 1549, 1685
Carrizo	40	25	206	1857	1247, 1393, 1457
Cholame	40	13	140	1857	1195
Parkfield Transition	40	15	25	1881, 1901, 1922, 1934, 1966, 2004	
San Andreas Creeping	40	0	n/a		
Santa Cruz Mountains (SA)	21	9	400	1838, 1890, 1906, 1989	1300, 1600
San Francisco Peninsula (SA)	21	9	400	1838, 1906	1300, 1600
San Andreas North Coast (SA)	25	19	760	1906	1300, 1600
South-Central Calaveras	19	7	60	1897, 1911, 1984	
North Calaveras	7	14	700	1858, 1864	
Concord	7	14	700		
Green Valley-Bartlett Springs	5	9	230		
South Hayward	12	16	525	1868	1470, 1630, 1730
North Hayward	12	16	525		1708
Rodgers Creek	12	19	286	1898	
Maacama	10	12	220		

4.5. Geodetic Data

Continuously operating GPS networks offer a way to track ground motions over extended periods of time [*Bock et al.*, 1997; *Nikolaidis*, 2002]. While horizontal GPS velocity estimates over the past three decades have commonly been used to constrain fault models, estimates of vertical velocity typically accompanied low signal to noise ratios, and hence large observational uncertainties, and were typically disregarded. However, these measurements may play an important role in refining our understanding of the rheological structure of the Earth's crust and underlying mantle [*Deng et al.*, 1998; *Pollitz et al.*, 2001]. Consequently, we use both horizontal and vertical velocity estimates from the Scripps Orbit and Permanent Array Center (SOPAC) from 315 stations within our region of study, operating for ~10 years. The SOPAC Refined Velocity data set contains estimated velocities through 2004 using a model that takes into account linear velocity, co-seismic offsets, postseismic exponential decay, and annual/semi-annual fluctuations [*Nikolaidis*, 2002]. To increase data coverage in northern California and in the Parkfield region, we acquired five additional data subsets (containing a total of 120 stations) from the US Geologic Survey (USGS) (both automatic and network (Quasi-Observational Combined Analysis [*Dong et al.*, 1998]) processing schemes). While data from eight campaigns were initially explored, only five of these (FtIrwin, MedicineLake, NorthSanFranciscoBay, SFBayArea, and Parkfield) were utilized in the final analysis due to reasons discussed below. While not entirely continuous (some data were gathered campaign-mode), most of the USGS data were collected from stations in operation for ~ 4 - 7 years.

The data were first refined by excluding all stations with velocity uncertainties (either horizontal or vertical) greater than 3 mm/yr. All remaining stations were subjected to an initial round of modeling, where outliers were removed that were both anomalous compared to their neighbors and had velocity model misfits greater than 10 mm/yr. Furthermore, preliminary least squares analyses revealed that velocities with small uncertainty estimates (< 0.5 mm/yr) dominated most of the weighted RMS model misfit and thus were adjusted to comply with a prescribed lower bound of 0.5 mm/yr. The remaining 292 stations with velocities satisfying these constraints form our total GPS velocity data set (Figure 4.2) and combine to form a total of 876 horizontal and vertical velocity measurements spanning much of the San Andreas Fault System. While the spatial distribution is not as complete as the SCEC Crustal Motion Map [*Shen et al.*, 2003] distribution, preliminary tests showed that vertical velocity information, not currently available from SCEC, provide an important constraint of the viscoelastic properties of the model.

4.6. Results

A least squares parameter search was used to identify optimal parameters for elastic plate thickness (H), half-space viscosity (η), geologic Poisson's ratio (v_g), and locking depth factor (f_d). Plate thickness affects the amplitude and wavelength of deformation and also plays a role in the timescale of observed deformation, particularly in the vertical dimension [*Smith and Sandwell*, 2004]. Thick elastic plate models yield larger-wavelength postseismic features but shorten the duration of the vertical response compared to thin plate models. Half-space viscosity determines how quickly the model responds to a redistribution of stress from coseismic slip. High viscosities correspond to a large response time while low viscosities give rise to more rapid deformation. Variations in Poisson's ratio ($v = 0.25 - 0.45$) determine the compressibility of the elastic material over varying timescales. Over geologic time, tectonic strains are large and thus elastic plates may behave like an incompressible fluid ($v \sim 0.5$). Alternatively, over short timescales, strains are smaller and plates may behave more like an elastic solid ($v = 0.25$). We adjust Poisson's ratio of the geologic model component only (v_g, observed at infinite time), requiring the episodic model to behave as an elastic solid. Lastly, we allow the entire set of locking depths to vary simultaneously using a single factor f_d to scale the

purely elastic estimates from *Smith and Sandwell* [2003]. This scaling depends largely upon the thickness of the elastic plate [*Thatcher*, 1983] and the viscosity of the half-space.

4.6.1 Present-day Velocity

Our best model is found by exploring the parameter space and minimizing the weighted residual misfit, χ^2, of the geodetic data set and the present day (calendar year 2004) modeled velocity field. The data misfit is defined by

$$V_{res}^i = \frac{V_{gps}^i - V_m^i}{\sigma^i} \quad \text{and} \quad \chi^2 = \frac{1}{N}\sum_{i=1}^{N}\left(V_{res}^i\right)^2,$$

where V_{gps} is the geodetic velocity estimate, V_m is the model estimate, σ^i is the uncertainty of the ith geodetic velocity, and N is the number of geodetic observations. The parameter search is executed in two phases and involves fourteen free parameters. First, two unknown horizontal velocity components for each of the five GPS networks are estimated by removing the mean misfit from a starting model. This exercise linearly shifts all horizontal data into a common reference frame. Second, we fix the ten velocity components and perform a 4-dimensional parameter search for elastic plate thickness, half-space viscosity, geologic Poisson's ratio, locking depth factor.

Before modeling, we calculate an unweighted RMS of 7.8439 mm/yr and a weighted RMS of 14.37 (dimensionless) for the 876 GPS velocities. We begin with a starting model that has $H = 50$ km, $\eta = 1\mathrm{x}10^{19}$ Pa s, $v_g = 0.25$, and $f_d = 1$. After adjusting the ten unknown velocity components for the starting model, a 4-dimensional parameter search is performed to locate the best-fitting model. Using over 140 trial models, the best model is identified, resulting in a weighted RMS residual of 4.5034 (2.4599 mm/yr unweighted), thus reducing the total variance of the data by over 90%. Individually, the x, y, and z velocity misfits vary considerably, producing weighted and unweighted RMS residuals of 4.29 (2.19 mm/yr), 5.20 (2.72 mm/yr), and 3.95 (2.45 mm/yr), respectively.

Optimal parameters for this model are $H = 70$ km, $\eta = 3\mathrm{x}10^{18}$ Pa s, $v_g = 0.40$, and $f_d = 0.70$, although a large span of parameters fit the model nearly as well (Figure 4.3). From these results, we place both upper and lower bounds on model parameters for a range of acceptable models. The weighted RMS residual is minimized for a plate thickness of 70 km, although the misfit curve of Figure 4.3a significantly flattens for $\sim H > 60$ km. Lower and upper bounds for half-space viscosity (Figure 4.3b) are $1\mathrm{x}10^{18}$ and $5\mathrm{x}10^{19}$ Pa s. The best-fitting geologic Poisson's ratio (Figure 4.3c) is 0.40, although models with $f_d = 0.35 - 0.45$ also fit well. And finally, the best-fit locking depth factor (Figure 4.3d) is 0.70, although models with $f_d = 0.65 - 0.80$ are also acceptable.

Comparisons between the model fault-parallel velocity and the GPS data for eight fault corridors are shown in Figure 4.4. Each model profile is acquired along a single fault-perpendicular trace, while the geodetic measurements are binned within the fault corridors and projected onto the perpendicular trace, thus some of the scatter is due to projection of the data onto a common profile. While the model accounts for most of the observed geodetic deformation, there are some local systematic residuals that require deformation not included in our model. For example, GPS velocities in the Eastern California Shear Zone are underestimated (Figure 4.4, Profiles 2-5), as we do not incorporate faults in the Owens Valley, Panamint Valley, and Death Valley fault zones. [e.g., *Bennett et al.*, 1997; *Hearn et al.*, 1998, *Dixon et al.*, 2000; *Gan et. al.*, 2000; *McClusky et al.*, 2001; *Miller et al.*, 2001; *Peltzer et al.*, 2001; *Dixon et al.*, 2003]. Observed
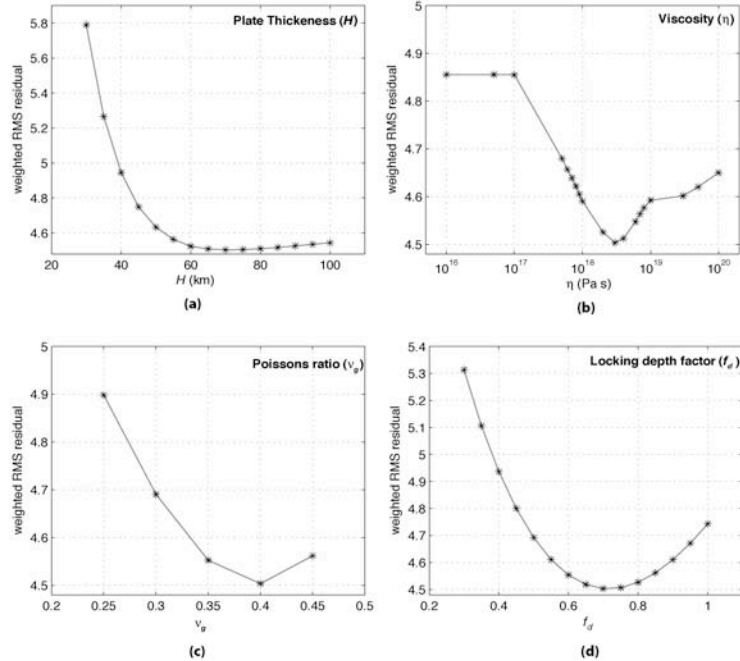
Figure 4.3. 1000-year viscoelastic model parameter search results for elastic plate thickness (H), half-space viscosity (η), geologic Poisson's ratio (v_g), and locking depth factor (f_d). The best fitting model (unweighted RMS residual = 2.46 mm/yr, weighted RMS residual = 4.03) requires (a) H = 70 km, (b) η = 3x10^{18} Pa s, (c) v_g = 0.4, and (d) f_d = 0.70. Weighted RMS residuals for 50 example models are also plotted. Note that best-fit parameters are held constant in each figure for display purposes, although an actual 4-D parameter search used to derive the best fitting model.

differences in the model are also due to approximations in the earthquake record, including the timing of prehistorical earthquakes, the rupture extent of both pre- and historical earthquakes, and our assumption of complete seismic moment release.

Results for the fault-perpendicular velocity model are shown in Figure 4.5a. The fault-perpendicular model has a pronounced west-trending (negative) zone of deformation (~ -2.5 mm/yr) to the west of the Mojave and Carrizo segment, while a complimentary diffuse east-trending (positive) region (~ 1.5 mm/yr) is observed to the northeast. An interesting butterfly-like feature is also noted along the creeping segment, just north of Parkfield. This feature is due the abrupt change in locking depth from the north (0 km) to the south (10.2 km). An unusual zone of deformation to the north of Parkfield has also been noted by other workers [*S. Wdowinski*, personal communication].

In addition, vertical deformation (Figure 4.5b) is in general agreement with geodetic measurements and reveals similar features to our previous elastic half-space model [*Smith and Sandwell*, 2003]. Uplift in the regions of the San Bernardino Mountains and Mojave segments is due to the associated compressional bends [*Williams and Richards*, 1991], while subsidence is observed in extensional regimes such as the Brawley segment (Salton Trough). The large lobate regions, such as the pair noted to the east and west of the Parkfield segment, are attributed to the combined effects of the creeping section and the long-standing strain accumulation along the 1857 Fort Tejon rupture. A future event similar to the 1857 rupture would significantly reduce the magnitude of these lobate features.

A time series of models spanning several earthquake cycles (Movie 4.1) shows that the vertical deformation pattern accumulates displacement during the interseismic period that is fully relaxed during the postseismic phase, such that long-term vertical deformation from repeated earthquake cycles is zero. Both
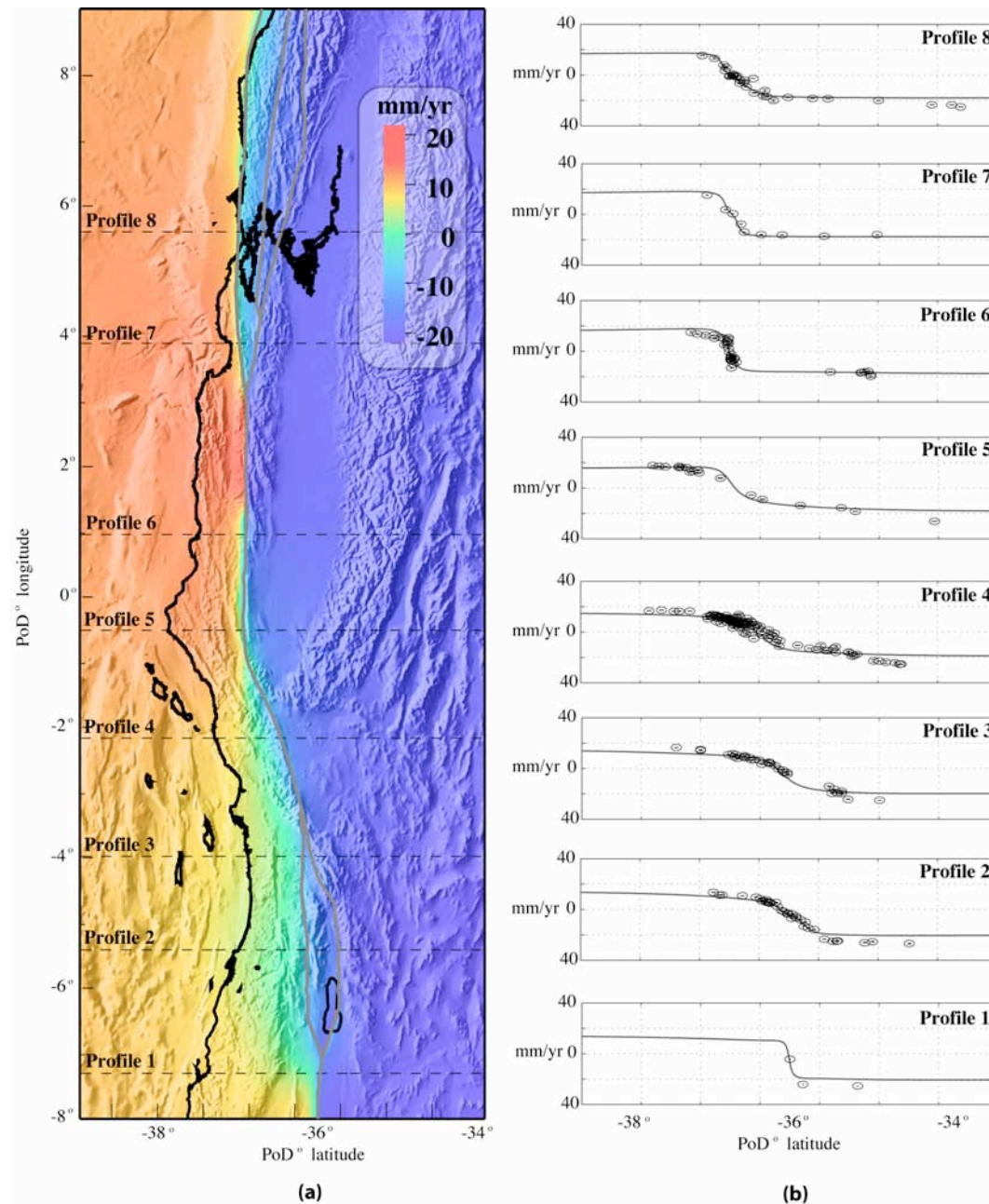
Figure 4.4. (a) Fault-parallel (or *y*-component) velocity map of best fitting model. Velocities are plotted in mm/yr and span +20 mm on the west side of the SAF System and –20 mm on the east side of the SAF System. Dashed lines represent horizontal model profiles of Figure 4.4b. (b) Modeled velocity profiles acquired across the fault-parallel velocity map with GPS velocities and uncertainties projected onto each profile for visual comparison. GPS stations located within the half-way mark between each mapped profile line of (a) are displayed in each profile section of (b). Note that the RMS differences between model and date were evaluated at actual GPS locations.
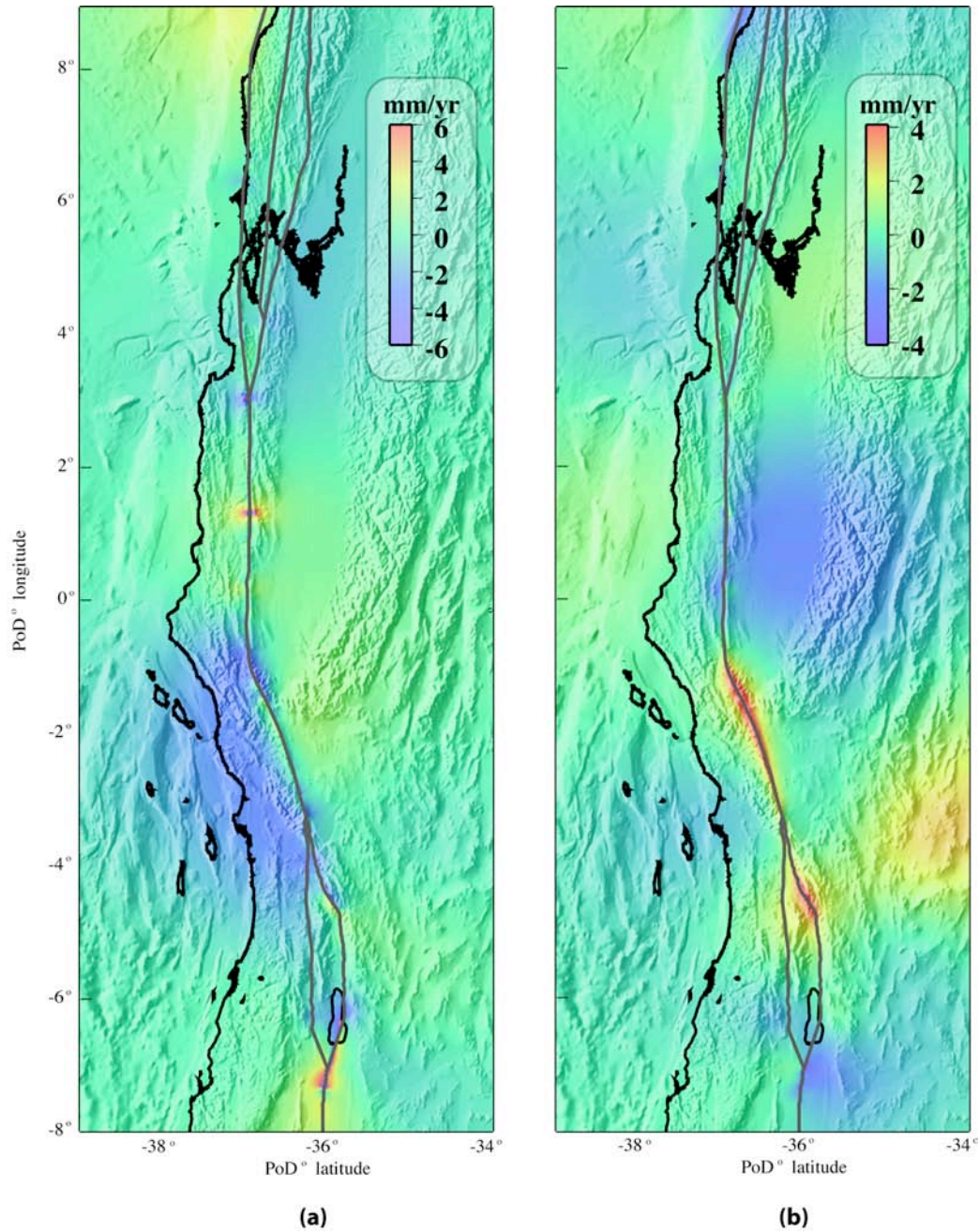
Figure 4.5. (a) Fault-perpendicular (or *x*-component) velocity map of best fitting model. Velocities are plotted in mm/yr and span +/- 6 mm/yr. Negative velocities correspond to displacement changes in the westward direction, while positive velocities correspond to displacement changes in the eastward direction. (b) Vertical (or *z*-component) velocity map of best fitting model. Velocities are plotted in mm/yr and span +/- 4 mm/yr. Negative velocities indicate subsidence, while positive velocities indicate uplift.

horizontal velocity components maintain secular deformation features throughout the earthquake cycle, except of course when an earthquake is prescribed and an appropriate coseismic response is observed. Large horizontal transients, lasting ~ 5-20 years, depending on the event, are only observed after the largest of earthquakes (e.g., 1857, 1906, 1940).

4.6.2 Present-day Coulomb Stress

Deep, secular slip along the San Andreas Fault System induces stress accumulation in the upper locked portions of the fault network. Because our model assumes complete slip release during each earthquake, the stress essentially drops to zero with the exception of postseismic transients. We use our semi-analytic model and the parameters described in Section 4.6.1 to calculate stress due to interseismic, coseismic, and postseismic phases of the earthquake cycle. The model (Appendix 4.A) provides the three-dimensional vector displacement field from which we compute the stress tensor. The stress tensor is computed along each fault segment and is resolved into shear stress, τ, and normal stress, σ_n, on the nearby fault segment to form the Coulomb failure function, σ_f

$$\sigma_f = \tau - \mu_f \sigma_n,$$

where μ_f is the effective coefficient of friction [*King et al.*, 1994; *Simpson and Reasenberg*, 1994]. Right-lateral shear stress and extension are positive and we assume $\mu_f = 0.6$. The calculations do not include the stress accumulation due to compression or extension beneath the locked portions of each fault segment. Because Coulomb stress is zero at the surface and becomes singular at the locking depth, we calculate the representative Coulomb stress at 1/2 of the local locking depth [*King et al.*, 1994]. This calculation is performed on a fault-segment by fault-segment basis for the San Andreas Fault System from earthquakes over the past 1000 years (Figure 4.6).

The present-day (calendar year 2004) model predicts quasi-static Coulomb stress along most fault segments ranging from 1-7 MPa (Figure 4.6c). Typical stress drops during major earthquakes are ~ 5 MPa and so the model provides compatible results to seismological constraints. Regions of reduced stress include the Parkfield, Superstition, Borrego, Santa Cruz Mountains, and South Calaveras segments where there has either been a recent (~ last 20 years) earthquake or Coulomb stress accumulation rate is low due to fault geometry and locking depth [*Smith and Sandwell*, 2003]. Alternatively, high stress regions include most of the southern San Andreas from the Cholame segment to the Coachella segment, the northern portion of the San Jacinto fault, and along the eastern Bay Area, where major earthquakes are possible. It should also be noted, although not evident in the present-day model capture (except in the Parkfield vicinity), that the model demonstrates a small, negative stress behavior due to time-dependent postseismic readjustment, commonly referred to as the stress shadow [*Harris*, 1998; *Kenner and Segall*, 1999]. Animated stress evolution (Movie 4.2) for years 1800-2004 shows the spatial decay and magnitude of stress shadows following earthquake events, particularly evident in major events such as the 1857 Fort Tejon and 1906 San Francisco earthquakes [*Harris and Simpson*, 1993, 1996, 1998; *Kenner and Segall*, 1999; *Parsons*, 2002]. These animations show how locked fault segments eventually become re-loaded with tectonic stress as relaxation ceases, resulting in positive stress accumulation surrounding the fault and a resumption of the earthquake cycle.
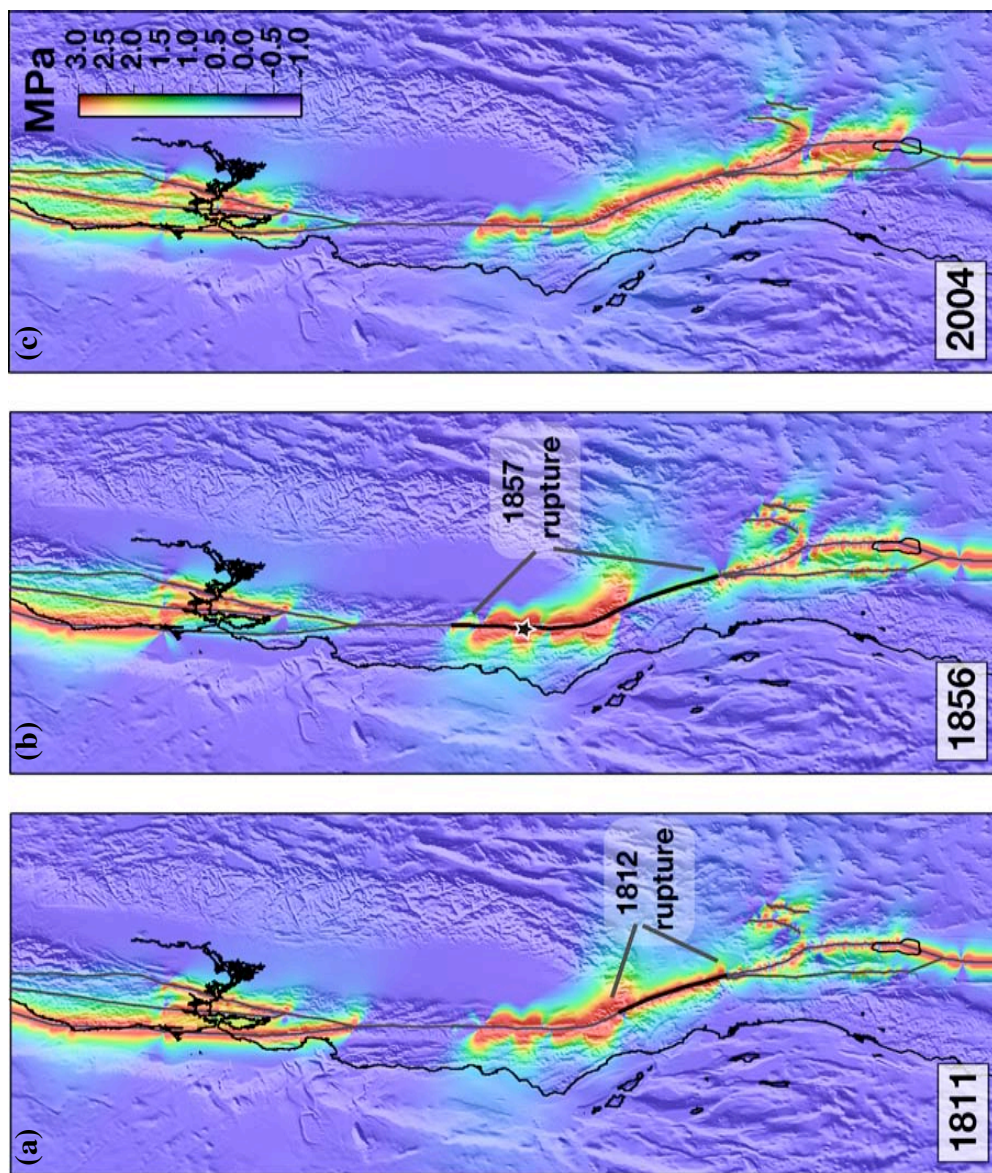
Figure 4.6. Coulomb stress in MPa for the SAF System for three model snapshots in time. (a) Coulomb stress for the 1811 calendar year model, representing the stress field prior to the 1812 M~7 Wrightwood Earthquakes (fault rupture estimated by black solid line). (b) Coulomb stress for the 1856 calendar year model, representing the stress field prior to the M7.9 1857 Great Fort Tejon Earthquake (epicenter represented by black star, fault rupture estimate by black solid line). (c) Coulomb stress for the 2004 calendar year model, representing stress of present day. Color scales range from −0.01 MPa, depicting stress shadow regions, to a saturated value of 3 MPa, depicting regions of accumulated stress.

4.7 Discussion

4.7.1 Implications of Best-Fit Model Parameters

Our best-fitting model (Figure 4.3) has a relatively thick elastic plate (70 km) with a moderate half-space viscosity ($3x10^{18}$ Pa s), in contrast to some previous studies. *Li and Rice* [1987] reported viscosity values of $2x10^{19}$ to $1x10^{20}$ Pa s from geodetic strain data on the San Andreas fault, assuming a lithospheric thickness of about 20-30 km. Alternatively, *Pollitz et al.* [2001] use a plate thickness of 30 km and an upper layer viscosity of $4x10^{17}$ Pa s to model deformation due to the 1999 Hector Mine earthquake in the Mojave desert. More recently, *Johnson and Segall* [2004] estimated an elastic thickness of 44 -100 km and a viscosity of $1x10^{19}$ – $2.9x10^{20}$ Pa s. While our estimate of plate thickness is in agreement with *Johnson and Segall* [2004], we suggest a lower bound plate thickness of ~60 km and stress the need for future far-field data to place better constraints on this parameter. Because our model represents both the lower crust and upper mantle as a single element, the half-space viscosity that we solve for reflects an average of the two values. A viscosity of $3x10^{18}$ Pa s, corresponding to a relaxation time of ~ 7 years, is likely a lower bound. In comparison, investigations of post-glacial rebound infer whole-mantle viscosities on the order of 10^{22} Pa s. Rebound estimates such as these tend to be uniformly higher than those determined from seismic studies, perhaps because the larger-scale rebound pattern samples far deeper into the mantle than the more localized fault deformation pattern. It may also be true that seismically-determined viscosities include a larger transient effect, although these hypotheses are nearly impossible to test without additional, long-term geodetic observations.

A model of finite plate thickness, as opposed to one representing an infinite elastic medium, broadens the observed model velocity step and requires a reduced locking depth to match the GPS data. We find that locking depths for a 70 km thick elastic plate are about 30% less than those needed for an elastic half-space model [*Smith and Sandwell*, 2003]. An important aspect of the plate model is that far-field deformation is partitioned into separate secular and post-seismic parts according to the ratio of the elastic plate thickness and the fault segment locking depth [*Savage and Prescott*, 1978; *Ward*, 1985; *Smith and Sandwell*, 2004]. Immediately following an earthquake, the step in velocity across the fault will match the full geological velocity prescribed on the fault in accordance with an elastic half-space model. After several Maxwell times, the step will broaden and be reduced in amplitude. For example, the Mojave region has a locking depth of ~20 km, which is roughly 30% of the elastic plate thickness. Therefore, only 70% of the far-field deformation is accommodated by the secular model. The remaining 30% of the far-field deformation results from repeated earthquakes. Elastic half-space block models do not contain this important physics and therefore estimated locking depths will be systematically too large and estimated slip rates will be systematically too low.

The model uses two Poisson's ratios depending on the timescale of the deformation process. The cyclical earthquake process (interseismic backslip and coseismic forward slip) is modeled using a standard Poisson's ratio for an elastic solid ($v = 0.25$). However, for geologic timescales ($t = \infty$), we allow the model to accommodate changes in Poisson's ratio (v_g), assuming that plates accumulate large tectonic strains over geologic timescales, which in turn alter the compressibility of the material. We began the modeling process using a Poisson's ratio of 0.25 for both timescales but found that the vertical deformation associated with the geologic portion of the model displayed unreasonable features in zones of known compression and extension. When Poisson's ratio was increased to ~0.45 for the geologic model, the vertical deformation became sensible for compressional and extensional features, regardless of elastic plate thickness. Since this parameter has an important effect on the vertical component of the model, we included it as a free parameter. Our parameter search identified an optimal Poisson's ratio of $v_g = 0.40$ for the geologic model, producing

realistic secular vertical features and indicating a preference for a more incompressible elastic plate over geologic timescales.

4.7.2 Temporal and Spatial Deficiencies of GPS Data

While we have identified a set of model parameters that minimize the residual data misfit, the available geodetic data do not *distinctly* prefer one set of model parameters over a variety of alternative ones. It is possible that additional data, particularly in areas of sparse coverage, would provide tighter bounds on rheological parameters. Data in northern California, for example, in comparison to those available in southern California, are sparse and thus provide weaker constraints on the model parameters for the northern California region. This is unfortunate, as many earthquakes have occurred along the northern portion of the SAF System and may contribute significantly to the overall deformation field. Furthermore, far-field data are lacking for the entire plate boundary. While the near-field horizontal GPS data provide tight constraints on slip rate and locking depth, the far-field vertical GPS data constrain the elastic plate thickness. The important length scale is the flexural wavelength and for a 70-km thick plate the wavelength is about 400-500 km, thus vertical GPS measurements acquired ~200 km from the fault zone provide critical information.

In an attempt to understand how results differ for horizontal and vertical geodetic velocity observations, preliminary analyses using the SCEC Crustal Motion Map 3.0 [*Shen et al.*, 2003] (horizontal velocity estimates only) were first performed, although parameter results trended toward an elastic plate thickness of 100 km and greater with no global minimum. These results imply a preference for a model of infinite elastic thickness, demonstrating that an elastic half-space model can be used to accurately model horizontal geodetic data only. Thus vertical velocity estimates are necessary for constraining viscoelastic model parameters [*Deng et al.*, 1998; *Pollitz et al.*, 2001]. Vertical data from the next release of the SCEC velocity model, combined with future estimates from the Plate Boundary Observatory, will provide better constraints in future models.

4.7.3 Present-day Stress Implications and Seismic Hazard

The actual stress along the San Andreas Fault System consists of the cyclical stress due to the earthquake cycle that we have estimated with our model, plus some background time-invariant stress field that is not modeled. Likewise, we have not included dynamic stress changes due to nearby coseismic events. These can be significantly larger than the static stress and may play an important role in modeling of the stress field, particularly for non-bilateral ruptures [*Kilb*, 2002]. Nevertheless, assume for a moment that the present day Coulomb stress model (Figure 4.6c) is an acceptable portrait of accumulated tectonic stress on the SAF System. Based on this idea, we can calculate how this model compares to historical stress distributions, earthquakes epicenters, and known surface ruptures. Figure 4.6(a,b) shows snapshots of the stress field prior to the 1812 Wrightwood and the 1857 Fort Tejon earthquakes, demonstrating the state of stress prior to the two most significant historical earthquakes along the southern San Andreas. According to our model, moderate stress levels had been reached along the Mojave segment prior to the 1812 event (Figure 4.6a). While the epicenter(s) of the 1812 events are poorly known, it is reasonable to assume that peak stress levels on the segment were enough to generate a large earthquake. Alternatively, the stress field prior to the 1857 Fort Tejon event indicates a significantly high amount of stress in the vicinity of the estimated epicenter (Figure 4.6b). Based on the behavior of these events, it is conceivable that the Mojave section of the SAF is presently experiencing a stress level similar to the stress level before the 1812 event. In contrast, the Carrizo and Cholame sections are presently experiencing lower stress levels than those indicated by our model prior to the 1857 event. Comparing this information with the present-day model, it is likely that most of the southern San Andreas and portions of the San Jacinto may be on the verge of a major earthquake, particularly

along the San Bernardino Mountains and Coachella sections where the last known event dates back to 1690 [*WGCEP*, 1995]. Again, this discussion implicitly assumes that the likelihood and size of an earthquake depends only on the stress accumulated since the last earthquake.

Justifying the extent of surface rupture for historical earthquakes and relating this to the present-day model requires further examination. While the events of 1812 relieved significant stress on the Mojave segment, the 1857 event 30 years later also ruptured this segment in addition to those to the north. According to our model, stress levels prior to the 1857 event were very high for the Cholame and Carrizo segments of the SAF, but were significantly lower for the Mojave portion. The Mojave segment does not indicate exceedingly high accumulation rates and in fact shows lower than average rates due to its faulting geometry and deep locking depth [*Smith and Sandwell*, 2003]. So why did the 1857 rupture propagate through this segment? Two explanations are plausible: 1) the 1812 event did not actually rupture this entire segment of the SAF, or 2) the 1812 event, and possibly many others, did not release its entire amount of accumulated interseismic moment and portions of this segment where indeed primed for another rupture only 30 years later. We prefer to eliminate the first explanation, as recent studies [*Jacoby et al.*, 1988; *Deng and Sykes*, 1996; *Toppozada et al.*, 2002] show excellent correlation for rupture on the Mojave segment in 1812. The suggestion of insufficient interseismic moment release appears more likely, with evidence for such behavior demonstrated by the 2004 M6.0 Parkfield earthquake [e.g., *Langbein et al.*, 2004; *Lienkaemper et al.*, 2004; *Murray et al.*, 2004]. Assuming that the Parkfield segment, which last ruptured in 1966, accumulated slip at a rate of 40 mm/yr over 40 years, then the Parkfield segment had accumulated at least 1.5 m of slip. Yet preliminary results indicate that the 2004 Parkfield event generated only 33 cm of coseismic slip [*Murray et al.*, 2004]. If our model is designed to generate coseismic slip according to purely kinematic assumptions, resulting in, for example, 1.5 m of slip at Parkfield in 2004, then we have obviously overestimated slip and stress drop in some occurrences. Future adjustments to this approach will need to be investigated by implementing actual historical seismic moments.

4.8 Conclusions

In summary, we have employed a previously-developed 3-D semi-analytic viscoelastic model [*Smith and Sandwell*, 2004] to estimate the velocity and stress accumulation along the entire San Andreas Fault System. Geometric complications of the fault system have no effect on the speed of the computation as 2-D convolutions are performed in the Fourier transform domain. Moreover, since the solution is analytic in time, no numerical time-stepping is needed. A model consisting of hundreds of fault elements embedded in a 2048 x 2048 grid requires less than 40s of CPU time on a desktop computer. A new model is computed for each locking depth, each earthquake, and each epoch, where, for example, a 1000-year simulation involving over 230 individual model computations can be computed in ~ 3 hours. This efficiency enables the computation of kinematically realistic 3-D viscoelastic models spanning thousands of years.

We use this method to estimate interseismic, coseismic, and postseismic deformation of the San Andreas Fault System over the past 1000 years. Both horizontal and vertical components of GPS-derived velocities (over 800 combined rates and uncertainties) that capture present-day plate motion are used to solve for elastic plate thickness (H), half-space viscosity (η), geologic Poisson's ratio (v_g), and locking depth factor (f_d). A least-squares parameter search over more than 100 models results in model parameters of $H > 60$ km, $\eta = 2 \times 10^{18} - 5 \times 10^{19}$ Pa s, $v_g = 0.30 - 0.40$, and $f_d = 0.65 - 0.80$ with a 4.091 weighted RMS misfit and a 90% data variance reduction. From analysis of Coulomb stress near the major fault strands, we find regions of elevated interseismic stress along most of the southern San Andreas and the northern San Jacinto, reflecting the 150[+] years that have transpired since a major seismic rupture occurred on specific fault segments.

While we believe that the differences between the model and the geodetic velocity data are primarily due to an imprecise knowledge of past earthquakes, there are also limitations to our model. Rheology of the crust and upper mantle is more complex than our single-layer laterally homogeneous model, both in the horizontal [*Malservisi et al.*, 2001] and in the vertical direction [*Pollitz et al.*, 2001]. We have ignored several important processes such as changes in local pore-pressure [*Massonnet et al.*, 1996; *Peltzer et al.*, 1996; *Fialko*, 2004a] and laterally varying rheology. Horizontal misfits are higher in the ECSZ than elsewhere, suggesting unmodeled strain accumulation. Nevertheless, this simple viscoelastic model provides an improved representation of crust-mantle rheology when compared to the elastic half-space model and agreement with existing geodetic data is encouraging.

While this study is the first of its kind to jointly consider geodetic and paleoseismic data in a large-scale, long-term model of the San Andreas Fault System, we admit that the entire deformation problem is a difficult one to solve and that future studies using more realistic rheologies and earthquake slip histories will certainly help further bound the solution. Yet perhaps the most important result of this study is a quantitative evaluation of elevated seismic hazards along specific areas of the San Andreas Fault System where a future major earthquake is more likely to occur. While models such as these are not yet capable of predicting the timing and extent of future ruptures, they are an important tool for understanding how different sections of the San Andreas Fault System store energy and release stress over time and the implications of these processes for future deformation.

4.9 Acknowledgements

4.10   References

Agnew, D.C., How complete is the pre-instrumental record of earthquake in Southern California, in *Environmental Perils: San Diego Region*, P. L. Abbott and W. J. Elliott (editors), San Diego Association of Geologists, San Diego, 1991.

Agnew, D. C., and K.E. Sieh, A documentary study of the felt effects of the great California earthquake of 1857, *Bull. Seismol. Soc. Am.* 68, 1717-1729, 1978.

Anderson, G., B. Aagaard, and K. Hudnut, Fault interactions and large complex earthquakes in the Los Angeles area, *Science*, 302, 1946-1949, 2003.

Bakun, W., Seismic Activity of the San Francisco Bay Region, *Bull. Seismol. Soc. Am.*, 89, 764-784, 1999.

Baldwin, J.N., Paleoseismic investigation of the San Andreas fault on the north coast segment, near Machester, California, *M.S. Thesis*, San Jose State University, California, 127 pp., 1996.

Becker, T.W., J. Hardebeck, and G. Anderson, Constraints on fault slip rates of the southern California plate boundary from GPS velocity and stress inversions, *Geophys. J. Int.*, doi:10.1111/j.1365-246X.2004.02528.x, 2004.

Bennett, R.A., B.P. Wernicke, J.L. Davis, P. Elosegui, J.K. Snow, M.J. Abolins, M.A. House, G.L. Stirewalt, and D.A. Ferrill, Global Positioning System constraints on fault slip rates in the Death Valley region, California and Nevada, *Geophys. Res. Lett.*, 24, 3073-3076, 1997.

Biasi, G.P., R.J. Weldon II, T.E. Fumal, and G.G. Seitz, Paleoseismic event dating and the conditional probability of large earthquake on the southern San Andreas fault, California, *Bull. Seismol. Soc. Am.*, 92, 2761-2781, 2002.

Bird, P., and X. Kong, Computer simulations of California tectonics confirm very low strength of major faults, *Geo. Soc. Am. Bull.*, 106, 159-174, 1994.

Bock Y., S. Wdowinski, P. Fang, J. Zhang, J. Behr, J. Genrich, S. Williams, D. Agnew, F. Wyatt, H. Johnson, K. Stark, B. Oral, K. Hudnut, S. Dinardo, W. Young, D. Jackson, and W. Gurtner, Southern California Permanent GPS Geodetic Array: Continuous measurements of crustal deformation between the 1992 Landers and 1994 Northridge earthquakes, *J. Geophys. Res.*, 102, 18,013-18,033, 1997.

Bolt, B.A., and R.D. Miller, Catalogue of earthquakes in northern California and adjoining areas, 1 January 1910-31 December 1972, Seismographic Stations, University of California, Berkeley, California, 567 pp., 1975.

Burgmann, R., D. Schmidt, R.M. Nadeau, M. d'Alessio, E. Fielding, D. Manaker, T.V. McEvilly, and M.H. Murray, Earthquake potential along the northern Hayward fault, California, *Science*, 289, 1178-1182, 2000.

Burmister, D.M., The theory of stresses and displacements in layered systems and applications of the design of airport runways, paper presented at the Annual Meeting, Highway Res. Board, Natl. Res. Counc., Washington, D.C., 1943.

Cohen, S.C., Numerical Models of Crustal Deformation in Seismic Zones, *Adv. Geophys*, 41, 133-231, 1999.

Cotton, W.R., N.T. Hall, and E.A. Hay, Holocene behavior of the San Andreas fault at Dogtown, Point Reyes National Seashore, California, *U.S. Geol. Survey Open File Rept.* 80-1142, 33pp., 1980.

Deng, J., and L.R. Sykes, Triggering of 1812 Santa Barbara earthquake by a great San Andreas shock: implications of future seismic hazards in southern California, *Geophys. Res. Lett.,* 23, 1155-1158, 1996.

Deng, J., M. Gurnis, H. Kanamori, and E. Hauksson, Viscoelastic flow in the lower crust after the 1992 Landers, California, earthquake, *Science*, 282, 1689-1692, 1998.

Dixon, T.H., M. Miller, F. Farina, H. Wang, and D. Johnson, Present-day motion of the Sierra Nevada block and some tectonic implications for the Basin and Range Province, North American Cordillera, *Tectonics*, 19, 1-24, 2000.

Dixon, T.H., E. Norabuena, and L. Hotaling, Paleoseismology and Global Positioning System; earhquake-cycle effects and geodetic versus geologic fault slip rates in the Eastern California Shear Zone, *Geology*, 31, 55-58, 2003.

Dong, D., T.A. Herring, and R.W. King, Estimating Regional Deformation from a Combination of Space and Terrestrial Geodetic Data, *J. Geodesy*, 72, 200-214, 1998.

Ellsworth, W.L., Earthquake history, 1769-1989, chap. 6 of Wallace, R.E., ed., The San Andreas Fault System, California: *U.S. Geological Survey Professional Paper* 1515, 152-187, 1990.

Fialko, Y., Evidence of fluid-filled upper crust from observations of post-seismic deformation due to the 1992 M_w 7.3 Landers earthquake, *J. Geophys. Res.*, 109, doi:10.1029/2003JB002985, 2004a.

Fialko, Y., Probing the mechanical properties of seismically active crust with space geodesy: Study of the co-seismic deformation due to the 1992 M_w 7.3 Landers (southern California) earthquake, *J. Geophys. Res.*, 109, doi:10.1029/2003JB002756, 2004b.

Fialko, Y., M. Simons, and D. Agnew, The complete (3-D) surface displacement field in the epicentral area of the 1999 M$_w$7.1 Hector Mine earthquake, California, from space geodetic observations, *Geophys. Res. Lett.*, 28, 3063-3066, 2001.

Feigl, K.L., D.C. Agnew, Y. Bock, D. Dong, A. Donnellan, B.H. Hager, T.A. Herring, D.D. Jackson, T.H. Jordan, R.W. King, S. Larsen, K.M. Larson, M.H. Murray, Z. Shen, and F.H. Webb, Space geodetic measurements of crustal deformation in Central and Southern California, 1984-1992, *J. Geophys. Res.*, 98, 21, 677-21,712, 1993.

Freed, A.M., and R. Burgmann, Evidence of power-law flow in the Mojave desert mantle, *Nature*, 430, 548-551, 2004.

Freed, A.M., and J. Lin, Delayed triggering of the 1999 Hector Mine earthquake by viscoelastic stress transfer, *Nature*, 411, 180-183, 2001.

Freymueller, J.T., M.H. Murray, P. Segall, and D. Castillo, Kinematics of the Pacific-North American plate boundary zone, northern California, *J. Geophys. Res.*, 104, 7419-7441, 1999.

Fumal, T. E., S. K. Pezzopane, R. J. Weldon II, and D. P. Shwartz, A 100-year average recurrence interval for the San Andreas fault at Wrightwood, California, *Science*, 259, 199-203, 1993.

Fumal, T.E., R.J. Weldon II, G.P. Biasi, T.E. Dawson, G.G. Seitz, W.T. Frost, and D.P. Schwartz, Evidence for large earthquakes on the San Andreas fault at the Wrightwood, California, paleoseismic site: A. D. 500 to Present, *Bull. Seismol. Soc. Am.*, 92, 2726-2760, 2002.

Fumal, T.E., M.J. Rymer, and G.G. Seitz, Timing of large earthquake since A. D. 800 on the Mission Creek strand of the San Andreas Fault Zone at Thousand Palms Oasis, near Palm Springs, California, *Bull. Seismol. Soc. Am.*, 92, 2841-2860, 2002.

Furlong, K.P., and D. Verdonck, Three-dimensional lithospheric kinematics in the Loma Prieta region, California: Implications for the earthquake cycle, in *The Loma Prieta, California, earthquake October 17, 1989 – Tectonic processes and models*, edited by R. W. Simpson, *U.S. Geol. Surv. Prof. Pap.*, 1550-F, F103-F131, 1994.

Gan, W., J. L. Svarc, J. C. Savage, and W. H. Prescott, Strain accumulation across the Eastern Caliornia Shear Zone at latitude 36 degrees 30 N, *J. Geophys. Res.*, 105, 16,229-16,236, 2000.

Grant, L.B., and W.R. Lettis, Introduction to the Special Issue on Paleoseismology of the San Andreas Fault System, *Bull. Seismol. Soc. Am.*, 92, 2552-2554, 2002.

Grant, L.B., and K. Sieh, Paleoseismic evidence of clusered earthquakes on the San Andreas fault in the Carrizo Plain, California, *J. Geophys. Res.*, 99, 6819-6841, 1994.

Harris, R.A., Introduction to special section: Stress triggers, stress shadows, and implications for seismic hazard, *J. Geophys. Res.*, 103, 24,347-24,358, 1998.

Harris, R.A., and R.W. Simpson, In the shadow of 1857: An evaluation of the static stress changes generated by the M8 Ft. Tejon, California, earthquake, *Eos Trans. AGU*, 74, Fall Meet. Suppl., 427, 1993.

Harris, R.A., and R.W. Simpson, In the shadow of 1857 – The effect of the great F. Tejon earthquake on subsequent earthquakes in southern California, *Geophys. Res. Lett.*, 23, 229-232, 1996.

Harris, R.A., and R.W. Simpson, Suppression of large earthquakes by stress shadows: A comparison of Coulomb and rate-and-state failure, *J. Geophys. Res.*, 103, 24,439-24,452, 1998.

Hearn, E.H., and E.D. Humphreys, Kinematics of the southern Walker Lane Belt and motion of the Sierra Nevada block, California, *J. Geophys. Res.*, 103, 27,033-27,049, 1998.

Hearn, E.H., R. Burgmann, and R.E. Reilinger, Dynamics of Izmit Earthquake Postseismic Deformation and Loading of the Duzce Earthquake Hypocenter, in preparation, 2004.

Heingartner, G.F., Paleoseismic recurrence investigation of the Santa Cruz Mountaints segment of the San Andreas fault near Watsonville, California, *M.S. Thesis*, San Jose State University, California, 136 pp., 1995.

Hileman, J.A., C.R. Allen, and J.M. Nordquist, *Seismicity of the Southern California Region, 1 January 1932 to 21 December 1972*, California Institute of Technology, Pasadena, Seismological Laboratory Contribution 2385, 81 pp., 1973.

Jacoby, G., P. Sheppard, and K. Sieh, Irregular recurrence of large earthquakes along the San Andreas fault: evidence from trees, *Science*, 241, 196-199, 1988.

Jennings, C.W., Fault activity map of California and adjacent areas with locations and ages of recent volcanic eruptions: California Division of Mines and Geology Data Map Series No. 6, 92, 2 plates, map scale 1:750,000, 1994.

Johnson, K.M., and P. Segall, Viscoelastic earthquake cycle models with deep stress-driven creep along the San Andreas fault system, *J. Geophys. Res.*, 109, doi:10.1029/2004JB003096, 2004.

Kenner, S.J., Rheological controls on fault loading rates in northern California following the 1906 San Francisco earthquake, *Geophys. Res. Lett.*, 31, doi: 10.1029/2003GL018903, 2004.

Kenner, S., and P. Segall, Time-dependence of the stress shadowing effect and its relation to the structure of the lower crust, *Geology*, 27, 119-122, 1999.

Kilb, D., A strong correlation between induced peak dynamic Coulomb stress change from the 1992 M7.3 Landers earthquake and the hypocenter of the 1999 M7.1 Hector Mine earthquake, *J. Geophys. Res.*, 108, doi:10.1029/2001JB000678, 2003.

King. G.C.P., R.S. Stein, and J. Lin, Static stress changes and the triggering of earthquakes, *Bull. Seismol. Soc. Am.*, 84, 935-953, 1994.

Knudsen, K.L., R.C. Witter, C.E. Garrison-Laney, J.N. Baldwin, and G.A. Carver, Past earthquake-induced rapid subsidence along the northern San Andreas fault: a paleoseismological method for investigating strike-slip faults, *Bull. Seismol. Soc. Am.*, 92, 2612-2636, 2002.

Langbein, J.H., A. Snyder, Y. Bock, and M.H. Murray, Deformation from the 2004 Parkfield, California, Earthquake measured by GPS and creepmeters, *EOS Trans. AGU 85(47)*, Fall Meet. Suppl., Abstract S51C-0170F, 2004.

Langbein, J.H., Overview of the 2004 M6 Parkfield, California, Earthquake, *EOS Trans. AGU 85(47)*, Fall Meet. Suppl., Abstract S53D-02, 2004.

Li., V.C., and H.S. Lim, Modeling surface deformations at complex strike-slip plate boundaries, *J. Geophys. Res.*, 93, 7943-7954, 1988.

Li, V.C., and J.R. Rice, Crustal deformation in great California earthquake cycles, *J. Geophys. Res.*, 92, 11,530-11,551, 1987.

Lienkaemper, J.J., T.E. Dawson, S.F. Personius, G.G. Seitz, L.M. Reidy, and D.P. Schwartz, A Record of Large Earthquakes on the southern Hayward fault for the past 500 years, *Bull. Seismol. Soc. Am.*, 92, 2637-2658, 2002.

Lienkaemper, J.J., B. Baker, and F.S. McFarland, Slip in the 2004 Parkfield, California, Earthquake Measured on Alinement Arrays, *EOS Trans. AGU 85(47)*, Fall Meet. Suppl., Abstract S54B-01, 2004

Lindvall, S.C., T.K. Rockwell, T.E. Dawson, J.G. Helms, K.W. Bowman, Evidence for two surface ruptures in the past 500 years on the San Andreas fault at Frazier Mountain, California, *Bull. Seismol. Soc. Am.*, 92, 2689-2703, 2002.

Lisowski, M., J.C. Savage, and W.H. Prescott, The velocity field along the San Andreas fault in central and southern California, *J. Geophys. Res.*, 96, 8369-8389, 1991.

Louderback, G.D., Centeral California earthquakes of the 1830's, *Bull. Seismol. Soc. Am.* 37, 33-74, 1947.

Lyons, S., and D. Sandwell, Fault creep along the southern San Andreas from interferometric synthetic aperature radar, permanent scatterers, and stacking,, *J. Geophys. Res.*, 108, 10:1029/2002JB001831, 2003.

Malservisi, R., K.P. Furlong, and T.H. Dixon, Influence of the earthquake cycle and lithospheric rheology on the dynamics of the eastern California shear zone, *Geophys. Res. Lett.*, 28, 2731-2734, 2001.

Massonnet, D., W. Thatcher, and H. Vadon, Radar interferometry detects two mechanism of postseismic relaxation following the Landers, California earthquake, *Nature*, 382, 612-612, 1996.

McClusky, S., S.C. Bjornstad, B.H. Hager, R.W. King, B.J. Meade, M.M. Miller, F.C. Monastero, and B.J. Souter, Present day kinematics of the Eastern California Shear Zone from a geodetically constrained block model, *Geophys. Res. Lett.*, 28, 3369-3372, 2001.

McGill, S.S. Dergham, D. Barton, T. Berney-Ficklin, D. Grant, C. Hartling, K. Hobart, R. Minnich, M. Rodriguez, E. Runnerstrom, J. Russell, K. Schmoker, M. Stumfall, J. Townsend, and J. Williams, Paleoseismology of the San Andreas fault at Plunge Creek, near San Bernardino, southern California, *Bull. Seismol. Soc. Am.*, 92, 2803-2840, 2002.

Meade, B.J., B.H. Hager, and R.W. King, Block models of present day deformation in Southern California constrained by geodetic measurements (abstract), *2002 SCEC Annual Meeting, Oxnard CA*, 96, 2002.

Meade, B. J., and B .H. Hager, Viscoelastic deformation for a clustered earthquake cycle, *Geophys. Res. Lett.*, 31, doi:10.1029/2004GL019643, 2004.

Miller, M.M., D.J. Johnson, T.H. Dixon, and R.K. Dokka, Refined kinematics of the Eastern California Shear Zone from GPS observations, 1992-1998, *J. Geophys. Res.,* 106, 2245-2263, 2001.

Murray, M.H., and P. Segall, Modeling broadscale deformation in northern California and Nevada from plate motions and elastic strain accumulation, *Geophys. Res. Lett.*, 28, 3215-4318, 2001.

Murray, J.R., P. Segall, and J. Svarc, Slip in the 2004 Parkfield M6 Earthquake: Comparison With Previous Events and Implications for Earthquake Recurrence Models, *EOS Trans. AGU 85(47)*, Fall Meet. Suppl., Abstract S54B-03, 2004.

Nikolaidis, R., Observation of Geodetic and Seismic Deformation with the Global Positioning System, *Ph.D. Thesis*, Univ. of Calif. San Diego, 2002.

Niemi, T. M., Late Holocene slip rate, prehistoric earthquakes, and Quaternary neotectonics of the northern San Andreas fault, Marin County, California, *Ph.D. Thesis*, Stanford University, Palo Alto, California, 199 pp., 1992.

Niemi, T.M., and N. T. Hall, Late Holocene slip rate and recurrence of great earthquakes on the San Andreas fault in northern California, *Geology*, 20, 195-198, 1992.

Noller, J.S., K.I. Kelson, W.R. Lettis, K.A. Wickens, G D. Simpson, K. Lightfoot, T. Wake, Prelimilary characterizations of Holocene activity on the San Andreas fault based on offset archaeologic sites, F. Ross State Historic Park, California, *U.S. Geol. Surv. NEHRP Final Tech. Rep.*, 1993.

Nur, A., and G. Mavko, Postseismic viscoelastic rebound, *Science*, 183, 204-206, 1974.

Parsons, T., Post-1906 stress recovery of the San Andreas fault system calculated from three-dimensional finite element analysis, *J. Geophys. Res.*, 107, doi:10.1029/2001JB001051, 2002.

Peltzer, G., F. Crampe, S. Hensley, and P. Rosen, Trasient strain accumulation and fault interaction in the Eastern California Shear Zone, *Geology*, 29, 975-978, 2001.

Peltzer, G.P., P. Rosen, F. Rogez, and K. Hudnut, Postseismic rebound in fault step-overs caused by pore fluid flow, *Science*, 273, 1202-1204, 1996.

Pollitz, F.F., G. Peltzer, and R. Burgmann, Mobility of continental mantle: Evidence from postseismic geodetic observations following the 1992 Landers earthquake, *J. Geophys. Res.*, 105, 8035-8054, 2000.

Pollitz, F.F., C. Wicks, and W. Thatcher, Mantle flow beneath a continental strike-slip fault: Postseismic deformation after the 1999 Hector Mine earthquake, *Science*, 293, 1814-1818, 2001.

Pollitz F., and S. Sacks, Modeling of postseismic relaxation following the great 1857 earthquake, Southern California, *Bull. Seismol. Soc. Am.*, 82, 454-480, 1992

Prentice, C.S., Earthquake geology of the northern San Andreas fault near Point Arena, California, *Ph.D. Dissertation*, California Institute of Technology, Pasadena, California, 252 pp., 1989.

Rockwell, T.K., J. Young, G. Seitz, A. Meltzner, D. Verdugo, F. Khatib, D. Ragona, O. Altangerel, and O. Altangerel, 3,000 years of ground-rupturing earthquakes in the Anza Seismic Gap, San Jacinto Fault, Southern California: Time to shake it up?, 2003 SCEC Annual Meeting, *Proceedings and Abstracts*, 13, 2003.

Rundle, J.B. and D.D. Jackson, A three-dimensional viscoelastic model of a strike slip fault, *Geophys. J. Roy. Astron. Soc.*, 49, 575-591, 1977.

Rybicki, K., The elastic residual field of a very long strike-slip fault in the presence of a discontinuity, *Bull. Seismol. Soc. Am.* 61, 72-92, 1971.

Sandwell, D.T., Sichiox, L., and B. Smith, The 1999 Hector Mine Earthquake, Southern California: Vector Near-Field Displacements from ERS InSAR, *Bull. Seismol. Soc. Am.*, 92, 1341-1354, 2002.

Savage, J.C., Equivalent strike-slip earthquake cycles in half-space and lithosphere-asthenosphere earth models, *J. Geophys. Res.,* 95, 4873-4879, 1990.

Savage, J.C., and W.H. Prescott, Asthenosphere readjustment and the earthquake cycle, *J. Geophys. Res.*, 83, 3369-3376, 1978.

Savage, J.C., and R.O. Burford, Geodetic determination of relative plate motion in central California, *J. Geophys. Res.,* 78, 832-845, 1973.

Savage, J.C., and M. Lisowski, Inferred depth of creep on the Hayward fault, central California, *J. Geophys. Res.*, 98, 787-793, 1993.

Savage, J.C., and J.L. Svarc, Postseismic deformation associated with the 1992 $M_w = 7.3$ Landers earthquake, southern California, *J. Geophys. Res.*, 102, 7565-7577, 1997.

Schwartz, D.P., D. Pantosti, K. Okumura, T.J. Powers, and J.C. Hamilton, Paleoseismic investigations in the Santa Cruz Mountains California: implications for recurrence of large-magnitude earthquakes on the San Andreas fault, *J. Geophys. Res.* 103, 17,985-18,001, 1998.

Segall, P., Integrating geological and geodetic estimates of slip rate on the San Andreas fault system, *Int. Geol. Rev.*, 44, 82, 2002.

Shen, Z., D. Jackson, Y. Feng, M. Cline, M. Kim, P. Fang, and Y. Bock, Postseismic deformation following the Landers earthquake, California, 28 June 1992, *Bull. Seismol. Soc. Am.*, 84, 780-791, 1994.

Shen, Z.K., D.C. Agnew, and R.W. King, The SCEC Crustal Motion Map, Version 3.0, http://epicenter.usc.edu/cmm3.

Sieh, K.E., Slip along the San Andreas fault associated with the great 1857 earthquake, *Bull. Seismol. Soc. Am.*, 68, 1421-1448, 1978a.

Sieh, K.E., Central California foreshocks of the great 1857 earthquake, *Bull. Seismol. Soc. Am.*, 68, 1731-1749, 1978b.

Sieh, K.E., M. Stuiver, and D. Brillinger, A more recise chronology of earthquake produced by the San Andreas fault in Southern California, *J. Geophys. Res.*, 95, 603-623, 1989.

Sieh, K.E., and P.L. Williams, Behavior of the southernmost San Andreas Fault during the past 300 years, *J. Geophys. Res.*, 95, 6629-6645, 1990.

Simpson, R.W., and P.A. Reasenberg, Earthquake-induced static stress changes on central California faults, *U.S. Geological Survey Professional Paper Report: P 1550-F*, F55-F89, 1994.

Simpson, G.D., J.S. Noller, K.I. Kelson, and W.R. Lettis, Logs of trenches across the San Andreas fault, Archae camp, Fort Ross State Historic Park, Northern California, U.*S. Geol. Surv. NEHRP Final Tech. Rept.*, 1996.

Smith, B.R., and D.T. Sandwell, Coulomb Stress along the San Andreas Fault System, *J. Geophys. Res.*, 108, doi:10.1029/2002JB002136, 2003.

Smith, B.R., and D.T. Sandwell, A 3-D Semi-Analytic Viscoelastic Model for Time-Dependent Analyses of the Earthquake Cycle, *J. Geophys. Res.*, 109, doi:10.1029/2004JB003185, 2004.

Stein, R.S., Contemporary plate motion and crustal deformation, *Rev. Geophys.,* 25, 855-863, 1987.

Stein, R.S., G.C.P. King, and J. Lin, Stress triggering of the 1994 M = 6.7 Northridge, California, earthquake by its predecessors, *Science*, 265, 1432-1435, 1994.

Stein, R.S., and T.C. Hanks, M > 6 earthquakes in southern California during the twentieth century: no evidene for a seismicity or moment deficit, *Bull. Seismol. Soc. Am.*, 99, 635-652, 1998.

Steketee, J.A., On Volterra's dislocations in a semi-infinite elastic medium, *Can. J. Phys., 36*, 1958.

Thatcher, W., Nonlinear strain buildup and the earthquake cycle on the San Andreas Fault, *J. Geophys. Res.*, 88, 5893-5902, 1983.

Thomas, A.P., and T.K. Rockwell, A 300- to 550- year history of slip on the Imperial fault near the U.S.–Mexico border: Missing slip at the Imperial fault bottleneck, *J. Geophys. Res.*, 101, 5987-5997, 1996.

Toppozada, T.R., D.M. Branum, B.S. Reichle, and C.L. Hallstrom, San Andreas Fault Zone, California: M >5.5 Earthquake History, *Bull. Seismol. Soc. Am.*, 92, 2555-2601, 2002.

Toppozada, T.R., C.R. Real, and D.L. Parke, Preparation of isoseismal maps and summaries of reported effects for pre-1900 California earthquakes, *Calif. Div. Mines Geol. Open File Rept. 81-11SAC*, 182 pp., 1981.

Townend, J., and M.D. Zoback, Regional tectonic stress near the San Andreas fault in central and southern California, *Geophys. Res. Lett.*, 31, doi:10.1029/2003GL018918, 2004.

Townley, S.D., Earthquakes in California, 1769 to 1928, *Bull. Seismol. Soc. Am.*, 29, 21-252, 1939.

Ulrich, F.P., The Imperial Valley Earthquakes of 1940, *Bull. Seismol. Soc. Am.*, 31, 13-31, 1941.

U.S. Geological Survey, the Southern California Earthquake Center, and the California Division of Mines and Geology, Preliminary Report on the 16 October 1999 M7.1 Hector Mine, California, Earthquake, *Seismol. Res. Lett.*, 71, 11-23, 2000.

Ward, S.N., A note on lithospheric bending calculations, *Geophys. J. Roy. Astron. Soc.*, 78, 241-253, 1984.

Ward, S.N., Quasi-static propagator matrices: creep on strike-slip faults, *Tectonophysics*, 120, 83-106, 1985.

Wdowinski, S., Y. Bock, J. Zhang, P. Fang, and J. Genrich, Southern California Permanent GPS Geodetic Array: Spatial filtering of daily position from estimating coseismic and postseismic displacement induced by the 1992 Landers earthquake, *J. Geophys. Res.*, 102, 18,057-18,070, 1997.

Weertman, J., Continuum distribution of dislocations on faults with finite friction, *Bull. Seismol. Soc. Am.*, 54, 1035-1058, 1964.

Williams, C.A., and R.M. Richardson, A rheologically layered three-dimensional model of the San Andreas Fault in central and southern California, *J. Geophys. Res.*, 96, 16,597-16,623, 1991.

Wood, H.O., The 1857 earthquake of California, *Bull. Seismol. Soc. Am.* 45, 47-67, 1955.

Working Group on California Earthquake Probabilities (WGCEP), Seismic hazards in southern California: Probable earthquakes, 1994 to 2024, *Bull. Seismol. Soc. Am., 85*, 379-439, 1995.

Working Group on California Earthquake Probabilities (WGCEP), Earthquake probabilities in the San Francisco Bay Region: 2000 to 2030 – A summary of findings, *U.S. Geol. Surv. Open File Rep.*, [Online] *99-517,* version 1.0, 1999.

124

Working Group on California Earthquake Probabilities (WGCEP), Earthquake Probabilities in the San Francisco Bay Region: 2002-2031, *USGS Open File Report 03-214*, 2003.

Working Group on Northern California Earthquake Potential (WGNCEP), Database of potential sources for earthquakes larger than magnitude 6 in northern California, *U.S. Geol. Surv. Open File Rep., 96-705*, 1996.

Yang, M., and M.N. Toksoz, Time dependent deformation and stress relaxation after strike slip earthquakes, *J. Geophys. Res.*, 86, 2889-2901, 1981.

Young, J.J., J.R. Arrowsmith, L. Colini, L.B. Grant, and B. Gootee, Three-dimensional excavation and recent rupture history along the Cholame segment of the San Andreas fault, *Bull. Seismol. Soc. Am.*, 92, 2670-2688, 2002.

Yu, E., and P. Segall, Slip on the 1868 Hayward earthquake from the analysis of historical trianulation data, *J. Geophys. Res*, 101, 16,101-16,118, 1996.

Yule, D., Neotectonic and paleoseismic investigation of the San Andreas Fault System, San Gorgoniao Pass, Annual Report, California State University Northridge, 2000.

Yule, D., and K. Sieh, Complexities of the San Andreas fault near San Gorgonio Pass: Implications for large earthquakes, *J. Geophys. Res.*, 108, 10.1029/2001JB000451, 2003.

Yule, D., and K. Sieh, Neotectonic and paleoseismic investigation of the San Andreas fault system, San Gorgonio Pass, *1996 SCEC annual report* 14-08-001-A0899, C.70-74, 1997.

Zeng, Y., Viscoelastic stress-triggering of the 1999 Hector Mine earthquake by the 1992 Landers earthquake, *Geophys. Res. Lett.*, 28, 3007-3010, 2001.

Appendix 4.A   3-D Viscoelastic Body Force Model

The Fourier model [*Smith and Sandwell*, 2004] consists of a grid of body-force couples (representing multiple fault elements) embedded in an elastic plate overlying a viscoelastic half-space (Figure 3.1, Chapter 3). The solutions that make up this model are based on the previous work of *Steketee* [1958], *Rybicki* [1971], *Nur and Mavko* [1974], and *Rundle and Jackson* [1977], who developed the first pieces of a 3-D analytic viscoelastic solution (i.e., Green's function) based on dislocation solutions. While the Green's function is computationally efficient for calculating displacement or stress at a few points due to slip on a small number of faults, it is less efficient for computing deformation on large grids representing fault systems, especially when the fault system has hundreds or thousands of segments. Because the force-balance equations are linear, the convolution theorem can be used to speed the computation. This substantially reduces the computational burden associated with an arbitrarily complex distribution of force couples necessary for fault modeling.

We begin by solving for the displacement vector **u**(*x,y,z*) due to a point vector body force at depth. The following text provides a brief outline of our mathematical approach while a more detailed derivation can be found in *Smith and Sandwell* [2004]. The full derivation and source code are available at http://topex.ucsd.edu/body_force.

(1) Develop differential equations relating a three-dimensional (3-D) vector body force to a 3-D vector displacement. To partially satisfy the boundary condition of zero shear traction at the surface, an image source [*Weertman, 1964*] is applied at a mirror location in the vertical direction.

(2) Take the 3-D Fourier transform to reduce the partial differential equations to a set of linear algebraic equations.

(3) Invert the linear system of equations to obtain the 3-D displacement vector solution.

(4) Perform the inverse Fourier transform in the z-direction (depth) by repeated application of the Cauchy Residue Theorem.

(5) Introduce a layer of thickness H into the system through an infinite summation of image sources [*Weertman*, 1964; *Rybicki*, 1971], reflected both above and below the surface $z = 0$.

(6) Integrate the point source Green's function over depths [d_1, d_2] to simulate a vertical fault plane. For the general case of a dipping fault, this integration can be done numerically.

(7) Analytically solve for Maxwell viscoelastic time-dependence using the Correspondence Principle and assuming a Maxwell time defined by $\tau_m=2\eta/\mu$. Following an approach similar to that of *Savage and Prescott* [1978], we map time and viscosity into an implied half-space shear modulus. We require the bulk modulus to remain constant and thus also solve for an implied Young's modulus.

(8) Calculate the non-zero normal traction at the surface and cancel this traction by applying an equal but opposite vertical load on an elastic layer over a viscoelastic half-space, similar to the Boussinesq Problem.

While this approach is an efficient way to address elaborate faulting and complex earthquake scenarios, it also incorporates a new analytic solution to the vertical loading problem for an elastic plate overlying a viscoelastic half space where the gravitational restoring force is included. The development of this analytic solution follows the approach of *Burmister* [1943] and *Steketee* [1958], but uses computer algebra to analytically invert a 6 by 6 matrix of boundary conditions.

The numerical aspects of this approach involve generating grids of vector force couples (i.e., F_x, F_y, and F_z) that simulate complex fault geometry, taking the Fourier transform of the grid, multiplying by the Fourier transform of the Green's function of the model, and finally, taking the inverse Fourier transform of the product to obtain the displacement or stress field. Arbitrarily complex curved and discontinuous faults can easily be converted to a grid of force vectors. The model parameters are: plate thickness (H), locking depths (d_1, d_2), shear modulus (μ), Young's modulus (E), density (ρ), gravitational acceleration (g), half-space viscosity (η), and Poisson's ratio (v). The solution satisfies the zero-traction surface boundary condition and maintains stress and displacement continuity across the base of the plate [see *Smith and Sandwell*, 2004]. The x-boundary condition of constant far-field velocity difference across the plate boundary is simulated using a cosine transform in the x-direction. The y-boundary condition of uniform velocity in the far-field is simulated by arranging the fault trace to be cyclic in the y-dimension.

Using this approach, the horizontal complexity of the model fault system has no effect on the speed of the computation. For example, computing vector displacement and stress on a 2048 x 2048 grid for a fault system consisting of 400 segments and a single locking depth requires less than 40 seconds of CPU time on a desktop computer. Because multiple time steps are required to fully capture viscoelastic behavior, a very efficient algorithm is needed for computing 3-D viscoelastic models with realistic 1000-year recurrence interval earthquake scenarios in a reasonable amount of computer time (i.e., days).

Chapter 5

Accuracy and Resolution of Shuttle Radar Topography Mission Data

Bridget R. Smith and David T. Sandwell

Abstract. We assess the accuracy and resolution of topography data provided by the Shuttle Radar Topography Mission (SRTM) through spectral comparisons with the National Elevation Dataset (NED) and a high-resolution laser data set of the 1999 Hector Mine earthquake rupture. We find that SRTM data and the NED are coherent for wavelengths greater than 200 m, however the spatial resolution of the NED is superior to the SRTM data for wavelengths shorter than 350 m, likely due to the application of a boxcar filter applied during final SRTM processing stages. From these results, a low-pass filter/decimation algorithm can be designed in order to expedite large-area SRTM data applications.

5.1   Introduction

The Shuttle Radar Topography Mission (SRTM) [*Farr and Kobrick*, 2001] collected radar interferometry data over 80% of Earth's landmass from 60 ºN to 56 ºS latitude in February of 2000. C-band (λ = 5.6 cm) data acquired during the mission, currently being processed by the Jet Propulsion Laboratory (JPL), is expected to have horizontal and vertical accuracy near 20 m and 16 m (linear error at 90% confidence), respectively, for the final 1 arc-second data release of the U.S. [*Jordan et al.*, 1996; *Slater et al.*, 2001]. While 1 arc-second data (30 m, SRTM-1) will only be available for locations within the U.S., under the NASA-NIMA Memorandum of Understanding for SRTM, data outside of the U.S. will eventually become publicly available at 3 arc-second sampling (90 m, SRTM-3) [*M. Kobrick*, personal communication, 2002].

Once complete, the SRTM data set will provide a new level of global topographic information critical for a number of scientific investigations, specifically in areas outside of the U.S. where the quality of data is typically poorer [*Berry et al.*, 2000]. Prior to the scientific applications of SRTM data, however, it is necessary to understand the vertical precision/accuracy and horizontal resolution of the data set. In the case of SRTM, the vertical precision of the data depends on the inherent phase noise in the SRTM radar, while the horizontal resolution depends on the signal-to-noise ratio as a function of horizontal wavelength. While the vertical accuracy of the final topography data can be determined using GPS control points, the relative vertical precision and horizontal resolution of the data can only be established by performing a cross-spectral analysis between SRTM data and another large-area "ground-truth" data set. Here we assess the quality of SRTM data through comparisons with two other data sets in the Mojave desert area of southern California. We examine the power and coherence of SRTM, the National Elevation Dataset (NED), and the Hector Mine Airborne Laser Swath Mapping (ALSM) data set in order to establish the horizontal resolution of C-band 30 m SRTM topography.

5.2. Data Characteristics

5.2.1 SRTM Data

Both ascending and descending C-band swaths from the Shuttle interferometer were processed into a digital elevation model (DEM) by the Jet Propulsion Laboratory [*Hensley et al.*, 2000]. Each data posting of the final DEM represents a height in meters above the WGS84 ellipsoid (PI Processor) or the WGS84 geoid (Production Processor) in the WGS84 latitude/longitude coordinate system [*NIMA*, 1994; *SRTM_Topo*, 2001]. For this study, both PI and Production Processor versions of SRTM data were analyzed; no significant differences (other than the geoid/ellipsoid reference and minor data voids) were identified in accuracy or resolution, and so the results discussed in this paper were chosen to reflect that of the PI Processor DEM. Data points within the C-band SRTM-1 grid are horizontally spaced at 1 arc-second intervals, or ~30 m intervals at the equator.

5.2.2 NED Data

The National Elevation Dataset (NED), assembled by the U.S. Geological Survey, is a compilation of many data sources (7.5 minute, 15 minute, 2 arc-second, and 3 arc-second DEMs extending as far back as 1978) of varying horizontal datum, map projections, and elevation units. The final raster NED product reflects elevation values that have been converted to consistent units, recast into a geographic projection, and referenced to the NAD83 horizontal datum [*Gesch et al.*, 2002]. Like the SRTM-1 data set, the NED DEM has approximately 30 m horizontal postings and is available for regions within the United States.

5.2.3 Hector Mine ALSM Data

The Hector Mine Airborne Laser Swath Mapping (ALSM) data set was acquired along the rupture zone of the M=7.2 1999 Hector Mine Earthquake [*Hudnut et al.*, 2002]. On April 19th, 2000, a field team from the U.S. Geological Survey acquired the entire high-resolution topography data set using a helicopter-based laser instrument platform. The helicopter flight lines traversed the rupture zone along most of its length (~50 km), acquiring multiple swath widths of, on average, 150 m. The laser beam scanned continuously, rotating through nadir angles of +/- 18º while flying along the fault scarp. The processed Hector Mine ALSM survey data have been geodetically referenced to the WGS84 ellipsoid using onboard GPS and have horizontal postings spaced ~25 cm.

5.3. Data Preparation

In order to assess the accuracy and resolution of the 30 m C-band SRTM DEM, cross-spectral analyses were performed between pairs of the above data sets in an area of southern California near the location of the 1999 Hector Mine Earthquake (Figure 5.1). Prior to these comparisons, the data were projected into a common latitude, longitude, and height system. The Hector Mine ALSM topography data required a tedious re-sampling scheme in order to make the data more compatible to that of SRTM and the NED. In doing so, we resampled the Hector Mine ALSM data as a function of nadir angle from –18.0º to –2.3º and +2.3º to +18.0º. We also constrained along-track spacing of data points to a minimum of 8 m (Figure 5.1, outset).

Six sub-regions of the N34W117 SRTM DEM were chosen for cross-comparison with the NED: three regions in the longitudinal direction (row analyses) and three in the latitudinal direction (column analyses). These specific analyses spanned regions of both high and low relief of the Hector Mine area grid (Figure 5.1). Each cross-spectral analysis contained 600 profiles of 2048 samples. A Hanning-tapered window of

128

length 2048 was applied to each profile segment. Spectral estimates from the 600 independent profile segments were then ensemble averaged to form both cross-spectral and coherence estimates.

Following the resampling algorithm discussed above, a maximum possible number of profiles were also extracted from the Hector Mine ALSM data and segmented into 402 independent profiles (Figure 5.1, outset). These subparallel profiles, each containing 512 samples, were also extracted from both NED and SRTM resampled grids for cross-comparison. Spectral estimates from the 402 independent profile segments were ensemble averaged to form both cross-spectral and coherence estimates. Because of the fewer, relatively shorter profiles available for cross-comparison, cross-spectral estimates of Hector Mine ALSM data are less reliable than those of the SRTM-NED comparison.
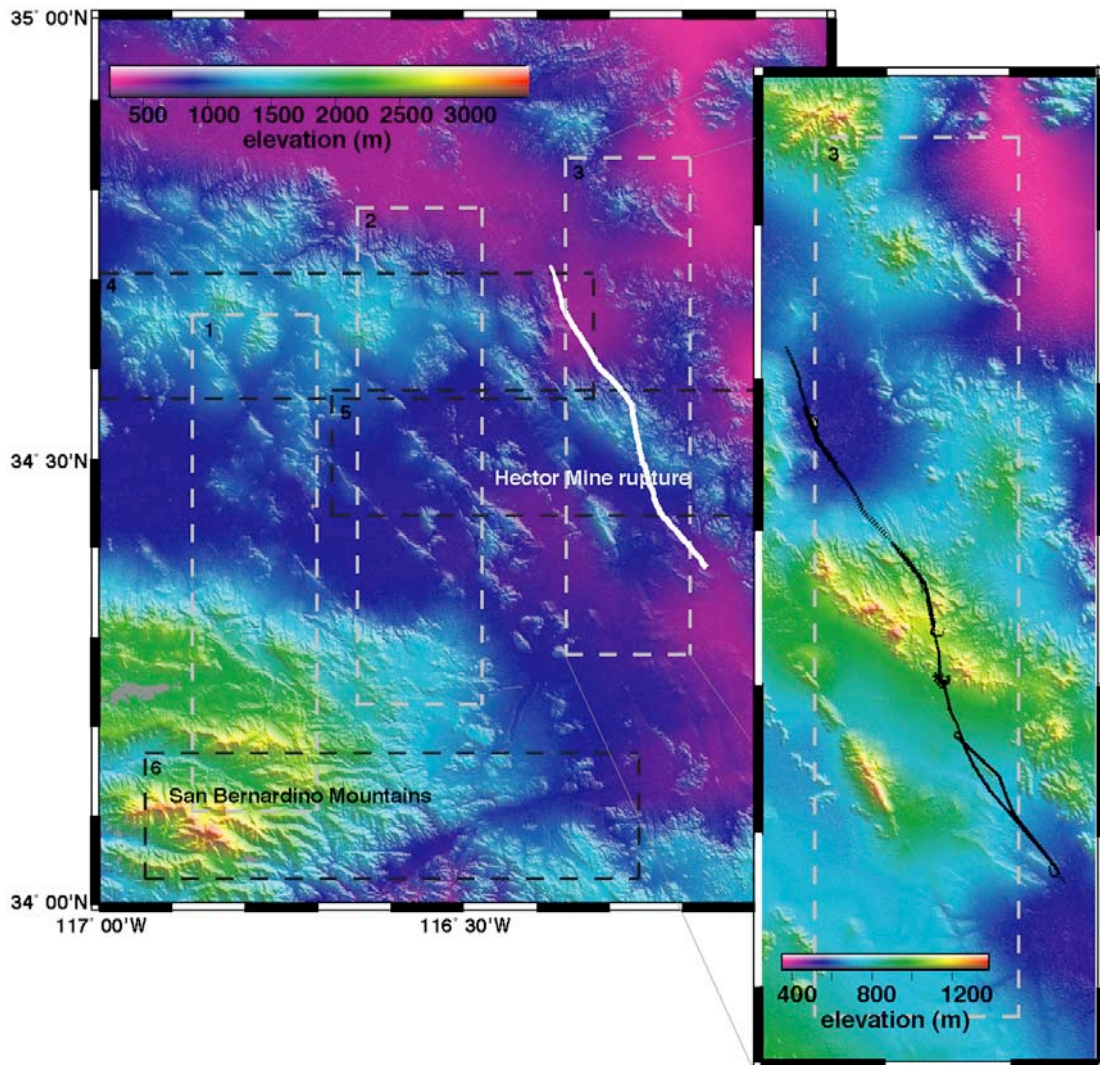
Figure 5.1. Location map of the N34W117 DEM of the SRTM data set. White dashed boxes depict examples of column (latitude) cross-spectral estimates performed on the SRTM and NED DEMs. Similarly, black dashed boxes depict row (longitude) estimates. Associated numbers in upper left corners of boxes correspond to the six cross-spectral analyses as noted in Table 5.1. Outset shows a close-up view of the Hector Mine ALSM tracks (black) used in this study.

5.4. Cross-Spectral Analyses Results

Using either multiple rows/multiple columns or multiple profiles along the helicopter flight track, three different cross-spectral analyses were performed in one dimension following the *Welch* [1967] method for estimates of both power and coherence. The coherence, γ_{xy}^2, is a measure of correlation between any combination of two signals (SRTM, NED, or Hector Mine ALSM). A high coherence (close to 1) indicates that the signal to noise ratio (SNR) of both data sets is high, while a low coherence indicates one or both of the data sets has a low SNR. When both data sets have similar SNR characteristics (initially hypothesized as that of SRTM and NED), a coherence of 0.25 indicates the longest wavelength at which both have a SNR of 1 and provides a good estimate of the resolution of the data sets [*Bendat and Piersol*, 1986]. Alternatively, if one data set has a much higher SNR than the other (such as Hector Mine ALSM data), a coherence of 0.5 identifies the spectral region at which the SNR of the inferior data set is 1. The degree of reliability for such spectral estimates of coherence depends significantly on the length of each profile and number of independent profiles available for the ensemble average.

5.4.1 SRTM vs. NED

First we inspect the results of the SRTM and NED cross-comparison. The coherence estimate between both data as a function of wavelength is shown in Figure 5.2a, where the grey curve corresponds to a representative column analysis (box 3, Figure 5.1), while the black curve corresponds to a representative row analysis (box 5, Figure 5.1). The remaining four analyses displayed similar coherence versus wavelength results (Table 5.1). Initially, we assume that the SRTM and NED data have similar signal and noise spectra and that a 0.25 coherence indicates the full wavelength (156 m) where their associated SNRs are 1. We next suppose that either the NED or SRTM data has high SNR at wavelengths near 156 m. In this case, a 0.5 coherence indicates the full wavelength (210 m) where the inferior data set has a SNR of 1. But which data set has the higher SNR in the 150 to 200 m wavelength band – NED or SRTM? In order to answer this question, the superior accuracy of the Hector Mine ALSM topography is required for cross-comparison with both SRTM and NED.

5.4.2 SRTM & NED vs. Hector Mine ALSM

Next we assess the accuracy and resolution of both the SRTM and NED data by comparing each to the higher quality Hector Mine ALSM data. The RMS difference between SRTM and Hector Mine ALSM data is 2.7 m, while the RMS difference between the NED and Hector Mine ALSM data is significantly higher (3.5 m). Thus the SRTM data are considerably more accurate than the NED data. The coherence analysis, however, reveals that the NED data have better short wavelength resolution. For the SRTM-Hector Mine ALSM comparison (Figure 5.2b), the coherence falls below 0.5 at a full wavelength of 204 m. Additionally, we note the significant drop in coherence at wavelengths between 500 and 180 m in the SRTM data, to be discussed below. For the NED-Hector Mine ALSM comparison (Figure 5.2c), the coherence falls to 0.5 at a full wavelength of 130 m. Thus, the NED has higher accuracy than the SRTM data at shorter wavelengths. However, the NED-Hector Mine ALSM coherence is only 0.82 at a wavelength of 500 m while the SRTM-Hector Mine ALSM coherence is higher (0.9). In fact, from Figure 5.2 (b and c), we note that the NED data are inferior to the SRTM data for wavelengths longer than ~350 m. The overall higher accuracy of the SRTM data is explained by the fact that the spectrum of topography is red, and thus the RMS difference is influenced more by the coherence at longer wavelengths.

Is there a logical reason why the SRTM data has worse short wavelength accuracy than the NED? We believe that such behavior is due to a boxcar filter applied in the final stage of SRTM processing in order to reduce the short-wavelength noise. We illustrate this thought by comparing the ratio of the power in SRTM
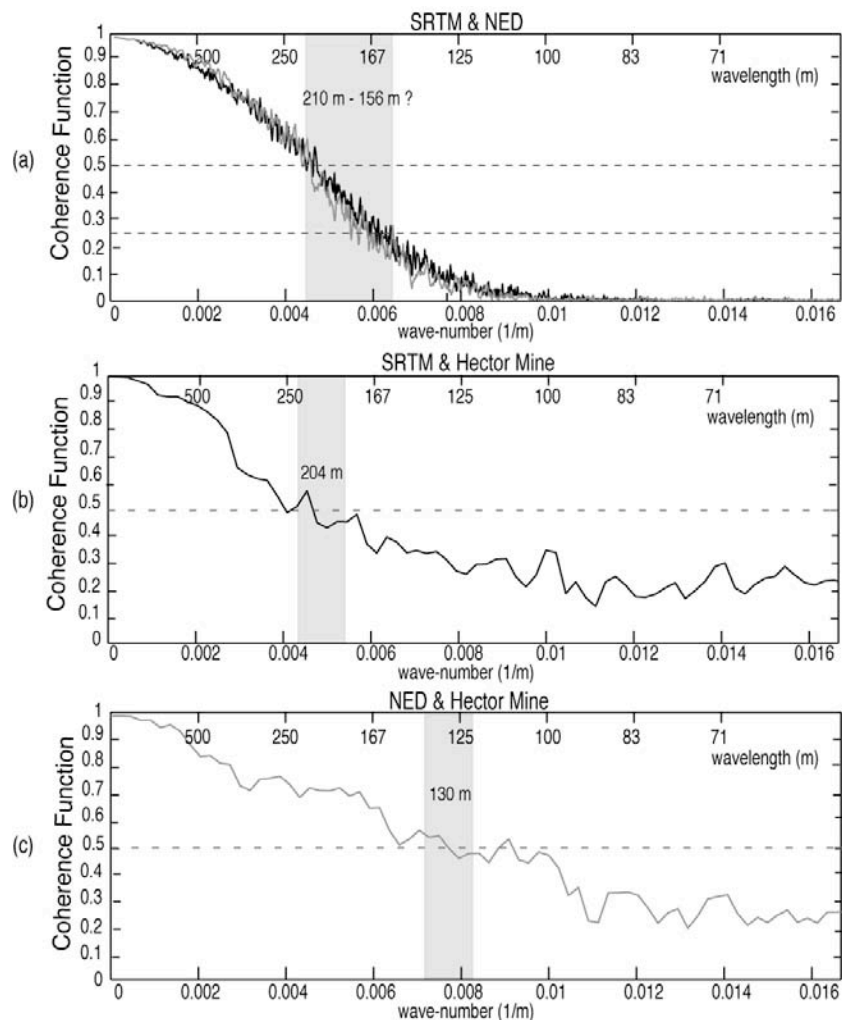
Figure 5.2. Coherence as a function of wavelength. (a) SRTM vs. NED coherence. Grey and black lines represent boxes 3 and 5 (Figure 5.1), respectively. (b) SRTM vs. Hector Mine ALSM coherence. (c) NED vs. Hector Mine ALSM coherence.

Table 5.1 Wavelength estimates of SRTM-NED cross-comparisons at 0.25 and 0.5 coherence. Boxed analyses correspond to the black and white dashed boxes of Figure 5.1. Calculated RMS differences (SRTM-NED) are also listed. Coherence and corresponding wavelengths are listed for each box.

	RMS difference	$\gamma_{xy}^2 = 0.25$	$\gamma_{xy}^2 = 0.5$
Box 1	5.72 m	152 m	195 m
Box 2	3.87 m	163 m	218 m
Box 3	4.75 m	156 m	204 m
Box 4	4.81 m	159 m	198 m
Box 5	4.90 m	161 m	211 m
Box 6	6.29 m	141 m	175 m

SRTM (and NED) data to the power in the Hector Mine ALSM data (Figure 5.3). Because we regard the Hector Mine ALSM power spectrum as precise, a ratio of less than one reflects a loss in power in SRTM (or the NED) due to filtering or smoothing of grids. From Figure 5.3, we note that for wavelengths shorter than 1250 m, the NED to ALSM ratio (grey) is consistently higher than the SRTM to ALSM ratio (black), reflecting a loss of power in the SRTM data. This observation was confirmed by *S. Hensley* [personal communication, 2002]; the SRTM DEM was smoothed during final processing with a boxcar filter of widths varying between 5 and 9 pixels, depending on terrain roughness. To illustrate the effect of such a filtering scheme, we compare the power of a 6-pixel boxcar/sinc-function filter in Figure 5.3 (black dashed curve) to the SRTM to ALSM power ratio (black). The two curves show similar power loss in the 500-1000 m band. For example, at 500 m the boxcar filter attenuates the SRTM amplitude by $\sqrt{0.5}$, or approximately 0.707. As an aside, we note that the NED to Hector Mine ALSM power ratio exceeds 1 near a wavelength of 900 m, perhaps reflecting the higher noise level of the NED data in this band.
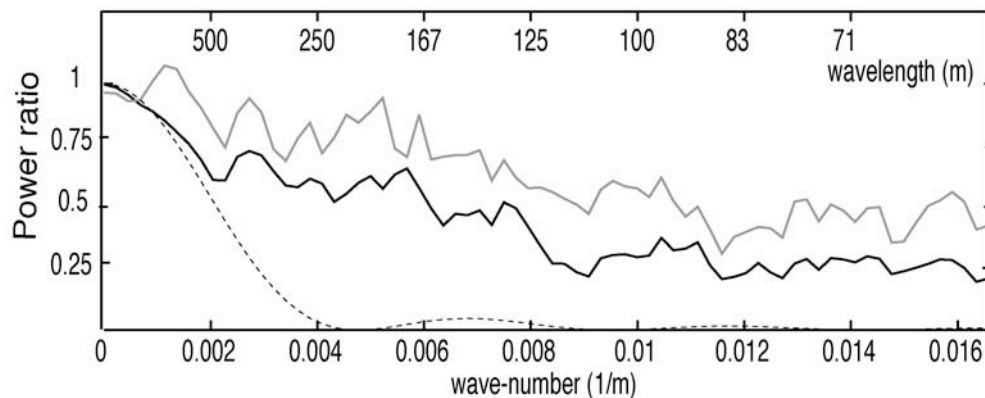
Figure 5.3. Power ratio of SRTM and NED signals to Hector Mine ALSM signal. Black line represents SRTM/Hector Mine ALSM power. Grey line represents NED/Hector Mine ALSM power. Black dashed line represents 6-pixel boxcar filter response in the wave-number domain.

5.4.3 Phase Shift

Large area SRTM and NED comparisons show a typical RMS difference of 5.70 m and display signatures associated with a relative systematic shift of one of the grids towards the northeast direction. For these areas, we calculate an average phase shift of 0.467 pixels in longitude (11.87 m) and 0.343 pixels in latitude (10.58 m) between SRTM and the NED. Again, we use the Hector Mine ALSM data to determine which data set is improperly shifted by computing coherence after shifting each data set in a variety of directions. For the NED, a shift of 11.87 m east and 10.58 m north results in the best coherence between the NED and Hector Mine ALSM spectrum. Shifting the SRTM data in all directions repeatedly produced lower coherence. Thus, we suspect that the NED contains the geo-location error. It is likely that this identified shift is a result of the inherent geo-location accuracy of the NED source data (12.2 m, circular error at 90% confidence) [*USGS*, 1999].

5.4.4 SRTM Filter and Decimation

As a final note, now that horizontal resolution has been established, a 2-D low-pass filter can be designed for a particular application, depending on whether a high resolution-high noise, or low resolution-low noise DEM is ideal. The cutoff wavelength of this filter should be selected to retain some of the low

SNR data because additional filters can be applied at a later time, if necessary. Based on this resolution analysis of SRTM data, we find that there is almost no significant power at wavelengths shorter than ~ 180 m (Figure 5.2b), which also corresponds to the first zero crossing of the sinc-function filter (Figure 5.3) applied to the data. Therefore, with no additional filtering, it would be safe to decimate the data from a 30 m sampling to perhaps a 60 m sampling without losing information. Alternatively, if the data are decimated from 30 m sampling to 90 m sampling to meet the security constraints imposed by NIMA, a low-pass filter should be designed with small side lobes in order to ensure that wavelengths above 180 m will not be aliased back into the longer wavelength part of the spectrum. The 90 m SRTM DEM that will eventually be made available for the entire globe will likely capture almost all of the information in the SRTM data.

5.5 Acknowledgements

5.6 References

Bendat, J.S., and A.G. Piersol, Random Data Analysis and Measurement Procedures. Second ed. New York: John Wiley & Sons, 1986.

Berry, P.A. M., J.E. Hoogerboord, and R.A. Pinnock, Identification of Common Error Signatures in Global Digital Elevation Models based on satellite Altimeter Reference Data, *Phys. Chem. Earth* (a), 25, 95-99, 2000.

Farr, T., and M. Kobrick, The Shuttle Radar Topography Mission, *Eos Trans. AGU*, 82, 47, 2001.

Gesch, D., M. Oimoen, S. Greenlee, C. Nelson, M. Steuck, and D. Tyler, The National Elevation Dataset, *J. Am. Soc. Phot. Rem. Sense.*, 68, 2002.

Hensley, S.P. Rosen, and E. Gurrola, Topographic map generation from the Shuttle Radar Topography Mission C-band SCANSAR interferometry, *Proc. SPIE*, 412, 179-189, 2000.

Hudnut, K., A. Borsa, C. Glennie, and J.B. Minster, High-Resolution Topography along Surface Rupture of the 16 October 1999 Hector Mine, California, Earthquake (M_w 7.1) from Airborne Laser Swath Mapping, *Bull. Seismol. Soc. Am.*, 92, 1570-1576, 2002.

Jordan, R., E. Caro, Y. Kim, M. Kobrick, Y. Shen, F. Stuhr, and M. Werner, Shuttle radar topography mapper (SRTM), *Proc. SPIE*, 2958, 412-422, 1996.

NIMA, Military Standard WGS84, http://164.214.2.59/publications/specs/printed/WGS84/wgs84.html, 1994.

Slater, J., J. Haase, B. Heady, G. Kroenung, J. Little, and C. Pessagno, NIMA's SRTM Data Processing Plans and Preliminary Data Assessments, *Eos Trans. AGU*, 82, 47, 2001.

SRTM_Topo, SRTM Readme file, ftp://fringe.jpl.nasa.gov, 2001.

Welch, P.D., The use of the fast Fourier transform for the estimation of power spectra: A method based on time averaging over short, modified periodograms, *IEEE Trans. Audio Electroacoust.*, 15, 70-73, 1967.

U. S. Geological Survey (USGS), Map Accuracy Standards, USGS Fact Sheet 171-99, 1999.